Anna Maria Wernbacher

# Hypersensitive transitions of rare earth ions

**Master's Thesis**

Graz University of Technology

Institute of Physical and Theoretical Chemistry
Head: Univ.-Prof. Mag.rer.nat. Dr.phil. Georg Gescheidt-Demner

Supervisor: Asst.Prof. Dipl.-Ing. Dr.techn. Anne-Marie Kelterer

Graz, March 2014

## Statutory Declaration

I declare that I have authored this thesis independently, that I have not used other than the declared sources/resources, and that I have explicitly marked all material which has been quoted either literally or by content from the used sources.

Graz, _____ _____

Date Signature

## Eidesstattliche Erklärung*

Ich erkläre an Eides statt, dass ich die vorliegende Arbeit selbstständig verfasst, andere als die angegebenen Quellen/Hilfsmittel nicht benutzt, und die den benutzten Quellen wörtlich und inhaltlich entnommenen Stellen als solche kenntlich gemacht habe.

Graz, am _____ _____

Datum Unterschrift

*Beschluss der Curricula-Kommission für Bachelor-, Master- und Diplomstudien vom 10.11.2008; Genehmigung des Senates am 1.12.2008

## Danksagung

Zunächst möchte ich mich bei meinen Betreuern Anne-Marie Kelterer und Karl Gatterer bedanken für ihre Hilfe bei den zahlreichen theoretischen sowie praktischen Herausforderungen und für ihre Geduld.

Des Weiteren möchte ich mich bei Christof Holzer bedanken, an dessen Arbeit diese Masterarbeit teilweise anschließt, und bei Dirk Andrae für hilfreiche Diskussionen über Symmetrie und den wichtigen Hinweis zur Zuordnung der Zustände von Neodym(III), sowie bei Lidia Smentek für ihre Hilfestellung bei der Judd-Ofelt Theorie.

Außerdem möchte ich mich beim Institut für Physikalische und Theoretische Chemie bedanken, insbesondere bei Professor Gescheidt-Demner, bei Helmut Eisenkölbl für seine Hilfe bei technischen Problemen, egal ob es sich um Computer, Experimente oder eine Klimaanlage im Sommer gehandelt hat, bei Hilde Freißmuth und Ines Gössler für ihre Hilfe, wenn es um die Laborausstattung und Chemikalienbeschaffung ging, und bei Marion Hofmeister für organisatorische Hilfestellungen.

Ich möchte mich darüber hinaus bei meiner Familie und bei Thomas bedanken für ihre Unterstützung, bei Thomas insbesondere auch für jegliche Hilfe mit LaTeX und Python.

# Abstract

Rare earth ions like neodymium(III) and europium(III) exhibit interesting optical properties owing to their partially filled f-orbitals, which lead to their application in laser materials or as luminophores.
The aim of this thesis was to investigate the so-called hypersensitive transitions of rare earth ions taking neodymium(III) and europium(III) as representatives. The intensities of these transitions are particularly sensitive to the environment, i.e. to the ligands surrounding the ion.
The main focus was the investigation of the symmetry dependence of the hypersensitive transitions.

Therefore, the absorbance and emission spectra of neodymium(III) and europium(III) in solvent mixtures of water, acetone and methanol were investigated experimentally in this thesis in order to evaluate the hypersensitive transitions in different environments. Furthermore, rare earth ion doped calcium aluminium borate (CAB) glasses were prepared corresponding to an environment of low symmetry. A Judd-Ofelt analysis of the optical spectra was performed yielding semi-empirical Judd-Ofelt intensity parameters, which were compared to literature values for neodymium(III) and europium(III) in various host materials. Particularly the parameter Omega-2 exhibited the expected dependence on the environment. Conclusions were drawn from these findings concerning the variation of the hypersensitive transition intensities in different environments.

In order to better understand these f-f transitions, theoretical studies using relativistic ab initio methods were performed to determine the electronic states, the transition energies as well as their oscillator strengths for neodymium(III) and europium(III). Various structures of the rare earth ion water complexes in different symmetries were optimized based on density functional theory calculations with large effective core potentials. These complexes were further investigated together with the free ions using several multi-reference methods like Kramers restricted configuration interaction and spin-orbit coupled CASSCF at the one-component Douglas-Kroll-Hess, two-component X2C and four-component Dirac-Coulomb

level of theory. The main findings of these calculations, i.e. the energy levels, oscillator strengths and computed Judd-Ofelt parameters, were compared to experimental and computed values. Calculations with increasing speed of light corresponding to the non-relativistic limit enabled the assignment of the states of neodymium(III).
A good agreement with the literature was found for the low energy states, while the description of the states of higher energy still needs improvement. As expected, non-zero oscillator strengths were only obtained for the low symmetric water complexes but not for centrosymmetric geometries.

# Kurzfassung

Seltenerdionen wie Neodym(III) und Europium(III) weisen interessante optische Eigenschaften auf, die durch ihre teilweise gefüllten f-Orbitale verursacht werden und zu Anwendungen in Lasermaterialien oder als Leuchtstoffe geführt haben.
Das Ziel dieser Masterarbeit war die Untersuchung der sogenannten hypersensitiven Übergänge der Seltenerdionen an den Beispielen Neodym(III) und Europium(III). Die Intensitäten dieser Übergänge variieren stark in Abhängigkeit von der Umgebung der Ionen, d.h. von den Liganden. Das Hauptaugenmerk lag dabei auf der Untersuchung der Symmetrie-Abhängigkeit der hypersensitiven Übergänge.

In dieser Masterarbeit wurden deswegen Absorptions- und Emissionsspektren von Neodym(III) und Europium(III) in Lösungsmittelmischungen von Wasser, Aceton und Methanol gemessen um die hypersensitiven Übergänge in unterschiedlichen Umgebungen zu untersuchen. Des Weiteren wurden Seltenerd-dotierte Calcium-Aluminium-Boratgläser (CAB-Gläser) hergestellt, die einer Umgebung von niedriger Symmetrie entsprechen.
Es wurde eine Judd-Ofelt Analyse der optischen Spektren durchgeführt. Die ermittelten semi-empirischen Judd-Ofelt Intensitätsparameter wurden mit Literaturwerten für Neodym(III) und Europium(III) in verschiedenen Wirtsmaterialien verglichen. Dabei zeigte der Parameter Omega-2 die erwartete Abhängigkeit von der Umgebung. Aus den Intensitätsänderungen der hypersensitiven Übergänge wurden Schlussfolgerungen bezüglich der Polarisierbarkeiten der unterschiedlichen Umgebungen gezogen.

Um diese f-f Übergänge besser verstehen zu können wurden weiters relativistische ab initio Methoden eingesetzt zur Bestimmung der elektronischen Zustände, der Energien der Übergänge sowie deren Oszillatorstärken. Dazu wurden verschiedene Strukturen von Neodym(III)- und Europium(III)-Wasser-Komplexen mit Dichtefunktionaltheorie und Pseudopotentialen optimiert. Diese Komplexe sowie die freien Ionen wurden darüber hinaus mit Multi-Referenz-Methoden wie Kramers restricted configuration interaction und Spin-Bahn gekoppeltem CASSCF untersucht unter Verwendung von skalar-relativistischen Douglas-Kroll-Hess, zweikomponentigen und vierkomponentigen Hamiltonoperatoren.

Die Ergebnisse der Rechnungen, d.h. die Energieniveaus, Oszillatorstärken und Judd-Ofelt Parameter, wurden mit experimentellen sowie theoretischen Werten verglichen. Rechnungen mit steigender Lichtgeschwindigkeit, die dem nichtrelativistischen Limit entsprechen, haben die Zuordnung der Zustände von Neodym(III) ermöglicht. Es wurde eine gute Übereinstimmung der energetisch niedrig liegenden Zustände mit Literaturwerten gefunden, während die Zustände höherer Energie noch Abweichungen von den Experimenten zeigten. Niedrig-symmetrische Strukturen ergaben von Null verschiedene Oszillatorstärken, während zentrosymmetrische Geometrien wie erwartet Oszillatorstärken gleich Null zeigten.

# Contents


Abstract v

1. Introduction 1

I. Theory 5

2. Crystal field and Judd-Ofelt theory 7
   2.1. Crystal field theory . . . 7
      2.1.1. Free ions . . . 7
      2.1.2. Ions in a crystal field . . . 16
   2.2. Judd-Ofelt theory . . . 18
   2.3. Hypersensitivity . . . 28

3. Computational methods 33
   3.1. Dirac's theory and four-component methods . . . 33
   3.2. Two-component Hamiltonians . . . 40
   3.3. Douglas-Kroll-Hess theory . . . 42
   3.4. Configuration Interaction . . . 44
   3.5. Multi-Configurational Self-Consistent Field – CASSCF . . . 47
   3.6. Basis sets and effective core potentials . . . 51
   3.7. Density Functional Theory . . . 56

4. Group theory and symmetry 65
   4.1. Double groups . . . 66
   4.2. The $SU(2)$, $SO(3)$ and other groups . . . 69
   4.3. Time reversal symmetry . . . 70
   4.4. Descent in symmetry . . . 72

II. Experiments and computations 75

5. Experiments 77
5.1. Reagents and instruments . . . 77
5.1.1. Synthesis of rare earth nitrates . . . 78
5.1.2. Glass preparation . . . 78
5.1.3. Sample solutions . . . 79
5.2. Experimental results of $Nd^{3+}$ . . . 82
5.2.1. Absorbance spectra . . . 82
5.2.2. Emission spectra . . . 89
5.2.3. Judd-Ofelt analysis . . . 91
5.3. Experimental results of $Eu^{3+}$ . . . 98
5.3.1. Absorbance spectra . . . 98
5.3.2. Emission spectra . . . 98
5.3.3. Judd-Ofelt analysis . . . 103

6. Computations 109
6.1. Methodology . . . 109
6.1.1. Calculation of geometries . . . 109
6.1.2. Calculation of states . . . 110
6.2. Symmetry . . . 111
6.3. Computational results of $Nd^{3+}$ . . . 113
6.3.1. Structures and energetics . . . 113
6.3.2. States of $Nd^{3+}$ . . . 115
6.4. Computational results of $Eu^{3+}$ . . . 122
6.4.1. Structures and energetics . . . 122
6.4.2. States of $Eu^{3+}$ . . . 122
6.4.3. Spectroscopy and Judd-Ofelt analysis . . . 132

7. Conclusion 137

Appendix 143

Bibliography 163

# List of Figures


2.1. Representation of vectors $\vec{r}_i$, $\vec{r}_j$ and $\vec{r}_{ij}$ of electrons $i$ and $j$ in the Cartesian coordinate system. . . . . 9
2.2. Some energy levels of $EuF_3$[28] as an example for the splitting of energy levels due to additional terms in the total Hamiltonian. . . . . 13

3.1. Concept of Generalized Active Spaces (GAS) taken from Fleig[70]. . . . . 47
3.2. Definition of an active space for CASSCF calculations taken from Jensen[71]. . 49

4.1. A Koch curve of third order. . . . . 65
4.2. Splitting of $^4F$ state taken from Tinkham[23]. . . . . 68

5.1. Colour of Nd-CAB-glass under different light sources. . . . . 82
5.2. Absorbance spectra of $Nd^{3+}$ in water-acetone mixtures. . . . . 84
5.3. Absorbance spectra of $Nd^{3+}$ in water-methanol mixtures. . . . . 84
5.4. Comparison of absorbance spectra of $Nd^{3+}$ in water, methanol and acetone. . 85
5.5. Absorbance spectra of $Nd^{3+}$ in water-acetone mixtures: absorption of solvents in UV and NIR region. . . . . 85
5.6. Absorbance spectrum of $Nd^{3+}$-CAB-glass. . . . . 86
5.7. Experimental energy levels of $Nd^{3+}$ compared with $NdF_3$[28]. . . . . 90
5.8. Emission spectra of $Nd^{3+}$ in water-DMSO mixtures and in acetone. . . . . 91
5.9. Judd-Ofelt parameters $\Omega_\lambda$ and oscillator strength of hypersensitive transition of $Nd^{3+}$ in water-acetone and water-methanol mixtures. . . . . 95
5.10. Absorbance spectra of $Eu^{3+}$ in water-acetone mixtures. . . . . 99
5.11. Absorbance spectra of $Eu^{3+}$ in water-methanol mixtures. . . . . 99
5.12. Absorbance spectrum of $Eu^{3+}$-CAB-glass. . . . . 100
5.13. Emission spectra of $Eu^{3+}$ in water-acetone mixtures. . . . . 100
5.14. Emission spectra of $Eu^{3+}$ in water-methanol mixtures. . . . . 101
5.15. Excitation spectrum and emission spectra of $Eu^{3+}$-CAB-glass. . . . . 101
5.16. Experimental energy levels of $Eu^{3+}$ compared with $EuF_3$[28]. . . . . 102

5.17. Judd-Ofelt parameters $\Omega_\lambda$ of $Eu^{3+}$ in water-acetone and water-methanol mixtures. . . . 106

6.1. $[Nd\ (H_2O)_3]^{3+}$, $D_{3h}$ ($C_{2v}$) (B3LYP ECP49MWB TZVP). . . . 115
6.2. **Nd-6w-Th**: $[Nd\ (H_2O)_6]^{3+}$, $T_h$ ($D_{2h}$) (B3LYP ECP49MWB TZVP). . . . 116
6.3. Energy levels of $Nd^{3+}$ (X2C KRCI Dyall cv3z) with increasing speed of light c equivalent to decreasing spin-orbit coupling (all states). . . . 117
6.4. Energy levels of $Nd^{3+}$ (X2C KRCI Dyall cv3z) with increasing speed of light c equivalent to decreasing spin-orbit coupling. . . . 118
6.5. Computed energy levels of $Nd^{3+}$ and $Nd^{3+}$-water complexes at different levels of theory compared with experimental values of $NdF_3$[28]. . . . 119
6.6. $[Eu\ (H_2O)_6]^{3+}$ (B3LYP ECP52MWB TZVP). . . . 122
6.7. $[Eu\ (H_2O)_8]^{3+}$ (B3LYP ECP52MWB TZVP). . . . 124
6.8. $[Eu\ (H_2O)_9]^{3+}$ (B3LYP ECP52MWB TZVP). . . . 124
6.9. $C_1$ structures of $\left[Eu\ (H_2O)_{6,8}\right]^{3+}$ (B3LYP ECP52MWB TZVP) used for multi-reference calculations. . . . 125
6.10. Computed energy levels of $Eu^{3+}$-water complexes (DKH SOC-CASSCF (6,7) TZVP-DKH) compared with experimental values. . . . 127
6.11. Holzer[128]: Computed energy levels of $Eu^{3+}$ and $Eu^{3+}$-water complexes at different levels of theory compared with experimental values of $EuF_3$[28]. . . . 129

.1. State diagram describing the Judd-Ofelt program . . . 146
.2. Descent in symmetry of D ($O(3)$). . . . 160
.3. Descent in symmetry of F ($O(3)$). . . . 161
.4. Descent in symmetry of G ($O(3)$). . . . 162

# 1. Introduction

Rare earth elements comprise lanthanum and the first row of the $f$-block from cerium to lutetium.[1] Many applications arise from their optical properties, e.g. as phosphors in television screens and computer displays, optical amplifiers in fiber optics, lasers and sensors,[2] just to mention a few of them.
Typical representatives of rare earth ions are neodymium and europium. Neodymium finds application in permanent magnets as Nd-Fe-B alloys[3–5] and in lasers, e.g. in green laser pointers using monopotassium phosphate crystals for frequency doubling.[6] A famous example is the Nd:YAG laser, i.e. neodymium-doped yttrium aluminium garnet $Nd:Y_3Al_5O_{12}$.[7,8] Europium(III) is widely used in phosphor technology as a red luminophore in TV sets, fluorescent lamps and some lasers.[2] Recent studies have discussed the use of $Eu^{3+}$ for water measurements in DMSO, in vivo imaging and other applications.[9,10]

The optical properties of rare earth elements are determined by their partially filled $f$-orbitals. The electronic transitions are mainly forced electric dipole transitions within the $4f$ configuration and therefore parity forbidden.[11] These $f \leftrightarrow f$ transitions have been the subject of many studies since the beginning of the twentieth century.
Many interesting spectroscopic properties are associated with rare earth ions. In the early years of the twentieth century the sharpness of the lines in absorbance and emission spectra of rare earth ions in crystals has stimulated the interest of many scientists.[12] Their spectra resemble the spectra of free ions or free atoms, in some cases with linewidths as narrow as 0.01 Å.[12] This suggests that the interaction with the surrounding ligands is very weak.[12] The small linewidths and weak interaction with the environment are a consequence of the shielding of the $4f$ shell by the outer filled $5s^2$ and $5p^6$ orbitals.[13] Rare earth ions are special in that their optical properties are caused by transitions within "core orbitals" that only participate to some extent in chemical bonding.[13–16] This explains the similarity to the spectra of free ions. Transition metal ions, on the contrast, exhibit $d \leftrightarrow d$ transitions, i.e. transitions between $d$-orbitals, which are also "binding orbitals".
The sharpness of the lines of rare earth ions, inter alia, makes them interesting as probes in biochemistry or generally as analytical sensors.[11,17,18]

Another very interesting phenomenon associated with $f \leftrightarrow f$ transitions of rare earth ions – and the topic of this thesis – are so-called hypersensitive transitions. Their intensities exhibit a great variation depending on the environment, while the intensities of the other transitions remain nearly unchanged. Various explanations exist, but there is still not a consistent theory available. A lot of theoretical as well as experimental studies have been conducted since Jørgensen & Judd[19] have introduced the term *hypersensitive* in 1964.

In this thesis the hypersensitive transitions of neodymium(III) and europium(III) were investigated experimentally in solvent mixtures showing the continuous increase in intensity of the hypersensitive transitions when going from water to another solvent like methanol or acetone. Several studies of rare earth ion doped glasses have been carried out. In the present thesis $Nd^{3+}$-doped and $Eu^{3+}$-doped calcium aluminium borate glasses were prepared as a model system of low symmetry.

Relativistic effects are of much importance when investigating rare earth ions. Scalar relativistic effects caused by the high velocities of the inner electrons due to heavy nuclei lead to a contraction of the *s*- and *p*-orbitals, therefore enhancing the shielding of the outer electrons from the nuclear potential.[13,20] This results in an expansion of the *d*- and *f*-orbitals.[13,20] Such scalar relativistic effects are for example responsible for the colour of gold.[20]
Even more important for this thesis were magnetic couplings, which involve spin-orbit coupling. The electron spin couples to the magnetic field associated with the orbital motion of the electrons.[20] As a consequence, states of mixed spin and orbital angular momentum quantum numbers arise and only the total angular momentum $J$ and $M_J$ quantum numbers are considered to be "good" quantum numbers.[20] Thus transitions that are spin-forbidden in a non-relativistic theory can be explained taking the spin-orbit coupling into account.[21] In the case of rare earth elements or ions, the spin-orbit splitting is even of the same order of magnitude as the electron-electron Coulomb interaction, which makes a proper description of this effect necessary using relativistic quantum chemical methods.[12,21]

In relatively few theoretical *ab initio* analyses the hypersensitive transition of $Nd^{3+}$ was investigated. More studies have been conducted on $Eu^{3+}$, but the number is still limited. In the past, Judd-Ofelt theory served as a useful tool to investigate $f \leftrightarrow f$ transitions. It is still very popular as a semi-empirical theory and there is extensive literature available concerning Judd-Ofelt analyses of rare earth ions in crystals, glasses or various complexes. Yet, modern *ab initio* Judd-Ofelt theory, e.g. extended to the relativistic framework by Smentek & Wybourne[22], is still rarely applied.

This thesis presents an *ab initio* investigation of the $f \leftrightarrow f$ transitions of $Nd^{3+}$ and $Eu^{3+}$ based on relativistic multi-reference methods. One-component Douglas-Kroll-Hess SOC-CASSCF calculations are compared to two-component X2C and four-component Dirac-Coulomb KRCI calculations of the free ions as well as of water complexes of the rare earth ions in different symmetries.

The present thesis is structured as follows:
The first part focuses on the theory behind the used methods. The theoretical background for Judd-Ofelt calculations is presented in chapter 2 and the computational methods are described in chapter 3. The group theoretical considerations are treated in chapter 4.
The second part of this thesis presents the results and conclusions. It is divided into experiments, chapter 5, and computations, which are shown in chapter 6.

# Part I.

# Theory

# 2. Crystal field and Judd-Ofelt theory

## 2.1. Crystal field theory

### 2.1.1. Free ions

#### Hamiltonian

The total Hamiltonian of the free ion with $N$ electrons, $\hat{H}_{FI}$, is given by the sum[12]

$$\hat{H}_{FI} = \hat{H}_0 + \hat{H}_C + \hat{H}_{SO} + \ldots \quad . \tag{2.1}$$

$$\hat{H}_0 = \sum_{i=1}^{N} \hat{h}_i = \sum_{i=1}^{N} \left( -\frac{\hbar^2}{2m_e} \nabla_i^2 - \frac{1}{4\pi\varepsilon_0} \frac{Ze^2}{R_i} \right) \tag{2.2}$$

$\hat{H}_0$ itself is the sum of one-electron operators describing the kinetic energy of the electrons and the electron-nucleus attraction potential due to the Coulomb force, where $\nabla^2 = \Delta$ denotes the Laplace operator, $m_e$ the mass of the electron, $e$ the elementary charge, $Z$ the nuclear charge and $R$ the electron-nucleus distance. In the *central field approximation* $Z$ is replaced by an effective nuclear charge, $Z_{eff}$, to account for the screening of the outer electrons from the force field of the nucleus by the inner (closed shell) electrons. $\hat{H}_0$ is a spherical symmetric operator.[12,23]

$$\hat{H}_C = \frac{1}{4\pi\varepsilon_0} \sum_{i<j=1}^{N} \sum \frac{e^2}{r_{ij}} \tag{2.3}$$

The two-electron operator $\hat{H}_C$ describes the electron-electron repulsion, which is also caused by a Coulomb force, $r_{ij}$ being the distance between the electrons $i$ and $j$.[12] For actual crystal field calculations, $\hat{H}_C$ is expanded into spherical harmonics.[21,24]

$$\frac{e^2}{r_{ij}} = \frac{e^2}{|\vec{r}_i - \vec{r}_j|} = \frac{e^2}{\sqrt{r_i^2 + r_j^2 - 2r_i r_j \cos\omega}}$$

Let $r_>$ be the larger of the two distances (either $r_i$ or $r_j$) and $r_<$ be the smaller distance, then one can express $\frac{e^2}{r_{ij}}$ as

$$\frac{e^2 r_>}{r_{ij} r_>} = \frac{e^2}{r_>}\left(1 + \frac{r_<^2}{r_>^2} - 2\frac{r_<}{r_>}\cos\omega\right)^{-\frac{1}{2}} \quad . \tag{2.4}$$

Using the known relation

$$(1 - 2ax + x^2)^{-\frac{1}{2}} = \sum_{k=0}^{\infty} x^k P_k(a) \tag{2.5}$$

and the connection between Legendre polynomials $P_k(\cos\omega)$ and spherical harmonics $Y_q^{(k)}$

$$P_k(\cos\omega) = \frac{4\pi}{2k+1} \sum_{q=-k}^{k} Y_q^{(k)*}(i) \cdot Y_q^{(k)}(j) \tag{2.6}$$

$$\begin{aligned} \frac{e^2}{r_{ij}} =& \frac{e^2}{r_>} \cdot \left(1 + \frac{r_<^2}{r_>^2} - 2\frac{r_<}{r_>}\cos\omega\right)^{-\frac{1}{2}} = e^2 \sum_{k=0}^{\infty} \frac{r_<^k}{r_>^{k+1}} P_k(\cos\omega) \\ =& e^2 \sum_{k=0}^{\infty} \frac{4\pi}{(2k+1)} \frac{r_<^k}{r_>^{k+1}} \sum_{q=-k}^{k} Y_q^{(k)*}(i) \cdot Y_q^{(k)}(j) \quad . \end{aligned} \tag{2.7}$$

In this way, the Coulomb operator $\hat{H}_C$ can be expanded into spherical harmonics.[24]

$$\hat{H}_C = \frac{e^2}{4\pi\varepsilon_0} \sum_{i<j=1}^{N} \sum_{k=0}^{\infty} \frac{4\pi}{(2k+1)} \frac{r_<^k}{r_>^{k+1}} \sum_{q=-k}^{k} Y_q^{(k)*}(i) \cdot Y_q^{(k)}(j) \tag{2.8}$$

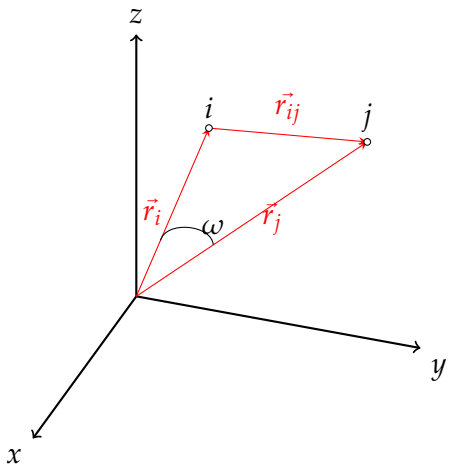


Figure 2.1.: Representation of vectors $\vec{r}_i$, $\vec{r}_j$ and $\vec{r}_{ij}$ of electrons $i$ and $j$ in the Cartesian coordinate system.

Finally, $\hat{H}_{SO}$ describes the spin-orbit coupling, i.e. the coupling of the spin of electron $i$ ($\mathbf{s}_i$) and the orbital angular momentum of the electron $i$ ($\boldsymbol{\ell}_i$).[12]

$$\hat{H}_{SO} = \sum_{i=1}^{N} \xi(r_i)\, \boldsymbol{\ell}_i \cdot \mathbf{s}_i \tag{2.9}$$

$\xi(r_i)$ is the spin-orbit coupling function of electron $i$ moving in the potential $U(r_i)$.[12]

$$\xi(r_i) = \frac{\hbar^2}{2m^2c^2r_i}\frac{dU(r_i)}{dr_i} \tag{2.10}$$

### Wave function

An electron may be described by a one-electron wave function[24,25]

$$\phi_{n\ell m_\ell m_s}(r,\vartheta,\varphi) = R_{n\ell}(r)\cdot Y_{m_\ell}^{(\ell)}(\vartheta,\varphi)\cdot\sigma_{m_s} \quad . \tag{2.11}$$

$R_{n\ell}(r)$ is the radial part, $Y_{m_\ell}^{(\ell)}(\vartheta,\varphi)$ the angular part, which is a spherical harmonic function, and $\sigma_{m_s}$ is the spin function. The N electron system can therefore be described by antisymmetrized products of $N$ such wave functions, so called Slater determinants $\Theta$ or determinantal wave functions, consistent with the Pauli principle (2.13). This principle states that the many-electron wave function must change sign if the space and spin coordinates $\mathbf{x}$ of two electrons are interchanged, i.e. the many-electron wave function must be antisymmetric.[26]

$$\Theta = \frac{1}{\sqrt{N!}} \begin{vmatrix} \phi_a(1) & \phi_a(2) & \phi_a(3) & \cdots & \phi_a(N) \\ \phi_b(1) & \phi_b(2) & \phi_b(3) & \cdots & \phi_b(N) \\ \phi_c(1) & \phi_c(2) & \phi_c(3) & \cdots & \phi_c(N) \\ \vdots & \vdots & \vdots & \ddots & \vdots \\ \phi_n(1) & \phi_n(2) & \phi_n(3) & \cdots & \phi_n(N) \end{vmatrix} \tag{2.12}$$

$$\Theta(\mathbf{x}_1, ..., \mathbf{x}_i, ..., \mathbf{x}_j, ..., \mathbf{x}_N) = -\Theta(\mathbf{x}_1, ..., \mathbf{x}_j, ..., \mathbf{x}_i, ..., \mathbf{x}_N) \tag{2.13}$$

The indices $a$, $b$, $c$, ..., $n$ label the different sets of the 4 quantum numbers $n$, $\ell$, $m_\ell$ and $m_s$, while the numbers 1, 2, 3, ..., $N$ refer to the coordinates ($r$, $\vartheta$, $\varphi$) of the $N$ electrons. These Slater determinants are eigenfunctions of $\hat{H}_0$, in which no electron-electron interaction is included. The number of different Slater determinants $\Theta$ for a given configuration of $N$ equivalent electrons corresponds to the number of ways of arranging $N$ electrons in $2 \cdot (2\ell + 1)$ spin orbitals.[24]

$$\frac{[2 \cdot (2\ell + 1)]!}{N![2 \cdot (2\ell + 1) - N]!} \tag{2.14}$$

All of these Slater determinants for a given configuration have the same eigenvalue, i.e. they are highly degenerate.[24]
In the case of $Nd^{3+}$ 354 Slater determinants are obtained for the configuration $4f^3$ ($Nd^{3+}$: [Xe]$4f^3$), whereas $Eu^{3+}$ yields 3,003 Slater determinants for the configuration $4f^6$ ($Eu^{3+}$: [Xe]$4f^6$) in the central field approximation.

When the electron-electron interaction, $\hat{H}_C$, is included in the total Hamiltonian of the system, the energy levels are split into new levels, i.e. the degeneracy is lifted to some extent, and new wave functions are needed, which can be expressed as linear combinations of the original eigenfunctions.[24] This is a general observation when an extra term is added to the Hamiltonian of the system.

At the level of electron-electron interaction, the individual angular momenta $\boldsymbol{\ell}_i$ and spins $\mathbf{s}_i$ couple to the total orbital angular momentum $\mathbf{L}$ and total spin $\mathbf{S}$ according to the vector model of atoms. This is called the *Russell-Saunders* or *LS*-coupling.[21]

$$\mathbf{L} = \sum_{i=1}^{N} \boldsymbol{\ell}_i \tag{2.15}$$

$$\mathbf{S} = \sum_{i=1}^{N} \boldsymbol{s}_i \tag{2.16}$$

The orbital angular momentum and spin projection quantum numbers, $M_L = -L, -L+1, \ldots, +L$ and $M_S = -S, -S+1, \ldots, +S$,* are given by[24]

$$M_L = \sum_{i=1}^{N} m_\ell(i) \tag{2.17}$$

$$M_S = \sum_{i=1}^{N} m_s(i) \quad . \tag{2.18}$$

The new Russell-Saunders wave functions are named $\Psi(L, M_L, S, M_S)$. They are $(2L+1)\cdot(2S+1)$-fold degenerate eigenfunctions of $(\hat{H}_0 + \hat{H}_C)$. Their energy levels are labelled with Russell-Saunders term symbols $^{2S+1}$L.[24]

$$\Psi = \sum_i c_i \cdot \Theta_i \tag{2.19}$$

Introducing $\hat{H}_{SO}$ into the total Hamiltonian again results in a splitting of energy levels and a mixing of wave functions. The spin and the orbital angular momentum couple to a total angular momentum given by the quantum number $J$. In other words, the effect of $\hat{H}_{SO}$ is the mixing of states with same $J$, but different $S$ and $L$ values.[12] The consequence is that neither the spin quantum number $S$, nor the (orbital) angular momentum quantum number $L$ are "good" quantum numbers any more at this level of theory.
The new wave functions are $(2J+1)$-fold degenerate eigenfunctions of $\hat{H}_{FI} = \hat{H}_0 + \hat{H}_C + \hat{H}_{SO}$ and can be expressed as linear combinations of the original Russell-Saunders wave functions[24]

$$\Psi(L, S, J, M_J) = \sum_{S,L} c_{S,L} \cdot \Psi(L, M_L, S, M_S) \quad . \tag{2.20}$$

*The $z$ component of $\mathbf{L}$ is given by $L_z = M_L\hbar$ and of $\mathbf{S}$ by $S_z = M_S\hbar$.[27]

The energy levels are denoted with the Russell-Saunders term symbol $^{2S+1}L_J$ of the term which gives the *largest contribution* to the linear combination (2.20). One should keep in mind that there are usually other contributions to this state as well, which may have another multiplicity $(2S+1)$ or angular momentum quantum number $L$.

In the case of rare earth ions $\hat{H}_{SO}$ is approximately of the order of $\hat{H}_C$, whereas the spin-orbit coupling is small for (first-row) transition metal ions, where it is therefore usually neglected or can be treated as a small perturbation.[12,24] For example, the splitting of the $^7F_J$ states of $Eu^{3+}$ due to $\hat{H}_{SO}$ lies in the order of some hundred to approximately 1,000 $cm^{-1}$ and the separation of the $^5D_J$ states in the order of 1,000 $cm^{-1}$ (up to 3,000 $cm^{-1}$). The energy differences between $^{2S+1}L_J$ states increase with increasing atomic number, thus reflecting a stronger spin-orbit coupling or larger $\xi$, respectively.[12] In the case of $Yb^{3+}$ ($4f^{13}$), a splitting of 10,000 $cm^{-1}$ between the $^2F_{7/2}$ and $^2F_{5/2}$ state is found.[12]

### Free ion energies

For energy calculations of free ions, the matrix elements of the spin-orbit wave functions between $(\hat{H}_C + \hat{H}_{SO})$, $\langle \Psi(L,S,J,M_J) | (\hat{H}_C + \hat{H}_{SO}) | \Psi(L,S,J,M_J) \rangle$, have to be evaluated. $\hat{H}_0$ does not need to be considered in spectroscopy where only energy differences are relevant.[24] On the one hand, the spin-orbit wave functions $\Psi(L,S,J,M_J)$ are expanded into linear combinations of Russell-Saunders wave functions $\Psi(L,M_L,S,M_S)$, which themselves are expressed in terms of Slater determinants $\Phi$, i.e. antisymmetrized products of one-electron wave functions $\phi_{n\ell m_\ell m_s}(r,\vartheta,\varphi)$. On the other hand, $\hat{H}_C$ is expanded into spherical harmonics. Thus, the integrals $\langle \Psi(L,S,J,M_J) | \hat{H}_C | \Psi(L,S,J,M_J) \rangle$ can be reduced to smaller integrals, which are essentially products of a radial part $R^k(ab;de)$, an angular part $A^k$ and a spin part.[24]

$$\begin{aligned} \hat{H}_C &= \frac{1}{4\pi\varepsilon_0} \sum_{i<j=1}^{N} \sum \frac{e^2}{r_{ij}} \\ &= \frac{1}{4\pi\varepsilon_0} \sum_{i<j=1}^{N} \sum e^2 \sum_{k=0}^{\infty} \frac{r_<^k}{r_>^{k+1}} \frac{4\pi}{(2k+1)} \sum_{q=-k}^{k} Y_q^{(k)*}(i) \cdot Y_q^{(k)}(j) \end{aligned} \tag{2.21}$$

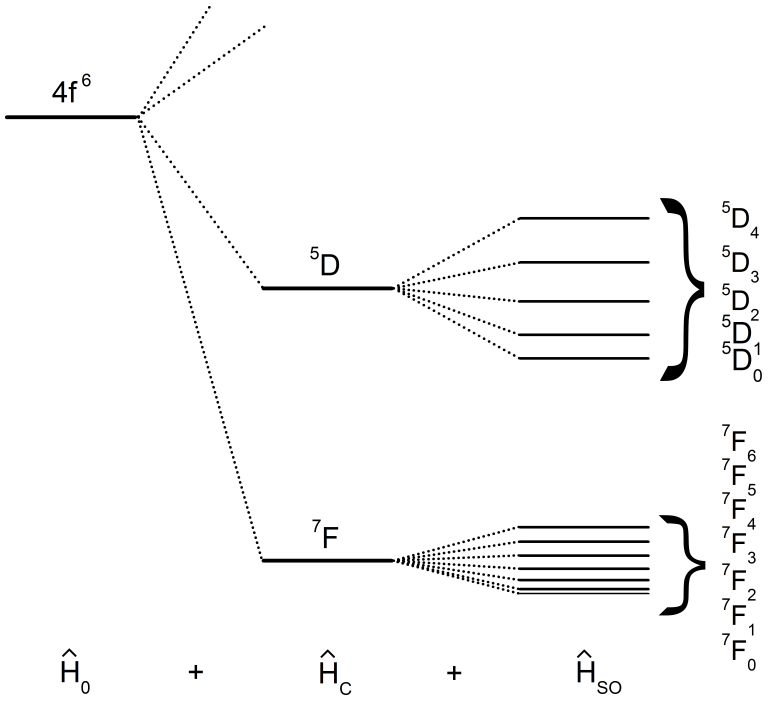


Figure 2.2.: Some energy levels of $EuF_3$[28] as an example for the splitting of energy levels due to additional terms in the total Hamiltonian.

$$\left\langle \Psi(L,S,J,M_J) \middle| \hat{H}_C \middle| \Psi(L,S,J,M_J) \right\rangle = \sum \left\langle \Phi_r \middle| \hat{H}_C \middle| \Phi_s \right\rangle \tag{2.22}$$

$$\left\langle \Phi_r \middle| \frac{e^2}{r_{ij}} \middle| \Phi_s \right\rangle = \sum \left\langle \phi_a(i)\phi_b(j) \middle| \frac{e^2}{r_{ij}} \middle| \phi_d(i)\phi_e(j) \right\rangle \cdot \delta(\phi_c(k), \phi_f(k)) \tag{2.23}$$

The two-electron operator $\hat{H}_C$ does not contain spin, so the integration over the spin coordinates can be carried out separately yielding the Kronecker delta function $\delta$ for the orthonormal spin functions $\sigma$.[29]

$$\phi_a(i) = R_a \cdot Y_{m_a}^{(\ell)}(i) \cdot \sigma_a$$

$$\left\langle \phi_a(i)\phi_b(j) \left| \frac{e^2}{r_{ij}} \right| \phi_d(i)\phi_e(j) \right\rangle =$$

$$\sum_{k=0}^{\infty} \left\langle R_a R_b \left| \frac{e^2 r_<^k}{r_>^{k+1}} \right| R_d R_e \right\rangle \tag{2.24}$$

$$\cdot \frac{4\pi}{(2k+1)} \sum_{q=-k}^{k} \left\langle Y_{m_a}^{(\ell)}(i) Y_{m_b}^{(\ell)}(j) \left| Y_q^{(k)*}(i) \cdot Y_q^{(k)}(j) \right| Y_{m_d}^{(\ell)}(i) Y_{m_e}^{(\ell)}(j) \right\rangle \tag{2.25}$$

$$\cdot \delta(\sigma_a, \sigma_d) \cdot \delta(\sigma_b, \sigma_e) \tag{2.26}$$

(2.24) is the radial part $R^k(ab;de)$, or Slater parameter $F^k$, which is an infinite sum over the radial parts of the wave functions and the operator. The calculation of these integrals is the major problem in crystal field calculations, so they are usually accounted for by empirical parameters called the *Racah parameters*. In the case of transition metal ions, there are three Racah parameters $A$, $B$ and $C$, whereas four Racah parameters $E^0$, $E^1$, $E^2$ and $E^3$ are obtained for rare earth ions. These parameters are fitted so as to obtain the best agreement between calculated and experimental energy levels of the free ions using atomic spectroscopy. The number of possible $k$ values is therefore limited to three for transition metal ions ($d$-elements) and to four for rare earth ions ($f$-elements).[24]

The angular part $A^k$ of the wave functions and the operator (2.25) is a product of spherical harmonics, one part of them depending solely on the coordinates of electron $i$, the other part depending on the coordinates of electron $j$. Hence, this integral can be written as a product[24]

Table 2.1.: The relationship between Slater parameters $F^k$, i.e. the radial integrals, Condon-Shortley parameters $F_k$ and Racah parameters $A$, $B$, $C$ for transition metal ions[24] (left) and $E^k$ for rare earth ions[12] (right).

| | | | |
|---|---|---|---|
| $F_0 = F^0$ | $A = F_0 - 49F_4$ | $F_0 = F^0$ | $E^0 = F_0 - 10F_2 - 33F_4 - 286F_6$ |
| $F_2 = (49)^{-1} F^2$ | $B = F_2 - 5F_4$ | $F_2 = (225)^{-1} F^2$ | $E^1 = \frac{1}{9}(70F_2 + 231F_4 + 2,002F_6)$ |
| $F_4 = (441)^{-1} F^4$ | $C = 35F_4$ | $F_4 = (1089)^{-1} F^4$ | $E^2 = \frac{1}{9}(F_2 - 3F_4 + 7F_6)$ |
| | | $F_6 = \frac{25}{184,041} F^6$ | $E^3 = \frac{1}{3}(5F_2 + 6F_4 - 91F_6)$ |

$$A^k = \frac{4\pi}{2k+1} \sum_{q=-k}^{k} \left\langle Y_{m_a}^{(\ell)}(i) \middle| Y_q^{(k)*}(i) \middle| Y_{m_d}^{(\ell)}(i) \right\rangle \left\langle Y_{m_b}^{(\ell)}(j) \middle| Y_q^{(k)}(j) \middle| Y_{m_e}^{(\ell)}(j) \right\rangle \quad .$$

Solutions to such integrals are known.[29] The only non-zero solutions for transition metal ions are those with $k = 0, 2, 4$ and for rare earth ions with $k = 0, 2, 4, 6$. This explains the number of Racah parameters.

$$\left\langle Y_{m_1}^{(\ell_1)} \middle| Y_q^{(k)} \middle| Y_{m_2}^{(\ell_2)} \right\rangle = \int_{\varphi=0}^{2\pi} \int_{\vartheta=0}^{\pi} Y_{m_1}^{(\ell_1)}(\vartheta,\varphi)\, Y_q^{(k)}(\vartheta,\varphi)\, Y_{m_2}^{(\ell_2)}(\vartheta,\varphi)\, \sin\vartheta \, d\vartheta d\varphi \tag{2.27}$$

$$= (-1)^{m_1} \left[ \frac{(2\ell_1+1)(2k+1)(2\ell_2+1)}{4\pi} \right]^{\frac{1}{2}} \begin{pmatrix} \ell_2 & k & \ell_1 \\ 0 & 0 & 0 \end{pmatrix} \begin{pmatrix} \ell_2 & k & \ell_1 \\ m_2 & q & -m_1 \end{pmatrix} \tag{2.28}$$

$$= (-1)^{\ell_1 - m_1} \begin{pmatrix} \ell_1 & k & \ell_2 \\ -m_1 & q & m_2 \end{pmatrix} \left\langle Y^{(\ell_1)} \middle\| \hat{Y}^{(k)} \middle\| Y^{(\ell_2)} \right\rangle \tag{2.29}$$

Equation (2.29) is the application of the *Wigner-Eckart theorem*[30,31], according to which such integrals can be expressed as products of the 3-$j$ symbol (2.30) and a so-called reduced matrix element, which is independent of the quantum numbers $m_1$, $m_2$ and $q$.[23,29]

$$\begin{pmatrix} \ell_1 & k & \ell_2 \\ -m_1 & q & m_2 \end{pmatrix} = (-1)^{\ell_1 - k - m_2} (2\ell_2+1)^{-\frac{1}{2}} \langle \ell_1 m_1, kq \,|\, \ell_2 \; -m_2 \rangle \tag{2.30}$$

The 3-$j$ symbol vanishes unless the relations (2.31) and (2.32) are fulfilled.[23]

$$-m_1 + q + m_2 = 0 \tag{2.31}$$

$$(\ell_2 + k) \geq \ell_1 \geq |\ell_2 - k| \tag{2.32}$$

From the "triangle relation" (2.32) follows for $d$-electron systems, i.e. transition metal ions, with $\ell_1 = \ell_2 = 2$ that $k$ can only take the values 0, 1, 2, 3, 4 and for $f$-electron systems, e.g. rare earth ions, with $\ell_1 = \ell_2 = 3$ that $k = 0, 1, 2, \ldots, 6$ ($k \in \mathbb{N}_0$).

Another general requirement for such integrals or matrix elements to be non-zero, which originates from group theoretical considerations, is that the integrals must be of even parity (g).[23†] As a consequence of $\ell_1 = \ell_2$ (equal parity), the parity $p$ of the spherical harmonic $Y_q^{(k)}$ must be even or $k$ must be an even number, respectively. Hence, the only possible numbers of $k$ for transition metal ions are 0, 2, 4 and for rare earth ions 0, 2, 4, 6.

$$p(Y_q^{(k)}) = (-1)^k \tag{2.33}$$

$$\ell_1 = \ell_2 = 2: \quad (-1)^2 \cdot (-1)^k \cdot (-1)^2 = +1 \tag{2.34}$$

$$\ell_1 = \ell_2 = 3: \quad (-1)^3 \cdot (-1)^k \cdot (-1)^3 = +1 \tag{2.35}$$

Integration over the orthonormal spin functions yields the Kronecker delta function (2.26), which is either zero for different spin quantum numbers $S$, or 1 for equal $S$.

If the Racah parameters $E$ and the spin-orbit coupling constants $\xi$ are known, the energy of the free ion can thus be calculated.[12]

### 2.1.2. Ions in a crystal field

In crystal field theory the interaction of ligands with a central metal ion is treated as a purely electrostatic interaction without any covalent contributions, which is one of the major drawbacks of this theory.[24] The electrostatic ligand field of a certain symmetry is described by an additional term, $\hat{H}_{CF}$, in the total Hamiltonian of the system. The crystal field operator $\hat{H}_{CF}$ gives rise to a further splitting of energy levels, the crystal field splitting, into Stark levels or crystal field levels as well as to a further mixing of the wave functions.[24] The symmetry of the crystal field determines the number of arising Stark levels, while its strength determines the magnitude of the splitting.[12]
In the case of rare earth ions, $\hat{H}_{CF}$ is very small compared to $\hat{H}_{SO}$, which is a consequence of the *shielding* of the $f$-electrons by the outer lying filled subshells. The crystal field splitting can therefore not be observed in experimental spectra of rare earth ions in solution or in

[†] A matrix element $\langle \psi_{k'}^{(j')} | \hat{H}' | \psi_k^{(j)} \rangle$ vanishes unless the totally symmetric representation is included in the direct product of the irreducible representations of the operator $\hat{H}'$ and the functions $\psi$.[23]

glasses, which exhibit greater line widths due to the *inhomogeneous broadening*.[24] However, for first-row transition metal ions the relation $\hat{H}_{SO} < \hat{H}_{CF} < \hat{H}_C$ is valid, i.e. the crystal field interaction is more important than the spin-orbit splitting.[24]
The resulting crystal field states are labelled with the irreducible representations of the symmetry point group $^{2S+1}\Gamma$. Interactions can only occur between states of the same symmetry.

In *Kramers ions* like $Nd^{3+}$ with an odd number of $f$-electrons and half-integer values of $J$ the free ion energy levels are split into $(J+\frac{1}{2})$ Stark levels in a crystal field of low symmetry, thus retaining a rest degeneracy of 2, the so-called Kramers degeneracy, while in *non-Kramers ions* like $Eu^{3+}$ with an even number of $f$-electrons and integer values of $J$ the free ion energy levels are split into $(2J+1)$ Stark levels in a crystal field of low symmetry, hence removing the degeneracy.[12,24]

$$\hat{H}_{CF} = \sum_i \int_\tau \frac{e \cdot \rho(\mathbf{R})}{|\mathbf{R} - \mathbf{r_i}|} d\tau \tag{2.36}$$

The operator $\hat{H}_{CF}$ is similar to $\hat{H}_C$, with $\rho(\mathbf{R})$ as the charge density at the position $\mathbf{R}$, which is caused by the ligands, i.e. a kind of a smeared instead of a localized charge.[12] This can be regarded as a special form of an electron-electron interaction with a charge cloud $\int \rho(\mathbf{R}) d\tau$ instead of a point charge $q_e = -e$.[24] Like $\hat{H}_C$, $\hat{H}_{CF}$ can be expanded into spherical harmonics[24]

$$\hat{H}_{CF} = e \cdot \sum_{k,q,i} \int_\tau \rho(\mathbf{R}) \frac{r_<^k}{r_>^{k+1}} \sqrt{\frac{4\pi}{2k+1}}\, \hat{Y}_q^{(k)*}(\vartheta,\varphi) \sqrt{\frac{4\pi}{2k+1}}\, \hat{Y}_q^{(k)}(\vartheta_i,\varphi_i) d\tau \tag{2.37}$$

$$= e \cdot \sum_{k,q,i} \int_\tau \rho(\mathbf{R}) \frac{r_<^k}{r_>^{k+1}}\, \hat{C}_q^{(k)*}(\vartheta,\varphi)\, \hat{C}_q^{(k)}(\vartheta_i,\varphi_i) d\tau \tag{2.38}$$

using the Racah normalization of spherical harmonics $\hat{C}_q^{(k)}(\vartheta,\varphi)$.[12]

$$\hat{C}_q^{(k)}(\vartheta,\varphi) = \sqrt{\frac{4\pi}{2k+1}}\, \hat{Y}_q^{(k)}(\vartheta,\varphi) \tag{2.39}$$

The crystal field parameters $B_{kq}$ are given by[12]

$$B_{kq} = e \cdot \int_\tau \rho(\mathbf{R})\, \hat{C}_q^{(k)*}(\vartheta,\varphi)\, \frac{r_<^k}{r_>^{k+1}}\, d\tau \quad . \tag{2.40}$$

The expansion of $\hat{H}_{CF}$ into spherical harmonics depends on the symmetry of the crystal field, which leads to a reduction of possible $k$ values, i.e. of the number of spherical harmonics which have to be included in the expansion.[24]

$$\hat{H}_{CF} = \sum_{k,q,i} B_{kq} \hat{C}_q^{(k)}(i) \tag{2.41}$$

First of all, the number of possible values of $k$ and $q = -k, -k+1, ..., +k$ are reduced by the Wigner-Eckart theorem (see equations (2.31) and (2.32)). Then, the number is further reduced by the symmetry of the crystal field. For example one obtains $k = 4$ and $q = -4, 0, 4$ for a $d$-electron system in an octahedral field, and only one crystal field parameter, $B_{40}$, remains[24]

$$\hat{H}_{CF,O_h} = B_{40}\left[\hat{C}_0^{(4)} + \sqrt{\frac{5}{14}}(\hat{C}_4^{(4)} + \hat{C}_{-4}^{(4)})\right] \quad . \tag{2.42}$$

In the case of rare earth ions ($f$-electron systems) in an octahedral field, the crystal field operator $\hat{H}_{CF,O_h}$ is given by[32]

$$\hat{H}_{CF,O_h} = B_{40}\left[\hat{C}_0^{(4)} + \sqrt{\frac{5}{14}}(\hat{C}_4^{(4)} + \hat{C}_{-4}^{(4)})\right] + B_{60}\left[\hat{C}_0^{(6)} + \sqrt{\frac{7}{2}}(\hat{C}_4^{(6)} + \hat{C}_{-4}^{(6)})\right] \quad . \tag{2.43}$$

## 2.2. Judd-Ofelt theory

### Interaction with light

The rare earth ions exhibit interesting optical properties. Their transitions in the visible region are mainly one-photon forced electric dipole transitions within the $4f^N$ configuration,[11] but magnetic dipole transitions like the $^5D_0 \rightarrow {}^7F_1$ transition[33] of $Eu^{3+}$ are also observed.[34] The problem at hand is to describe such *Laporte forbidden*, i.e. parity forbidden, electric dipole $f \leftrightarrow f$ transitions.[11,35]

The intensity $I$ of a transition is proportional to the square of the transition moment according to Fermi's golden rule.[23,24] In the case of an electric dipole transition this is given by the integrals of the electric dipole moment operator[34]

$$\hat{\boldsymbol{\mu}}_{ed} = -e \sum_i \mathbf{r}_i = -e \sum_i r_i \, \mathbf{C}^{(1)}(i) = -e \sum_q \mathbf{D}_q^{(1)} \quad . \tag{2.44}$$

Here $\mathbf{D}^{(1)}$ is a tensor operator of rank 1, i.e. a vector, with the components $\mathbf{D}_q^{(1)}$ where $q = 1, 0, -1$.[34] This is the result of converting the Cartesian vector operator into a spherical tensor operator.[23,34]

Such a matrix element (2.45)

$$I \propto \left| \left\langle A' \left| \hat{\boldsymbol{\mu}}_{ed} \right| A \right\rangle \right|^2 \quad , \tag{2.45}$$

and therefore the intensity $I$, is zero unless the totally symmetric irreducible representation (irrep) is contained in the direct product of the irreps.[23] The matrix element must thus be of even parity (gerade, $g$) in the case of inversion symmetry.[23] The parity of the electric dipole moment operator is odd and if both states $A$ and $A'$ belong to the same configuration, which is the case for $f \leftrightarrow f$ transitions, they possess the same parity.[24] This always leads to zero matrix elements according to $g \otimes u \otimes g = u$ and $u \otimes u \otimes u = u$. Still, these transitions occur and can even have relatively high intensities suggesting that other mechanisms make these so-called *forced* electric dipole transitions possible.[24,35]

### Forced electric dipole transitions

The approach by Judd[36] and Ofelt[37] is based on Rayleigh-Schrödinger perturbation theory.[11] The odd components of the crystal field operator $\hat{H}_{CF}$ are used as perturbing operator, which mix states of opposite parity into the original states $|A\rangle$ representing the states of the spin-orbit coupled free ion $4f^N$ configuration, or $\Psi(L, S, J, M_J)$ see above (eq. (2.20)).[11,34] In actual theoretical calculations, symmetry adapted functions, i.e. proper linear combinations that form the basis of the corresponding irreps of the point group, are used for the eigenstates $|A\rangle$ of $\hat{H}_{FI}$.[11] This is the static approach, which neglects the multipole $\leftrightarrow$ dipole interactions between the central ion and a ligand treated in the "dynamic coupling" or "ligand polarization model".[11]

$$\hat{H}_{CF} = \sum_{t,p} A_{t,p} \sum_i r_i \, \mathbf{C}_p^{(t)}(i) = \sum_{t,p} A_{t,p} \, \mathbf{D}_p^{(t)} \tag{2.46}$$

Equation (2.46) again describes the crystal field operator in terms of Racah's spherical harmonics $\mathbf{C}_p^{(t)}$ or the tensor operator $\mathbf{D}_p^{(t)}$ and the crystal field parameters $A_{t,p}$.[34] The notation was changed compared to equation (2.41) to emphasize that we are now interested in the odd components of $\hat{H}_{CF}$ as a perturbing operator, i.e. $t$ is an odd number. The new states of mixed parity $|B\rangle$ up to first order in the perturbation can be expressed as[11,24,34]

$$|B\rangle = |A\rangle + \sum_{\Psi''} \frac{\left\langle \Psi'' \middle| \hat{H}_{CF} \middle| A \right\rangle}{E(A) - E(\Psi'')} |\Psi''\rangle \quad . \tag{2.47}$$

Here $|\Psi''\rangle$ denotes an excited configuration of opposite parity, e.g. $4f^{N-1}n''\ell''$ with $\ell'' = d$, $g$, with the energy $E(\Psi'')$, while $|A\rangle$ and $E(A)$ belong to the original $4f^N$ configuration.[11] This also explains why $\hat{H}_{CF}$ must be of odd parity, because otherwise the matrix element in equation (2.47) would be zero.

In order to calculate the intensity of a transition $B \rightarrow B'$, matrix elements of the type

$$-e \left\langle B' \middle| \mathbf{D}_q^{(1)} \middle| B \right\rangle \tag{2.48}$$

(compare to eq. (2.44) and (2.45)) have to be evaluated with[11,34]

$$\left\langle B' \middle| \mathbf{D}_q^{(1)} \middle| B \right\rangle = \sum_{\Psi''} \sum_{t,p} A_{t,p} \left( \frac{\left\langle A' \middle| \mathbf{D}_q^{(1)} \middle| \Psi'' \right\rangle \left\langle \Psi'' \middle| \mathbf{D}_p^{(t)} \middle| A \right\rangle}{E(A) - E(\Psi'')} + \frac{\left\langle A' \middle| \mathbf{D}_p^{(t)} \middle| \Psi'' \right\rangle \left\langle \Psi'' \middle| \mathbf{D}_q^{(1)} \middle| A \right\rangle}{E(A') - E(\Psi'')} \right) \quad . \tag{2.49}$$

The next step is the introduction of some simplifications which lead to an expression that can be calculated.

*$1^{st}$ approximation:*
The energies $E(\Psi'')$ of all levels of the excited configuration $4f^{N-1}n''\ell''$ are equal, i.e. the excited levels are considered as degenerate.[11,34]

*$2^{nd}$ approximation:*
The energy differences in both denominators in equation (2.49) are roughly the same, $E(A) - E(\Psi'') \approx E(A') - E(\Psi'')$. Hence, they are replaced by an average energy difference $\Delta E(\Psi'')$.[11,34]

These approximations are considered to be the weak point of the Judd-Ofelt theory.[34] However, they are needed in order to make calculations possible.[11] In the case of well separated $4f^N$ and $4f^{N-1}n''\ell''$ (e.g. $4f^{N-1}5d^1$) configurations with large $\Delta E(\Psi'')$, these approximations are justified.[38] Now it is possible to perform the closure relation over $\Psi''$.[11] Furthermore, the tensor operators $\mathbf{D}_q^{(1)}$ of the electric dipole operator and $\mathbf{D}_p^{(t)}$ of the crystal field operator are expressed as $\sum_i r_i \, \mathbf{C}_q^{(1)}(i)$ and $\sum_i r_i^t \, \mathbf{C}_p^{(t)}(i)$.[34] The first term of equation (2.49) is then given by[34]

$$\sum_{\Psi'',t,p} A_{t,p} \left( \frac{\left\langle A' \middle| \mathbf{D}_q^{(1)} \middle| \Psi'' \right\rangle \left\langle \Psi'' \middle| \mathbf{D}_p^{(t)} \middle| A \right\rangle}{\Delta E(\Psi'')} \right) =$$
$$\sum_{\Psi'',t,p} A_{t,p} \, \langle A' | \sum_i \mathbf{C}_q^{(1)}(i) | \Psi'' \rangle \, \langle \Psi'' | \sum_i \mathbf{C}_p^{(t)}(i) | A \rangle \, \langle 4f \, | \, r_i \, | \, n\ell \rangle \, \left\langle n\ell \middle| r_i^t \middle| 4f \right\rangle \, \Delta E(\Psi'')^{-1} \tag{2.50}$$

where the $\langle n\ell | r^k | n'\ell' \rangle$ denote the radial integrals over the corresponding radial parts of the one-electron wave functions, where $|4f\rangle$ belongs to the $4f^N$ and $|n\ell\rangle$ to the excited $4f^{N-1}n''\ell''$ configuration.[34] Application of the closure procedure then yields[34]

$$\sum_{\Psi'',t,p} \langle A' | \sum_i \mathbf{C}_q^{(1)}(i) | \Psi'' \rangle \, \langle \Psi'' | \sum_i \mathbf{C}_p^{(t)}(i) | A \rangle =$$
$$(-1)^{p+q+\lambda} \, (2\lambda+1)^{\frac{1}{2}} \begin{pmatrix} 1 & \lambda & t \\ q & -p-q & p \end{pmatrix} \left\langle A' \middle| \sum_i [\mathbf{C}_q^{(1)}(i) \cdot \mathbf{C}_p^{(t)}(i)]^{\lambda}_{-p-q} \middle| A \right\rangle \quad . \tag{2.51}$$

Here the combined tensor operator $\mathbf{T}_\mu^{(\lambda)}(i)$[29]

$$\mathbf{T}_\mu^{(\lambda)}(i) = \sum_{q,p} \mathbf{C}_q^{(1)}(i) \cdot \mathbf{C}_p^{(t)}(i) \, \langle 1q, tp | \lambda\mu \rangle \tag{2.52}$$

was used with the *Clebsch-Gordan* or *vector coupling coefficients*[29] $\langle 1q, tp | \lambda\mu \rangle$ and the condition $\mu = -p - q$ for a non-vanishing 3-$j$ symbol (see eq. (2.31)).

$$\langle 1q, tp | \lambda(-\mu) \rangle = (-1)^{\lambda-\mu} \, (2\lambda+1)^{\frac{1}{2}} \begin{pmatrix} 1 & \lambda & t \\ q & \mu & p \end{pmatrix} \tag{2.53}$$

Equation (2.53) was obtained using the phase factor $(-1)^{j_3+m_3}$ and the exchange of two columns, which does not change the sign because of $(-1)^{1+t+\lambda} = +1$, $t$ being an odd number

and $\lambda$ an even number (see below).
The introduction of the *unit tensor operator* $\mathbf{U}$ makes the elimination of the sum $\sum_i$ possible, with $\mathbf{U}^{(\lambda)} = \sum_i \mathbf{u}_i^{(\lambda)}$ and the reduced matrix element of the one-particle unit tensor operator $\langle n\ell||\mathbf{u}^{(\lambda)}||n'\ell'\rangle = \delta_{nn'} \cdot \delta_{\ell\ell'}$.[34]

$$\left\langle A' \left| \sum_i \mathbf{T}_\mu^\lambda(i) \right| A \right\rangle =$$
$$(-1)^{f+1}(2f+1)^{\frac{1}{2}}(2\ell+1)^{\frac{1}{2}} \begin{Bmatrix} 1 & t & \lambda \\ f & f & \ell \end{Bmatrix} \left\langle f \left\| \mathbf{C}^{(1)} \right\| \ell \right\rangle \left\langle \ell \left\| \mathbf{C}^{(t)} \right\| f \right\rangle \left\langle A' \left| \mathbf{U}_{-p-q}^{(\lambda)} \right| A \right\rangle \tag{2.54}$$

Here the 6-$j$ symbol $\{\cdots\}$ was introduced and the reduced matrix elements $\langle||\mathbf{C}^{(k)}||\rangle$ of the spherical tensors $\mathbf{C}^{(k)}$.
The second part of the matrix element $\langle B'|\mathbf{D}_q^{(1)}|B\rangle$ (2.49) can be expressed in an analogous way yielding the same terms, expect for the 3-$j$ symbol. By applying the symmetry relation of the 3-$j$ symbols[29,34]

$$\begin{pmatrix} 1 & \lambda & t \\ q & -p-q & p \end{pmatrix} = (-1)^{1+\lambda+t} \begin{pmatrix} t & \lambda & 1 \\ p & -p-q & q \end{pmatrix} \tag{2.55}$$

it becomes evident that the two 3-$j$ symbols will cancel for an odd $\lambda$, thus removing all odd $\lambda$ terms, and only even $\lambda$ terms survive. A further limit $\lambda \leq 6$ is caused by the 6-$j$ symbol.[34] Therefore $\lambda$ can only take the values 2, 4, 6.

The reduced matrix elements $\langle||\mathbf{C}^{(k)}||\rangle$, the 6-$j$ symbol, the radial integrals and the energy denominator are usually summarized in the function $\Xi(t,\lambda)$.[34]

$$\begin{aligned} \Xi(t,\lambda) =& 2\sum_{n\ell} (-1)^{f+\ell}(2f+1)^{\frac{1}{2}}(2\ell+1)^{\frac{1}{2}} \begin{Bmatrix} 1 & \lambda & t \\ f & \ell & f \end{Bmatrix} \left\langle f \left\| \mathbf{C}^{(1)} \right\| \ell \right\rangle \left\langle \ell \left\| \mathbf{C}^{(t)} \right\| f \right\rangle \\ & \cdot \langle 4f|r|n\ell\rangle \left\langle n\ell \left| r^t \right| 4f \right\rangle \Delta E(\Psi'')^{-1} \end{aligned} \tag{2.56}$$

$$\left\langle B' \left| \mathbf{D}_q^{(1)} \right| B \right\rangle = \sum_{t,p} \sum_{\lambda=2,4,6} (-1)^{p+q}(2\lambda+1)^{\frac{1}{2}} A_{t,p} \begin{pmatrix} 1 & \lambda & t \\ q & -p-q & p \end{pmatrix} \Xi(t,\lambda) \left\langle A' \left| \mathbf{U}_{-p-q}^{(\lambda)} \right| A \right\rangle \text{ §} \tag{2.57}$$

§ $(-1)^{p+q+\lambda} = (-1)^{p+q}$ because $\lambda$ is an even number.

A reduction of the unit tensor matrix element yields[34]

$$\left\langle A' \left| \mathbf{U}^{(\lambda)}_{-p-q} \right| A \right\rangle = (-1)^{J'-M'_J} \begin{pmatrix} J' & \lambda & J \\ -M'_J & -p-q & M_J \end{pmatrix} \left\langle 4f^N \alpha' [S'L'] J' \left\| \mathbf{U}^{(\lambda)} \right\| 4f^N \alpha [SL] J \right\rangle \quad (2.58)$$

where the $|4f^N \alpha [SL] J\rangle$ denote spin-orbit coupled wave functions of the free ion. The reduced matrix element is again independent of $M_J$.

The equations derived above are also valid for transitions between individual Stark levels, which cannot be resolved in solution or in glasses.[34] Hence, a last approximation is made.

*$3^{rd}$ approximation:*
The population of all ground state Stark levels is assumed to be equal and one sums over all these Stark levels, i.e. over all $M_J$ and $M'_J$.[24,34]
At the same time a summation over the components of $\mathbf{D}^{(1)}_q$ and of $\mathbf{D}^{(t)}_p$ is carried out, which causes the 3-$j$ symbols to be replaced by $3^{-1}(2J+1)^{-1}(2t+1)^{-1}$.[34]

This corresponds to the original Judd-Ofelt theory, which made the calculation of oscillator strengths of the $f \leftrightarrow f$ transitions possible, see below.

## Judd-Ofelt parameter

The oscillator strength $f_{ed}$ of an electric dipole transition $B \rightarrow B'$ is given by[34]

$$f_{ed} = \frac{8\pi^2 m_e c\, \tilde{\nu}}{h} \chi \left| \left\langle B' \left| \mathbf{D}^{(1)}_q \right| B \right\rangle \right|^2 \quad (2.59)$$

where $\tilde{\nu}$ is the transition energy in $\mathrm{cm}^{-1}$, $\chi = \frac{(n^2+2)^2}{9n}$ is the Lorentz field correction with the refractive index $n$ of the medium.[34] The constants have their usual meanings.

Combining the above derived terms for the transition moment $\langle B'|\mathbf{D}^{(1)}_q|B\rangle$ results in the expression[34]

$$f_{ed} = \frac{8\pi^2 m_e c\, \tilde{\nu}}{3h(2J+1)} \frac{(n^2+2)^2}{9n} \sum_{\lambda=2,4,6} \Omega_\lambda \left| \left\langle 4f^N \alpha' [S'L'] J' \left\| \mathbf{U}^{(\lambda)} \right\| 4f^N \alpha [SL] J \right\rangle \right|^2 \quad (2.60)$$

with the *Judd-Ofelt parameters* $\Omega_\lambda$[34]

$$\Omega_\lambda = (2\lambda+1)^{\frac{1}{2}} \sum_{t,p} |A_{t,p}|^2\, \Xi^2(t,\lambda)\, (2t+1)^{-1} \quad . \quad (2.61)$$

Thus, if the three Judd-Ofelt parameters $\Omega_\lambda$ of a system are known together with the reduced matrix elements of the unit tensor operator $\langle \| \mathbf{U}^{(\lambda)} \| \rangle$, which were calculated and tabulated e.g. by Carnall *et al.*[28], and the other terms, $\tilde{\nu}$ and $n$, the oscillator strength of a transition can be calculated. These reduced matrix elements are not very sensitive to the environment, i.e. to the ligands, therefore tabulated values can be used for different rare earth ion systems.[34] However, they can also be calculated based on the intermediate coupling scheme[28] and using fractional parentage coefficients for the doubly reduced matrix elements, see Nielson & Koster[39], or by direct integration of a single simple matrix element ($\mu = 0$, $M_J = M_J'$) and comparison to the Wigner-Eckart theorem (see eq. (2.58)).[23]

## Judd-Ofelt calculations

It is common to perform Judd-Ofelt calculations based on a semi-empirical approach, although also *ab initio* calculations are carried out.[11,38] In semi-empirical calculations the Judd-Ofelt parameters $\Omega_\lambda$ are obtained as phenomenological parameters from a least squares fitting procedure between experimental $f_{exp}$ and calculated oscillator strengths $f_{calc}$ (2.60).[34] An example of such a Judd-Ofelt program, which uses the tabulated squared reduced matrix elements of the unit tensor operator published by Carnall *et al.*[28], is given in the Appendix.

$$f_{exp} = 4.318 \cdot 10^{-9} \int \varepsilon(\tilde{\nu})\, d\tilde{\nu} \tag{2.62}$$

$$A = \log_{10}\left(\frac{I_0}{I}\right) = \varepsilon \cdot c \cdot d \tag{2.63}$$

Experimental oscillator strengths can be calculated by measuring the integrated molar absorptivity $\int \varepsilon(\tilde{\nu})\, d\tilde{\nu}$ in the absorbance spectra and using the relation (2.62).[28,40,41] Lambert-Beer's law (2.63) defines the molar absorption coefficient or molar absorptivity $\varepsilon$. The equation for the experimental oscillator strength can be derived according to[40]

$$f = \frac{8\pi^2 m_e\, c}{h\, e^2} \tilde{\nu}_0\, D \tag{2.64}$$

and

$$\tilde{\nu}_0\, D = \frac{2303\, h\, c}{8\pi^3 N_A} \int \varepsilon(\tilde{\nu})\, d\tilde{\nu} \tag{2.65}$$

which leads to

$$f = \frac{2303\, m_e\, c^2}{N_A \pi\, e^2} \int \varepsilon(\tilde{\nu})\, d\tilde{\nu} \quad . \tag{2.66}$$

Here, $D$ is the dipole strength of a transition,[40] $2303 = \ln(10) \cdot 1000$.

$$D = \left| \left\langle \Psi_f \left| \hat{\boldsymbol{\mu}} \right| \Psi_i \right\rangle \right|^2 \tag{2.67}$$

$$\int \varepsilon(\tilde{\nu})\, d\tilde{\nu} = \frac{8\pi^3}{h\, c} \frac{N_A}{2303} \tilde{\nu}_0\, D \tag{2.68}$$

The root mean square deviation (rms) gives the difference between the experimental and calculated oscillator strengths.[34,41]

$$\begin{aligned} \text{rms} &= \left( \frac{\text{sum of squares of deviations}}{\text{number of observations} - \text{number of parameters}} \right)^{\frac{1}{2}} \\ &= \left( \frac{\sum (f_{calc} - f_{exp})^2}{\text{number of bands} - 3} \right)^{\frac{1}{2}} \end{aligned} \tag{2.69}$$

Special care must be taken with the units in Judd-Ofelt calculations or when using the above formulas, particularly when using the elementary charge $e$. The quantities in these formulas are based on the older CGS system (centimetre-gram-second) and not on the SI system.[40] Therefore, Table 2.2 summarizes the constants that have to be used for Judd-Ofelt calculations. The unit of the $\Omega_\lambda$ parameters is usually $\text{cm}^2$.

In the case of $\mathbf{Eu^{3+}}$, there are often not enough transitions resolved in the experimental spectra to perform a least squares fitting procedure to calculate the Judd-Ofelt parameters. An alternative strategy is to obtain the $\Omega_\lambda$ by a comparison of the radiative transition probabilities of magnetic and electric dipole transitions in the emission spectra.[43] The $^5\text{D}_0 \rightarrow {}^7\text{F}_1$ transition of $\text{Eu}^{3+}$ could be shown to be a magnetic dipole transition,[33] whose radiative transition probability $A_{01}$ is independent of the environment of the rare earth ion,[43] while the $^5\text{D}_0 \rightarrow {}^7\text{F}_J$ ($J$ = 2, 4, 6) are electric dipole transitions,[33] where $A_{0J}$ only depends on the $\Omega_\lambda$ parameters ($\lambda$ = 2, 4, 6).[43] A great simplification in the special case of $\text{Eu}^{3+}$ is that the intensity or oscillator strength of the $^5\text{D}_0 \rightarrow {}^7\text{F}_2$ transition is solely determined by $\Omega_2$, of the $^5\text{D}_0 \rightarrow {}^7\text{F}_4$ transition by $\Omega_4$ and of the $^5\text{D}_0 \rightarrow {}^7\text{F}_6$ transition by $\Omega_6$.[43] This is a result of the reduced matrix elements of the unit tensor operator $\langle \| \mathbf{U}^{(\lambda)} \| \rangle$, which vanish in the cases $J = 0 \longrightarrow J'$ and $\lambda \neq J'$.[28] Thus, the following formulas were used in this thesis for the determination of the Judd-Ofelt parameters of $\text{Eu}^{3+}$.[44,45]

Table 2.2.: Constants and their meanings and units in the CGS system.[42]

| Symbol | Value | CGS unit | Definition |
|---|---|---|---|
| $m_e$ | $9.10938215 \cdot 10^{-28}$ | g | electron mass |
| $c$ | $2.99792458 \cdot 10^{10}$ | cm $s^{-1}$ | speed of light |
| $h$ | $6.62606885 \cdot 10^{-27}$ | erg s = g $cm^2$ $s^{-1}$ | Planck's constant |
| $e$ | $4.80320427 \cdot 10^{-10}$ | esu = $g^{\frac{1}{2}}$ $cm^{\frac{3}{2}}$ $s^{-1}$ | elementary charge |
| $N_A$ | $6.02214 \cdot 10^{23}$ | (mol) | Avogadro's constant |
| $\tilde{\nu}$, $\tilde{\nu}_0$ | / | $cm^{-1}$ | wavenumber of a transition |

$$A_{0J} = A_{01} \left( \frac{\int I_{0J}\, d\tilde{\nu}}{\int I_{01}\, d\tilde{\nu}} \right) \left( \frac{\tilde{\nu}_{01}}{\tilde{\nu}_{0J}} \right) \tag{2.70}$$

Here the radiative transition probability of the magnetic dipole transition is given by $A_{01} \approx 50\ s^{-1}$.[44,45] $\int I_{0J}\, d\tilde{\nu}$ is the integrated intensity of the $0 \rightarrow J$ transition and $\tilde{\nu}_{0J}$ the associated wavenumber. The Judd-Ofelt parameters $\Omega_\lambda$ can then be calculated according to[44]

$$\Omega_2 = \frac{3\, h\, c^3\, A_{02}}{8\pi\, e^2\, \omega^3\, \chi\, \left\langle {}^7F_2 \left\| \mathbf{U}^{(2)} \right\| {}^5D_0 \right\rangle^2 (2J+1)} \tag{2.71}$$

where $\omega$ is the angular frequency of the transition, $\omega = 2\pi\nu = 2\pi c\tilde{\nu} \cdot 100$ in rad $s^{-1}$ ($\tilde{\nu}$ in $cm^{-1}$), $\chi$ is the Lorentz field correction, in this case $\chi = \frac{n(n^2+2)^2}{9}$ with the refractive index $n$,[44] $J$ denotes the $J$-value of the initial state of the transition, i.e. $J = 0$, and the constants are listed in Table 2.2. $\Omega_4$ and $\Omega_6$ can be obtained in an analogous way by replacing $A_{02}$ and $\langle {}^7F_2 \| \mathbf{U}^{(2)} \| {}^5D_0 \rangle$ by the corresponding terms.[44]

It should be noted that such phenomenological or semi-empirical Judd-Ofelt parameters also contain dynamic or vibronic contributions from the interaction of the rare earth ion with the ligands, as opposed to the above presented static $\Omega_\lambda$ parameters of the original Judd-Ofelt theory, which is based on a static perturbation by the crystal field potential.[11,34] In addition, electron correlation and higher-order effects caused by the (static and dynamic) crystal field potential, the spin-orbit coupling and the mass polarization shift are also accounted for.[38] Accordingly, the semi-empirical Judd-Ofelt theory is more general than

the original *ab initio* theory derived by Judd and Ofelt.
However, the theory was further developed, for example by Wybourne[46], who introduced third-order contributions to the intensities, or more recently by Smentek & Wybourne[22] with the extension to the relativistic formalism, which makes the calculation of transitions possible that are forbidden in the non-relativistic theory, e.g. the $0 \leftrightarrow 0$ transitions of $Eu^{3+}$.[38]

### Selection rules

The 3-$j$ and 6-$j$ symbols together with the reduced matrix elements $\langle \| \mathbf{U}^{(\lambda)} \| \rangle$ and the orthogonality of the spin functions yield the following selection rules[34]

- $\Delta \ell = \pm 1$, $|\Delta L| = \leq 6$, $\Delta S = 0$
- $|\Delta J| = \begin{cases} 2, 4, 6 & \text{if } J \text{ or } J' = 0 \\ \leq 6 & \text{else} \end{cases}$
- $|\Delta M_J| = p + q$ .

Furthermore, $J = 0 \leftrightarrow 0 = J'$ transitions are forbidden.[24,34] However, the selection rules on $L$ and $S$ are lifted to some extent due to the spin-orbit coupling.[34] Also the selection rules on $J$ are not obeyed strictly because of the $J$-mixing, but still they are much more important than the constraints on $\Delta L$ and $\Delta S$.[34]

### Magnetic dipole transitions

As mentioned above, also magnetic dipole transitions occur in the spectra of rare earth ions. In contrast to the electric dipole $f \leftrightarrow f$ transitions, they are allowed, because the magnetic dipole operator $\hat{\boldsymbol{\mu}}_{md}$ is of even parity.[24]

$$\hat{\boldsymbol{\mu}}_{md} = -\frac{e}{2\, m_e c}(\mathbf{L} + 2\mathbf{S}) \tag{2.72}$$

The following selection rules are valid for magnetic dipole transitions.[34]

- $\Delta \ell = 0$, $|\Delta L| = 0$, $\Delta S = 0$
- $|\Delta J| = 0, \pm 1$ and not $0 \leftrightarrow 0$

Again, the selection rules on $L$ and $S$ are not obeyed strictly.[34] Carnall *et al.*[41,47] have calculated the magnetic dipole oscillator strengths of a number of trivalent rare earth ions. Electric quadrupole and especially higher multipole transitions were not observed in experimental spectra.[34]

## 2.3. Hypersensitivity

One of the most interesting features in rare earth ion spectra are so-called *hypersensitive transitions*. The intensities of these transitions are particularly sensitive to the environment of the rare earth ion in contrast to the intensities of the majority of $f \leftrightarrow f$ transitions.[34] They were first called *hypersensitive* by Jørgensen & Judd[19]. Since then the hypersensitive transitions were investigated by many authors for a variety of rare earth ions in crystals, glasses and solutions and different explanations for this phenomenon were suggested.[34,48–51] However, there is still no consistent theory available that explains hypersensitive transitions.

The selection rules of hypersensitive transitions are[34]

- $|\Delta J| \leq 2$
- $|\Delta L| \leq 2$
- $|\Delta S| = 0$,

which correspond to the selection rules on $\langle \| \mathbf{U}^{(2)} \| \rangle$.[34] The selection rules on $L$ and $S$ are again lifted to some extent due to spin-orbit coupling. As a consequence, $\Omega_2$ is expected to be especially sensitive to the environment compared to $\Omega_{4,6}$.[34]

Some of the properties of hypersensitive transitions are given below. To begin with, their pure electronic transition intensity is zero if the rare earth ion is situated at an inversion

Table 2.3.: Hypersensitive transitions[34] and their wavenumbers[28] $\tilde{\nu}$ of $Nd^{3+}$ and $Eu^{3+}$.

| Lanthanide | Hypersensitive transition | $\tilde{\nu}$ ($cm^{-1}$) |
|---|---|---|
| $Nd^{3+}$ | $^4G_{5/2} \leftarrow {}^4I_{9/2}$ | 17,193 |
| $Eu^{3+}$ | $^5D_1 \leftarrow {}^7F_1$ | 18,655 |
| | $^5D_2 \leftarrow {}^7F_0$ | 21,483 |
| | $^5D_0 \rightarrow {}^7F_2$ | 16,267 |

centre,[¶] just like in the case of normal, i.e. non-hypersensitive, transitions, whereas slight deviations from the centrosymmetry lead to relatively high intensities of the hypersensitive transitions while the intensities of the other transitions remain unchanged (see e.g. for $Eu^{3+}$ Blasse *et al.*[52]).[34] The spectra of aqueous solutions exhibit comparatively low intensities of the hypersensitive transitions. In general, the intensity dependence on the ligands is given by[34]

$$I^- > Br^- > Cl^- > H_2O > F^-$$
and
aryl > alkyl .

Furthermore, basic or electron donating ligands seem to enhance the intensity of the hypersensitive transition, i.e. there is a dependence on the $pK_a$ of the ligands.[49]

### Theories of hypersensitivity

Judd[19,36] proposed that the effect can be described in the formalism of *Judd-Ofelt theory* by the crystal field parameter $A_{1,p}$ ($t = 1$), which solely occurs in the expression for $\Omega_2$ and not for $\Omega_{4,6}$.[34] Only the point groups $C_s$, $C_n$ ($n = 1-4,6$), $C_{nv}$ ($n = 2-4,6$) allow $A_{1,p}$ parameters. However, several experimental examples of lanthanides in other point groups have shown high intensities of the hypersensitive transitions.[34]

Also the *vibronic mechanism* for $\Omega_2$ proposed by Jørgensen & Judd[19] cannot account for the observed properties of hypersensitive transitions.[34]

The inclusion of *covalency* in the description has been discussed by some authors, which results in an increase of the calculated intensity and mainly affects $\Omega_2$, but also $\Omega_4$.[34]

Moreover, the selection rules of hypersensitive transitions correspond to those of *quadrupole transitions*, which was also considered as a cause of hypersensitivity. However, the intensity of quadrupole transitions is very low and does not explain the high intensities observed in the experiments.[34] Besides, in this case $\Omega_2$ would be proportional to the square of the wavenumber of the transition $\tilde{\nu}^2$, which could also not be verified by experiments.[34]

Jørgensen & Judd[19] also proposed the *inhomogeneous dielectric* model, which is based on the assumption that the radiation induces dipoles in the environment of the rare earth ion.

[¶] Non-zero transition intensities in centrosymmetric sites are caused by vibronic mechanisms.[34,49]

This causes a variation of the electric field across the ion $(\nabla E)_p^{(2)}$. The electric quadrupole operator is then given by[34]

$$\hat{\boldsymbol{\mu}}_{eq} = -e\left(\frac{2}{3}\right)^{\frac{1}{2}} \sum_i r_i^2 \, \mathbf{C}_q^{(2)}(i) \, (\nabla E)_p^{(2)}(i) \quad . \tag{2.73}$$

Under these circumstances, a considerable enhancement of the quadrupole transition intensity can be achieved, which the authors expressed as $\Omega_2(\text{inhomogeneous dielectric}) = const. \cdot \Omega_2(\text{quadrupole})$.[34] These transitions are called "pseudo-quadrupole" transitions.[49]

Finally, one of the most promising explanations is the *dynamic coupling* model. It considers the perturbation of the ligand wave functions caused by the central ion as well, in addition to the perturbation due to the ligand field. The perturbed wave function of the total system up to first order is[34]

$$|\Psi_i\rangle = |M_0 L_0\rangle - \sum_b (E_a - E_b)^{-1} \left\langle M_a L_b \middle| \hat{V} \middle| M_0 L_0 \right\rangle |M_a L_b\rangle \tag{2.74}$$

where total state of the system is written as a product of the ground and excited functions of the metal ion, $|M_0\rangle$ and $|M_a\rangle$, and of the ligand, $|L_0\rangle$ and $|L_b\rangle$. $E_a$ denotes the energy of the $|M_a\rangle \leftarrow |M_0\rangle$ transition and $E_b$ of the $|L_b\rangle \leftarrow |L_0\rangle$ transition. Evaluation of the transition matrix element $-e\left\langle \Psi_f \middle| \mathbf{D}_q^{(1)} \middle| \Psi_i \right\rangle$ leads to the following term for the oscillator strength[34]

$$f(\text{dyn}) = \frac{8\pi^2 m_e c \tilde{\nu}}{3h(2J+1)} \chi \, \Omega_2(\text{dyn}) \left| \left\langle 4f^N \alpha_f [S_f L_f] J_f \middle\| \mathbf{U}^{(2)} \middle\| 4f^N \alpha_i [S_i L_i] J_i \right\rangle \right|^2 \quad . \tag{2.75}$$

$$\Omega_2(\text{dyn}) = \left(\frac{2}{15}\right)\left(\frac{\alpha^2}{R^8}\right) \left\langle f \middle\| \mathbf{C}^{(2)} \middle\| f \right\rangle^2 \langle 4f | r^2 | 4f \rangle^2 \sum_{q,m} \left\{ [B^{q,m}] \left| \sum_{L=1}^{N} \mathbf{C}_{-q-m}^{(3)} \right|^2 \right\} \tag{2.76}$$

Thus, there is only a dynamic (dyn) contribution to $\Omega_2$, but not to $\Omega_{4,6}$. Here $\alpha$ is the average polarisability of the ligands, $R$ denotes the ligand–metal bond distance and $B^{q,m}$ is a numerical factor.[34]

The dynamic coupling model predicts that the $Y_m^{(3)}$ spherical harmonic function must be contained in the expansion of the potential of the rare earth ion in order to exhibit hypersensitivity. This limits the possible point groups to $C_s$, $C_n$ ($n = 1-8$), $C_{nv}$ ($n = 2-6$ and $\infty$), $C_{3h}$, $D_n$ ($n = 2-6$), as well as $D_{2d}$, $D_{3h}$, $S_4$, T and $T_d$.[34]

The dynamic coupling method made the prediction of hypersensitive transitions of the neodymium trihalides $NdX_3$ possible, where many of the above mentioned theories failed. Furthermore, many properties of hypersensitive transitions can be explained like the

dependence on the polarisability of the ligands ($I^- > Br^- > Cl^- > H_2O > F^-$; aryl > alkyl).[34] In contrast to the inhomogeneous dielectric model, the charge distribution due to the $f \leftrightarrow f$ transition induces dipoles in the ligands in the case of the dynamic coupling model.[34]

Presumably a combination of these effects should be considered when describing the hypersensitivity of a transition. The symmetry alone cannot account for the considerable intensity changes,[51] though there seems to be a relation between certain point groups and the intensity of the hypersensitive transition. An inversion centre affects all transitions, not only the hypersensitive ones.[49] The polarisability of the ligands seems to play an important role as well.[51]

# 3. Computational methods

This part focuses on relativistic quantum mechanics, i.e. the combination of Einstein's theory of special relativity and quantum mechanics, starting with the Dirac equation. It is mainly based on the books by Reiher and Wolf[21] and Dyall and Fægri[53]. Quantum electrodynamics would be the fundamental physical theory fulfilling the requirements of special relativity and the state of the art in the description of the interaction of light (photons) and matter (electrons), but it is not suited for the description of molecular systems.

## 3.1. Dirac's theory and four-component methods

The **Dirac equation of a freely moving electron** is given by[21]

$$i\hbar\frac{\partial}{\partial t}\Psi = \left[\frac{\hbar c}{i}\alpha^k\partial_k + \beta m_e c^2\right]\Psi \tag{3.1}$$

or, equivalently, by

$$i\hbar\frac{\partial}{\partial t}\Psi = \left[c(\boldsymbol{\alpha}\cdot\mathbf{p}) + \beta m_e c^2\right]\Psi \tag{3.2}$$

which can be derived using the correspondence principle together with Dirac's approach for the square root operator.[21,53]

The Dirac parameters $\alpha^k$ and $\beta$ can be shown to be $4 \times 4$ matrices, in the standard representation given by

$$\alpha^i = \begin{pmatrix} 0 & \sigma_i \\ \sigma_i & 0 \end{pmatrix} \text{ and } \beta = \begin{pmatrix} \mathbf{1_2} & 0 \\ 0 & \mathbf{1_2} \end{pmatrix} \tag{3.3}$$

with $\mathbf{1_2}$ being the $2 \times 2$ unit matrix and $\sigma_i$ are the three Pauli matrices

$$\sigma_x = \begin{pmatrix} 0 & 1 \\ 1 & 0 \end{pmatrix}, \quad \sigma_y = \begin{pmatrix} 0 & -i \\ i & 0 \end{pmatrix} \text{ and } \sigma_z = \begin{pmatrix} 1 & 0 \\ 0 & -1 \end{pmatrix}, \tag{3.4}$$

or represented by a vector

$$\boldsymbol{\alpha} = (\alpha^i) = (\alpha^1, \alpha^2, \alpha^3) \tag{3.5}$$

$$\boldsymbol{\sigma} = (\sigma_x, \sigma_y, \sigma_z) \ . \tag{3.6}$$

The $\boldsymbol{\alpha}$ parameters, which simply resulted from the mathematical treatment[53], can be considered to represent the spin[21], whereas $c\boldsymbol{\alpha}$ can be identified with the velocity operator in accordance with the classical velocity four-vector.[53] The term $c(\boldsymbol{\alpha} \cdot \mathbf{p})$ then corresponds to the kinetic energy operator in the relativistic framework[21], where $\mathbf{p}$ refers to the canonical momentum operator ($\mathbf{p} \rightarrow -i\hbar\nabla$).
Because of the $4 \times 4$ structure of the Dirac matrices, the quantum mechanical state is necessarily a vector of four functions or a "*4-spinor*".[21] The Dirac equation is Lorentz covariant, i.e. it fulfils the requirements of special relativity, as opposed to the time-dependent Schrödinger equation, which does not treat time and space variables in the same manner (second derivatives with respect to space, but only first derivatives with respect to time).[53] The 4-spinor $\Psi$ can also be written in terms of 2-spinors or bi-spinors, the large component $\Psi^L$ and the small component $\Psi^S$, because of the block structure of the Dirac matrices.[21]

$$\Psi = \begin{pmatrix} \Psi_1 \\ \Psi_2 \\ \Psi_3 \\ \Psi_4 \end{pmatrix} = \begin{pmatrix} \Psi^L \\ \Psi^S \end{pmatrix} \tag{3.7}$$

The Dirac equation in split notation then reads[21]

$$c(\boldsymbol{\sigma} \cdot \mathbf{p})\Psi^S + m_e c^2 \Psi^L = i\hbar \frac{\partial}{\partial t} \Psi^L \tag{3.8}$$

$$c(\boldsymbol{\sigma} \cdot \mathbf{p})\Psi^L - m_e c^2 \Psi^S = i\hbar \frac{\partial}{\partial t} \Psi^S \tag{3.9}$$

One should keep in mind that these equations represent four coupled first-order differential equations. The Dirac equation for a freely moving particle has four solutions, two of which correspond to positive energy eigenvalues, which are physically meaningful, and the other two belonging to negative energy eigenvalues.[21] An interpretation of these negative energy states is given in the books by Reiher & Wolf[21] (p. 178) and Dyall & Knut Fægri[53] (p. 54).

The **Dirac equation of an electron in an external electromagnetic potential** can be derived using the minimal coupling scheme[21,54*]

$$i\hbar\frac{\partial}{\partial t}\Psi = \left[c(\boldsymbol{\alpha}\cdot\mathbf{p}) + \beta m_e c^2 + q_e\phi - q_e(\boldsymbol{\alpha}\cdot\mathbf{A})\right]\Psi \quad , \tag{3.10}$$

where $\phi$ denotes a scalar potential and $\mathbf{A}$ an external vector potential, $q_e = -e$ is the charge of an electron. This equation can also be written in terms of the mechanical or kinematic momentum operator $\boldsymbol{\pi}$.[21,53]

$$\boldsymbol{\pi} \equiv \mathbf{p} - \frac{q_e}{c}\mathbf{A} \tag{3.11}$$

## Kinetic balance

If the speed of light is increased, $c \to \infty$, the non-relativistic limit is reached. It will be shown later how the Schrödinger equation is recovered for $c \to \infty$. In order to compare the relativistic and non-relativistic energy, the origin of the energy scale must be shifted by $-m_e c^2$ in the case of the Dirac equation.[21]

$$i\hbar\frac{\partial}{\partial t}\begin{pmatrix}\Psi^L\\ \Psi^S\end{pmatrix} = c\cdot\begin{Bmatrix}(\boldsymbol{\sigma}\cdot\boldsymbol{\pi})\Psi^S\\ (\boldsymbol{\sigma}\cdot\boldsymbol{\pi})\Psi^L\end{Bmatrix} - 2m_e c^2\begin{pmatrix}0\\ \Psi^S\end{pmatrix} + V\begin{pmatrix}\Psi^L\\ \Psi^S\end{pmatrix} \tag{3.12}$$

A relation between the 2-spinors $\Psi^L$ and $\Psi^S$ can be obtained using the lower part of this equation together with the assumption $2m_e c^2 \gg E - V$, with the energy $E \to i\hbar\frac{\partial}{\partial t}$ and the potential $V$.

*$\mathbf{p} \to \mathbf{p} - q\mathbf{A}$ and $E \to E - q\phi$ .[20]

$$\left(i\hbar\frac{\partial}{\partial t} + 2m_e c^2 - V\right)\Psi^S = c(\boldsymbol{\sigma}\cdot\boldsymbol{\pi})\Psi^L \tag{3.13}$$

$$\Psi^S = \frac{c(\boldsymbol{\sigma}\cdot\boldsymbol{\pi})}{i\hbar\frac{\partial}{\partial t} + 2m_e c^2 - V}\Psi^L \tag{3.14}$$

$$\Psi^S \approx \frac{\boldsymbol{\sigma}\cdot\boldsymbol{\pi}}{2m_e c^2}\Psi^L \tag{3.15}$$

This relation (3.15) is known as *kinetic balance*. On account of $\Psi^S$ being by a factor of $c^{-1} \approx 1/137$ smaller than $\Psi^L$, the former is called the *small component* ($S$) and the latter the *large component* ($L$). The small component vanishes for $c \to \infty$, i.e. in the non-relativistic limit, while the large component then yields the uncoupled $\alpha$- and $\beta$-spin orbitals.[21]

## Time-independent Dirac equation

In quantum chemistry one is mostly interested in the eigenstates of a time-independent Hamiltonian, the stationary states. In this case a product ansatz for the wave function can be made.[53]

$$\Psi(\mathbf{r}, t) = \Psi(\mathbf{r})\theta(t) \tag{3.16}$$

$$\theta(t) = e^{\frac{Et}{i\hbar}} \tag{3.17}$$

After substitution this yields the time-independent Dirac equation.

$$\hat{H}\Psi(\mathbf{r}) = E\Psi(\mathbf{r}) \tag{3.18}$$

### Many particle systems

In the case of atoms and molecules, the Hamiltonian can be expressed as a sum of one-particle ($\hat{h}$) and two-particle operators ($\hat{g}$), describing also the electron-electron and electron-nucleus interaction.[20,21,55]

$$\hat{H} = \sum_{i}^{N} \hat{h}(i) + \sum_{i<j}^{N} \hat{g}(i,j) + V_{NN} \tag{3.19}$$

Here, the *Born-Oppenheimer approximation*[56] has been applied, i.e. the nuclear and electronic degrees of freedom are separated.

$$\hat{H} \rightarrow \hat{H}'_{el}\Psi_{el,A} = E'_{el,A}\Psi_{el,A} \tag{3.20}$$

$$\hat{H}_{el}\Psi_{el,A} = E_{el,A}\Psi_{el,A} = (E'_{el,A} - V_{NN})\Psi_{el,A} \tag{3.21}$$

Further approximations are made, for example the neglect of nuclear spin, point-like particles and simplifications of the interaction potentials.

The one-electron operator $\hat{h}$, which only depends on the coordinates of one electron $i$, is given by the Dirac Hamiltonian, here without an external vector potential $\mathbf{A}$[21]

$$\hat{h}(i) = c(\boldsymbol{\alpha}_i \cdot \mathbf{p}_i) + (\beta_i - 1)m_e c^2 + V_{nuc}(\mathbf{r_i}) \tag{3.22}$$

$$\hat{h} = \begin{pmatrix} V_{nuc} & c(\boldsymbol{\sigma} \cdot \mathbf{p}) \\ c(\boldsymbol{\sigma} \cdot \mathbf{p}) & V_{nuc} - 2m_e c^2 \end{pmatrix} \tag{3.23}$$

where $V_{nuc}$ is a scalar potential representing the interaction of one electron with the clamped nuclei, which reads in Gaussian units ($4\pi\varepsilon_0 = 1$)

$$V_{nuc}(\mathbf{r}_i) = -\sum_{I}^{M} \frac{Z_I e^2}{|\mathbf{r}_i - \mathbf{R}_i|} \quad . \tag{3.24}$$

$V_{NN}$ denotes the nucleus-nucleus repulsion, which is again a Coulomb-type operator like $V_{nuc}$. In the following chapters the Born-Oppenheimer approximation is applied, i.e. a constant shift of the energy is assumed, without the specification *el* for "electronic". The wave function and the energy are thus functions of a given nuclear geometry. Furthermore, the by $m_e c^2$ shifted energy is used. Still, the electronic solutions are called "positive-energy solutions" and the positronic solutions "negative-energy solutions".[21]

The *spin-orbit coupling*, $\sigma \cdot \ell$, is "embedded" in the term $\boldsymbol{\alpha} \cdot \mathbf{p}$ or $\sigma \cdot \mathbf{p}$, respectively, i.e. in the off-diagonal elements of the one-electron (Dirac) Hamiltonian.[21]

$$\sigma \cdot \mathbf{p} = \left( \frac{\sigma \cdot \mathbf{r}}{r} \right) \frac{1}{r} [\mathbf{r} \cdot \mathbf{p} + i(\sigma \cdot \ell)] \tag{3.25}$$

Here $\ell$ denotes the orbital angular momentum operator $\ell = \mathbf{r} \times \mathbf{p}$.

The remaining unknown is the exact expression for the two-electron operator $\hat{g}$. The simplest interaction potential, a Coulomb operator, can be described analogous to $V_{nuc}$ or $V_{NN}$. Unretarded interactions, where the effects of the electromagnetic fields generated by the electrons are felt simultaneously, are given by the Gaunt operator[21]

$$G_0(i,j) = -q_i q_j \frac{\boldsymbol{\alpha}_i \boldsymbol{\alpha}_j}{r_{ij}} = -\frac{q_i q_j}{r_{ij}} \frac{4}{\hbar^2} \begin{pmatrix} 0 & \mathbf{s}_i \mathbf{s}_j \\ \mathbf{s}_i \mathbf{s}_j & 0 \end{pmatrix} . \tag{3.26}$$

Here $\boldsymbol{\alpha}_i \boldsymbol{\alpha}_j$ is the scalar product $\boldsymbol{\alpha}_i \boldsymbol{\alpha}_j = \sum_{k=1}^{3} \alpha_{i,k} \alpha_{j,k}$. The Gaunt interaction describes the instantaneous magnetic interaction of the electrons and spin-spin interactions.[21,55]

The Breit operator $B_0(i,j)$ accounts for retarded interactions.[21]

$$B_0(i,j) = -\frac{q_i q_j}{2} \left( \frac{\boldsymbol{\alpha}_i \boldsymbol{\alpha}_j}{r_{ij}} + \frac{(\mathbf{r}_{ij} \cdot \boldsymbol{\alpha}_i)(\mathbf{r}_{ij} \cdot \boldsymbol{\alpha}_j)}{r_{ij}^3} \right) \tag{3.27}$$

$$= G_0(i,j) + B_{\text{ret.}}(i,j) \tag{3.28}$$

This is the frequency-independent Breit operator, where $B_{\text{ret.}}(i,j)$ denotes the true retardation operator, but one can also derive a frequency-dependent Breit operator $B_\omega(i,j)$ using

quantum electrodynamics. The combined Coulomb-Breit operator[57] can also be written as[20,55]

$$\hat{g}_{ij}^{Breit} = \hat{g}_{ij}^{Coulomb} + \hat{g}_{ij}^{Gaunt} + \hat{g}_{ij}^{gauge} \tag{3.29}$$

$$= \frac{\mathbf{1_4} \otimes \mathbf{1_4}}{r_{ij}} - \frac{(c\boldsymbol{\alpha}_i)(c\boldsymbol{\alpha}_j)}{c^2 r_{ij}} - \frac{(c\boldsymbol{\alpha}_i \cdot \nabla_i)(c\boldsymbol{\alpha}_j \cdot \nabla_j) r_{ij}}{2c^2} \tag{3.30}$$

However, in this work only the Coulomb interaction term was used, which includes spin-same-orbit,[58,59] but not spin-other-orbit interaction, which is described by the Gaunt term.[20,55]

$$\begin{aligned} \hat{H}^{DC} &= \sum_{i=1}^{N} \hat{h}(i) + \sum_{i<j}^{N} \hat{g}_{ij}^{Coulomb} \\ &= \sum_{i=1}^{N} \left[ c\boldsymbol{\alpha}_i \cdot \mathbf{p}_i + (\beta_i - 1) m_e c^2 + V_{nuc}(\mathbf{r}_i)\, \mathbf{1_4} \right] + \sum_{i<j}^{N} \frac{\mathbf{1_4} \otimes \mathbf{1_4}}{r_{ij}} \end{aligned} \tag{3.31}$$

This is the *Dirac-Coulomb Hamiltonian* $\hat{H}^{DC}$,[20] which was used in this thesis, where the last term corresponds to the Coulomb repulsion between the electrons $\hat{g}(i,j) \rightarrow V_C(i,j) = \frac{e^2}{|\mathbf{r_i} - \mathbf{r_j}|}$. This relativistic four-component Hamiltonian for molecular calculations is often called "fully relativistic" Hamiltonian, though it is no longer Lorentz covariant.[21]

A problem arises in relativistic four-component calculations which is caused by the possibility of infinitely large negative energies or the unboundedness of the one-electron Dirac Hamiltonian, respectively. This could lead to a variational collapse when the variational principle is applied.[21] A possible solution to this problem is to apply the *minimax principle*[60], where the minimum of the electronic energy with respect to the large component of the spinor is determined and the maximum of the energy with respect to the small component.[21]
The DIRAC[61] program uses this principle together with the "empty Dirac" picture[20,53], where the negative-energy states are treated as virtual states during the Hartree-Fock optimization.[20] A coupling or pair-creation process between the positive-energy (electronic) and negative-energy (positronic) states should be prohibited - this is the case for *no-pair Hamiltonians*.[21]

### Non-relativistic limit

For increasing speed of light $c \to \infty$, the four-component one-electron Dirac operator $\hat{h}$ turns into the *one*-component one-electron operator $\hat{h}^S$ of non-relativistic Schrödinger quantum mechanics.[21]

$$\hat{h}(i) = c\boldsymbol{\alpha}_i(\mathbf{p}_i - \frac{q_i}{c}\mathbf{A}_{ext}) + (\beta_i - 1)m_e c^2 + V_{nuc}(\mathbf{r}_i)$$

$$\Downarrow$$

$$\hat{h}^S(i) = -\frac{\hbar^2}{2m_e}\Delta_i + V_{nuc}(\mathbf{r}_i)$$

This is a consequence of the vanishing small components of the spinor, see page 36 (3.1).

## 3.2. Two-component Hamiltonians

It is desirable to reduce the four-component Hamiltonian to a two-component Hamiltonian representing only the positive-energy solutions.[21,55] This can be achieved using, for example, *elimination techniques* that substitute the small component $\psi^S$ according to[21]

$$\psi^S = R\psi^L \quad . \tag{3.32}$$

$$R = R(\epsilon) = (\epsilon - V + 2m_e c^2)^{-1}\, c\,(\boldsymbol{\sigma}\cdot\mathbf{p}) \tag{3.33}$$

This relation holds because of the $(2\times 2)$-superstructure of the one-electron Fock-type operator $\hat{f}$, where $V$ is diagonal and $\hat{h}^{free}$ corresponds to the field-free one-electron Dirac Hamiltonian[21], see for example (3.1) on page 36.

$$\hat{f} = \hat{h}^{free} + \underbrace{V_{nuc} + V_{ee}}_{=V} \tag{3.34}$$

$$\hat{f}\psi = \epsilon\psi \tag{3.35}$$

Hence, the $R$-operator depends on the energy eigenvalue $\epsilon$. It is also called "exact coupling".[55] Heully *et al.*[62] were able to derive an expression for $R$ which is not explicitly energy dependent.[55] Starting from the one-electron Dirac equation

$$h_{LL}\psi^L + h_{LS}\psi^S = E\psi^L \tag{3.36}$$
$$h_{SL}\psi^L + h_{SS}\psi^S = E\psi^L \tag{3.37}$$

and eliminating $\psi^S$ using $R$

$$(h_{LL} + h_{LS}R)\psi^L = E\psi^L \tag{3.38}$$

an equation which is not explicitly relating to the energy $E$ can be obtained[55]

$$h_{SL} + h_{SS}R = Rh_{LL} + Rh_{LS}R \quad . \tag{3.39}$$

The two sets of solutions, $R_+$ and $R_-$, of this operator equation belong to the positive- and negative-energy solutions, respectively. Finally, a general form of the Foldy-Wouthuysen transformation[63] could be derived giving the required transformation matrix $U$.[55,62]

$$U = \begin{pmatrix} \Omega_+ & -R^\dagger\Omega_- \\ R\Omega_+ & \Omega_- \end{pmatrix} \tag{3.40}$$

$$\Omega_+ = \frac{1}{\sqrt{1 + R^\dagger R}} = N_+^{-1} \tag{3.41}$$
$$\Omega_- = \frac{1}{\sqrt{1 + RR^\dagger}} \tag{3.42}$$

$$U^\dagger \begin{pmatrix} h_{LL} & h_{LS} \\ h_{SL} & h_{SS} \end{pmatrix} U = \begin{pmatrix} \tilde{h}_{++} & 0 \\ 0 & \tilde{h}_{--} \end{pmatrix} \tag{3.43}$$

The two-component equation describing the positive-energy (electronic) spectrum is given by[55]

$$h_{++}\psi_+^{2c} = E\psi_+^{2c} \quad . \tag{3.44}$$

In order to develop an *exact* two-component Hamiltonian, called X2C, the solution of the one-electron Dirac equation is required. However, the calculation of two-electron terms in molecular computations is much more expensive, so this does not present a problem. It is therefore possible to obtain the X2C Hamiltonian starting from the matrix representation of the parent four-component Hamiltonian and then extracting the exact coupling $R$.[55]

## 3.3. Douglas-Kroll-Hess theory

The Douglas-Kroll-Hess (DKH) transformations[64,65] lead to a block diagonalization of the Hamiltonian, i.e. a to decoupling of the negative-energy states (see eq. (3.43)).[21] A sequence of unitary transformations $U_i$, starting with the free-particle Foldy-Wouthuysen transformation $U_0$,[63] is performed.[21,55] This corresponds to a stepwise decoupling of the Hamiltonian in orders of the potential $V$.[21,55]

$$U = \cdots U_3 U_2 U_1 U_0 = \prod_{i=0}^{\infty} U_i \tag{3.45}$$

$$U_0 = A_p \begin{pmatrix} 1 & \boldsymbol{\sigma} \cdot \mathbf{P}_p \\ -\boldsymbol{\sigma} \cdot \mathbf{P}_p & 1 \end{pmatrix} \tag{3.46}$$

where the factors are given by

$$\begin{aligned} A_p &= \sqrt{\frac{E_p + m_e c^2}{2E_p}} \quad , \quad \mathbf{P}_p = \frac{c\,\mathbf{p}}{E_p + m_e c^2} \quad , \quad R_p = \boldsymbol{\alpha} \cdot \mathbf{P}_p = \frac{c(\boldsymbol{\alpha} \cdot \mathbf{p})}{E_p + m_e c^2} \\ E_p &= \sqrt{\mathbf{p}^2 c^2 + m_e^2 c^4} \quad . \end{aligned} \tag{3.47}$$

$E_p$ is the (positive) relativistic energy of a freely moving particle, $A_p$ and $R_p$ denote kinematic factors.[21]

*1st unitary transformation:*[21]

$$\hat{f}_1 = U_0 \left( \hat{h}^{free} + V \right) U_0^{\dagger} = \varepsilon_0 + \varepsilon_1 + \mathcal{O}_1 \tag{3.48}$$

$$\varepsilon_0 = \beta E_p - m_e c^2 \tag{3.49}$$

$$\varepsilon_1 = A_p V A_p + A_p R_p V R_p A_p \tag{3.50}$$

$$\mathcal{O}_1 = \beta A_p [R_p, V] A_p \tag{3.51}$$

The arising $\varepsilon$ terms are called *even*, because they exhibit the desired block-diagonal $LL$ and $SS$ structure, while the *odd* operator $\mathcal{O}$ contains the off-diagonal elements. The aim is to cancel the odd operators, which is accomplished by odd and antihermitian operators $W$ ($W^\dagger = -W$).[21]

*2nd unitary transformation:*[21]

$$\hat{f}_2 = U_1 \hat{f}_1 U_1^\dagger \tag{3.52}$$

$$= \varepsilon_0 + \varepsilon_1 + \mathcal{O}_1^{(2)} + \varepsilon_2 + \mathcal{O}_2^{(2)} + \varepsilon_3 + \mathcal{O}_3^{(2)} + \sum_{k=4}^{\infty} \left( \varepsilon_k^{(2)} + \mathcal{O}_k^{(2)} \right) \tag{3.53}$$

The antihermitian operator $W_1$, which is first order in $V$, is defined in such a way as to obtain $\mathcal{O}_1^{(2)} = 0$.[21] After this second unitary transformation $U_1$, which is the first DK transformation, all terms needed for the third order DKH Hamiltonian are determined, i.e. $\varepsilon_{0-3}$.[21]
Further unitary transformations lead to higher order DKH Hamiltonians. The $n$-th order DKH Hamiltonian is given by[21]

$$\hat{h}_{\mathrm{DKH}n} = \varepsilon_0 + \varepsilon_1 + \varepsilon_2 + \cdots = \sum_{k=0}^{n} \varepsilon_k \tag{3.54}$$

where $\varepsilon_0$ and $\varepsilon_1$ are given above and[21]

$$\varepsilon_2 = \frac{1}{2}[W_1', \mathcal{O}_1] \tag{3.55}$$

$$W_1'(i,j) = \beta \frac{\mathcal{O}_1^{(1)}(i,j)}{E_i + E_j} \quad . \tag{3.56}$$

For explicit expressions of the other terms and higher order $\varepsilon$ see the book by Reiher & Wolf[21].

It should be noted that the occurring operators are defined in momentum space.[21,55] Accordingly, all operators first need to be transformed to $p^2$-space for the construction of the DKH Hamiltonian and afterwards the reversed transformation back to position space is carried out.[21]

$$\hat{h}_{\mathrm{DKH}\infty} = \sum_{k=0}^{\infty} \varepsilon_k = \sum_{k=0}^{\infty} \begin{pmatrix} \varepsilon_{k+} & 0 \\ 0 & \varepsilon_{k-} \end{pmatrix} = \sum_{k=0}^{\infty} \begin{pmatrix} \varepsilon_{k+}^{\mathrm{sf}} + \varepsilon_{k+}^{\mathrm{sd}} & 0 \\ 0 & \varepsilon_{k-}^{\mathrm{sf}} + \varepsilon_{k-}^{\mathrm{sd}} \end{pmatrix} \tag{3.57}$$

Equation (3.57) highlights the possibility to decompose each even operator $\varepsilon$ into spin-free (sf) and spin-dependent (sd) parts.[21] When going from the four-component theory to the two-component theory, only the $LL$ blocks are of interest in order to reproduce the positive-energy spectrum. Then, the $(2 \times 2)$-block diagonal operator up to fourth order ($n = 4$) is given by[21]

$$\hat{h}^{2c}_{\mathrm{DKH}n} = \sum_{k=0}^{n} \varepsilon_{k+} \quad . \tag{3.58}$$

A successful modification is the *scalar-relativistic* or one-component DKH method. In this approximation, the spin-dependent operators are neglected ($\boldsymbol{\alpha} \cdot \mathbf{p} \Rightarrow \sigma \cdot \mathbf{p} \Rightarrow \mathbf{p}$) and only one-electron operators are altered in order to account for scalar-relativistic effects.[21] The reason why two-electron operators are not considered is that the DKH Hamiltonian is determined before the start of the SCF iterations, which makes the inclusion of the two-electron terms of the Fock operator impossible since they depend on the solution functions $\psi$. This causes the *picture change error* since these terms are not transformed and only accounted for in the non-relativistic form.[21] The scalar-relativistic DKH method can be readily implemented in non-relativistic quantum chemistry programs.[21] The ORCA program package uses for example the second-order spin-free, i.e. scalar-relativistic, DKH Hamiltonian.[66]

## 3.4. Configuration Interaction

A single determinant approach like the (Dirac-)Hartree-Fock method is not a good choice for quantum chemical calculations. The difference between the exact electronic energy and the (Dirac-)Hartree-Fock energy, the so called *correlation energy*, amounts to < 5% of the exact energy.[21]
A systematic improvement is, for example, an expansion of the total electronic state A $\Psi_A$, e.g., into configuration state functions (CSF) $\Phi_I$, which themselves are given by a superposition of Slater determinants, here denoted $\Theta_K$.[21] This technique is known as *configuration interaction*. It accounts for the so called *dynamic correlation*.[21]

$$\Psi_A = \sum_{I=0}^{\infty} \Phi_I C_{IA} \tag{3.59}$$

$$\Phi_I = \sum_K \Theta_K B_{KI} \tag{3.60}$$

Equation (3.59) gives the full configuration interaction (FCI) wave function, which corresponds to an expansion into the complete set of CSFs (or Slater determinants).[21] The expansion coefficients $C_{IA}$ of state A are called "CI coefficients".
The CI expansion is usually truncated according to a specific substitution pattern, where occupied spinors (or spin orbitals) of the Slater determinant are replaced by new orthogonal virtual spinors.[21] CI-Singles-Doubles (CISD) for example corresponds to a truncation after double substitutions, i.e. only single- $\Phi_a^r$ and double-excited determinants $\Phi_{ab}^{rs}$ are included, where one occupied spinor (spin orbital) $a$ has been replaced by a virtual spinor $r$, or in general $a$, $b$, $c$, ... occupied spinors are substituted by $r$, $s$, $t$, ... virtual spinors ($\Phi_{abc\ldots}^{rst\ldots}$). The virtual spinors are obtained through the solution of the Roothaan equation.[21]

$$\Psi_A^{CISD} = \Phi_0\, C_{0,A} + \sum_{ar}^{N} \Phi_a^r\, C_{(ar),A} + \sum_{\substack{a<b \\ r<s}}^{N} \Phi_{ab}^{rs}\, C_{(ar),(bs),A} \tag{3.61}$$

$\Phi_0$ gives the (Dirac-)Hartree-Fock ground state wave function.[26] Using the notation $|S\rangle$ for $|\Phi_a^r\rangle$ (*s*ingle excitation), $|D\rangle$ for $|\Phi_{ab}^{rs}\rangle$ (*d*ouble excitation), $|T\rangle$ for $|\Phi_{abc}^{rst}\rangle$ (*t*riple excitation) etc., the upper part of the Hermitian CI matrix $\mathbf{H}$ is given by[26]

$$\begin{array}{c} \\ \langle\Phi_0| \\ \langle S| \\ \langle D| \\ \langle T| \\ \vdots \end{array} \begin{array}{c} \begin{array}{ccccc} |\Phi_0\rangle & |S\rangle & |D\rangle & |T\rangle & \cdots \end{array} \\ \begin{pmatrix} \langle\Phi_0|\hat{H}|\Phi_0\rangle & 0 & \langle\Phi_0|\hat{H}|D\rangle & 0 & \cdots \\ & \langle S|\hat{H}|S\rangle & \langle S|\hat{H}|D\rangle & \langle S|\hat{H}|T\rangle & \cdots \\ & & \langle D|\hat{H}|D\rangle & \langle D|\hat{H}|T\rangle & \cdots \\ & & & \langle T|\hat{H}|T\rangle & \cdots \\ & & & & \vdots \end{pmatrix} \end{array} \tag{3.62}$$

However, each truncated CI expansion suffers from the lack of *size consistency*.

A further improvement is given by the multi-reference configuration interaction MRCI method, which employs a linear combination of N-electron basis functions $\{\Phi^{ref}\}$ instead of a single (Dirac-)Hartree-Fock reference determinant $\Phi_0$.[21]

$$\Psi_A^{MRCI} = \sum_{\nu} \Phi_{\nu}^{ref} C_{\nu,A} + \sum_{\nu,ar}^{N} \Phi_{\nu,a}^{ref,r} C_{(ar),A} + \sum_{\substack{\nu \\ a<b \\ r<s}}^{N} \Phi_{\nu,ab}^{ref,rs} C_{(ar),(bs),A} \tag{3.63}$$

The CI eigenvalue problem is solved variationally yielding the matrix equation for all electronic states[21]

$$\mathbf{HC} = \mathbf{E}_{el}\mathbf{C} \tag{3.64}$$

The columns of the matrix $\mathbf{C}$ contain the CI coefficients and $\mathbf{E}_{el}$ is the diagonal matrix of the total electronic energies. The solution of the CI eigenvalue problem, i.e. the diagonalization of $\mathbf{H}$, can be achieved using, for example, the Davidson algorithm.[21]

The relativistic CI method is more complicated than the non-relativistic approach, because classes of integrals are non-zero which vanish in the latter case. The Hamiltonian is of block-pentadiagonal form. Problems of an increased number of determinants or increased size of the Hamiltonian matrix have to be faced. For example, in the case of CI with double excitations, the expansion is four times longer in the relativistic case compared to the non-relativistic counterpart. This is a consequence of the Kramers pairs and their properties.[53] The concept of Kramers pairs, i.e. a spinor and its Kramers partner, instead of $\alpha$- and $\beta$-spin orbitals, is given in (4.3) on page 70.

### Kramers Restricted Configuration Interaction

In this thesis the relativistic program module LUCIAREL[67–70], which is implemented in the DIRAC program package, was employed to perform *Kramers Restricted Configuration Interaction* (KRCI)[20,68,70] calculations. The one-particle functions in this multi-reference CI program constitute Kramers-paired spinors $\{\psi_p\ ,\psi_{\bar{p}}\}$, which transform according to the irreducible representations (irreps) of *double groups*.[20,68] As a consequence, the fermion irrep for each shell must be specified in an input for such a relativistic calculation rather than the spatial symmetry. All calculations were performed in the double group $D_{2h}^*$, i.e. in a group with inversion center, where there are two possible fermion irreps corresponding to *gerade* and *ungerade* spinors.

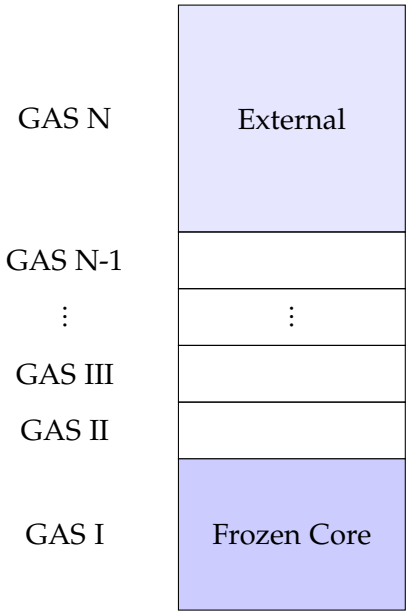


Figure 3.1.: Concept of Generalized Active Spaces (GAS) taken from Fleig[70].

An important feature of the KRCI module is the *Generalized Active Space* (GAS)[67,70] concept. The one-particle space can be divided into subspaces, where different excitations and occupation numbers are allowed. This offers the possibility to design an active space flexibly.[70] Figure 3.1 highlights the underlying principle of GA spaces, dividing the one-particle space into a frozen core, several subsequent GA spaces exhibiting different occupation numbers and excitation levels, i.e. single, double, triple, etc. excitations into the next GA space, and finally the external orbitals. Excitations out of the outer core shells of GAS I are also possible, therefore enabling core-valence correlation.

## 3.5. Multi-Configurational Self-Consistent Field – CASSCF

The *Multi-Configurational Self-Consistent Field* (MCSCF) method is again based on a linear combination of determinants or configuration state functions (CSF) $\Phi$. In this method not only the expansion coefficients $C_\nu$, but also the molecular orbitals $\Phi_\nu^{opt}$ are optimized, as opposed to CI methods.[21]

$$\Psi_A^{MCSCF} = e^{-\kappa} \sum_{\nu \epsilon S} \Phi_\nu \, C_{\nu A} \tag{3.65}$$

The expansion is carried out in a chosen subspace $S$,[21] because the number of configurations that can be included in an MCSCF calculation is restricted for computational reasons.
The second-generation MCSCF methods optimize the configurational coefficients and orbitals, or "orbital (spinor) rotation parameters", simultaneously, which can be achieved using the Newton-Raphson technique.[21] It is based on the first and second derivatives of the energy with respect to the variational parameters. The optimization of the orbitals is accomplished using a unitary matrix $U$ that contains the orbital rotation parameters $\kappa_{pq}$.[21]

$$U = e^{-\boldsymbol{\kappa}} \tag{3.66}$$

$$UU^{\dagger} = \mathbf{1} \;\rightarrow\; U^{\dagger} = (e^{-\boldsymbol{\kappa}})^{T} = e^{\boldsymbol{\kappa}} \tag{3.67}$$

$$\boldsymbol{\kappa}^{\dagger} = -\boldsymbol{\kappa} \;\text{ (antihermitian)} \tag{3.68}$$

The MCSCF wave function (3.65) is a qualitatively correct description of the system, which accounts for *static correlation* due to the flexibility of the wave function.[71] It can therefore describe near-degeneracy effects, i.e. systems in which some configurations have nearly the same energy,[71] for example $f$-elements.[20]

A variant of the MCSCF method is the *Complete Active Space Self-Consistent Field* (CASSCF) technique, which divides the molecular orbitals into active and inactive orbitals. In the active space, which usually consists of the highest occupied and lowest unoccupied orbitals, a full CI is carried out.[71] This limits of course the number of electrons and orbitals that can be included in the active space and a thorough choice of the orbitals has to be made. [$n$,$m$]-CASSCF indicates that $n$ electrons in $m$ orbitals are included the active space.[71] The CASSCF concept is shown in Figure 3.2.

## SOC-CASSCF

The ORCA[72] program package provides a "fully variational spin-orbit coupled CASSCF" method based on quasi-degenerate perturbation theory.[66] An effective spin-orbit coupling (SOC) operator, the *spin-orbit mean-field* (SOMF) operator by Heß *et al.*[73], is employed.[74] It was derived starting from the Breit-Pauli SOC operator with the approximation to approach the two-electron part of the operator by a mean-field, thus yielding an effective one-electron operator[74]

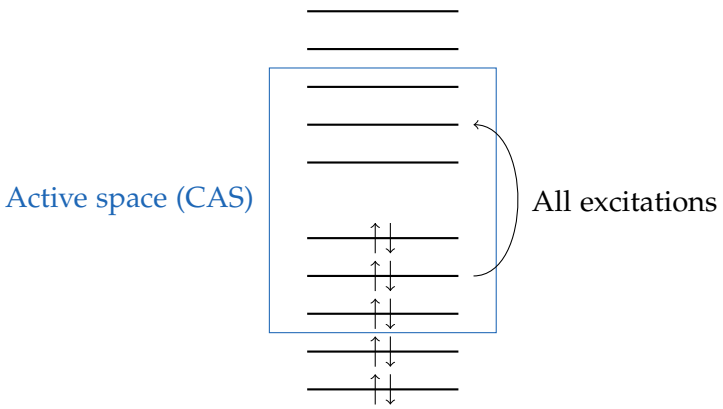


Figure 3.2.: Definition of an active space for CASSCF calculations taken from Jensen[71].

$$\hat{H}_{SOMF} = \sum_i \hat{\mathbf{z}}_i \, \hat{\mathbf{s}}_i \quad . \tag{3.69}$$

The one-electron part of the SOC operator is given by[74]

$$\hat{H}^{(1)}_{SOC} = \sum_i \hat{\mathbf{h}}_i^{1el-SOC} \, \hat{\mathbf{s}}_i \tag{3.70}$$

$$= \frac{\alpha^2}{2} \sum_i \sum_A Z_A \, r_{iA}^{-3} \, \hat{\mathbf{l}}_{iA} \, \hat{\mathbf{s}}_i \quad , \tag{3.71}$$

which is equivalent to the one-electron part in the Breit-Pauli SOC operator.[74] Here $\alpha = c^{-1} \approx 1/137$ is the fine structure constant in atomic units, $Z_A$ is the charge of nucleus $A$ and $\hat{\mathbf{s}}_i$ is the spin operator of electron $i$. The distance between the $i$-th electron and nucleus $A$ is given by $r_{iA} = |\mathbf{r}_i - \mathbf{R}_A|$ and $\hat{\mathbf{l}}_{iA} = (\hat{\mathbf{r}}_i - \mathbf{R}_A) \times \hat{\mathbf{p}}_i$ denotes the angular momentum of electron $i$ relative to nucleus $A$, with $\hat{\mathbf{p}}_i$ being the momentum operator of the $i$-th electron.[74]

The two-electron part uses the operator[74]

$$\hat{\mathbf{g}}^{SOC}(i,j) = -\frac{\alpha^2}{2} \, \hat{\mathbf{l}}_{ij} \, r_{ij}^{-3} \quad . \tag{3.72}$$

Together, $\hat{\mathbf{h}}^{1el-SOC}$ and $\hat{\mathbf{g}}^{SOC}$ define the matrix elements of the spatial part $\hat{\mathbf{z}}$ of the mean-field SOC operator $\hat{H}_{SOMF}$[74]

$$\langle \phi_i \,|\, \hat{\mathbf{z}} \,|\, \phi_a \rangle = \left\langle \phi_i \left| \hat{\mathbf{h}}^{1el-SOC} \right| \phi_a \right\rangle + \sum_j n_j \Big[ (\phi_i \phi_a | \hat{\mathbf{g}}^{SSO} | \phi_j \phi_j) - \frac{3}{2} (\phi_i \phi_j | \hat{\mathbf{g}}^{SOC} | \phi_j \phi_a) - \frac{3}{2} (\phi_j \phi_a | \hat{\mathbf{g}}^{SOC} | \phi_i \phi_j) \Big] \quad . \tag{3.73}$$

Here, the sum $\sum_j$ is carried out over the spatial orbitals $\phi_j$ with fixed occupation numbers $n_j$.[73] A special notation is used to indicate the spatial integrals $(\cdots)$.[74]

$$\left\langle \psi_p \psi_q \left| \hat{g}_{1,2}^{2el-SOC} \right| \psi_r \psi_s \right\rangle = (\phi_p \phi_r | \hat{\mathbf{g}}^{SOC} | \phi_q \phi_s) \left\{ \delta_{\chi_q \chi_s} \langle \chi_p | \hat{s} | \chi_r \rangle + 2 \delta_{\chi_p \chi_r} \langle \chi_q | \hat{s} | \chi_s \rangle \right\} \tag{3.74}$$

The orthonormal spin orbitals $\psi_k$ can be written as a product of a spatial $\phi_k$ and a spin part $\chi_k$.

$$\psi_k = \phi_k(\mathbf{r}) \, \chi_k(s) \tag{3.75}$$

$$\chi_k(s) = \alpha(s) \quad \text{or} \quad \beta(s) \tag{3.76}$$

For actual calculations the spatial orbitals are expanded in a set of basis functions.[74] The CASSCF wave function is obtained as a linear combination of wave functions with specific multiplicities $S$ and the associated $M_S = S, S-1, ..., -S$.[66]

$$\Psi^{(rel)} = \Psi^{SM_S} + \Psi^{SM_S-1} + \cdots + \Psi^{S-1M_S-1} + \Psi^{S-1M_S-2} + \cdots \tag{3.77}$$

$$\Psi^{SM_S} = \sum_I^N C_I^{SM_S} \, \Phi_I^{SM_S} \tag{3.78}$$

$\Phi$ again represents a CSF. The eigenvectors and energy levels of the coupled states are obtained by diagonalizing the corresponding matrix with the elements[66]

$$\left\langle \Psi_I^{SM_S} \left| \hat{H}_{BO} + \hat{H}_{SOC} \right| \Psi_J^{S'M'_S} \right\rangle = \delta_{IJ} \, \delta_{SS'} \, \delta_{M_S M'_S} \, E_I^{(S)} + \left\langle \Psi_I^{SM_S} \left| \hat{H}_{SOMF} \right| \Psi_J^{S'M'_S} \right\rangle \quad . \tag{3.79}$$

$\hat{H}_{BO}$ represents the Born-Oppenheimer Hamiltonian.

## 3.6. Basis sets and effective core potentials

### Basis set expansion technique and spinor basis

In the independent particle model, the total wave function $\Psi$ of a system can be expressed as an antisymmetrized product of molecular 4-spinors $\psi_i(\mathbf{r})$ or a Slater determinant, respectively, in an analogous way like the one presented in (2.1.1) on page 9. On the basis of the LCAO model (linear combination of atomic orbitals), a molecular spinor is expanded in a set of atomic $(at)$ 4-spinors $\psi_k^{(at)}(\mathbf{r}, \mathbf{R}_A)$, which themselves are expressed in terms of known *basis functions* $\phi_\mu^{(a)}(\mathbf{r}, \mathbf{R}_A)$. $\mathbf{R}_A$ is the coordinate of nucleus A, at which the specific spinor or basis function is centred,[21] and $\mathbf{r}$ is the electronic coordinate.

$$\psi_i(\mathbf{r}) = \sum_k^{m'} d_{ik}\, \psi_k^{(at)}(\mathbf{r}, \mathbf{R}_A) \tag{3.80}$$

Here the coefficients $d_{ik}$ correspond to the occupation numbers.[21]

$$\psi_k^{(at)}(\mathbf{r}, \mathbf{R}_A) = \sum_\mu^{m'_k} \begin{pmatrix} b_{k\mu}^{(1)}\, \phi_\mu^{(1)}(\mathbf{r}, \mathbf{R}_A) \\ b_{k\mu}^{(2)}\, \phi_\mu^{(2)}(\mathbf{r}, \mathbf{R}_A) \\ b_{k\mu}^{(3)}\, \phi_\mu^{(3)}(\mathbf{r}, \mathbf{R}_A) \\ b_{k\mu}^{(4)}\, \phi_\mu^{(4)}(\mathbf{r}, \mathbf{R}_A) \end{pmatrix} \tag{3.81}$$

The superscripts $(a)$ label the different components of the spinor. However, a single basis set $\{\phi_\mu(\mathbf{r}, \mathbf{R}_A)\}$ can be used for all components as well.[21]

$$\psi_i(\mathbf{r}) = \sum_k^{m'} \sum_\mu^{m'_k} d_{ik} \begin{pmatrix} b_{k\mu}^{(1)}\, \phi_\mu^{(1)}(\mathbf{r}, \mathbf{R}_A) \\ b_{k\mu}^{(2)}\, \phi_\mu^{(2)}(\mathbf{r}, \mathbf{R}_A) \\ b_{k\mu}^{(3)}\, \phi_\mu^{(3)}(\mathbf{r}, \mathbf{R}_A) \\ b_{k\mu}^{(4)}\, \phi_\mu^{(4)}(\mathbf{r}, \mathbf{R}_A) \end{pmatrix} \equiv \sum_\mu^{m} \begin{pmatrix} c_{i\mu}^{(1)}\, \phi_\mu^{(1)}(\mathbf{r}, \mathbf{R}_A) \\ c_{i\mu}^{(2)}\, \phi_\mu^{(2)}(\mathbf{r}, \mathbf{R}_A) \\ c_{i\mu}^{(3)}\, \phi_\mu^{(3)}(\mathbf{r}, \mathbf{R}_A) \\ c_{i\mu}^{(4)}\, \phi_\mu^{(4)}(\mathbf{r}, \mathbf{R}_A) \end{pmatrix} \tag{3.82}$$

Here the $c_{i\mu}^{(a)}$ are the combined expansion coefficients of the basis functions and $m' = s(A) \times d(s) \times M$ denotes the number of basis spinors with the number of shells per atom, $s(A)$, the degeneracy of each shell, $d(s)$, and the number $M$ of atoms in the molecule (minimal basis). There are $m'_k$ expansion coefficients $b_{k\mu}^{(a)}$ of the basis functions, also called "*contraction coefficients*", hence the total number of basis functions is $4 \times m$, where $m = m' \times m'_k$.[21] For an

exact representation of a molecular spinor a *complete* basis would be needed, i.e. an infinite number of basis spinors. However, in actual calculations the number of basis spinors is restricted.[21] A *contracted* basis set uses frozen expansion coefficients $b_{k\mu}^{(a)}$, therefore reducing the number of basis functions.[21]

The kinetic balance condition can also be formulated for the molecular spinors $\psi_i$.[21]

$$\psi_i^S \approx \frac{\boldsymbol{\sigma} \cdot \boldsymbol{\pi}}{2m_e c} \psi_i^L \tag{3.83}$$

Instead of using four independent expansions for the four components of a molecular spinor, one can also expand them in terms of 2-spinors[21]

$$\psi_i(\mathbf{r}) = \begin{pmatrix} \sum_\mu c_{i\mu}^{(L)} \, \phi_\mu^L(\mathbf{r}_A) \\ \sum_\mu c_{i\mu}^{(S)} \, \phi_\mu^S(\mathbf{r}_A) \end{pmatrix} \tag{3.84}$$

where $\mathbf{r}_A = \mathbf{r} - \mathbf{R}_A$.

$$\phi_\mu^L(\mathbf{r}_A) = \frac{P_\mu(r_A)}{r_A} \chi_{\kappa_\mu m_\mu}(\vartheta_A, \varphi_A) \tag{3.85}$$

$$\phi_\mu^S(\mathbf{r}_A) = i \frac{Q_\mu(r_A)}{r_A} \chi_{-\kappa_\mu m_\mu}(\vartheta_A, \varphi_A) \tag{3.86}$$

The two-component spherical spinors $\chi_{\pm\kappa_\mu m_\mu}(\vartheta_A, \varphi_A)$ correspond to the Pauli spinors, which are eigenfunctions of the squared two-component angular momentum $\mathbf{j}^2$ and $j_z$.[21]

$$\chi_{jm_j}^{(\pm)} = \begin{pmatrix} \pm\sqrt{\frac{\ell \pm m_j + 1/2}{2\ell+1}} \, Y_{\ell(m_j - \frac{1}{2})} \\ \sqrt{\frac{\ell \mp m_j + 1/2}{2\ell+1}} \, Y_{\ell(m_j + \frac{1}{2})} \end{pmatrix} \tag{3.87}$$

$$\chi_{\kappa m_j} = \chi_{jm_j}^{(+)} \tag{3.88}$$

$$\chi_{-\kappa m_j} = \chi_{jm_j}^{(-)} \tag{3.89}$$

$Y$ are spherical harmonics and $\kappa^{(+)} = j + \frac{1}{2}$, $\kappa^{(-)} = -j - \frac{1}{2} = -\kappa^{(+)}$ are quantum numbers.[21]

The radial parts $P_\mu(r_A)$ and $Q_\mu(r_A)$ could be expressed as Slater-type functions. However, this usually leads to unsolvable SCF equations. For this reason, mainly Gauss-type functions (GTO) are used. They exhibit a different short and long range behaviour, therefore more Gaussian functions are needed than Slater-type functions to represent an atomic orbital.[21]

$$P_\mu^{GTO}(r_A) = N_\mu^L \, r_A^{\ell_\mu+1} \, e^{-\zeta_\mu r_A^2} \tag{3.90}$$

$$Q_\mu^{GTO}(r_A) = N_\mu^S \left[(\kappa_\mu + \ell_\mu + 1) - \zeta_\mu r_A\right] r_A^{\ell_\mu} \, e^{-\zeta_\mu r_A^2} \tag{3.91}$$

The factors $\zeta_\mu$ are the only adjustable parameters of the basis. They are determined before the calculation and are called the "*exponents*".[21]
This basis functions can also be expressed in Cartesian coordinates, in contrast to the above polar coordinates, where the sum of the exponents $(\alpha_\mu + \beta_\mu + \gamma_\mu)$ is associated with the angular quantum number $\ell$.[21]

$$\phi_\mu^L(\mathbf{r}_A) = N_\mu^L \, x^{\alpha_\mu} \, y^{\beta_\mu} \, z^{\gamma_\mu} \, e^{-\zeta_\mu^L r_A^2} \tag{3.92}$$

$$\phi_\mu^S(\mathbf{r}_A) = N_\mu^S \, x^{\alpha_\mu} \, y^{\beta_\mu} \, z^{\gamma_\mu} \, e^{-\zeta_\mu^S r_A^2} \tag{3.93}$$

The kinetic balance is applied to the radial function of the small component.[21]

In this thesis Dyall's triple-zeta core-valence basis set cv3z[75] was used, which is available in the DIRAC program.[†] Dyall's basis sets are more or less correlation-consistent[76]. The triple-zeta (3z) refers to the usage of three basis functions for the description of one valence orbital, i.e. the $s$ and $p$ set in this case. The (core-)valence (cv) basis comprises functions for the correlation of the $ns$, $np$, $nd$, $nf$, $(n+1)s$, $(n+1)p$, $(n+1)d$, and $(n+2)s$ shells for the lanthanides.[77] The cv3z basis set consists of 2-spinor Gaussian functions. Here, the primitive functions for the small component are obtained using the kinetic balance condition.[78]
The use of a spinor basis in relativistic calculations should be preferred to the use of "scalar relativistic molecular orbitals", which are obtained without regard to spin-orbit coupling, according to Fleig *et al.*[68]. The spinors require the integration of double group symmetry into a program.[68]

[†]http://dirac.chem.sdu.dk/basisarchives/dyall/index.html (28.02.2014).

## Effective core potentials

The idea behind *effective core potentials* (ECP) is to include only the valence electrons in an actual calculation, which are considered to determine the chemical behaviour of an atom or molecule. This leads not only to a considerable reduction of computational effort compared to the use of an all-electron basis set, but it also makes the inclusion of relativistic effects in a simple way possible by a proper design of the potentials.[79] These potentials then replace the core electrons.[21]

One starts with an effective *valence-only* ($v$) model Hamiltonian[79]

$$\hat{H}_v = \sum_i^{n_v} \hat{h}_v(i) + \sum_{i<j}^{n_v} \hat{g}_v(i,j) + V_{cc} + V_{cpp} \quad . \tag{3.94}$$

Here $V_{cc}$ is the repulsion between the core electrons and nuclei of the system and $V_{cpp}$ is the "core polarization potential"; the subscript $v$ denotes the valence electrons and $c$ the core electrons. The number of valence electrons, $n_v$, is given by $n_v = n - \sum_\lambda^N (Z_\lambda - Q_\lambda)$, where $Q_\lambda$ denotes the charge of the core $\lambda$.
The non-relativistic Hamiltonian (in atomic units) can be used to model the one- and two-electron operators[79]

$$\hat{h}_v(i) = -\frac{1}{2}\Delta_i + V_{cv}(i) \tag{3.95}$$

$$\hat{g}_v(i,j) = \frac{1}{r_{ij}} \quad . \tag{3.96}$$

The **effective core potential** (ECP) is given by $V_{cv}$. It describes the interaction of a valence electron with the core and the nuclei. Relativistic effects are accounted for by an appropriate design of $V_{cv}$. In the case of molecular systems, $V_{cv}$ is defined as a superposition of the atomic pseudopotentials.[21,79]

$$V_{cv}(i) = \sum_\lambda^N \left( -\frac{Q_\lambda}{r_{\lambda i}} + \Delta V_{cv}^\lambda(r_{\lambda i}) \right) + \cdots \tag{3.97}$$

The interaction between the nuclei and cores, $V_{cc}$, is obtained in an analogous way.

$$V_{cc} = \sum_{\lambda<\mu}^{N} \left( \frac{Q_\lambda Q_\mu}{r_{\lambda\mu}} + \Delta V_{cc}^{\lambda\mu}(r_{\lambda\mu}) \right) + \cdots \tag{3.98}$$

In both potentials (3.97) and (3.98), the first term corresponds to an attractive or repulsive Coulomb interaction, respectively, while $\Delta V_{cv}^{\lambda}$ and $\Delta V_{cc}^{\lambda\mu}$ represent correction terms. $Q_\lambda = (Z_\lambda - n_\lambda^{core})e$ is the charge of the atomic core $\lambda$, $r_{\lambda i} = |\mathbf{R}_\lambda - \mathbf{r}_i|$ denotes the distance between nucleus $\lambda$ and electron $i$ and $r_{\lambda\mu} = |\mathbf{R}_\lambda - \mathbf{R}_\mu|$ the distance between the two nuclei $\lambda$ and $\mu$.[21] In order to ensure that the valence orbitals are orthogonal to the core and moved out of the core, projection operators are included in the effective core potentials.[21]

The ECPs used in this thesis are based on a semilocal pseudopotential $V(r_i)$[80]

$$V(r_i) = -\frac{Q}{r_i} + \sum_{\ell} \sum_{k} A_{k\ell}\, e^{-a_{k\ell} r_i^2}\, P_\ell \quad . \tag{3.99}$$

Here the charge of the core is given by $Q$, $i$ and $j$ are electron indices and $P_\ell$ denotes a projection operator onto the Hilbert subspace with angular symmetry $\ell$[80]

$$P_\ell = \sum_{m_\ell} |\ell\, m_\ell\rangle \langle \ell\, m_\ell| \quad . \tag{3.100}$$

The exponents $a_{k\ell}$ are determined by a single electron fit to valence energies of Hartree-Fock calculations, while the coefficients $A_{k\ell}$ can be obtained by a fit to quasi-relativistic all-electron Hartree-Fock valence energies in the case of quasi-relativistic pseudopotentials.[80] Here, this quasi-relativistic equations are given by the Wood-Boring (WB) approach[81] including a mass-velocity term and an averaged Darwin-spin-orbit term.[80] For explicit analytical forms of pseudopotentials see Dolg[79].
Apart from the given *quasi-relativistic* WB pseudopotential, there are also *non-relativistic* (HF) and *relativistic* (DF) pseudopotentials.

Besides the *shape-consistent* pseudopotentials, which yield pseudo-orbitals of nearly the same shape as the original valence orbitals and are needed for an accurate description of bond lengths, there are *energy-consistent* pseudopotentials.[79] These reproduce the energies accurately via a fit to the total valence energy obtained by all-electron multi-configuration

Dirac-Hartree-Fock calculations.[79] The parameters of the pseudopotential are determined such as to obtain the best agreement of the total valence energies. ‡

*Model potentials* are an alternative to pseudopotentials. They conserve the radial-node structure of the original atomic valence orbitals in contrast to the latter potentials.[21]

In this thesis the energy-consistent quasi-relativistic (Wood-Boring WB) pseudopotentials ECP49MWB (for $Nd^{3+}$) and ECP52MWB (for $Eu^{3+}$) published by Dolg *et al.*[80,82] were used. The number (49 or 52) indicates the number of core electrons that have been replaced by the pseudopotential. These ECPs have a *large core*, which includes the $f$-electrons, therefore leaving only 8 valence electrons for $Nd^{3+}$ and $Eu^{3+}$ ($5s$ and $5p$ shells). "M" signifies that a neutral atom was used as a reference system for the generation of the pseudopotential.[83]

## 3.7. Density Functional Theory

In contrast to the above presented wave mechanic methods, density functional theory (DFT) is based on the fact that the energy can be directly defined as a functional of the electron density $\rho$.[71] The underlying principles are the *Hohenberg-Kohn theorems*.[84] If the exact functional relationship was known, DFT would give the exact energy including electron correlation.[71] However, this is not the case and an effort is made to design approximate functionals. The modern application of DFT is mainly based on the *Kohn-Sham theory*, which corresponds to a re-introduction of orbitals in order to calculate the kinetic energy $T$.[71]

The electron density function $\rho_1$ (or $\rho$) is given by

$$\rho_1(\mathbf{r}_1) = N \int \cdots \int |\Psi(\mathbf{x}_1, \mathbf{x}_2, ..., \mathbf{x}_N)|^2 \, ds_1 d\mathbf{x}_2 \cdots d\mathbf{x}_N \tag{3.101}$$

where the integral is equal to the probability of finding an electron at position $\mathbf{r}_1$ and the prefactor guarantees that the integral of the density yields the number of electrons $N$.

$$\hat{H}_\lambda = \hat{T} + \hat{V}_{ext}(\lambda) + \lambda \hat{V}_{ee} \tag{3.102}$$

In equation (3.102) the Hamiltonian of a system is written in terms of the kinetic energy operator $\hat{T}$, the external potential operator $\hat{V}_{ext}$ and the electron-electron interaction operator

‡Energy-consistent ECPs are, for example, available under http://www.theochem.uni-stuttgart.de/pseudopotentials/index.en.html (28.02.2014).

$\hat{V}_{ee}$ with $0 \leq \lambda \leq 1$. Setting $\lambda = 0$ results in a system composed of non-interacting electrons. In such a case the exact solution of the Schrödinger equation is given by a Slater determinant and the exact kinetic energy can be written as[71]

$$T_S = \sum_{i=1}^{N} \left\langle \phi_i \left| -\frac{1}{2}\nabla^2 \right| \phi_i \right\rangle \tag{3.103}$$

where the subscript $S$ indicates that the kinetic energy was calculated from a Slater determinant composed of molecular orbitals $\phi_i$. The idea of Kohn and Sham was to calculate the kinetic energy in this idealised limit.[71]
Yet a real system corresponds to the case $\lambda = 1$, because electrons are interacting particles possessing a charge and a spin, so their motion is correlated. A correction term to the idealised kinetic energy, which is the (kinetic) correlation energy, is therefore introduced.[71]
The external potential operator, which is given by the nuclear-electron attraction $\hat{V}_{ne}$ for $\lambda = 1$, is adapted in such a way as to yield the same density $\rho$ for all $\lambda$ values.[71] The total energy $E_{\mathrm{DFT}}$ can then be expressed as a sum of the contributions from the kinetic energy, the nuclear-electron attraction, the Coulomb part of the electron-electron repulsion $J$ and an exchange-correlation term $E_{xc}$ including the exchange part of the electron-electron repulsion and the remaining correlation energy.[71]

$$E_{\mathrm{DFT}}[\rho] = T_S[\rho] + E_{ne}[\rho] + J[\rho] + E_{xc}[\rho] \tag{3.104}$$

This exchange-correlation functional $E_{xc}[\rho]$ is defined by the deviation of $T_S$ from the exact kinetic energy $T$ and of the Coulomb electron-electron repulsion $J$ from the real interaction $E_{ee}$.[71] It is the only unknown functional in Kohn-Sham theory.[71]

$$E_{xc}[\rho] = (T[\rho] - T_S[\rho]) + (E_{ee}[\rho] - J[\rho]) \tag{3.105}$$

$$E_{ne}[\rho] = -\sum_{A}^{M} \int \frac{Z_A \rho(\mathbf{r})}{|\mathbf{R}_A - \mathbf{r}|} d\mathbf{r} \tag{3.106}$$

$$J[\rho] = \frac{1}{2} \iint \frac{\rho(\mathbf{r})\,\rho(\mathbf{r}')}{|\mathbf{r} - \mathbf{r}'|} d\mathbf{r}\, d\mathbf{r}' \tag{3.107}$$

### Exchange and correlation holes

Electrons avoid each other due to their charge and spin. According to the Pauli principle, the total wave function of such a fermionic system must be antisymmetric with respect to the

interchange of two particles.[26] This leads to the exchange energy. In addition, the charges result in a correlated motion of the electrons giving rise to the (dynamical) correlation energy. This can be described in terms of reduced probabilities of finding an electron in the vicinity of another electron.[71] In the case of $N$ independent particles, the electron pair-density $\rho_2$ can be expressed as the product of two one-electron densities $\rho_1$.[71]

$$\rho_2^{\text{indep}}(\mathbf{r}_1, \mathbf{r}_2) = \left(1 - \frac{1}{N}\right) \rho_1(\mathbf{r}_1)\, \rho_1(\mathbf{r}_2) \tag{3.108}$$

The description of real particles requires the introduction of a reduced probability given by the so-called *exchange-correlation hole* $h_{xc}$.[71]

$$\rho_2(\mathbf{r}_1, \mathbf{r}_2) = \rho_1(\mathbf{r}_1)\, \rho_1(\mathbf{r}_2) + \rho_1(\mathbf{r}_1)\, h_{xc}(\mathbf{r}_1, \mathbf{r}_2) \tag{3.109}$$

$$h_{xc}(\mathbf{r}_1, \mathbf{r}_2) = \frac{\rho_2(\mathbf{r}_1, \mathbf{r}_2)}{\rho_1(\mathbf{r}_1)} - \rho_1(\mathbf{r}_2) \tag{3.110}$$

The exchange-correlation hole can be decomposed into a *Fermi hole* caused by the exchange part and a *Coulomb hole* owing to the dynamical correlation.[71]

$$h_{xc} = h_x + h_c \tag{3.111}$$

$$h_x = h_x^{\alpha\alpha} + h_x^{\beta\beta} \tag{3.112}$$

$$h_c = h_c^{\alpha\alpha} + h_c^{\beta\beta} + h_c^{\alpha\beta} \tag{3.113}$$

The integral of the Fermi hole equals −1, while the integral of the Coulomb hole is zero.[71] The integral of $h_{xc}$ is given by[71]

$$\begin{aligned} \int h_{xc}(\mathbf{r}_1, \mathbf{r}_2) d\mathbf{r}_2 &= \int \frac{\rho_2(\mathbf{r}_1, \mathbf{r}_2)}{\rho_1(\mathbf{r}_1)} d\mathbf{r}_1 d\mathbf{r}_2 - \int \rho_1(\mathbf{r}_2)\, d\mathbf{r}_2 \\ &= \frac{N(N-1)}{N} - N \\ &= -1 \quad . \end{aligned} \tag{3.114}$$

The expression of the Coulomb energy functional $J[\rho]$ (3.107) contains a non-physical self-interaction, which must be corrected. This correction for the self-repulsion is included in the exchange term.[71]

### Exchange-correlation functional

The exchange-correlation functional $E_{xc}[\rho]$ can be expressed in different forms and the choice of the particular functional depends on the problem at hand. In general, it can be distinguished between functionals where the parameters are determined using the requirement to fulfil several criteria, e.g. that the functional should be self-interaction free and that the exchange and correlation energy exhibit different scaling properties, and empirical functionals where the parameters are determined by a fit to experimental data.[71]

The *local density approximation* (LDA) is based on the assumption that the density can locally be approximated as a uniform electron gas, i.e. that the density function varies slowly.[71] In the more general local spin density approximation (LSDA), the exchange energy per particle, $\varepsilon$, is given by[71]

$$\varepsilon_x^{\mathrm{LSDA}} = -\frac{3}{4}\left(\frac{3}{\pi}\right)^{\frac{1}{3}} f_1(\zeta)\,\rho^{\frac{1}{3}} \quad . \tag{3.115}$$

$$E_{xc}[\rho] = E_x[\rho] + E_c[\rho] = \int \rho(\mathbf{r})\,\varepsilon_x[\rho(\mathbf{r})]\,d\mathbf{r} + \int \rho(\mathbf{r})\,\varepsilon_c[\rho(\mathbf{r})]\,d\mathbf{r} \tag{3.116}$$

$\zeta$ is the spin polarization, i.e. the normalized difference between $\rho_\alpha$ and $\rho_\beta$, and $\rho \equiv \rho_1(\mathbf{r})$.[71]

$$f_1(\zeta) = \frac{1}{2}\left[(1+\zeta)^{\frac{4}{3}} + (1-\zeta)^{\frac{4}{3}}\right] \tag{3.117}$$

$$\zeta = \frac{\rho_\alpha - \rho_\beta}{\rho_\alpha + \rho_\beta} \tag{3.118}$$

The LSDA correlation energy can be obtained by interpolating the correlation energy of a uniform electron gas.[71] An important parametrization of this term was published by Vosko, Wilk and Nusair[85] (VWN).

$$\varepsilon_c^{\mathrm{VWN}}(r_s,\zeta) = \varepsilon_c(r_s,0) + \varepsilon_a(r_s)\left(\frac{f_2(\zeta)}{f_2''(0)}\right)(1-\zeta^4) + \left[\varepsilon_c(r_s,1) - \varepsilon_c(r_s,0)\right] f_2(\zeta)\,\zeta^4 \tag{3.119}$$

$$f_2(\zeta) = \frac{f_1(\zeta) - 2}{2^{1/3} - 1} \tag{3.120}$$

The parametrization of the $\varepsilon_c(r_s,\zeta)$ and $\varepsilon_a(r_s)$ functions is given in equation (3.121) with the fitting constants $A$, $x_0$, $b$ and $c$.[71]

$$\begin{aligned}\varepsilon_{c/a}(x) = A\Bigg\{&\ln\left(\frac{x^2}{X(x)}\right)\frac{2b}{Q}\tan^{-1}\left(\frac{Q}{2x+b}\right)\\ &-\frac{bx_0}{X(x_0)}\left[\ln\left(\frac{(x-x_0)^2}{X(x)}\right)+\frac{2(b+2x_0)}{Q}\tan^{-1}\left(\frac{Q}{2x+b}\right)\right]\Bigg\}\end{aligned} \tag{3.121}$$

$$\begin{aligned}x &= \sqrt{r_s}\\ X(x) &= x^2+bx+c\\ Q &= \sqrt{4c-b^2}\end{aligned}$$

It should be noted that in the original publication different parametrizations were suggested, which lead to different implementations of VWN as a local correlation part in the various quantum chemistry programs. The ORCA program uses the "VWN-5" parametrization, while the Gaussian program employs "VWN-3", which leads to slightly different numerical results.[66]

The *generalized gradient approximation* (GGA) provides a means to improve the LSDA method using derivatives of the density, while at the same time ensuring that the Fermi and Coulomb holes integrate to −1 and 0, respectively.[71]
One of the most successful GGA exchange functionals was published by A. D. Becke[86] (1988).

$$\begin{aligned}\varepsilon_x^{\mathrm{B88}} &= \varepsilon_x^{\mathrm{LDA}} + \Delta\varepsilon_x^{\mathrm{B88}}\\ \Delta\varepsilon_x^{\mathrm{B88}} &= -\beta\,\rho^{1/3}\frac{x^2}{1+6\,\beta\,x\sinh^{-1}x}\\ x &= \frac{|\nabla\rho|}{\rho^{4/3}}\end{aligned} \tag{3.122}$$

The parameter of this functional, $\beta$, was determined by a fit to data from the rare gas atoms.[71]

The LYP correlation functional, published by Lee, Yang and Parr[87], is an important GGA correlation functional, which is often combined with the B88 exchange functional (3.122)

yielding BLYP.[71]

$$\begin{aligned}\varepsilon_c^{\mathrm{LYP}} = &-4a\frac{\rho_\alpha\rho_\beta}{\rho^2(1+d\rho^{-1/3})} - a\,b\,\omega\Bigg\{\frac{\rho_\alpha\rho_\beta}{18}\Big[144\,(2^{2/3})\,C_F\,(\rho_\alpha^{8/3}+\rho_\beta^{8/3}) \\ &+(47-7\delta)|\nabla\rho|^2 - (45-\delta)\left(|\nabla\rho_\sigma|^2+|\nabla\rho_\beta|^2\right) + 2\rho^{-1}(11-\delta)\left(\rho_\sigma|\nabla\rho_\sigma|^2+\rho_\beta|\nabla\rho_\beta|^2\right)\Big] \\ &+\frac{2}{3}\rho^2\left(|\nabla\rho_\sigma|^2+|\nabla\rho_\beta|^2-|\nabla\rho|^2\right) - \left(\rho_\alpha^2|\nabla\rho_\beta|^2+\rho_\beta^2|\nabla\rho_\alpha|^2\right)\Bigg\}\end{aligned} \tag{3.123}$$

$$\begin{aligned}C_F &= \frac{3}{10}(3\pi^2)^{2/3} \\ \omega &= \frac{e^{-c\rho^{-1/3}}}{\rho^{14/3}(1+d\rho^{-1/3})} \\ \delta &= c\rho^{-1/3} + \frac{d\rho^{-1/3}}{(1+d\rho^{-1/3})}\end{aligned}$$

The parameters $a$, $b$, $c$ and $d$ were obtained from a fit to data from the helium atom.[71] Another example of a GGA functional is the non-empirical PBE functional by Perdew, Burke and Ernzerhof.[88]

According to the adiabatic connection formula, the relationship between the exchange-correlation energy and the associated hole potential is given by[71]

$$E_{xc} = \int_0^1 \left\langle \Psi_\lambda \middle| \hat{V}_{xc}^{\mathrm{hole}}(\lambda) \middle| \Psi_\lambda \right\rangle d\lambda \tag{3.124}$$

which can be approximated[71]

$$E_{xc} \approx \frac{1}{2}\Big( \left\langle \Psi_0 \middle| \hat{V}_{xc}^{\mathrm{hole}}(0) \middle| \Psi_0 \right\rangle + \left\langle \Psi_1 \middle| \hat{V}_{xc}^{\mathrm{hole}}(1) \middle| \Psi_1 \right\rangle \Big) \quad . \tag{3.125}$$

The first term in equation (3.125) corresponds to the $\lambda = 0$ limit of non-interacting electrons. In this case the exchange energy is exactly given by Hartree-Fock theory based on a single Slater determinant of Kohn-Sham orbitals and the correlation energy is accordingly zero. The second term ($\lambda = 1$ limit) can be approximated using an LSDA functional, or better using an LSDA functional in combination with a gradient correction. Such an approximation to the exchange-correlation functional is called *hybrid* method as it also includes Hartree-Fock exchange (HF).[71]
One of the most successful hybrid functionals is the "Becke 3 parameter Lee Yang Parr" (B3LYP)[87,89,90] functional.

$$E_{xc}^{\mathrm{B3LYP}} = (1-a)E_x^{\mathrm{LSDA}} + a\,E_x^{\mathrm{HF}} + b\,\Delta E_x^{\mathrm{B88}} + (1-c)E_c^{\mathrm{LSDA}} + c\,E_c^{\mathrm{LYP}} \tag{3.126}$$

The three parameters $a$, $b$ and $c$ were determined by a fit to experimental data ($a \approx 0.2$, $b \approx 0.7$, $c \approx 0.8$).[71]
Another example is the one parameter hybrid functional PBE0. The addition of exact Hartree-Fock exchange could be shown to improve the results of DFT calculations.[71]

## DFT calculations

The theory behind DFT calculations is very similar to the Hartree-Fock theory. The orthogonal orbitals from a basis set expansion are determined in such a way as to minimize the energy based on the Lagrange method, i.e. by setting the variation of the Lagrange functional[71]

$$L[\rho] = E_{\mathrm{DFT}}[\rho] - \sum_{ij}^{N} \lambda_{ij} \left( \langle \psi_i | \psi_j \rangle - \delta_{ij} \right) \tag{3.127}$$

equal to zero. This yields, after a unitary transformation that makes the matrix of Lagrange multipliers diagonal, the Kohn-Sham pseudo-eigenvalue equations.[71]

$$\mathbf{h}_{KS}\, \psi_i = \varepsilon_i\, \psi_i \tag{3.128}$$

or after expansion of the orbitals $\psi$ into a basis set $\{\phi\}$[71]

$$\mathbf{h}_{KS}\, \mathbf{C} = \mathbf{S}\, \mathbf{C}\, \boldsymbol{\varepsilon} \quad . \tag{3.129}$$

$$h_{ab} = \langle \phi_a | \hat{h}_{KS} | \phi_b \rangle \tag{3.130}$$

$$S_{ab} = \langle \phi_a | \phi_b \rangle \tag{3.131}$$

The operators can be written as[71]

$$\hat{h}_{KS} = -\frac{1}{2}\nabla^2 + V_{eff} \tag{3.132}$$

$$V_{eff}(\mathbf{r}) = V_{ne}(\mathbf{r}) + \int \frac{\rho(\mathbf{r}')}{|\mathbf{r} - \mathbf{r}'|} d\mathbf{r}' + V_{xc}(\mathbf{r}) \tag{3.133}$$

$$\begin{aligned} V_{xc}(\mathbf{r}) &= \frac{\delta E_{xc}[\rho]}{\delta \rho(\mathbf{r})} \\ &= \varepsilon_{xc}[\rho(\mathbf{r})] + \int \rho(\mathbf{r}') \frac{\delta \varepsilon_{xc} \mathbf{r}'}{\delta \rho(\mathbf{r})} d\mathbf{r}' \quad . \end{aligned} \tag{3.134}$$

The integrals of the exchange-correlation part $V_{xc}$ cannot be determined analytically, therefore a numerical integration based on a grid is performed.[71]

$$\int \phi_a(\mathbf{r})\ V_{xc}[\rho(\mathbf{r}), \nabla\rho(\mathbf{r})]\ \phi_b(\mathbf{r}) d\mathbf{r} \approx \sum_{k}^{G} V_{xc}[\rho(\mathbf{r}_k), \nabla\rho(\mathbf{r}_k)]\ \phi_a(\mathbf{r}_k)\, \phi_b(\mathbf{r}_k)\, \Delta\mathbf{v}_k \tag{3.135}$$

Here the sum runs over the number of grid points $G$.

DFT calculations are popular for optimizations of (transition) metal complexes.[91] The computational costs are comparatively low, but the obtained results are more accurate than those provided by Hartree-Fock[71] or even MP2 calculations in this case. Hybrid functionals could be shown to give a good performance in geometry optimizations of various transition metal complexes yielding only small deviations from the experiments.[92] The PBE hybrid (PBE0), together with B3P86 and B3PW91, gives particularly good results and the authors conclude that it is superior to B3LYP for such applications.[92] However, hybrid functionals should be in general preferred over non-hybrid functionals for geometry optimizations of metal complexes.[92]

# 4. Group theory and symmetry

Symmetry plays an important role in chemistry and physics, as the previous chapters have shown. The spectroscopic selection rules, for instance, were derived using group theoretical considerations, see the rule for non-vanishing matrix elements. The spinors and wave functions of a system can be classified according to the irreducible representations of the point group. In a symmetry-adapted basis the operators adopt block diagonal form, which can be exploited in computational chemistry because in this way matrix operations can be performed more efficiently.[21] Relativistic theories and half-integer values of the total angular momentum quantum number $J$ make the introduction of time reversal symmetry and double groups necessary.

The starting point for the derivation of crystal field theory, the free ion, transforms according to the irreducible representations (irrep) of the group of all rotations in three dimensions $O(3)$. In this full rotation group, the spherical harmonics $Y_\ell^m(\vartheta, \varphi)$ form the basis for the $(2\ell+1)$-dimensional irreps.[23,93] The (reducible) character $\chi$ of a spherical representation with an angular momentum quantum number $\ell$ under a rotation $\alpha$* can be calculated according to[23]

$$\chi(\alpha) = \frac{\sin\left(\left\{\ell + \frac{1}{2}\right\}\alpha\right)}{\sin\left(\frac{\alpha}{2}\right)} \tag{4.1}$$

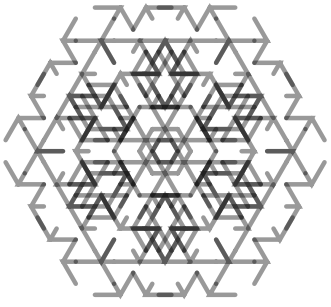

Figure 4.1.: A Koch curve of third order.

*$\chi(C_2) = \chi(\pi)$, $\chi(C_3) = \chi\left(\frac{2\pi}{3}\right)$, $\chi(C_4) = \chi\left(\frac{\pi}{2}\right)$ etc.

In a crystal field, the symmetry group and thus the dimensionality of the irreps is reduced, which leads to the lifting of degeneracy mentioned in the above chapters.[23] The remaining degeneracy can be determined using group theory. In the weak crystal field limit, which is the case for rare earth ions, the total angular momentum quantum number $J$ can still be considered a good quantum number, because the crystal field only acts as a small perturbation.[23] This allows the use of the free ion terms $^{2S+1}L_J$ together with the concept of double groups.

In the case of inversion symmetry, it should be noted that "*g terms split only into g terms and u terms split only into u terms*"[†]. The parity of a many-electron wave function is $\prod_k (-1)^{\ell_k}$, where $\ell$ denotes the orbital angular momentum quantum number and $k$ runs over all electrons.[23] The wave function of $Nd^{3+}$ is therefore always $u$ in the presence of an inversion centre, and that of $Eu^{3+}$ is always $g$.

$$\begin{aligned} Nd^{3+}: \ 4f^3 \ &\Rightarrow \qquad (-1)^3(-1)^3(-1)^3 = -1 \\ Eu^{3+}: \ 4f^6 \ &\Rightarrow \qquad (-1)^3(-1)^3(-1)^3(-1)^3(-1)^3(-1)^3 = +1 \end{aligned}$$

The parity selection rule was already mentioned in 2.2. Electric dipole transitions between states of the same parity are forbidden, because the operator $\hat{\boldsymbol{\mu}}_{ed}$ belongs to the $u$ representation. The magnetic dipole operator however, being an axial vector, is $g$ and so transitions between states of the same parity are allowed.[23] It should be noted that in real systems the inversion symmetry is often destroyed, e.g. by vibrations, making these "parity-forbidden" electric dipole transitions possible.[23]

## 4.1. Double groups

In the case of an even number of electrons, or integer values of $J$, the same scheme can be used as for normal point groups. Equation (4.1) then gives the reducible character, which upon reduction produces the irreps arising from state $^{2S+1}L_J$ in the given point group (using $\hat{\sigma} \equiv \hat{C}_2 \cdot \hat{\imath}$ for a reflection and the fact that the character of the inversion $i$ equals $\pm$ the character of the identity $E$ for even or odd $J$, respectively).[23] This is, for example, the case of $Eu^{3+}$.
However, if the system has an odd number of electrons, or half-integer values of $J$, like

[†]Tinkham, M. *Group Theory and Quantum Mechanics* unabridged republication of the work originally published by McGraw-Hill Book Company, New York, in 1964 (Dover Publications, Inc., Mineola, New York, 2003).

$Nd^{3+}$, two-valued representations and double groups need to be used.[23] The character for a rotation through an angle $\alpha$ can again be written as[23]

$$\chi_J(\alpha) = \frac{\sin\left(\left\{J+\frac{1}{2}\right\}\alpha\right)}{\sin\left(\frac{\alpha}{2}\right)} \tag{4.2}$$

but now a rotation by $(\alpha + 2\pi)$ results in[23]

$$\chi_J(\alpha + 2\pi) = (-1)^{2J}\,\chi_J(\alpha) \tag{4.3}$$

and only a rotation by $4\pi$ corresponds to the identity.[23]

$$\chi_J(\alpha \pm 4\pi) = \chi_J(\alpha) \tag{4.4}$$

A new group element $R$ is introduced, which corresponds to a rotation by $2\pi$ with the properties $R \neq E$, but $R^2 = E$.[23] The new extended group is called *double group* and has twice as many elements as the corresponding ordinary point group, i.e. the order of the double group is $2n$ instead of $n$. The concept of double groups allows the use of the same formulas as for the normal case, e.g. equation (4.2).[23] This equation produces the normal single-valued representations for integer $J$, called *boson* irreps and having a positive character for $R$,[53] and it produces the new double-valued representations for half-integer $J$,[23] called *fermion* irreps[53] or spinor representations[93] and having a negative character for $R$.[53] A reduction of $\chi_J$ with half-integer $J$ leads to irreps that are at least two-fold degenerate. This is a consequence of time reversal symmetry or Kramers' theorem,[23] see below. The standard reduction formula can be used.[23]

$$D_L = \sum_i a_i \Gamma_i \quad \text{and} \quad a_i = n^{-1} \sum_k N_k\, \chi_i(\mathcal{C}_k)\, \chi_L(\mathcal{C}_k) \tag{4.5}$$

Here $D_L$ is the representation ("Darstellung"), whose characters $\chi_L$ can be reduced and which therefore can be expressed in terms of the irreps $\Gamma$ of the given point group. $N_k$ is the number of elements in the class $\mathcal{C}_k$ and $n$ denotes the order of the group, i.e. the number of group elements.

Figure 4.2 depicts the splitting of the $^4$F state in a weak and a strong crystal field of cubic symmetry (double group O'). The irreps $\Gamma$ of the crystal field states can be determined using equation (4.2) and reducing the obtained $\chi_J$ in the double group O' (equation (4.5) and Table 4.1). The total number of states, which remains unchanged,[23] is given in parenthesis. Without spin-orbit splitting, i.e. case (d), the levels of the F state split into the irreps

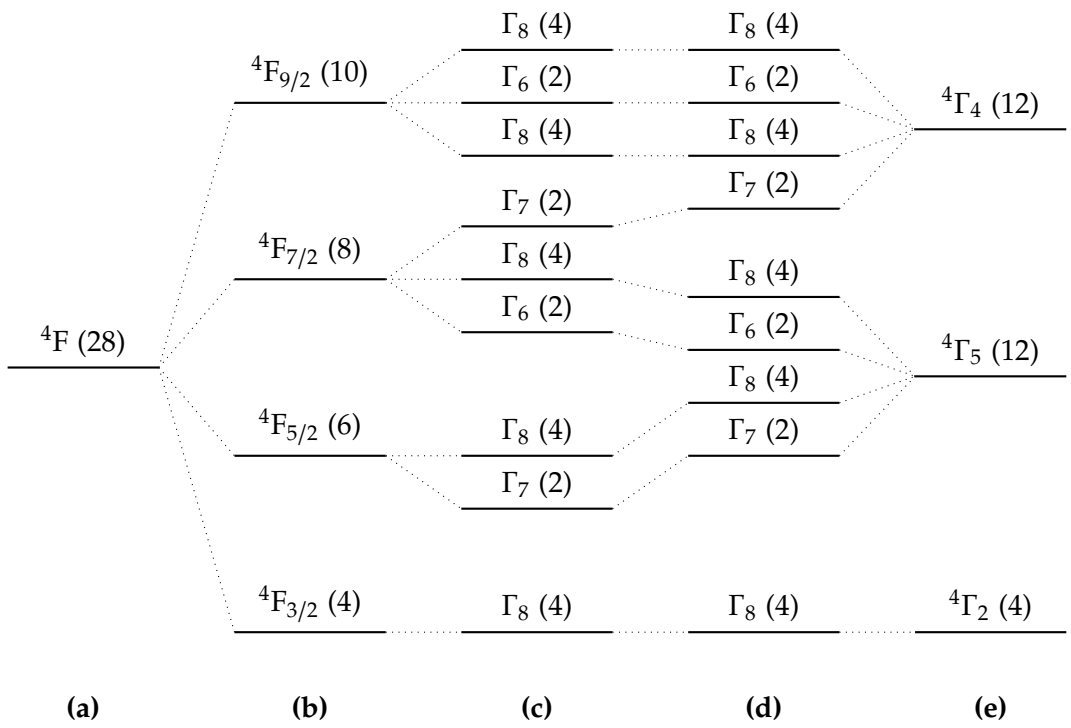


Figure 4.2.: Splitting of $^4$F state taken from Tinkham[23]; **(a)** Russell-Saunders or *LS*-coupling, **(b)** *LS* and spin-orbit (*SO*) coupling, **(c)** *LS*-, *SO*-coupling together with crystal field splitting in the double group O′ (weak crystal field), **(d)** same as (c) but in a strong crystal field, **(e)** *LS* and crystal field splitting, but no *SO*-splitting (non-relativistic limit).

$D_F = \Gamma_2 \oplus \Gamma_4 \oplus \Gamma_5 = A_2 \oplus T_1 \oplus T_2$ of O′. Forming the direct product of these representations with the representation of the spin ($D_{3/2} = \Gamma_8$) gives the decomposition[23]

$$\begin{aligned}\Gamma_2 \otimes \Gamma_8 &= \Gamma_8 \\ \Gamma_4 \otimes \Gamma_8 &= \Gamma_6 \oplus \Gamma_7 \oplus 2\Gamma_8 \\ \Gamma_5 \otimes \Gamma_8 &= \Gamma_6 \oplus \Gamma_7 \oplus 2\Gamma_8 \quad .\end{aligned}$$

It should be noted that it is not possible to know the order of the levels if the sign of the perturbation, i.e. of the crystal field, is not known.[23]

Double group character tables can be found in the book by Altmann & Herzig[93].

## 4.2. The $SU(2)$, $SO(3)$ and other groups

Operations in spin space can only be carried out using unitary transformations $\hat{\Omega}$.[53] These transformations constitute the special unitary group of dimension 2, $SU(2)$.[53] The basis functions are taken to be the eigenfunctions of $\hat{s}_z$, $|\frac{1}{2}, \frac{1}{2}\rangle$ and $|\frac{1}{2}, -\frac{1}{2}\rangle$.[53]

$$\hat{\Omega}^\dagger \hat{\Omega} = 1 \tag{4.6}$$

The linear transformations $\hat{\Omega}$ in the three-dimensional Euclidean space $R_3$ that do change the lengths or angles are real, orthogonal $(3 \times 3)$ matrices[53]

$$\hat{\Omega}^T \hat{\Omega} = \mathbf{1}_3 \quad . \tag{4.7}$$

They form the real orthogonal group of dimension 3, $O(3)$,[53] which is the continuous group of all "*proper and improper rotations of a sphere with a fixed center*"[‡]. If the determinants of the transformation matrices equal 1, $|\mathbf{R_n}(\phi)| = 1$, these transformations constitute a subgroup of $O(3)$, namely the special orthogonal group of dimension 3 $SO(3)$,[53] or the continuous group of all "*proper rotations of a sphere with a fixed centre*"[‡]The inversion and reflections belong to $O(3)$, but not to $SO(3)$ because their determinants equal −1 and not 1.[53]

The symmetry group that has to be considered in case of spherical symmetry, e.g. free ions, is $SU(2) \otimes O(3)$ and in case of lower symmetry, e.g. in a crystal field, is $SU(2) \otimes G$ where

[‡]Altmann, S. L. & Herzig, P. *Point-Group Theory Tables* 2nd. <https://phaidra.univie.ac.at/detail_object/o:104731> (Wien, 2011).

Table 4.1.: Character table of O′ and characters of fermion representation $D_J$ taken from Tinkham[23].

| O′ | | $E$ | $R$ | $8C_3$ | $8RC_3$ | $3C_2+3RC_2$ | $6C_2'+6RC_2'$ | $6C_4$ | $6RC_4$ |
|---|---|---|---|---|---|---|---|---|---|
| $A_1$ | $\Gamma_1$ | 1 | 1 | 1 | 1 | 1 | 1 | 1 | 1 |
| $A_2$ | $\Gamma_2$ | 1 | 1 | 1 | 1 | 1 | -1 | -1 | -1 |
| E | $\Gamma_3$ | 2 | 2 | -1 | -1 | 2 | 0 | 0 | 0 |
| $T_1$ | $\Gamma_4$ | 3 | 3 | 0 | 0 | -1 | -1 | 1 | 1 |
| $T_2$ | $\Gamma_5$ | 3 | 3 | 0 | 0 | -1 | 1 | -1 | -1 |
| $E_{1/2}$ | $\Gamma_6$ | 2 | -2 | 1 | -1 | 0 | 0 | $\sqrt{2}$ | $-\sqrt{2}$ |
| $E_{5/2}$ | $\Gamma_7$ | 2 | -2 | 1 | -1 | 0 | 0 | $-\sqrt{2}$ | $\sqrt{2}$ |
| $F_{3/2}$ | $\Gamma_8$ | 4 | -4 | -1 | 1 | 0 | 0 | 0 | 0 |
| $D_J$ | | $(2J+1)$ | $-(2J+1)$ | 1 | -1 | 0 | 0 | $\sqrt{2}$ | $-\sqrt{2}$ |
| | | | | -1 | 1 | | | 0 | 0 |
| | | | | 0 | 0 | | | $-\sqrt{2}$ | $\sqrt{2}$ |

$G$ denotes the ordinary single point group.[53] These direct products lead to the double groups,[53] see 4.1 on page 69.

As already stated in 3.1 the Hamiltonian must be invariant under Lorentz transformations in a relativistic theory. These coordinate transformations form the *Lorentz group* $\mathcal{L}$.[23] A combination of $\mathcal{L}$ with translations in space and time produces the *proper Poincaré group* and the addition of space and time inversions leads to the *unrestricted Poincaré group*.[23]

## 4.3. Time reversal symmetry

At the beginning of this chapter the inversion was mentioned. The relativistic theory, taking place in the four-dimensional Minkowski space with the equivalence of space and time,[21] rather than in a three-dimensional space, leads to the definition of a time-reversal operator $\hat{K}$, which turns $t$ into $-t$.[23] $\hat{K}$ is an antilinear and antiunitary operator and can be expressed as the product of a unitary operator $\hat{U}$ and the operator of complex conjugation $\hat{K}_0$.[23]

$$\hat{K} = \hat{U}\hat{K}_0 \tag{4.8}$$

It has the following properties[21,53]

$$\hat{K}\,(a\psi_i) = a^*\psi_i \tag{4.9}$$

$$\hat{K}\,\mathbf{r}\,\hat{K}^\dagger = \mathbf{r}\ , \quad \hat{K}\,\mathbf{p}\,\hat{K}^\dagger = -\mathbf{p}\ , \quad \hat{K}\,\sigma\,\hat{K}^\dagger = -\sigma \tag{4.10}$$

i.e. it keeps the positions $\mathbf{r}$ invariant, but changes the sign of the momentum operator (and of the velocity) and induces spin $\sigma$ flips.[53] Equation (4.9) gives the antilinear property of $\hat{K}$.[21] As a consequence, this operator does not correspond to an observable and has no eigenvalue.[53]

In the four-component relativistic theory $\hat{K}$ can be written as[21,53]

$$\hat{K} = -i\,\mathbf{\Sigma}_y\,\hat{K}_0 = -i\begin{pmatrix}\sigma_y & 0\\ 0 & \sigma_y\end{pmatrix}\hat{K}_0 \tag{4.11}$$

where $\mathbf{\Sigma}_y$ denotes the $y$ component of the total spin operator $\mathbf{\Sigma}$. Hence, $\hat{U}$ can be expressed as product of $n$ Pauli matrices $\sigma$ in a many particle system, where $n$ is the number of particles. This leads to[23]

$$\hat{K}^2\psi = \psi \quad \text{if } n \text{ is even} \tag{4.12}$$

$$\hat{K}^2\psi = -\psi \quad \text{if } n \text{ is odd.} \tag{4.13}$$

According to *Kramers' theorem*,[94] the states of odd electron systems are at least doubly degenerate even in the lowest symmetry in the absence of an external vector potential,[53] which follows directly from the time reversal symmetry. Degeneracy in even electron systems, on the other hand, can only be caused by spatial symmetry.[23]

$$\hat{K}\psi_i = \bar{\psi}_i \tag{4.14}$$

The time reversal operator relates a set of degenerate $\psi_i$ to a new set $\bar{\psi}_i$.[23] These two sets are called *Kramers pairs*.[21] $\hat{K}\psi$ is orthogonal to $\psi$ and they are linearly independent. Both possess the same eigenvalue, because the non-relativistic as well as the relativistic Hamiltonian are invariant under time reversal.[53]

A new nomenclature is introduced, that is the term "corepresentation" is used rather than representation, because the group contains antiunitary and unitary operations.[23]

Relativistic quantum chemistry programs like DIRAC exploit Kramers time reversal and double group symmetry,[68] i.e. a basis of Kramers pairs $\{\psi, \bar{\psi}\}$ is used instead of $\alpha$- and $\beta$-spin orbitals,[20,53] which can be efficiently treated using quaternion algebra.[21,95]

## 4.4. Descent in symmetry

The descent in symmetry or subduction from a (point) group gives the corresponding representations of a point group of lower symmetry (subgroup) which arise in the reduction of the representations of the original (point) group.[93] The subduction from $O(3)$ for the boson representations (integer values of $j$) or fermion (spinor) representations (half-integer values of $j$) to some subgroups is summarized in Table 4.2. Care must be taken with point groups with inversion centre, which are labelled with the symbol ♣. States arising from $g$ terms, like in the case of $Eu^{3+}$, remain *gerade* in the subgroup, and $u$ terms remain $u$ ($Nd^{3+}$). Besides, equations (4.1) or (4.2) may be used for the subduction from $O(3)$, which corresponds to the free ion case, together with the reduction formula (4.5). Descent in symmetry diagrams can be found in the Appendix, for tables see Altmann & Herzig[93].

Table 4.2.: Subduction from $O(3)$.[93]

| **j =** | **O(3) →** | $\mathbf{D_{2h}}$ ♣ |
|---|---|---|
| 2n | | $(n+1)\,A_g \oplus n\,(B_{1g} \oplus B_{2g} \oplus B_{3g})$ |
| 2n + 1 | | $n\,A_u \oplus (n+1)\,(B_{1u} \oplus B_{2u} \oplus B_{3u})$ |
| $n + \frac{1}{2}$ | | $(n+1)\,E_{1/2,g}$ |
| **j =** | **O(3) →** | $\mathbf{D_2}$ |
| 2n | | $(n+1)\,A \oplus n\,(B_1 \oplus B_2 \oplus B_3)$ |
| 2n + 1 | | $n\,A \oplus (n+1)\,(B_1 \oplus B_2 \oplus B_3)$ |
| $n + \frac{1}{2}$ | | $(n+1)\,E_{1/2}$ |
| **j =** | **O(3) →** | $\mathbf{C_{2v}}$ |
| 2n | | $(n+1)\,A_1 \oplus n\,(A_2 \oplus B_1 \oplus B_2)$ |
| 2n + 1 | | $n\,A_2 \oplus (n+1)\,(A_1 \oplus B_1 \oplus B_2)$ |
| $n + \frac{1}{2}$ | | $(n+1)\,E_{1/2}$ |
| **j =** | **O(3) →** | $\mathbf{C_2}$ |
| 2n | | $(2n+1)\,A \oplus 2n\,B$ |
| 2n + 1 | | $(2n+1)\,A \oplus (2n+2)\,B$ |
| $n + \frac{1}{2}$ | | $(n+1)\,({}^1E_{1/2} \oplus {}^2E_{1/2})$ |
| **j =** | **O(3) →** | $\mathbf{C_s}$ |
| n | | $(n+1)\,A' \oplus n\,A''$ |
| $n + \frac{1}{2}$ | | $(n+1)\,({}^1E_{1/2} \oplus {}^2E_{1/2})$ |

n = 0, 1, 2, ...

# Part II.

# Experiments and computations

# 5. Experiments

## 5.1. Reagents and instruments

The lanthanide oxides $Nd_2O_3$ and $Eu_2O_3$ from Treibacher Industrie AG (99.9 %) were used as starting materials, together with $HNO_3$ puriss. p.a., ≥ 65 % from Fluka Chemie AG, Sigma-Aldrich Chemie GmbH. $Nd_2O_3$ and $Eu_2O_3$ were subjected to a heat treatment at 800°C for one hour. The further components of the calcium aluminium borate (CAB) glasses, $CaCO_3$ (min. 99 %) and $Al_2O_3$ were obtained from Merck, while $BH_3O_3$ (purum p.a., ≥ 99.0 % (T)) was supplied by Fluka Chemie AG. Acetone (ROTISOLV® HPLC, min. 99.9 % (GC)) and methanol (ROTIDRY®, ≥ 99.9 % (GC)) were supplied by Carl Roth GmbH + Co. KG, while dimethyl sulfoxide (DMSO; purum, ≥ 99.0 % (GC)) was obtained from Fluka Chemie GmbH, Sigma-Aldrich Chemie GmbH. The solvents were used as received.

The refractive indices were measured with the NAR-1T Abbe *refractometer* of ATAGO® CO., LTD. with digital thermometer at the wavelength of the sodium D-line (589 nm). 1-Bromonaphthalene was used as contact liquid for the measurement of the glasses.
The Nabertherm® L3/S27 *furnace* was used for the heat treatment of the lanthanide oxides as well as in the glass preparation for the preheating of the casting mould and the glass annealing. The raw materials of the glasses were melted in the Nabertherm® HT04/17 high-temperature furnace in a platinum crucible.
A *thermogravimetric analysis* was carried out with the Netzsch STA 449 C Jupiter® TG-DSC system by Ing. J. Hobisch using an aluminium crucible and a temperature program (5 min at 20°C, then heated at a rate of 10°C/min, 15 min at 550°C, afterwards cooling to ambient temperature) under He inert gas.

The *absorbance spectra* were recorded with the PerkinElmer Lambda 950 UV/VIS/NIR Spectrometer. The spectrometer is equipped with a tungsten halogen light source for the VIS-NIR region, a photomultiplier tube as detector in the UV-VIS region (1 nm PMT slit) and a Peltier controlled PbS detector for the NIR region (detector changeover at approximately

800 nm). The spectra were recorded in the range from 1,400 to 320 nm and from 900 to 320 nm with a data interval of 0.1 nm. Baseline corrections were performed with air as reference. A holmium filter was used to determine the accuracy of the wavelength. Furthermore, the repeatability of the measurements was tested.
*Excitation* and *emission spectra* were recorded with the PerkinElmer LS 55 Fluorescence Spectrometer. The spectrometer is equipped with a pulsed Xenon source for excitation and the R 928 photomultiplier tube as detector. The emission spectra were recorded at different excitation wavelengths using various cut-off filters and a data interval of 0.5 nm.
UV/VIS fused silica cuvettes of PerkinElmer™ instruments and Hellma® 110-OS precision cells made of special optical glass (crown glass) were used for the sample solutions.
The spectra were analysed and plotted with the OriginPro 8 data analysis and graphing software.

### 5.1.1. Synthesis of rare earth nitrates

The lanthanide oxides were heated with nitric acid (2 mL $HNO_3$ / 1 g $Ln_2O_3$) and the mixture was evaporated to dryness. The obtained amorphous solid was solved in water and it was tried to precipitate crystals. However, also slow drying of the concentrated aqueous solutions over phosphorus pentoxide in a desiccator did not produce crystals. The solution was concentrated nearly to dryness and then further dried over night at 80°C. The product was, after grinding, equilibrated in the air at ambient temperature. The water content of the synthesized lanthanide nitrates, $Nd(NO_3)_3 \cdot 5H_2O$ and $Eu(NO_3)_3 \cdot 4H_2O$, was determined by a thermogravimetric analysis by Ing. J. Hobisch.

### 5.1.2. Glass preparation

The raw materials, $Nd(NO_3)_3 \cdot 5H_2O$ or $Eu(NO_3)_3 \cdot 4H_2O$ together with $CaCO_3$, $Al_2O_3$ and $BH_3O_3$, were kept in a platinum crucible at 800°C to allow the formed gases to escape and then heated to 1,200°C in 30 min and held at this temperature for approximately 1 h. The molten glass was poured into a preheated cuvette-shaped mould and then annealed to relieve the internal stress (1 h at 350°C and then cooled down to 50 – 30°C in 24 h). Tables 5.1 and 5.2 summarize the composition and properties of the CAB glasses.

Table 5.1.: Composition of prepared Nd- and Eu-CAB-glasses.

| Glass | Composition (mol-%) |
|---|---|
| Nd-CAB-glass | 11 CaO · 5.7 $Al_2O_3$ · 83 $B_2O_3$ · 0.1 $Nd_2O_3$ |
| Eu-CAB-glass | 11 CaO · 5.9 $Al_2O_3$ · 83 $B_2O_3$ · 0.1 $Eu_2O_3$ |

Table 5.2.: Prepared Nd-CAB-glass and Eu-CAB-glass: molar mass M, density $\rho$, concentration c of $Nd^{3+}$ and $Eu^{3+}$, optical path length OPL and refractive indices n (at temperatures T).

| Glass | M ($g\ mol^{-1}$) | $\rho$ ($g\ cm^{-3}$) | c($Ln^{3+}$) ($mol\ L^{-1}$) | OPL (cm) | n (T) (°C) |
|---|---|---|---|---|---|
| Nd-CAB-glass | 70.301 | 1.755 | 0.0629 | 1.2 | 1.5545 (24.1) |
| Eu-CAB-glass | 70.327 | 1.747 | 0.0663 | 1.2 | 1.5555 (24.1) |

The densities of the glasses were measured using Archimedes' principle. First, the weight of the glass was measured and then it was hung into a water-filled beaker and the weight increase caused by the displaced water was determined. Using the density of water at the given temperature, the displaced mass can be converted to a volume which is just the volume of the glass.
The refractive indices were measured with an Abbe refractometer and 1-Bromonaphthalene as contact liquid.

### 5.1.3. Sample solutions

Stock solutions of the lanthanide nitrates in the pure solvents, i.e. distilled water, acetone, methanol and DMSO, were prepared. The concentrations and properties of the sample solutions in the mixed solvents are listed in Tables 5.3 and 5.4. As the sample solutions in the solvent mixtures exhibit a volume contraction upon mixing,[96] the volumetric flasks were filled up with the pure mixtures of the same ratio.

Table 5.3.: Measured solutions of $Nd^{3+}$ in water-acetone and water-methanol mixtures: concentrations c and refractive indices n (at temperatures T).

| Sample | V-% acetone in water | c($Nd^{3+}$) (mol $L^{-1}$) | n (T (°C)) |
|---|---|---|---|
| Nd-100-water (I) | 0 | 0.0526 | 1.3355 (24.4) |
| Nd-90-w-a | 10 | 0.0526 | 1.3400 (24.7) |
| Nd-80-w-a | 20 | 0.0526 | 1.3451 (25.0) |
| Nd-70-w-a | 30 | 0.0526 | 1.3501 (25.2) |
| Nd-60-w-a | 40 | 0.0526 | 1.3545 (25.5) |
| Nd-50-w-a | 50 | 0.0523 | 1.3580 (25.7) |
| Nd-40-w-a | 60 | 0.0523 | 1.3620 (25.5) |
| Nd-30-w-a | 70 | 0.0523 | 1.3640 (25.6) |
| Nd-20-w-a | 80 | 0.0523 | 1.3642 (25.1) |
| Nd-10-w-a | 90 | 0.0523 | 1.3629 (24.9) |
| Nd-100-acetone | 100 | 0.0523 | 1.3582 (24.8) |
| **Sample** | **V-% methanol in water** | **c($Nd^{3+}$) (mol $L^{-1}$)** | **n (T (°C))** |
| Nd-100-water (II) | 0 | 0.0526 | 1.3365 (22.7) |
| Nd-90-w-m | 10 | 0.0526 | 1.3370 (22.8) |
| Nd-80-w-m | 20 | 0.0526 | 1.3391 (23.1) |
| Nd-70-w-m | 30 | 0.0526 | 1.3415 (23.3) |
| Nd-60-w-m | 40 | 0.0526 | 1.3431 (23.7) |
| Nd-50-w-m | 50 | 0.0526 | 1.3440 (23.7) |
| Nd-40-w-m | 60 | 0.0526 | 1.3440 (23.1) |
| Nd-30-w-m | 70 | 0.0526 | 1.3430 (23.1) |
| Nd-20-w-m | 80 | 0.0526 | 1.3405 (23.1) |
| Nd-10-w-m | 90 | 0.0526 | 1.3370 (23.1) |
| Nd-100-methanol | 100 | 0.0526 | 1.3305 (23.0) |

Table 5.4.: Measured solutions of $Eu^{3+}$ in water-acetone and water-methanol mixtures: concentrations c and refractive indices n (at temperatures T).

| Sample | V-% acetone in water | c($Eu^{3+}$) (mol $L^{-1}$) | n (T (°C)) |
|---|---|---|---|
| Eu-100-water (I) | 0 | 0.1466 | 1.3390 (24.5) |
| Eu-90-w-a | 10 | 0.1466 | 1.3449 (24.9) |
| Eu-80-w-a | 20 | 0.1466 | 1.3490 (25.1) |
| Eu-70-w-a | 30 | 0.1466 | 1.3541 (25.2) |
| Eu-60-w-a | 40 | 0.1466 | 1.3595 (25.3) |
| Eu-50-w-a | 50 | 0.1466 | 1.3631 (25.5) |
| Eu-40-w-a | 60 | 0.1467 | 1.3661 (25.6) |
| Eu-30-w-a | 70 | 0.1467 | 1.3670 (25.6) |
| Eu-20-w-a | 80 | 0.1467 | 1.3685 (25.6) |
| Eu-10-w-a | 90 | 0.1467 | 1.3671 (23.5) |
| Eu-100-acetone | 100 | 0.1467 | 1.3630 (24.0) |
| **Sample** | **V-% methanol in water** | **c($Eu^{3+}$) (mol $L^{-1}$)** | **n (T (°C))** |
| Eu-100-water (II) | 0 | 0.1466 | 1.3385 (22.6) |
| Eu-90-w-m | 10 | 0.1466 | 1.3400 (22.6) |
| Eu-80-w-m | 20 | 0.1466 | 1.3420 (22.5) |
| Eu-70-w-m | 30 | 0.1466 | 1.3440 (22.4) |
| Eu-60-w-m | 40 | 0.1466 | 1.3460 (22.3) |
| Eu-50-w-m | 50 | 0.1466 | 1.3470 (22.2) |
| Eu-40-w-m | 60 | 0.1466 | 1.3465 (22.3) |
| Eu-30-w-m | 70 | 0.1466 | 1.3460 (22.2) |
| Eu-20-w-m | 80 | 0.1466 | 1.3440 (22.1) |
| Eu-10-w-m | 90 | 0.1466 | 1.3400 (22.0) |
| Eu-100-methanol | 100 | 0.1466 | 1.3350 (22.0) |

## 5.2. Experimental results of $Nd^{3+}$

The $f \leftrightarrow f$ transitions of $Nd^{3+}$ give rise to colours of the Nd-compounds. Figure 5.1 shows the colours of the prepared Nd-CAB-glass under different light sources.* The colour change is caused by an interplay between the absorption bands of $Nd^{3+}$ and the characteristic spectrum of the light source. The synthesised neodymium nitrates exhibit an even stronger colour and colour change than the glass, which only contains 0.0629 mol $L^{-1}$ $Nd^{3+}$. The different colours of rare earth compounds under different (white) light sources are known and other examples can be found in the literature.[97]

(a) Tungsten lamp. (b) White LED. (c) Fluorescent lamp.

Figure 5.1.: Colour of Nd-CAB-glass under different light sources.

### 5.2.1. Absorbance spectra

Figures 5.2, 5.11 and 5.6 show the absorbance spectra of $Nd^{3+}$ in water-acetone and water-methanol mixtures and in the pure solvents, as well as of the Nd-CAB-glass. The change in intensity of the hypersensitive $^4G_{5/2} \leftarrow {}^4I_{9/2}$ transition when going from water to another solvent can be clearly seen, e.g. in Figures 5.2b, 5.3b and 5.4. In all the cases, the hypersensitive transition in water exhibits the lowest intensity. It seems that the coordination of water is preferred to the coordination of acetone or methanol, because in both mixtures the increase in intensity starts at approximately 50 % acetone or methanol in water.
The $^2G_{7/2} \leftarrow {}^4I_{9/2}$ transition is close to the hypersensitive transition and the two transitions could not be resolved separately. The intensity in the spectra of the solutions with a water content greater than 50 % is presumably mainly caused by the $^2G_{7/2} \leftarrow {}^4I_{9/2}$ transition,

*The photographs of the Nd-CAB-glass were taken by M. Reiter.

which has a larger transition energy, and not by the hypersensitive transition. It can be seen how the shape of this band changes with decreasing water content. At the same time, the barycentre of the band is shifted towards lower energies, which corresponds to an increasing contribution of the hypersensitive transition. The band is dominated by the $^4G_{5/2} \leftarrow {}^4I_{9/2}$ transition in the 100 % acetone and methanol solutions.

In the case of the water-DMSO mixtures, no hypersensitive effect was observed, i.e. the intensity of the $^4G_{5/2} \leftarrow {}^4I_{9/2}$ transition remained constant irrespective of the solvent ratio. The absorbance spectra in water-DMSO are therefore not shown in this thesis. The reason why the intensity variation of the hypersensitive transition was not observed lies probably in the preferred coordination of water. The solutions were not heated under nitrogen like described in the literature,[9,10] therefore presumably not enough energy was provided for the formation of DMSO compounds.

The variation of absorption bands of water and acetone in the UV and NIR region is shown in Figure 5.5. The "optical window" can be seen, i.e. the range where visible light can pass through the solvents. Electronic transitions at the UV edge and vibrational excitations at the NIR edge cause solvent absorptions, hence no $f \leftrightarrow f$ transitions of the rare earth ions can be observed in these regions in the solvents. In methanol, the absorption in the UV region starts at higher wavenumbers than in acetone.[98] The absorbance spectra of $Nd^{3+}$ in water-acetone mixtures are therefore shown from 11,111 to 25,000 $cm^{-1}$ and of $Nd^{3+}$ in water-methanol mixtures from 11,111 to 29,700 $cm^{-1}$.

The absorbance spectrum of the Nd-CAB-glass is shown in Figure 5.6. It is analogous to the spectra of $Nd^{3+}$ in the solvent mixtures, the bands merely exhibit a greater linewidth.

Tables 5.5, 5.6 and 5.7 list the transition energies of $Nd^{3+}$. Only the solutions in the pure solvents and the 50-50 % mixtures are presented in the tables. In Figure 5.7 the experimental energy levels of the $^{2S+1}L_J$ states of $Nd^{3+}$ in water, acetone and methanol, which were obtained from an evaluation of the transition energies, are compared with the published values for $NdF_3$ by Carnall *et al.*[28], which were also used for the band assignment.
It can be seen that the shift of the energies in the different environments is very small. In general, the results are in good agreement with the literature.[28,49,99] It should be noted that the individual Stark levels cannot be resolved in solution or glasses, because of the inhomogeneous broadening. The linewidths are generally greater than in the lanthanide spectra in crystals. The reported energies therefore correspond to the barycentres of the transitions between different Stark levels.

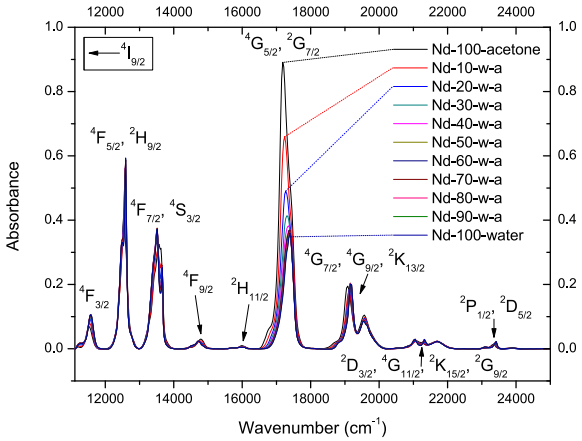


(a) Absorbance spectra.

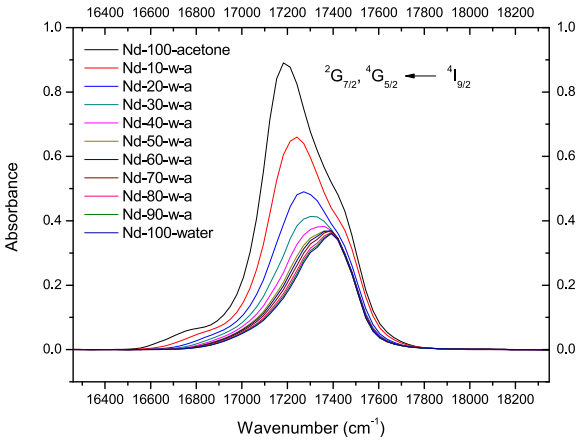


(b) Hypersensitive $^4G_{5/2} \leftarrow {}^4I_{9/2}$ transition.

Figure 5.2.: Absorbance spectra of $Nd^{3+}$ in water-acetone mixtures.

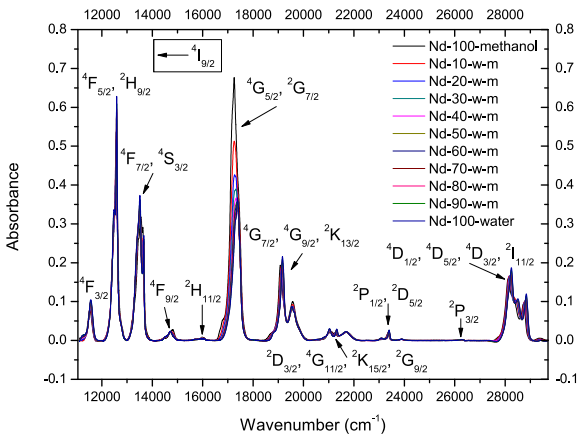


(a) Absorbance spectra.

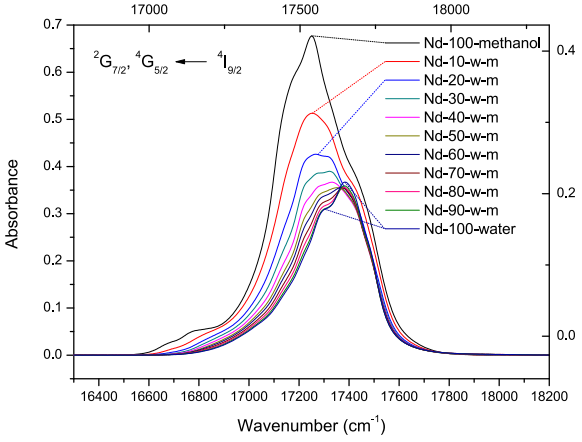


(b) Hypersensitive $^4G_{5/2} \leftarrow {}^4I_{9/2}$ transition.

Figure 5.3.: Absorbance spectra of $Nd^{3+}$ in water-methanol mixtures.

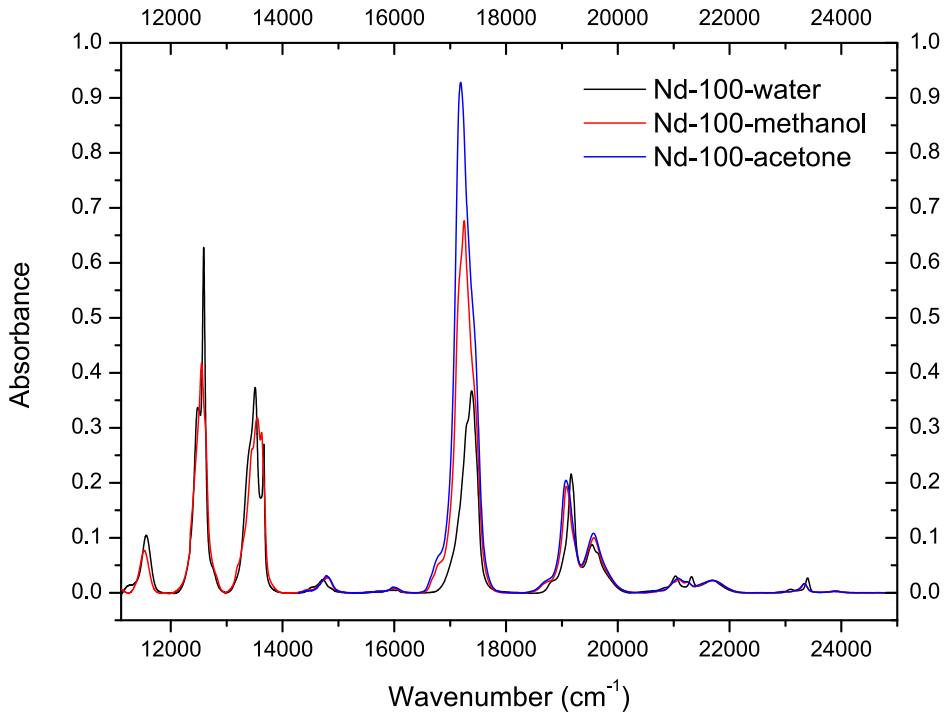


Figure 5.4.: Comparison of absorbance spectra of $Nd^{3+}$ in water, methanol and acetone.

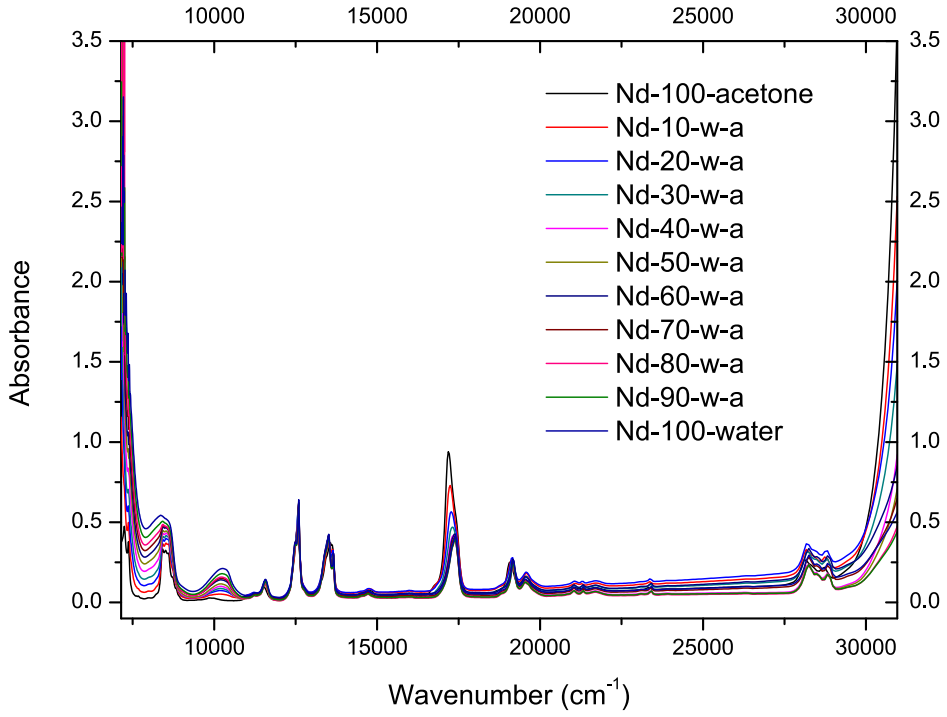


Figure 5.5.: Absorbance spectra of $Nd^{3+}$ in water-acetone mixtures: absorption of solvents in UV and NIR region.

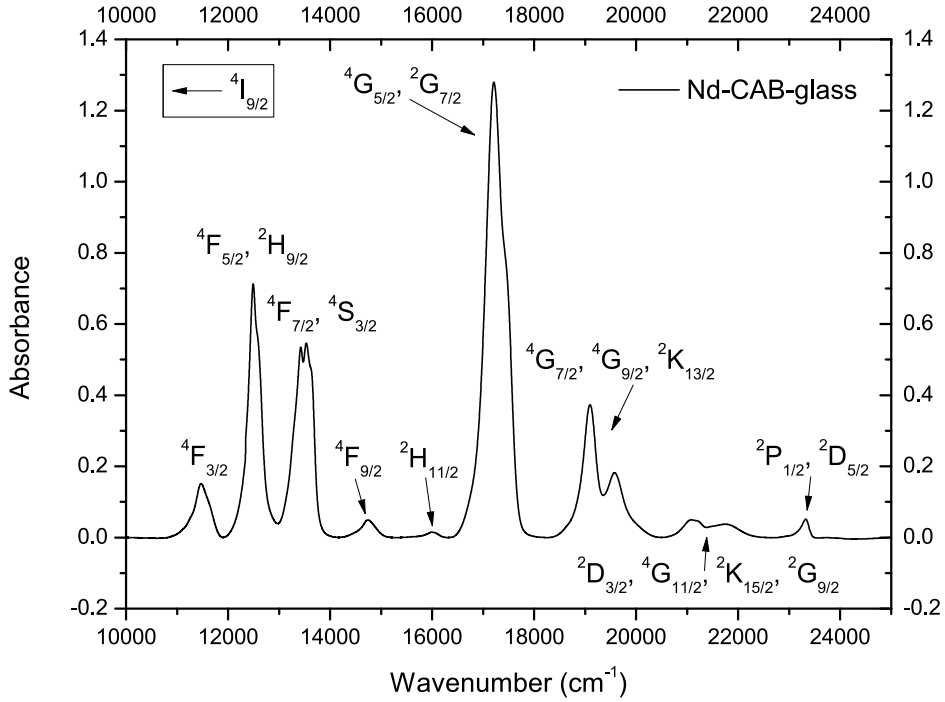


Figure 5.6.: Absorbance spectrum of $Nd^{3+}$-CAB-glass.

The experimental oscillator strengths $f_{osc}$(exp), which were determined using equation (2.62), and calculated oscillator strengths $f_{osc}$(JO) obtained using Judd-Ofelt theory (eq. (2.60)) are also listed in Tables 5.5, 5.6 and 5.7. The Judd-Ofelt analysis, rms of the Judd-Ofelt calculations and (m2) expression is explained later in this chapter. It can be seen from the oscillator strengths that the hypersensitive transition, together with the $^2G_{7/2} \leftarrow {}^4I_{9/2}$ transition, has the highest intensity in all the mixtures. While the variation of the oscillator strengths of the other transitions is small in different environments, i.e. in water, acetone and methanol, except for some transitions with lower intensity which exhibit a greater error in the determination of $f_{osc}$, there is a considerable increase in the oscillator strength of the hypersensitive transition when going from water to acetone or methanol. This increase is more pronounced in acetone than in methanol. The oscillator strengths are in good agreement with the literature.[41,99,100] Merely the transitions with higher energies near the UV region that were more difficult to determine in the experimental spectra vary more from other published values.[41,99,100]

Table 5.5.: Experimental results of $Nd^{3+}$ in water-acetone mixtures: wavenumbers $\tilde{\nu}$, areas $\int A\, d\tilde{\nu}$ and experimental and calculated (Judd-Ofelt) oscillator strengths $f_{osc}$ of transitions.

| v-% a | $\longleftarrow {}^4I_{9/2}$ | $\tilde{\nu}$ ($cm^{-1}$) | $\int A\, d\tilde{\nu}$ ($cm^{-1}$) | $f_{osc}$ ($\times 10^{-5}$) | |
|---|---|---|---|---|---|
| | | | | exp | JO |
| 0 | $^4F_{3/2}$ | 11533 | 24.8 | 0.203 | 0.274 |
| | $^4F_{5/2}$, $^2H_{9/2}$ | 12536 | 107.1 | 0.879 | 0.867 |
| | $^4F_{7/2}$, $^4S_{3/2}$ | 13484 | 107.7 | 0.884 | 0.902 |
| | $^4F_{9/2}$ | 14698 | 6.7 | 0.055 | 0.068 |
| | $^2H_{11/2}$ | 15900 | 1.8 | 0.015 | 0.019 |
| | $^4G_{5/2}$, $^2G_{7/2}$ | 17325 | 125.6 | 1.03 | 1.04 |
| | $^4G_{7/2}$, $^4G_{9/2}$, $^2K_{13/2}$ | 19335 | 79.8 | 0.655 | 0.604 |
| | $^2D_{3/2}$, $^4G_{11/2}$, $^2K_{15/2}$ | 21369 | 20.9 | 0.171 | 0.152 |
| | $^2P_{1/2}$, $^2D_{5/2}$ | 23398 | 4.7 | 0.038 | 0.079 |
| 50 | $^4F_{3/2}$ | 11521 | 24.2 | 0.200 | 0.281 |
| | $^4F_{5/2}$, $^2H_{9/2}$ | 12532 | 109.9 | 0.907 | 0.895 |
| | $^4F_{7/2}$, $^4S_{3/2}$ | 13483 | 110.5 | 0.912 | 0.932 |
| | $^4F_{9/2}$ | 14700 | 6.9 | 0.057 | 0.070 |
| | $^2H_{11/2}$ | 15900 | 1.9 | 0.016 | 0.020 |
| | $^4G_{5/2}$, $^2G_{7/2}$ | 17309 | 142.3 | 1.17 | 1.18 |
| | $^4G_{7/2}$, $^4G_{9/2}$, $^2K_{13/2}$ | 19327 | 83.3 | 0.688 | 0.630 |
| | $^2D_{3/2}$, $^4G_{11/2}$, $^2K_{15/2}$ | 21369 | 21.9 | 0.181 | 0.157 |
| | $^2P_{1/2}$, $^2D_{5/2}$ | 23397 | 4.8 | 0.040 | 0.081 |
| 100 | $^4F_{3/2}$ | 11513 | 15.6 | 0.129 | 0.248 |
| | $^4F_{5/2}$, $^2H_{9/2}$ | 12535 | 99.8 | 0.823 | 0.854 |
| | $^4F_{7/2}$, $^4S_{3/2}$ | 13509 | 109.0 | 0.899 | 0.902 |
| | $^4F_{9/2}$ | 14750 | 8.7 | 0.072 | 0.069 |
| | $^2H_{11/2}$ | 15947 | 2.7 | 0.022 | 0.019 |
| | $^4G_{5/2}$, $^2G_{7/2}$ | 17236 | 352.1 | 2.91 | 2.91 |
| | $^4G_{7/2}$, $^4G_{9/2}$, $^2K_{13/2}$ | 19283 | 101.8 | 0.840 | 0.723 |
| | $^2D_{3/2}$, $^4G_{11/2}$, $^2K_{15/2}$ | 21412 | 21.0 | 0.173 | 0.146 |
| | $^2P_{1/2}$, $^2D_{5/2}$ | 23373 | 3.4 | 0.028 | 0.070 |

Table 5.6.: Experimental results of $Nd^{3+}$ in water-methanol mixtures: wavenumbers $\tilde{\nu}$, areas $\int A\, d\tilde{\nu}$ and experimental and calculated (Judd-Ofelt) oscillator strengths $f_{osc}$ of transitions.

| **v-% m** | $\longleftarrow$ $^4I_{9/2}$ | $\tilde{\nu}$ **(cm$^{-1}$)** | $\int A\, d\tilde{\nu}$ **(cm$^{-1}$)** | $f_{osc}$ **(×10$^{-5}$)** | |
|---|---|---|---|---|---|
| | | | | **exp** (m2)[a] | **JO** (m2)[a] |
| | $^4F_{3/2}$ | 11526 | 23.4 | 0.192 | 0.193 |
| | $^4F_{5/2}$, $^2H_{9/2}$ | 12532 | 109.8 | 0.901 | 0.833 |
| | $^4F_{7/2}$, $^4S_{3/2}$ | 13481 | 107.7 | 0.885 | 0.969 |
| | $^4F_{9/2}$ | 14694 | 6.6 | 0.055 | 0.070 |
| | $^2H_{11/2}$ | 15887 | 1.8 | 0.015 | 0.019 |
| **0** | $^4G_{5/2}$, $^2G_{7/2}$ | 17320 | 125.9 | 1.03 | 1.05 |
| | $^4G_{7/2}$, $^4G_{9/2}$, $^2K_{13/2}$ | 19326 | 80.2 | 0.659 | 0.510 |
| | $^2D_{3/2}$, $^4G_{11/2}$, $^2K_{15/2}$ | 21342 | 21.3 | 0.175 | 0.129 |
| | $^2P_{1/2}$, $^2D_{5/2}$ | 23398 | 4.9 | 0.040 | 0.049 |
| | $^2P_{3/2}$ | 26264 | 0.3 | 0.002 | 0.007 |
| | $^4D_{1/2}$, $^4D_{3/2}$, $^4D_{5/2}$, $^2I_{11/2}$ | 28420 | 99.0 | 0.813 | 0.861 |
| | $^4F_{3/2}$ | 11522 | 19.7 | 0.162 | 0.183 |
| | $^4F_{5/2}$, $^2H_{9/2}$ | 12527 | 108.4 | 0.890 | 0.815 |
| | $^4F_{7/2}$, $^4S_{3/2}$ | 13477 | 105.9 | 0.869 | 0.956 |
| | $^4F_{9/2}$ | 14697 | 6.7 | 0.055 | 0.069 |
| | $^2H_{11/2}$ | 15889 | 2.0 | 0.016 | 0.019 |
| **50** | $^4G_{5/2}$, $^2G_{7/2}$ | 17296 | 142.1 | 1.17 | 1.18 |
| | $^4G_{7/2}$, $^4G_{9/2}$, $^2K_{13/2}$ | 19316 | 78.8 | 0.647 | 0.505 |
| | $^2D_{3/2}$, $^4G_{11/2}$, $^2K_{15/2}$ | 21351 | 20.4 | 0.168 | 0.125 |
| | $^2P_{1/2}$, $^2D_{5/2}$ | 23390 | 4.6 | 0.038 | 0.045 |
| | $^2P_{3/2}$ | 26246 | 0.4 | 0.003 | 0.006 |
| | $^4D_{1/2}$, $^4D_{3/2}$, $^4D_{5/2}$, $^2I_{11/2}$ | 28401 | 93.2 | 0.765 | 0.809 |
| | $^4F_{3/2}$ | 11521 | 15.7 | 0.129 | 0.180 |
| | $^4F_{5/2}$, $^2H_{9/2}$ | 12532 | 105.1 | 0.863 | 0.819 |
| | $^4F_{7/2}$, $^4S_{3/2}$ | 13501 | 107.8 | 0.885 | 0.958 |
| | $^4F_{9/2}$ | 14734 | 8.3 | 0.068 | 0.069 |

| | | | | | |
|---|---|---|---|---|---|
| | $^2H_{11/2}$ | 15914 | 2.4 | 0.020 | 0.019 |
| **100** | $^4G_{5/2}$, $^2G_{7/2}$ | 17247 | 265.0 | 2.18 | 2.19 |
| | $^4G_{7/2}$, $^4G_{9/2}$, $^2K_{13/2}$ | 19295 | 92.6 | 0.760 | 0.583 |
| | $^2D_{3/2}$, $^4G_{11/2}$, $^2K_{15/2}$ | 21417 | 20.4 | 0.168 | 0.125 |
| | $^2P_{1/2}$, $^2D_{5/2}$ | 23389 | 4.4 | 0.036 | 0.044 |
| | $^2P_{3/2}$ | 26217 | 0.4 | 0.004 | 0.006 |
| | $^4D_{1/2}$, $^4D_{3/2}$, $^4D_{5/2}$, $^2I_{11/2}$ | 28317 | 91.6 | 0.752 | 0.794 |

[a] See page 92 for explanation.

The oscillator strengths of the Nd-CAB-glass deviate more from the values in solution than the $f_{osc}$ values in solution among themselves, but the results are again in accordance with other published values for $Nd^{3+}$ doped glasses.[101] The oscillator strength of the hypersensitive transition exhibits a greater variation in different glasses,[101,102] as expected because of its sensitivity to the environment. The highest oscillator strength is observed in the Nd-CAB-glass, i.e. $3.66 \cdot 10^{-5}$ (compared to $2.91 \cdot 10^{-5}$ in acetone, $2.18 \cdot 10^{-5}$ in methanol and $1.03 \cdot 10^{-5}$ in water).

### 5.2.2. Emission spectra

The emission spectra of $Nd^{3+}$ in water-DMSO mixtures and in pure acetone are shown in Figure 5.8. The maximum intensity of the band is observed at 367.5 nm ($2.721 \cdot 10^4$ $cm^{-1}$) in DMSO, at 413.5 nm ($2.418 \cdot 10^4$ $cm^{-1}$) in acetone and at 386.5 nm ($2.587 \cdot 10^4$ $cm^{-1}$) in Nd-90-w-d (10 % DMSO in water). The highest intensities were observed in the Nd-70-w-d mixture (at 386 nm or $2.591 \cdot 10^4$ $cm^{-1}$, 30 % DMSO in water) and the Nd-40-w-d mixture (again at 386 nm or $2.591 \cdot 10^4$ $cm^{-1}$, 60 % DMSO in water). The water-DMSO emission spectra were recorded in the range from 300 to 800 nm with an excitation wavelength of 270 nm, which was determined in an excitation spectrum, while the emission spectrum in acetone was recorded at an excitation wavelength of 254 nm.

There are a few reasons against describing this band as being caused by $f \leftrightarrow f$ transitions of $Nd^{3+}$. First of all, the emission bands are very broad, as opposed to the bands of $f \leftrightarrow f$ transitions. Moreover, it is well-known that $Nd^{3+}$ exhibits luminescence in the NIR region, not in the visible region.[103,104] An investigation of the luminescence lifetime of a $Nd^{3+}$-DMSO solution by Yao *et al.*[10] has shown that the lifetime also differs from the

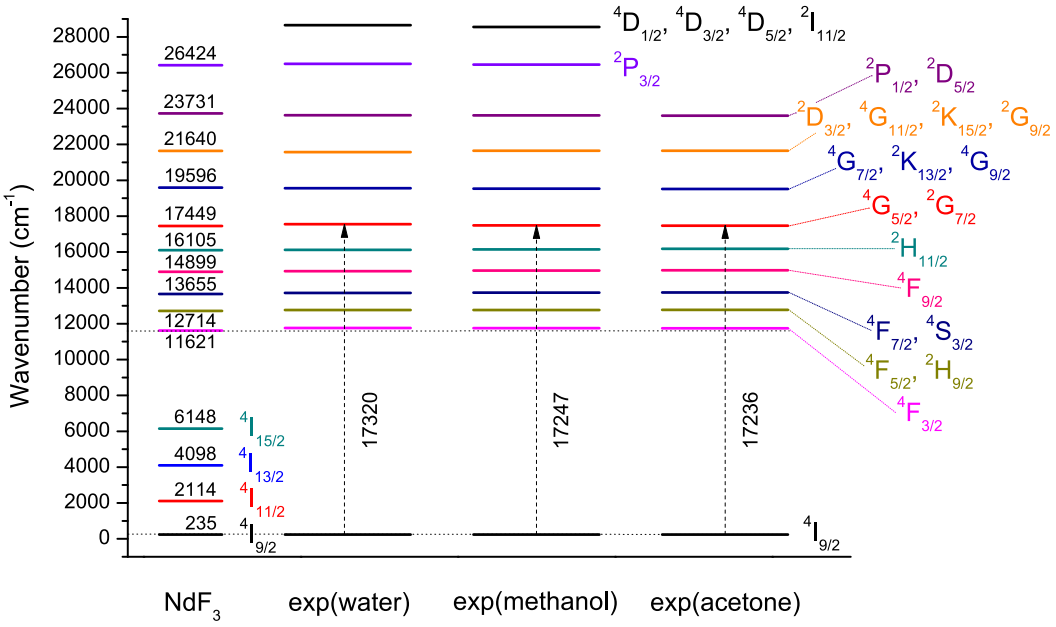


Figure 5.7.: Experimental energy levels of $Nd^{3+}$ compared with $NdF_3$[28].

Table 5.7.: Absorbance spectrum of Nd-CAB-glass: wavenumbers $\tilde{\nu}$, areas $\int A\, d\tilde{\nu}$ and experimental and calculated (Judd-Ofelt) oscillator strengths $f_{osc}$ of the transitions.

| $\longleftarrow {}^4I_{9/2}$ | $\tilde{\nu}$ (cm$^{-1}$) | $\int A\, d\tilde{\nu}$ | $f_{osc}$ ($\times 10^{-5}$)[a] | |
|---|---|---|---|---|
| | | | exp | JO |
| $^4F_{3/2}$ | 11458 | 58.9 | 0.337 | 0.433 |
| $^4F_{5/2}$, $^2H_{9/2}$ | 12515 | 230 | 1.31 | 1.37 |
| $^4F_{7/2}$, $^4S_{3/2}$ | 13464 | 246 | 1.40 | 1.39 |
| $^4F_{9/2}$ | 14726 | 17.9 | 0.103 | 0.108 |
| $^2H_{11/2}$ | 15952 | 4.67 | 0.027 | 0.030 |
| $^4G_{5/2}$, $^2G_{7/2}$ | 17233 | 639 | 3.66 | 3.66 |
| $^4G_{7/2}$, $^4G_{9/2}$, $^2K_{13/2}$ | 19282 | 217 | 1.24 | 1.12 |
| $^2D_{3/2}$, $^4G_{11/2}$, $^2K_{15/2}$ | 21436 | 46.9 | 0.268 | 0.243 |
| $^2P_{1/2}$, $^2D_{5/2}$ | 23260 | 11.2 | 0.064 | 0.126 |

[a] rms = $7.26 \cdot 10^{-7}$.

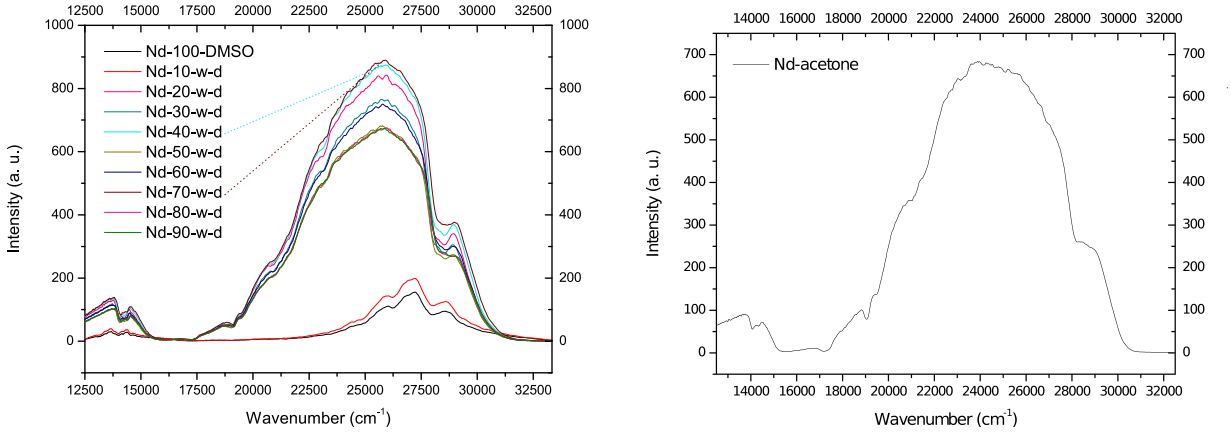


(a) $Nd^{3+}$ in water-DMSO.

(b) $Nd^{3+}$ in acetone.

Figure 5.8.: Emission spectra of $Nd^{3+}$ in water-DMSO mixtures and in acetone.

expected value for lanthanide emissions. These emissions are presumably *metal-to-ligand charge-transfer* bands, rather than $f \leftrightarrow f$ transitions.[10]

### 5.2.3. Judd-Ofelt analysis

A semi-empirical Judd-Ofelt analysis of the absorbance spectra of $Nd^{3+}$ in the solvent mixtures and the CAB glass was conducted. The Judd-Ofelt parameters $\Omega_\lambda$ ($\lambda = 2, 4, 6$) were obtained from a least squares fit between calculated and experimental oscillator strengths. A program was written for this purpose based on a software by Dr. K. Gatterer, see Appendix. The results are reported in Tables 5.8, 5.9 and 5.10. Figure 5.9 shows the dependence of the three $\Omega_\lambda$ parameters on the environment of $Nd^{3+}$ and the influence of the solvents on the oscillator strength of the hypersensitive transition is demonstrated in Figure 5.9c. An increasing acetone or methanol content leads to greater oscillator strengths of the hypersensitive transition, $f_{osc}$(hyp), and to an increase of $\Omega_2$, while $\Omega_4$ and $\Omega_6$ remain nearly unchanged, as expected. This increase in $f_{osc}$(hyp) and $\Omega_2$ is even more pronounced in acetone than in methanol, as was already seen in the spectra. In water the relation $\Omega_2 < \Omega_4 < \Omega_6$ holds, in methanol $\Omega_4 < \Omega_2 \approx \Omega_6$ and in acetone $\Omega_4 < \Omega_6 < \Omega_2$. This is in line with the polarisabilities of the solvents, $\alpha$(water) = $1.65 \cdot 10^{-40}$ $C^2$ $m^2$ $J^{-1}$ < $\alpha$(methanol) = $3.69 \cdot 10^{-40}$ $C^2$ $m^2$ $J^{-1}$ < $\alpha$(acetone) = $7.12 \cdot 10^{-40}$ $C^2$ $m^2$ $J^{-1}$.[105] It seems that the change of the intensity of the hypersensitive transition can be explained with the change in the polarisability of the environment of $Nd^{3+}$, at least to some extent.

More bands were resolved in the $Nd^{3+}$ spectra in the water-methanol mixtures than in the water-acetone mixtures, presumably because of the starting absorption of acetone in the UV region,[106] see Figure 5.5. As a consequence, more bands were available in the water-methanol mixtures for the least squares fit to determine the $\Omega_\lambda$ parameters and calculated oscillator strengths, $f_{osc}$ JO. Therefore, the Judd-Ofelt analysis was first carried out using the same bands as for the water-acetone mixtures, subsequently referred to as (m1), in order to enable a direct comparison between the two solvent mixtures, and then using in addition the $^4D_{1/2}$, $^4D_{3/2}$, $^4D_{5/2}$, $^2I_{11/2} \leftarrow {}^4I_{9/2}$ transition (also called L group[28]), in the further work named (m2).

The obtained Judd-Ofelt parameters in water, see Tables 5.8 and 5.9 (m1), are in comparatively good agreement with the results for $Nd^{3+}$(aq) by Carnall *et al.*[41], $\Omega_2 = 0.93 \pm 0.3$, $\Omega_2 = 5.0 \pm 0.3$ and $\Omega_2 = 7.9 \pm 0.4$.[34] However, the results for $\Omega_{2,4}$ of $Nd^{3+}$ in the water-methanol mixtures when taking the absorbance peaks of the L group into account as well, Table 5.9 (m2), deviate from the literature values,[34,41] especially $\Omega_2$. The results in acetone are similar to the published values for $Nd(NO_3)_3$ in ethyl acetate by Carnall *et al.*[47], $\Omega_2 = 9.2 \pm 0.4$, $\Omega_2 = 5.4 \pm 0.3$ and $\Omega_2 = 7.7 \pm 0.45$.[34]

The fit between experimental and calculated oscillator strengths is in most cases better in the (m1) analysis, except for the transitions $^4F_{3/2} \leftarrow {}^4I_{9/2}$ and $^2P_{1/2}$, $^2D_{5/2} \leftarrow {}^4I_{9/2}$, where a better agreement is obtained in the (m2) analysis. The root mean square deviations (rms) of the Judd-Ofelt calculations are smaller for (m1), however the standard error of the $\Omega_\lambda$ parameter is smaller for (m2), which is highlighted in Figure 5.9b, or in Table 5.9. Figure 5.9a shows the dependence of the Judd-Ofelt parameters on the acetone content in water and is consistent with the observations in the literature,[34,41] as well as the (m1) analysis (Figure 5.9b, unfilled symbols □). The (m2) analysis shows the same tendency as the (m1) analysis, but different values for the Judd-Ofelt parameters are obtained, especially for $\Omega_{2,4}$. To sum up, the (m1) analysis without L group gives a better agreement with literature values, better rms values and better fit between $f_{exp}$ and $f_{calc}$(JO) for most transitions, while the (m2) analysis yields Judd-Ofelt parameters with a smaller standard error.

A lot of studies have been carried out of $Nd^{3+}$ doped glasses, a few examples from the literature for the range of the $\Omega_\lambda$ parameters in various glasses are given in Table 5.10. Devi & Jayasankar[107] have compared the Judd-Ofelt parameters of almost forty different glasses. Numerous studies have shown the large variation of $\Omega_2$, e.g. $\Omega_2 = 37 \cdot 10^{-20}$ cm$^2$ in poly(methyl methacrylate)[108] or even $275 \cdot 10^{-20}$ cm$^2$ ($NdI_3$, $D_{3h}$).[34] The prepared Nd-CAB-glass is in good agreement with other borate glasses,[109,110] as can be seen in Table 5.10.

Table 5.8.: Judd-Ofelt results of $Nd^{3+}$ in water-acetone mixtures: Judd-Ofelt parameters $\Omega_\lambda$ ($\lambda$ = 2, 4, 6), experimental (exp) and calculated (JO) oscillator strengths $f_{osc}$ of hypersensitive $^2G_{7/2}$, $^4G_{5/2} \leftarrow {}^4I_{9/2}$ transition and root mean square deviations (rms) of the Judd-Ofelt calculations.

| **v-% a** | **Ω (×10$^{-20}$ cm$^2$)** | | | **$f_{osc}$ (×10$^{-5}$)** | | **rms (×10$^{-7}$)** |
|---|---|---|---|---|---|---|
| | $\Omega_2$ | $\Omega_4$ | $\Omega_6$ | exp | JO | |
| 0 | 0.536 ± 0.46 | 6.24 ± 0.70 | 7.41 ± 0.34 | 1.03 | 1.04 | 4.14 |
| 10 | 0.572 ± 0.47 | 6.28 ± 0.70 | 7.43 ± 0.34 | 1.05 | 1.05 | 4.18 |
| 20 | 0.642 ± 0.48 | 6.31 ± 0.73 | 7.47 ± 0.36 | 1.07 | 1.08 | 4.33 |
| 30 | 0.812 ± 0.49 | 6.34 ± 0.74 | 7.59 ± 0.36 | 1.12 | 1.12 | 4.43 |
| 40 | 1.03 ± 0.50 | 6.20 ± 0.76 | 7.60 ± 0.37 | 1.15 | 1.15 | 4.55 |
| 50 | 1.08 ± 0.51 | 6.29 ± 0.77 | 7.55 ± 0.38 | 1.17 | 1.18 | 4.64 |
| 60 | 1.50 ± 0.52 | 6.22 ± 0.78 | 7.64 ± 0.38 | 1.26 | 1.27 | 4.71 |
| 70 | 2.31 ± 0.54 | 5.95 ± 0.82 | 7.60 ± 0.40 | 1.40 | 1.41 | 4.94 |
| 80 | 3.66 ± 0.56 | 5.66 ± 0.84 | 7.56 ± 0.41 | 1.66 | 1.67 | 5.09 |
| 90 | 6.44 ± 0.60 | 5.18 ± 0.90 | 7.16 ± 0.44 | 2.20 | 2.21 | 5.46 |
| 100 | 9.58 ± 0.80 | 5.40 ± 1.2 | 7.32 ± 0.59 | 2.91 | 2.91 | 7.25 |

Table 5.9.: Judd-Ofelt results of $Nd^{3+}$ in water-methanol mixtures: Judd-Ofelt parameters $\Omega_\lambda$ ($\lambda$ = 2, 4, 6), experimental (exp) and calculated (JO) oscillator strengths $f_{osc}$ of hypersensitive $^2G_{7/2}$, $^4G_{5/2} \leftarrow {}^4I_{9/2}$ transition and root mean square deviations (rms) of the Judd-Ofelt calculations.

| **v-% m** | **Ω (×10$^{-20}$ cm$^2$)** | | | **$f_{osc}$ (×10$^{-5}$)** | | **rms (×10$^{-7}$)** |
|---|---|---|---|---|---|---|
| | $\Omega_2$ (m1) | $\Omega_4$ (m1) | $\Omega_6$ (m1) | exp (m1) | JO (m1) | (m1) |
| 0 | 0.514 ± 0.52 | 6.28 ± 0.79 | 7.49 ± 0.39 | 1.03 | 1.04 | 4.68 |
| 10 | 0.590 ± 0.52 | 6.20 ± 0.78 | 7.37 ± 0.38 | 1.04 | 1.04 | 4.66 |
| 20 | 0.733 ± 0.53 | 6.15 ± 0.81 | 7.35 ± 0.40 | 1.06 | 1.07 | 4.81 |
| 30 | 0.922 ± 0.55 | 6.04 ± 0.83 | 7.38 ± 0.41 | 1.09 | 1.10 | 4.93 |
| 40 | 1.16 ± 0.57 | 5.98 ± 0.87 | 7.44 ± 0.42 | 1.14 | 1.14 | 5.16 |
| 50 | 1.43 ± 0.58 | 5.76 ± 0.88 | 7.41 ± 0.43 | 1.17 | 1.17 | 5.25 |
| 60 | 1.77 ± 0.62 | 5.69 ± 0.94 | 7.40 ± 0.46 | 1.23 | 1.23 | 5.60 |
| 70 | 2.28 ± 0.63 | 5.55 ± 0.96 | 7.46 ± 0.47 | 1.32 | 1.33 | 5.72 |
| 80 | 3.05 ± 0.65 | 5.40 ± 0.99 | 7.44 ± 0.48 | 1.47 | 1.47 | 5.86 |
| 90 | 4.45 ± 0.69 | 5.39 ± 1.0 | 7.64 ± 0.51 | 1.77 | 1.77 | 6.22 |
| 100 | 6.30 ± 0.73 | 5.58 ± 1.1 | 7.51 ± 0.54 | 2.18 | 2.18 | 6.55 |

| **v-% m** | **Ω (×10$^{-20}$ cm$^2$)** | | | **$f_{osc}$ (×10$^{-5}$)** | | **rms (×10$^{-7}$)** |
|---|---|---|---|---|---|---|
| | $\Omega_2$ (m2) | $\Omega_4$ (m2) | $\Omega_6$ (m2) | exp (m2) | JO (m2) | (m2) |
| 0 | 2.07 ± 0.41 | 3.70 ± 0.38 | 8.16 ± 0.53 | 1.03 | 1.05 | 7.47 |
| 10 | 2.13 ± 0.41 | 3.65 ± 0.38 | 8.03 ± 0.53 | 1.04 | 1.05 | 7.40 |
| 20 | 2.24 ± 0.41 | 3.64 ± 0.38 | 8.00 ± 0.53 | 1.06 | 1.07 | 7.41 |
| 30 | 2.41 ± 0.41 | 3.57 ± 0.38 | 8.02 ± 0.53 | 1.09 | 1.10 | 7.41 |
| 40 | 2.66 ± 0.42 | 3.49 ± 0.39 | 8.09 ± 0.54 | 1.14 | 1.15 | 7.58 |
| 50 | 2.84 ± 0.41 | 3.41 ± 0.38 | 8.02 ± 0.52 | 1.17 | 1.18 | 7.37 |
| 60 | 3.11 ± 0.41 | 3.46 ± 0.38 | 7.98 ± 0.52 | 1.23 | 1.24 | 7.39 |
| 70 | 3.60 ± 0.41 | 3.35 ± 0.38 | 8.02 ± 0.53 | 1.32 | 1.33 | 7.41 |
| 80 | 4.26 ± 0.40 | 3.38 ± 0.37 | 7.96 ± 0.51 | 1.47 | 1.48 | 7.21 |
| 90 | 5.61 ± 0.41 | 3.47 ± 0.38 | 8.13 ± 0.52 | 1.76 | 1.78 | 7.32 |
| 100 | 7.65 ± 0.45 | 3.33 ± 0.42 | 8.09 ± 0.57 | 2.18 | 2.19 | 8.03 |

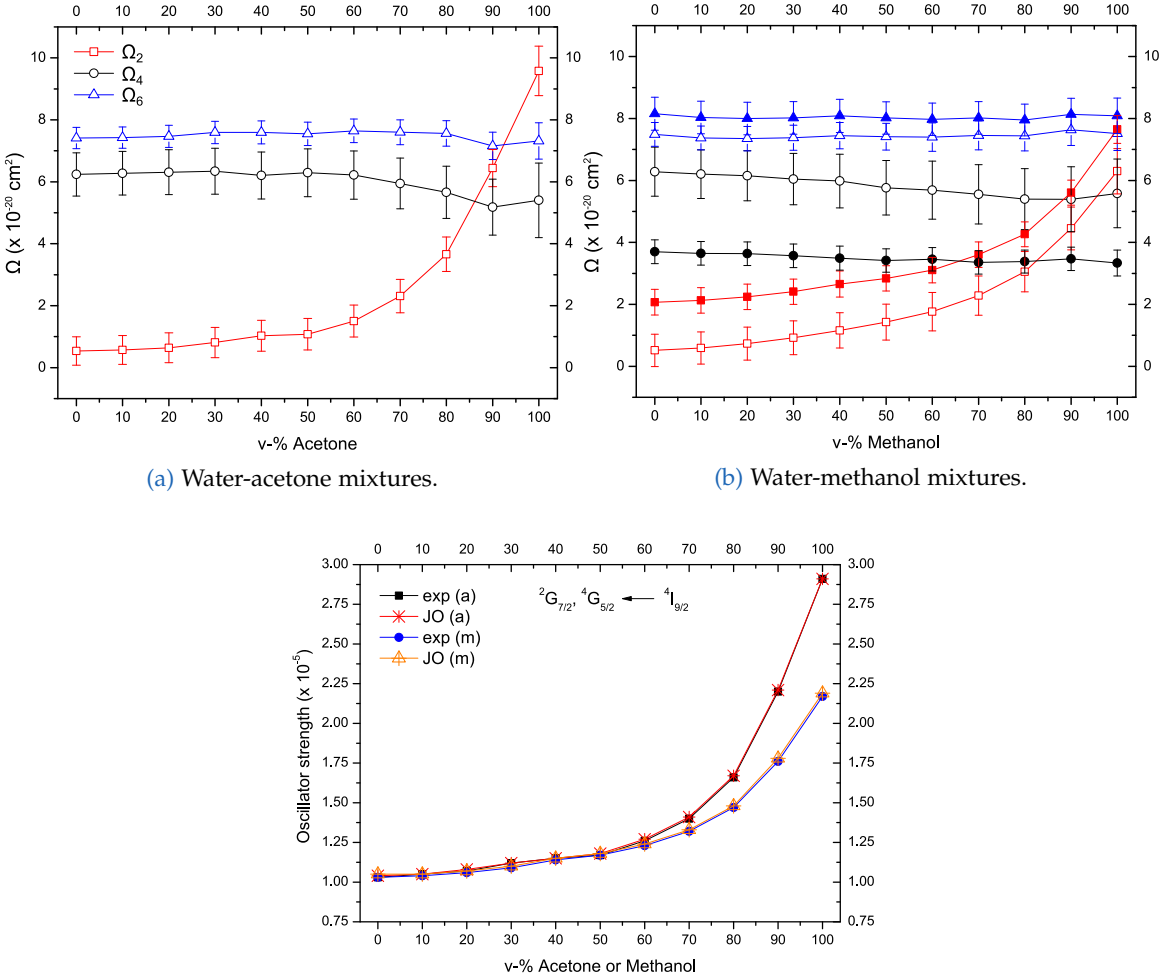


(a) Water-acetone mixtures.

(b) Water-methanol mixtures.

(c) Experimental and calculated oscillator strengths of hypersensitive transition.

Figure 5.9.: Judd-Ofelt parameters $\Omega_\lambda$ ($\lambda$ = 2, 4, 6) of $Nd^{3+}$ in water-acetone and water-methanol mixtures (filled symbols (m2) ■: Judd-Ofelt analysis taking $^4D_{1/2}$, $^4D_{3/2}$, $^4D_{5/2}$, $^2I_{11/2} \leftarrow {}^4I_{9/2}$ transitions into account ≙ L group; unfilled symbols (m1) □: without L group) and experimental (exp) and calculated (JO) oscillator strengths $f_{osc}$ of $Nd^{3+}$ in water-acetone and water-methanol (m2) mixtures.

Table 5.10.: Judd-Ofelt parameters $\Omega_\lambda$ ($\lambda$ = 2, 4, 6) of Nd-CAB-glass and root mean square deviation (rms) of calculation and range of $\Omega_\lambda$ parameters of various $Nd^{3+}$-doped glasses reported in the literature.

| | | | |
|---|---|---|---|
| **Nd-CAB-glass (present work)**[a] | | | |
| $\mathbf{\Omega_2}$ = | $8.73 \pm 0.69 \cdot 10^{-20}$ cm$^2$ | | |
| $\mathbf{\Omega_4}$ = | $8.55 \pm 1.0 \cdot 10^{-20}$ cm$^2$ | | |
| $\mathbf{\Omega_6}$ = | $9.76 \pm 0.51 \cdot 10^{-20}$ cm$^2$ | | |
| **$Nd^{3+}$-doped borate glasses** | | | |
| $\mathbf{\Omega_2}$ = | $7.3 \cdot 10^{-20}$ cm$^2$ | , | $8.53 \cdot 10^{-20}$ cm$^2$ |
| $\mathbf{\Omega_4}$ = | $9.9 \cdot 10^{-20}$ cm$^2$ | , | $7.47 \cdot 10^{-20}$ cm$^2$ |
| $\mathbf{\Omega_6}$ = | $8.54 \cdot 10^{-20}$ cm$^2$ | , | $9.60 \cdot 10^{-20}$ cm$^2$ |
| | $Nd^{3+}$ doped strontium lithium bismuth borate glass[109] | , | $Nd^{3+}$ doped $24Li_2O{\cdot}8Na_2O{\cdot}67B_2O_3$[110] |
| **Other $Nd^{3+}$-doped glasses** | | | |
| $\mathbf{\Omega_2}$ = | $0.25 \cdot 10^{-20}$ cm$^2$ $20ZnO{\cdot}50SiO_2{\cdot}29.5Bi_2O_3{\cdot}0.5Nd_2O_3$[111] | – | $7.75 \cdot 10^{-20}$ cm$^2$ $Nd^{3+}$ doped strontium titanium phosphate glass[112] |
| $\mathbf{\Omega_4}$ = | $1.17 \cdot 10^{-20}$ cm$^2$ $TeO_2$-LiF-$Nd_2O_3$[112] | – | $7.89 \cdot 10^{-20}$ cm$^2$ $Nd^{3+}$ doped lithium fluoro-borate glass with Mg-Ca[101] |
| $\mathbf{\Omega_6}$ = | $1.36 \cdot 10^{-20}$ cm$^2$ $20ZnO{\cdot}50SiO_2{\cdot}29.5Bi_2O_3{\cdot}0.5Nd_2O_3$[111] | – | $8.27 \cdot 10^{-20}$ cm$^2$ $Nd^{3+}$ doped lithium fluoro-borate glass with Mg[101] |

[a] rms = $7.26 \cdot 10^{-7}$.

In conclusion, the continuous variation of the intensity of the hypersensitive $^4G_{5/2} \leftarrow {}^4I_{9/2}$ transition of $Nd^{3+}$ was observed in the water-acetone and water-methanol mixtures, as could be seen in the spectra and on the basis of the oscillator strengths. The results of the Judd-Ofelt analysis are in line with these findings. The highest oscillator strength of the hypersensitive transition, $f_{osc}$(hyp), and the largest value for the $\Omega_2$ parameter, which is sensitive to the environment, were found in acetone, and the lowest values for $f_{osc}$(hyp) and $\Omega_2$ in water.
The Nd-CAB-glass yielded a high value for $\Omega_2$ compared to other $Nd^{3+}$-doped glasses. These results are in close agreement with the literature.

## 5.3. Experimental results of $Eu^{3+}$

### 5.3.1. Absorbance spectra

The absorbance spectra of $Eu^{3+}$ in water-acetone and water-methanol mixtures and of the Eu-CAB-glass are shown in Figures 5.10, 5.11 and 5.12. The large increase in intensity of the hypersensitive $^5D_2 \leftarrow {}^7F_0$ transition when going from water to methanol or acetone, which was already found for the $^4G_{5/2} \leftarrow {}^4I_{9/2}$ transition of $Nd^{3+}$, can be seen in Figures 5.10b and 5.11b. The "hot bands" $^5D_1 \leftarrow {}^7F_1$ and, to a lesser extent, $^5D_3 \leftarrow {}^7F_1$ also exhibit some hypersensitive character. The starting material, $Eu_2O_3$ (99.9 %), contained other lanthanide oxide impurities. The transitions of $Eu^{3+}$ in the absorbance spectra are much weaker than the $Nd^{3+}$ or $Ho^{3+}$ transitions, so their hypersensitive transitions $^4G_{5/2} \leftarrow {}^4I_{9/2}$ (at $\approx 1.72 \cdot 10^4$ $cm^{-1}$) and $^5G_6 \leftarrow {}^5I_8$ (at $\approx 2.21 \cdot 10^4$ $cm^{-1}$[34]), exhibiting high intensities, can also be seen in the spectra of $Eu^{3+}$, despite the low concentrations of $Nd^{3+}$ and $Ho^{3+}$. The $^5D_0 \leftarrow {}^7F_0$ could not be observed because it is hidden under the neodymium transition.

A larger spectral range was resolved in the water-methanol mixtures than in the water-acetone samples, including the $^5L_6 \leftarrow {}^7F_0$ transition, which has the highest intensity of the $Eu^{3+}$ transitions in the (UV-)VIS region. The identification of the bands on the higher energy side of the $^5L_6 \leftarrow {}^7F_0$ peak is difficult because of the high density of states in this region and overlapping bands. Figure 5.11a gives an assignment of these bands on a trial basis.

### 5.3.2. Emission spectra

Europium(III) exhibits a red to orange-red luminescence, which is mainly caused by the hypersensitive $^5D_0 \rightarrow {}^7F_2$ transition at $1.62 \cdot 10^4$ $cm^{-1}$ or 617 nm. Figures 5.13, 5.14 and 5.15 present the emission spectra of $Eu^{3+}$ in water-acetone and water-methanol mixtures and of the Eu-CAB-glass. All spectra of the solutions were measured with an excitation wavelength of 396 nm. They clearly demonstrate the change of intensity of the hypersensitive transition, which has the lowest intensity in water. The solutions in 100 % acetone and 100 % methanol yield comparable intensities of the hypersensitive transition.
The CAB glass was measured with different excitation wavelengths, see Figure 5.15.

The transition energies of $Eu^{3+}$ are listed in Tables 5.11 and 5.13, while Figure 5.16 compares them to the published values for $EuF_3$ by Carnall *et al.*[28], which were also used for the band

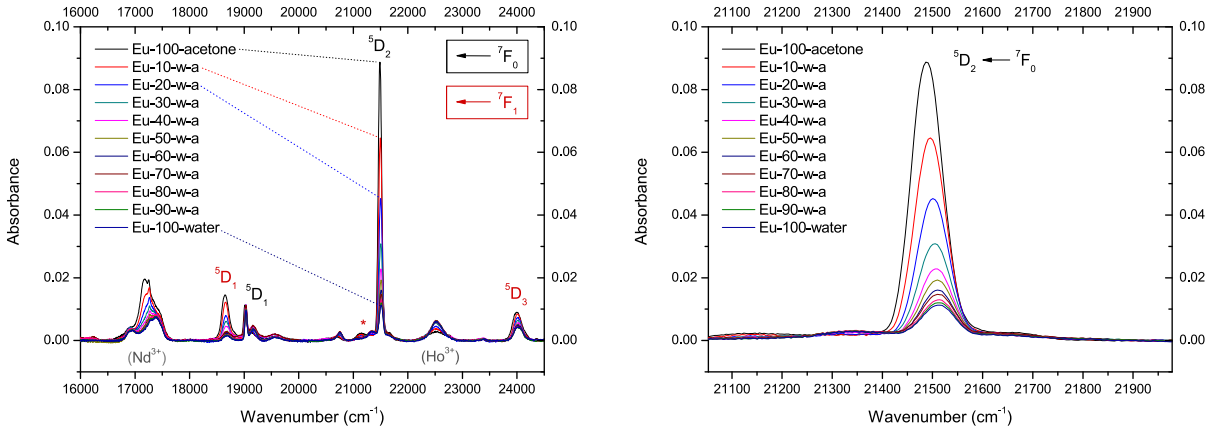


(a) Absorbance spectra.

(b) Hypersensitive $^5D_2 \leftarrow {}^7F_0$ transition.

Figure 5.10.: Absorbance spectra of $Eu^{3+}$ in water-acetone mixtures.

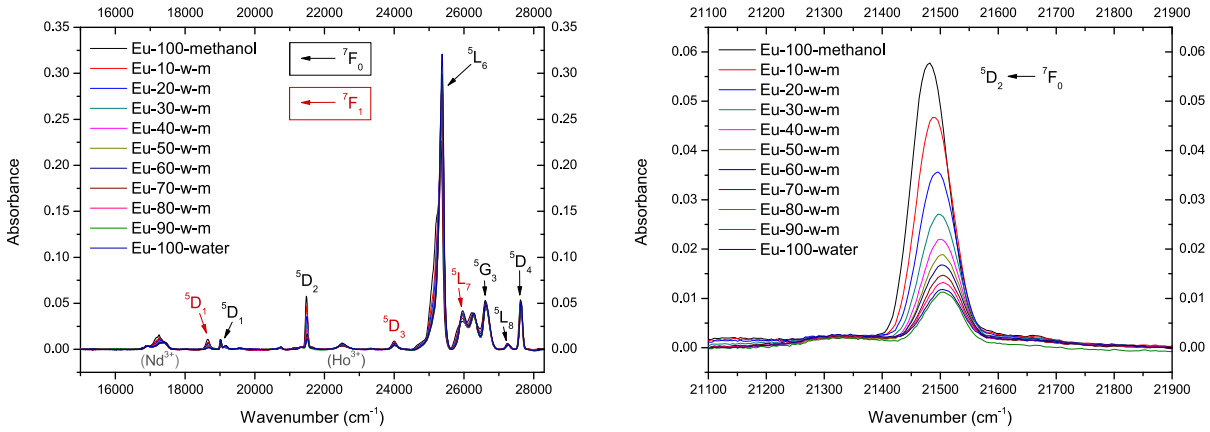


(a) Absorbance spectra.

(b) Hypersensitive $^5D_2 \leftarrow {}^7F_0$ transition.

Figure 5.11.: Absorbance spectra of $Eu^{3+}$ in water-methanol mixtures.

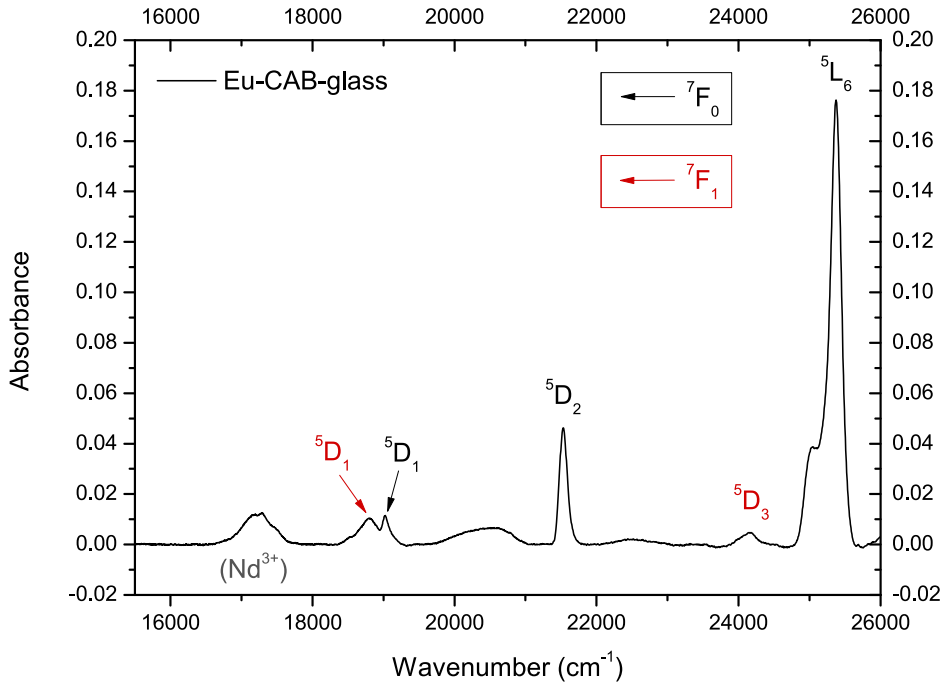


Figure 5.12.: Absorbance spectrum of $Eu^{3+}$-CAB-glass.

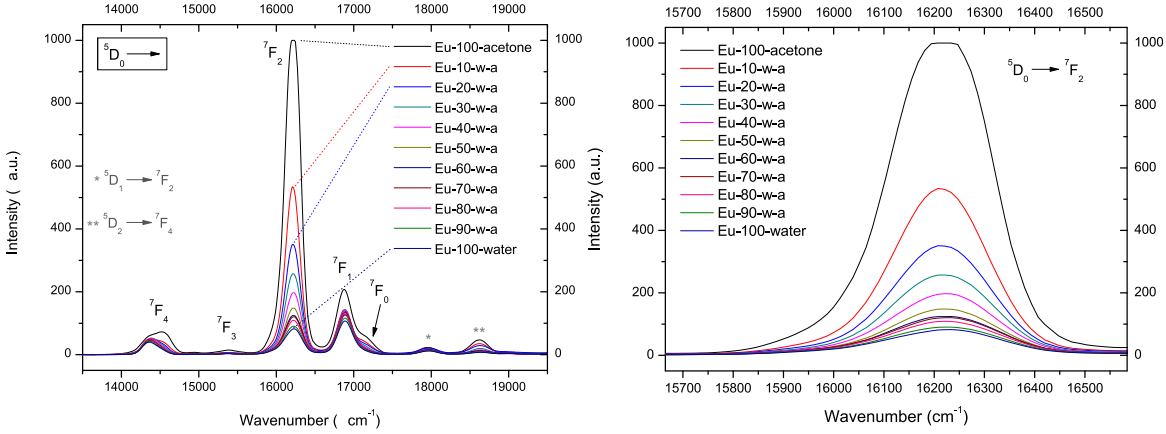


(a) Emission spectra.

(b) Hypersensitive $^5D_0 \rightarrow {}^7F_2$ transition.

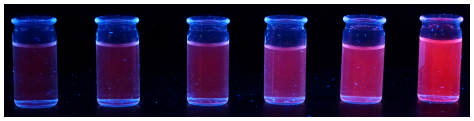

(c) Luminescence of $Eu^{3+}$ solutions in 50 (left) – 90 v-% acetone in water and in 100 % acetone (right).

Figure 5.13.: Emission spectra of $Eu^{3+}$ in water-acetone mixtures.

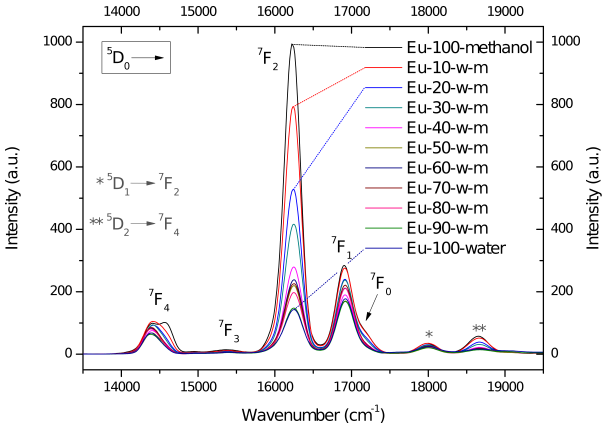


(a) Emission spectra. (b) Hypersensitive $^5D_0 \rightarrow {}^7F_2$ transition.

Figure 5.14.: Emission spectra of $Eu^{3+}$ in water-methanol mixtures.

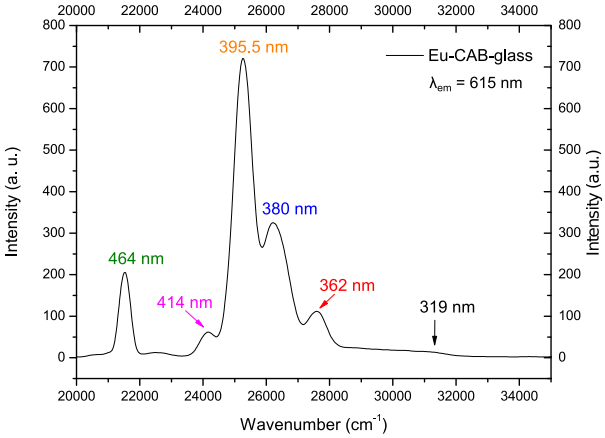


(a) Excitation spectrum. (b) Emission spectra.

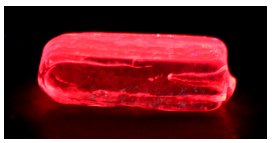

(c) Luminescence at $\lambda_{ex}$ = 254 nm.

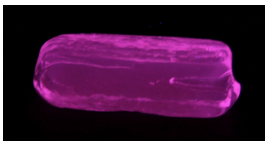

(d) Luminescence at $\lambda_{ex}$ = 365 nm.

Figure 5.15.: Excitation spectrum and emission spectra of $Eu^{3+}$-CAB-glass recorded at different excitation wavelengths and luminescence of Eu-CAB-glass.

assignment. Only the solutions in the pure solvents and the 50-50 % mixtures are presented in the tables.

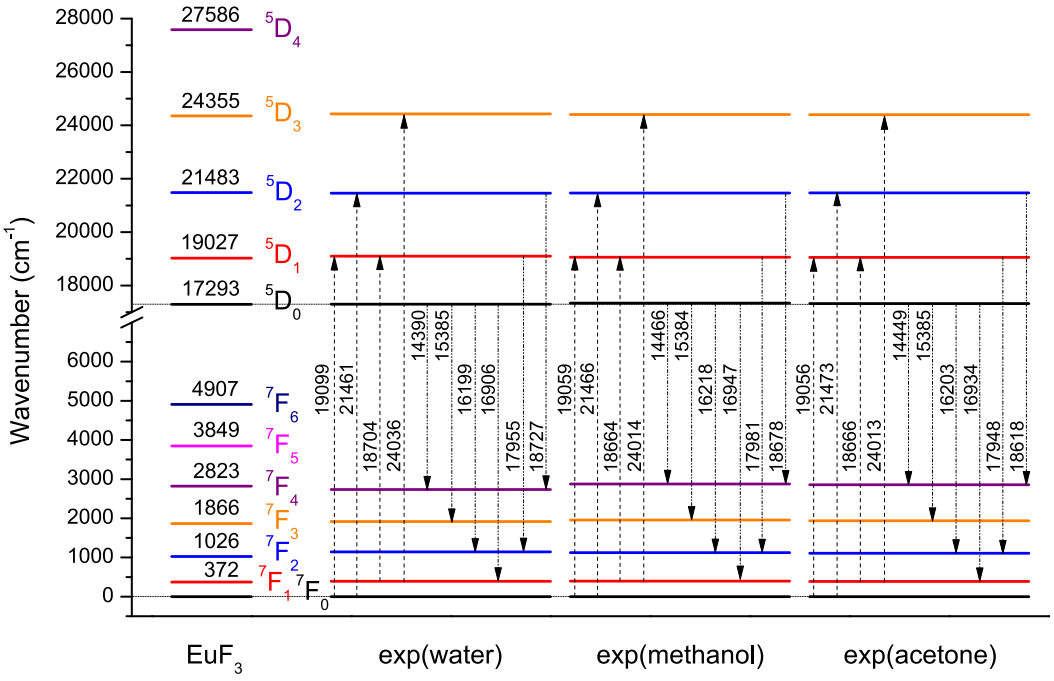


Figure 5.16.: Experimental energy levels of $Eu^{3+}$ compared with $EuF_3$[28].

It can be seen that the energies remain nearly the same in the different environments, i.e. the position of the states stays approximately the same, which was also observed for $Nd^{3+}$ and can be explained by the shielding of the $f$-electrons from the environment.[11,13] The environment of the rare earth ion thus has no substantial influence on the position of the states. There is an overlap between the $^5D_0 \rightarrow {}^7F_0$ band with the more intense $^5D_0 \rightarrow {}^7F_1$ band, therefore the position of the $0 \rightarrow 0$ transition could not be determined. The transition energies are in accordance with the literature.[28,43,99,113,114]

The photographs (Figures 5.13c, 5.15c and 5.15d) show the luminescence of $Eu^{3+}$ caused by $f \leftrightarrow f$ transitions. The increase in luminescence intensity can also be seen in Figure 5.13c, i.e. in a series of $Eu^{3+}$ in water-acetone mixtures ranging from 50 to 100 % acetone in water, confirming the higher intensity in acetone compared to water.

### 5.3.3. Judd-Ofelt analysis

Judd-Ofelt calculations were performed based on the theory outline in chapter 2.2 on page 25, i.e. using the ratio of the radiative transition probabilities $A$ of the magnetic dipole $^5D_0 \rightarrow {}^7F_1$ transition to the electric dipole $^5D_0 \rightarrow {}^7F_J$ ($J = 2, 4, 6$) transitions. The $^5D_0 \rightarrow {}^7F_6$ transition at $1.24 \cdot 10^4$ cm$^{-1}$ or approximately 807 nm was outside the recorded spectral range, therefore the $\Omega_6$ parameter could not be determined. The results are summarized in Tables 5.12 (solutions) and 5.13 (CAB glass). A large variation of the $\Omega_2$ parameter is observed, while $\Omega_4$ nearly stays the same, as was already found for $Nd^{3+}$. This demonstrates the well-known sensitivity of $\Omega_2$ to the environment. Figure 5.17 depicts the dependence of the Judd-Ofelt parameters on the acetone and methanol content in water. The increase of $\Omega_2$ is more pronounced in the water-acetone mixtures than in the water-methanol mixtures. The relation $\Omega_4 < \Omega_2$ was found for all the (pure) solvents and solvent mixtures, in contrast to the findings of $Nd^{3+}$. The acetone solution yields the largest value of $\Omega_2$. This tendency is, like in the case of $Nd^{3+}$, associated with an increase in the polarisability of the environment of $Eu^{3+}$. However, the polarisability is only one possible explanation for the hypersensitivity. There seems to be a dependence on the symmetry as well, as was already mentioned in chapter 2.3. The experimental spectra of the solutions cannot be used for an interpretation in terms of symmetry, because there is no definite point group since the environment is dynamic, but the CAB glass is a good example of a host of low symmetry.

The asymmetry ratio (ar) describes the ratio of the intensities of the hypersensitive transition to the magnetic dipole $^5D_0 \rightarrow {}^7F_1$ transition, which remains nearly unchanged irrespective of the environment.[43]

$$\text{ar} = \frac{\text{Int}\left({}^5D_0 \rightarrow {}^7F_2\right)}{\text{Int}\left({}^5D_0 \rightarrow {}^7F_1\right)} \tag{5.1}$$

The higher the asymmetry ratio, the stronger is the hypersensitive effect. Tables 5.11 and 5.13 give the asymmetry ratios together with the radiative transition probabilities A. It can be seen how the asymmetry ratio increases when going from water to acetone or methanol, in line with the increase of the $\Omega_2$ parameter, showing the hypersensitivity of the $^5D_0 \rightarrow {}^7F_2$ transition. The largest asymmetry ratio is observed in acetone (ar = 4.05). The Eu-CAB-glass yields an asymmetry ratio of only 2.78, which is lower than in methanol (ar = 2.92), but still larger than in water (ar = 0.88). That is to say, the following order of the asymmetry ratios is observed

$$\text{water} < \text{CAB glass} \approx \text{methanol} < \text{acetone} .$$

Table 5.11.: Emission spectra of $Eu^{3+}$ in water-acetone and water-methanol mixtures: wavenumbers $\tilde{\nu}$, areas $\int I\,d\tilde{\nu}$, radiative transition probabilities A for electric (*ed*) and magnetic (*md*) dipole transitions and asymmetry ratios (ar).

| **v-% a** | **$^5D_0 \rightarrow$** | **$\tilde{\nu}$ (cm$^{-1}$)** | **$\int I\,d\tilde{\nu}$** | **$A_{ed}$ (s$^{-1}$)** | **$A_{md}$ (s$^{-1}$)** | **ar** |
|---|---|---|---|---|---|---|
| **0** | $^7F_4$ | 14390 | 11126 | 22.3 | 0 | |
| | $^7F_2$ | 16199 | 25892 | 46.1 | 0 | 0.884 |
| | $^7F_1$ | 16906 | 29281 | 0 | 50 | |
| **50** | $^7F_4$ | 14398 | 13817 | 22.7 | 0 | |
| | $^7F_2$ | 16202 | 42613 | 62.3 | 0 | 1.19 |
| | $^7F_1$ | 16911 | 35708 | 0 | 50 | |
| **100** | $^7F_4$ | 14449 | 30340 | 26.6 | 0 | |
| | $^7F_2$ | 16203 | 270489 | 212 | 0 | 4.05 |
| | $^7F_1$ | 16934 | 66813 | 0 | 50 | |
| **v-% m** | **$^5D_0 \rightarrow$** | **$\tilde{\nu}$ (cm$^{-1}$)** | **$\int I\,d\tilde{\nu}$** | **$A_{ed}$ (s$^{-1}$)** | **$A_{md}$ (s$^{-1}$)** | **ar** |
| **0** | $^7F_4$ | 14411 | 19772 | 21.1 | 0 | |
| | $^7F_3$ | 15402 | 1642 | | | |
| | $^7F_2$ | 16219 | 48299 | 45.8 | 0 | 0.877 |
| | $^7F_1$ | 16940 | 55050 | 0 | 50 | |
| | ($^5D_1 \rightarrow$ $^7F_2$ | 17971 | 10668) | | | |
| | ($^5D_2 \rightarrow$ $^7F_4$ | 18808 | 11669) | | | |
| **50** | $^7F_4$ | 14418 | 20580 | 22.7 | 0 | |
| | $^7F_3$ | 15393 | 1573 | | | |
| | $^7F_2$ | 16226 | 67638 | 66.4 | 0 | 1.27 |
| | $^7F_1$ | 16940 | 53169 | 0 | 50 | |
| | ($^5D_1 \rightarrow$ $^7F_2$ | 17997 | 7058) | | | |
| | ($^5D_2 \rightarrow$ $^7F_4$ | 18741 | 8151) | | | |
| **100** | $^7F_4$ | 14466 | 44139 | 27.1 | 0 | |
| | $^7F_3$ | 15384 | 5695 | | | |
| | $^7F_2$ | 16218 | 278313 | 152 | 0 | 2.92 |
| | $^7F_1$ | 16947 | 95412 | 0 | 50 | |
| | ($^5D_1 \rightarrow$ $^7F_2$ | 17981 | 11664) | | | |
| | ($^5D_2 \rightarrow$ $^7F_4$ | 18678 | 21229) | | | |

The obtained $\Omega_\lambda$ parameters of $Eu^{3+}$ in water, $\Omega_2 = 2.2 \cdot 10^{-20}$ cm$^2$ and $\Omega_2 = 2.0 - 2.1 \cdot 10^{-20}$ cm$^2$, deviate from the reported values published by Carnall *et al.*[41] (1968), where $\Omega_2 = 1.45 \cdot 10^{-20}$ cm$^2$, $\Omega_4 = 6.63 \cdot 10^{-20}$ cm$^2$ and $\Omega_6 = 5.37 \cdot 10^{-20}$ cm$^2$ was found for aqueous solutions of $Eu^{3+}$. However, the Judd-Ofelt parameters of the investigated mixtures still lie in the reported range, as shown in Table 5.14.

Table 5.12.: Judd-Ofelt parameters $\Omega_\lambda$ ($\lambda$ = 2,4) of $Eu^{3+}$ in water-acetone (v-% acetone in water) and water-methanol (v-% m) mixtures.

| **v-% a** | **$\Omega$ ($\times 10^{-20}$ cm$^2$)** | | **v-% m** | **$\Omega$ ($\times 10^{-20}$ cm$^2$)** | |
|---|---|---|---|---|---|
| | $\Omega_2$ | $\Omega_4$ | | $\Omega_2$ | $\Omega_4$ |
| 0 | 2.2 | 2.1 | 0 | 2.2 | 2.0 |
| 10 | 2.2 | 2.1 | 10 | 2.3 | 2.0 |
| 20 | 2.3 | 2.1 | 20 | 2.4 | 2.0 |
| 30 | 2.4 | 2.0 | 30 | 2.6 | 2.1 |
| 40 | 2.5 | 2.0 | 40 | 2.8 | 2.1 |
| 50 | 2.8 | 2.0 | 50 | 3.1 | 2.1 |
| 60 | 3.3 | 2.0 | 60 | 3.4 | 2.1 |
| 70 | 4.0 | 2.0 | 70 | 3.9 | 2.1 |
| 80 | 5.0 | 2.0 | 80 | 4.8 | 2.2 |
| 90 | 7.0 | 2.1 | 90 | 6.0 | 2.3 |
| 100 | 9.5 | 2.4 | 100 | 7.3 | 2.5 |

Table 5.13.: Emission spectrum of Eu-CAB-glass: wavenumbers $\tilde{\nu}$, areas $\int I\,d\tilde{\nu}$, radiative transition probabilities A for electric (*ed*) and magnetic (*md*) dipole transitions, Judd-Ofelt parameters $\Omega_\lambda$ ($\lambda$ = 2,4) and asymmetry ratios (ar).

| **$^5D_0 \rightarrow$** | **$\tilde{\nu}$ (cm$^{-1}$)** | **$\int I\,d\tilde{\nu}$** | **A$_{ed}$ (s$^{-1}$)** | **A$_{md}$ (s$^{-1}$)** | **$\Omega$ ($\times 10^{-20}$ cm$^2$)** | | **ar** |
|---|---|---|---|---|---|---|---|
| | | | | | $\Omega_2$ | $\Omega_4$ | |
| $^7F_4$ | 14378.9 | 35269 | 19.8 | 0 | | | |
| $^7F_2$ | 16227.4 | 292593 | 146 | 0 | 1.18 | 4.36 | 2.78 |
| $^7F_1$ | 16973.4 | 105196 | 0 | 50 | | | |

There is extensive literature concerning Judd-Ofelt parameters of $Eu^{3+}$.[16,41,43–45,114–117] Table 5.14 lists only a selection of the published values. The calculated $\Omega_4$ parameter of the Eu-

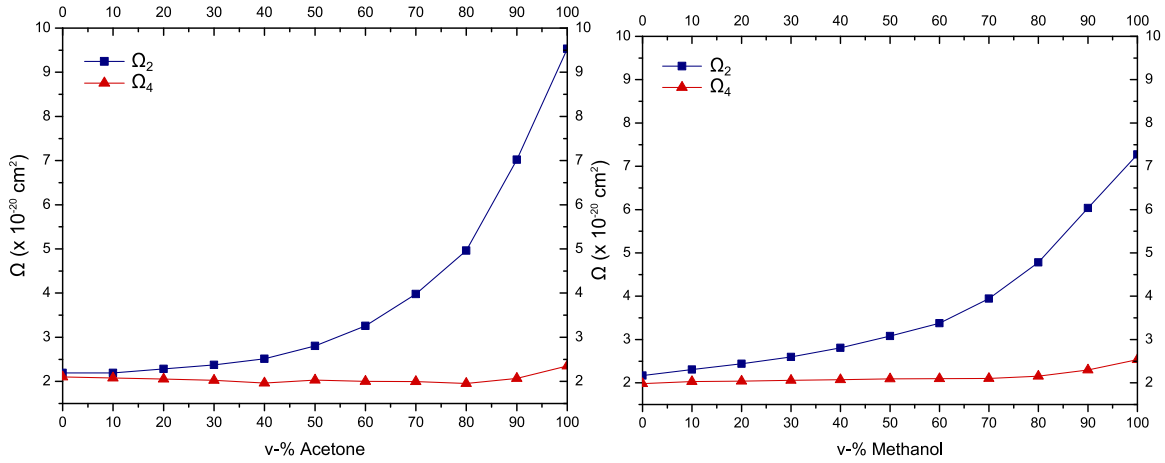


(a) Water-acetone mixtures.

(b) Water-methanol mixtures.

Figure 5.17.: Judd-Ofelt parameters $\Omega_\lambda$ ($\lambda$ = 2,4) of $Eu^{3+}$ in water-acetone and water-methanol mixtures.

CAB-glass is in agreement with the literature values,[16,43,116] e.g. in agreement with many $Eu^{3+}$ doped glasses, also borate glasses, that have been reported by Babu & Jayasankar[43]. The $\Omega_2$ parameter of the Eu-CAB-glass ($\Omega_2 = 1.18 \cdot 10^{-20}$ cm$^2$) is smaller than some published values for other $Eu^{3+}$ doped borate glasses, e.g. $\Omega_2 = 5.64 \cdot 10^{-20}$ cm$^2$ for a lithium borate glass,[43] but still lies in the observed range, see Table 5.14. Most studies do not report $\Omega_6$ values for the same reason as mentioned in this thesis.

Table 5.14.: Range of $\Omega_\lambda$ parameters of $Eu^{3+}$ in various hosts reported in the literature.

| | | | |
|---|---|---|---|
| $\mathbf{\Omega_2}$ = | $0.46 \cdot 10^{-20}$ cm$^2$ | – | $33.0 \cdot 10^{-20}$ cm$^2$ |
| | $57ZrF_4{\cdot}35BaF_2{\cdot}1LaF_3{\cdot}3AlF_3{\cdot}3EuF_3$[118] | | $Eu(TTA)_3 2H_2O$[16] |
| | | | (TTA = thenoyltrifluoroacetonate) |
| $\mathbf{\Omega_4}$ = | $0.18 \cdot 10^{-20}$ cm$^2$ | – | $5.53 \cdot 10^{-20}$ cm$^2$ |
| | $Eu_2(DDBM)_3H_2O$[114] | | $Eu(3\text{-}NH_2pic)_3$*o*-phen[16] |
| | (chelating $\beta$-diketone complex) | | (3-$NH_2$pic = 3-aminopyridine-2-carboxylic acid) |
| $\mathbf{\Omega_6}$ = | $0.51 \cdot 10^{-20}$ cm$^2$ | – | $6.30 \cdot 10^{-20}$ cm$^2$ |
| | $Eu^{3+}$ doped KMgSi glass[43,119] | | $49.5Li_2CO_3{\cdot}49.5H_3BO_3{\cdot}1Eu_2O_3$[43] |

In summary, the variation of the intensities of the hypersensitive transitions of $Eu^{3+}$ depending on the environment were observed both in the aborbance and in the emission spectra, showing the lowest intensities in water and the highest intensities in acetone. The transition energies were only affected to a small extent by the change of the solvents owing to the shielding of the $f$-electrons by the outer filled $5s$ and $5p$ shells.[11,13] In line with the increase in intensity and of the oscillator strength of the hypersensitive transition was the increase in the $\Omega_2$ parameter. For the asymmetry ratio, the relation water < CAB glass ≈ methanol < acetone was found.
The Eu-CAB-glass yielded a relatively small $\Omega_2$ parameter compared to other borate glasses. The results are generally in accordance with the literature.

# 6. Computations

## 6.1. Methodology

### 6.1.1. Calculation of geometries

*Geometry optimizations* and frequency calculations of the lanthanide water complexes, i.e. $Nd^{3+}$ and $Eu^{3+}$ aquo complexes, were performed using the Gaussian09 program package[120] and density functional theory calculations with the hybrid functional B3LYP[87,89,90]. For the water molecules the triple-zeta basis set TZVP[121,122] was used and the effective core potentials ECP49MWB[80,82] and ECP52MWB[80,82] for $Nd^{3+}$ and $Eu^{3+}$, respectively. The large core ECPs, which include the $f$-electrons in the core, can be used for geometry optimizations of lanthanide complexes, because it was shown that the $f$-electrons do not contribute significantly in the lanthanide–ligand bonding.[14–16] Some molecular mechanics investigations have reported that the ligand–ligand interaction is dominating the geometries of lanthanide complexes.[16,123,124] Maron & Eisenstein[14] have evaluated geometrical parameters with small as well as large core ECPs and concluded that the large core ECPs can safely be used and that DFT should be preferred over MP2.

Different symmetries of the coordination polyhedra were generated, mainly based on a calculation of the coordinates in a spherical coordinate system and back transformation to Cartesian coordinates. The quadratic antiprisms were generated by rotating the four Ln–O bonds of the optimized cubes using[125]

$$R_{\hat{n}}(\alpha)\,\vec{v}$$

with the rotation matrix[125]

$$R_{\hat{n}}(\alpha) = \begin{pmatrix} n_1^2(1-\cos\alpha)+\cos\alpha & n_1n_2(1-\cos\alpha)-n_3\sin\alpha & n_1n_3(1-\cos\alpha)+n_2\sin\alpha \\ n_2n_1(1-\cos\alpha)+n_3\sin\alpha & n_2^2(1-\cos\alpha)+\cos\alpha & n_2n_3(1-\cos\alpha)-n_1\sin\alpha \\ n_3n_1(1-\cos\alpha)-n_2\sin\alpha & n_3n_2(1-\cos\alpha)+n_1\sin\alpha & n_3^2(1-\cos\alpha)+\cos\alpha \end{pmatrix}$$

where $\hat{n} = (n_1, n_2, n_3)^T$ denotes the unit vector of the rotational axis and $\alpha$ is the rotation angle. This corresponds to a rotation about an arbitrary axis passing through the origin. Other geometries were also created by a rotation along the Ln–O bonds using this rotation matrix.
$C_1$ geometries often required a partial optimization in internal coordinates with some variables held constant, because otherwise the optimization yields again a higher symmetric structure, especially of the oxygens.

### 6.1.2. Calculation of states

Kramers Restricted Configuration Interaction (KRCI) calculations of $Nd^{3+}$ using the four-component Dirac-Coulomb (DC) Hamiltonian (keyword DOSSSS) and two-component X2C Hamiltonian[126] together with Dyall's triple-zeta core-valence basis set cv3z[75] were performed with the DIRAC[61] program.
Calculations with increasing speed of light were carried out, from $c = 137$ a.u. to $1 \cdot 10^6$ a.u., in order to simulate the non-relativistic limit and to assign the states accordingly. The four-component Hamiltonian exhibited convergence problems for $c > 137$ a.u. due to "intruding positron states", i.e. large negative-energy states that were occupied, therefore the two-component Hamiltonian was chosen for these calculations. Calculations with the General Open Shell CI Program (GOSCIP) of DIRAC, i.e. complete open-shell CI[127] (COSCI), provided information about the degeneracies and symmetry classifications of the states thus facilitating the assignment of the states. Table 6.1 gives the used partitioning of the space into generalized active (GA) spaces in $Nd^{3+}$ KRCI calculations, corresponding to the correlation of 29 electrons in 29 orbitals. Other partitionings were also tested, particularly the inclusion of more virtual orbitals, but these calculations did not converge and needed a large computational effort. The results of the $Eu^{3+}$-water complexes are compared to the findings of Holzer[128], who computed $Eu^{3+}$ states with KRCI and correlated 32 electrons in 29 orbitals (Figure 6.11).

The energy levels of the $[Nd\ (H_2O)_6]^{3+}$ $T_h$ ($D_{2h}$) structure (Nd-6w-Th) were determined with Dirac-Hartree-Fock calculations with the two-component X2C4 Hamiltonian[126], triple-zeta basis set TZVP[121,122] for the water molecules and cv3z[75] for $Nd^{3+}$.
Calculations with increasing speed of light of Nd-6w-Th were also performed, based on the previous work by C. Holzer. However they are not presented here as the state assignment was beyond the scope of this thesis.

Table 6.1.: Generalized Active Spaces of $Nd^{3+}$ KRCI calculations: number of *gerade* (left) and *ungerade* functions (right), minimum (left) and maximum electron occupation (right) after this GAS and function types in the GAS.

| GAS | GAS Kramers pairs | | Occupation | | Orbital shells |
|---|---|---|---|---|---|
| | $g$ | $u$ | min. | max. | |
| I | 7 | 6 | 24 | 26 | $4s$, $4p$, $4d$, $5s$, $5p$ |
| II | 0 | 7 | 27 | 29 | $4f$ |
| III | 6 | 3 | 29 | 29 | $5d$, $6s$, $6p$ |

State average spin-orbit coupled (SOC)[73,74] CASSCF calculations of the lanthanide water complexes were conducted with the ORCA program package[72] using the second-order scalar-relativistic DKH method and triple-zeta basis set TZVP-DKH[129–131] for all the elements, i.e. H, O and Nd or Eu. DFT orbitals from calculations at the DKH B3LYP[87,89,90] TZVP-DKH[129–131] level of theory were used as starting orbitals for the SOC-CASSCF calculations. In the case of the $Eu^{3+}$ complexes, pure $f$-orbitals were obtained in a straightforward manner. However, more problems were encountered in the case of the $Nd^{3+}$ structures, where several SOC-CASSCF calculations and orbital rotations were necessary to obtain pure $f$-orbitals in the desired order.* Moreover, convergence problems arose for $Nd^{3+}$. For the $Eu^{3+}$ structures two SOC-CASSCF calculations were performed. None of structures with nine water molecules converged following this procedure.

## 6.2. Symmetry

Molecular symmetry was exploited in all the calculations, except for the optimizations of the $C_1$ structures. However, the programs only support Abelian groups. Table 6.2 gives the subduction from $O(3)$ to some Abelian subgroups. It can be seen how, for example, the F term of $Eu^{3+}$ splits into the irreps $1\ A_g \oplus 2\ B_{1g} \oplus 2\ B_{2g} \oplus 2\ B_{3g}$ in the subgroup $D_{2h}$. Basically the (Abelian) groups $D_{2h}$ and $C_1$ were used for the calculations.

*Despite the usage of the "forbs" keyword.

Table 6.2.: Subduction from $O(3)$.[93]

| L = | O(3) → | $D_{2h}$ ♣ | L = | O(3) → | $C_2$ |
|---|---|---|---|---|---|
| 0 | S | $1\ A_g$ | 0 | S | $1\ A$ |
| 1 | P | $1\ B_{1u} \oplus 1\ B_{2u} \oplus 1\ B_{3u}$ | 1 | P | $1\ A \oplus 2\ B$ |
| 2 | D | $2\ A_g \oplus 1\ B_{1g} \oplus 1\ B_{2g} \oplus 1\ B_{3g}$ | 2 | D | $3\ A \oplus 2\ B$ |
| 3 | F | $1\ A_u \oplus 2\ B_{1u} \oplus 2\ B_{2u} \oplus 2\ B_{3u}$ | 3 | F | $3\ A \oplus 4\ B$ |
| 4 | G | $3\ A_g \oplus 2\ B_{1g} \oplus 2\ B_{2g} \oplus 2\ B_{3g}$ | 4 | G | $5\ A \oplus 4\ B$ |
| 5 | H | $2\ A_u \oplus 3\ B_{1u} \oplus 3\ B_{2u} \oplus 3\ B_{3u}$ | 5 | H | $5\ A \oplus 6\ B$ |
| 6 | I | $4\ A_g \oplus 3\ B_{1g} \oplus 3\ B_{2g} \oplus 3\ B_{3g}$ | 6 | I | $7\ A \oplus 6\ B$ |

| L = | O(3) → | $D_2$ | L = | O(3) → | $C_s$ |
|---|---|---|---|---|---|
| 0 | S | $1\ A$ | 0 | S | $1\ A'$ |
| 1 | P | $1\ B_1 \oplus 1\ B_2 \oplus 1\ B_3$ | 1 | P | $2\ A' \oplus 1\ A''$ |
| 2 | D | $2\ A \oplus B_1 \oplus B_2 \oplus B_3$ | 2 | D | $3\ A' \oplus 2\ A''$ |
| 3 | F | $A \oplus B_1 \oplus B_2 \oplus B_3$ | 3 | F | $4\ A' \oplus 3\ A''$ |
| 4 | G | $3\ A \oplus 2\ B_1 \oplus 2\ B_2 \oplus 2\ B_3$ | 4 | G | $5\ A' \oplus 4\ A''$ |
| 5 | H | $2\ A \oplus 3\ B_1 \oplus 3\ B_2 \oplus 3\ B_3$ | 5 | H | $6\ A' \oplus 5\ A''$ |
| 6 | I | $4\ A \oplus 3\ B_1 \oplus 3\ B_2 \oplus 3\ B_3$ | 6 | I | $7\ A' \oplus 6\ A''$ |

| L = | O(3) → | $C_{2v}$ |
|---|---|---|
| 0 | S | $1\ A_1$ |
| 1 | P | $1\ A_1 \oplus 1\ B_1 \oplus 1\ B_2$ |
| 2 | D | $2\ A_1 \oplus 1\ A_2 \oplus 1\ B_1 \oplus 1\ B_2$ |
| 3 | F | $1\ A_2 \oplus 2\ A_1 \oplus 2\ B_1 \oplus 2\ B_2$ |
| 4 | G | $3\ A_1 \oplus 2\ A_2 \oplus 2\ B_1 \oplus 2\ B_2$ |
| 5 | H | $2\ A_2 \oplus 3\ A_1 \oplus 3\ B_1 \oplus 3\ B_2$ |
| 6 | I | $4\ A_1 \oplus 3\ A_2 \oplus 3\ B_1 \oplus 3\ B_2$ |

♣ Group with inversion centre: $Eu^{3+}$ has *gerade* states ($g$) and $Nd^{3+}$ *ungerade* states ($u$).

Table 6.3.: Subduction from $O(3)^o$ into fermion corepresentations for $Nd^{3+}$.[93]

| J = | O(3) → | $D_{2h}$ ♣ |
|---|---|---|
| $\frac{1}{2}$ | | 1 $E_{1/2,u}$ |
| $\frac{3}{2}$ | | 2 $E_{1/2,u}$ |
| $\frac{5}{2}$ | | 3 $E_{1/2,u}$ |
| $\frac{7}{2}$ | | 4 $E_{1/2,u}$ |
| $\frac{9}{2}$ | | 5 $E_{1/2,u}$ |
| $\frac{11}{2}$ | | 6 $E_{1/2,u}$ |
| $\frac{13}{2}$ | | 7 $E_{1/2,u}$ |
| $\frac{15}{2}$ | | 8 $E_{1/2,u}$ |

♣ Group with inversion centre: only *ungerade* states ($u$) shown.

## 6.3. Computational results of $Nd^{3+}$

### 6.3.1. Structures and energetics

The relative energies and point groups of the optimized $Nd^{3+}$-water complexes in different symmetries, $[Nd(H_2O)_x]^{3+}$ ($x = 3, 4, 6, 8, 9$), are summarized in Table 6.4. The highly symmetric geometries correspond in most cases to saddle points yielding imaginary frequencies, which are indicated with the superscript $*(i)$, where $i$ denotes the number of imaginary frequencies. The only exception is the $T_h$ structure, i.e. the octahedron of the oxygens, which is a highly symmetric minimum structure. However, the aim of this thesis is to determine the dependence of the intensity of the hypersensitive transition on the symmetry. Therefore not only the lower symmetric minimum structures are of interest, but also some structures of high symmetry. The $C_1$ geometries have the lowest relative energies within the complexes with eight and nine water molecules, which are common coordination numbers of lanthanides.[1,12,132] The coordination number of $Nd^{3+}$ in water was found to be nine.[1,133] The corresponding coordination polyhedron is a triaugmented triangular prism ($D_{3h}$). The actual used structure for the further correlated multi-reference calculations, Nd-6w-Th, is indicated in bold. The other structures with six, eight and nine water molecules exhibited

convergence problems.

Table 6.4.: Relative energies $E_{rel}$, point group and structural characterization of optimized $[Nd(H_2O)_x]^{3+}$ complexes (B3LYP ECP49MWB TZVP), * imaginary frequencies (number).

| **Name** | **Number $H_2O$** | **$E_{rel}$ (kJ mol$^{-1}$)** | **Point group** (largest Abelian subgroup) | **Coordination polyhedron of O** |
|---|---|---|---|---|
| Nd-3w-D3h-1 | 3 | 0.00 | $D_{3h}$ ($C_{2v}$)[a] | trigonal planar |
| Nd-3w-D3 | 3 | 0.002625 | $D_3$ ($C_2$) | trigonal planar |
| Nd-3w-D3h-2 | 3 | 11.56 *(4) | $D_{3h}$ ($C_{2v}$) | trigonal planar |
| Nd-4w-D2h | 4 | / *(3) | $D_{2h}$ | square planar |
| Nd-6w-Cs | 6 | 0.00 | $C_s$ | octahedron |
| Nd-6w-C1-1 | 6 | 0.005251 | $C_1$ | octahedron |
| Nd-6w-C1-2 | 6 | 7.007 | $C_1$ | “twisted” oxygens |
| **Nd-6w-Th** | **6** | **0.1103** | **$T_h$ ($D_{2h}$)** | **octahedron** |
| Nd-6w-Td | 6 | 24.42 *(6) | $T_d$ ($D_2$) | octahedron |
| Nd-8w-C1-1 | 8 | 0.00 | $C_1$ | quadratic antiprism |
| Nd-8w-C1-2 | 8 | 0.01838 | $C_1$ | quadratic antiprism |
| Nd-8w-C1-3 | 8 | 0.05776 | $C_1$ | quadratic antiprism |
| Nd-8w-C1-4 | 8 | 16.90 | $C_1$ | cube |
| Nd-8w-C2 | 8 | 11.15 *(1) | $C_2$ | quadratic antiprism |
| Nd-8w-C4 | 8 | 16.69 *(1) | $C_4$ ($C_2$) | “twisted” oxygens |
| Nd-8w-D2d | 8 | 17.21 *(1) | $D_{2d}$ ($C_{2v}$) | cube (distorted) |
| Nd-8w-D4d | 8 | 39.15 *(8) | $D_{4d}$ ($C_{2v}$) | quadratic antiprism |
| Nd-8w-D4h-1 | 8 | 96.18 *(10) | $D_{4h}$ ($D_{2h}$) | cube |
| Nd-8w-D4h-2 | 8 | 97.14 *(10) | $D_{4h}$ ($D_{2h}$) | cube |
| Nd-9w-C1-1 | 9 | 0.00 | $C_1$ | |
| Nd-9w-C1-2 | 9 | 0.2494 | $C_1$ | triaugmented |
| Nd-9w-D3h-1 | 9 | 22.71 *(4) | $D_{3h}$ ($C_{2v}$) | triangular |
| Nd-9w-D3h-2 | 9 | 31.32 *(6) | $D_{3h}$ ($C_{2v}$) | prism |

[a] In frequency calculation output: $C_{3h}$ ($C_s$, $C_1$).

Figures 6.1 and 6.2 show the structures of Nd-3w-D3h-1 and Nd-6w-Th. For other $Nd^{3+}$-

water complexes see chapter 6.4.1 ($Eu^{3+}$-water complexes) on page 122 as the geometries are nearly the same for the $Nd^{3+}$-water complexes and $Eu^{3+}$-water complexes, except for the bond lengths.

### 6.3.2. States of $Nd^{3+}$

The $^{2S+1}L_J$ states of neodymium(III) are very dense in the region above the $^4I$ states, which led to overlapping bands in the experimental spectra. In the case of quantum chemical computations it complicates the assignment of the states. This problem is even more pronounced in the water complexes than in the free ion, because of the additional crystal field splitting. Therefore KRCI calculations of the free ion, $Nd^{3+}$, were performed as a starting point. However, additional calculations with increasing speed of light were necessary for a definite assignment of the states. If $c \rightarrow \infty$, the non-relativistic limit is reached which corresponds to *LS*-coupled $^{2S+1}L$ states without spin-orbit coupling, i.e. all terms arising from the same *LS*-coupled state can be identified. The additional information of the calculations is the *J* value. Figures 6.3 and 6.4 present the results of these calculations, i.e. the effect of spin-orbit coupling and assignment of the computed $Nd^{3+}$ $^{2S+1}L_J$ states. The energies of these calculations with increasing speed of light can be found in the Appendix. Constant values for the energies of the *LS*-coupled $^{2S+1}L$ states are reached from a value of $c = 1 \cdot 10^5$ au. The calculations were performed until $c = 1 \cdot 10^6$ au.

The results of the KRCI calculations of the $Nd^{3+}$ ion with two-component X2C Hamiltonian ($Nd^{3+}$ 1) and the four-component DC Hamiltonian ($Nd^{3+}$ 2) are compared to the published experimental values for $NdF_3$ by Carnall *et al.*[28] in Figure 6.5. The results of the SOC-CASSCF (Nd-6w 1), i.e. the first 88 crystal field levels, and of the Dirac-Hartree-Fock calculation (Nd-6w 2), i.e. the first 120 crystal field levels, of Nd-6w-Th are also shown in Figure 6.5, however the band assignment was beyond the scope of this thesis. It should

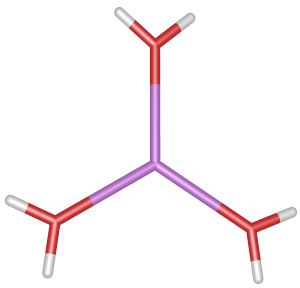

Figure 6.1.: $[Nd(H_2O)_3]^{3+}$, $D_{3h}$ ($C_{2v}$) (B3LYP ECP49MWB TZVP).

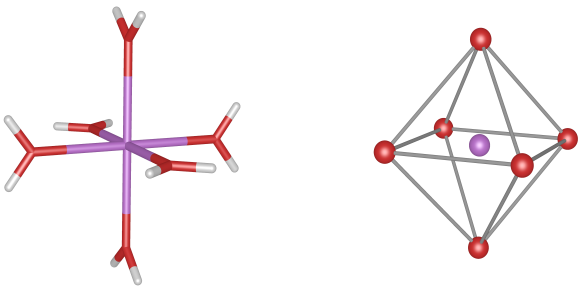

Figure 6.2.: **Nd-6w-Th**: $[Nd\ (H_2O)_6]^{3+}$, $T_h$ ($D_{2h}$) (B3LYP ECP49MWB TZVP).

be noted that the highly symmetric $T_h$ geometry yielded zero oscillator strengths for all transitions in the SOC-CASSCF calculation, owing to the centrosymmetry of the system.

The four-component calculations ($Nd^{3+}$ 2) give slightly better results than the two-component calculations ($Nd^{3+}$ 1), i.e. the computed energies are in better agreement with the experiment, e.g. with $Nd^{3+}$ doped $LaF_3$ ("$NdF_3$").[28] It should be noted that only states with $J \geq 5/2$ were considered in the former case. The experimental values correspond to the centres of gravity of the individual Stark levels of $Nd^{3+}$ doped $LaF_3$ and are labelled with the free ion term $^{2S+1}L_J$ with the largest contribution to the eigenstate.[28] These average energies differ of course from the computed *free ion* states, e.g. the (experimental) average energy of the $^4I_{9/2}$ term is 235 $cm^{-1}$, while the $^4I_{9/2}$ state is the degenerate ground state of the free ion corresponding to 0 $cm^{-1}$ in the absence of a crystal field. In general, the computed $^4I$ states are in comparatively good agreement with the literature values for $NdF_3$ with a difference in the order of 50 - 100 $cm^{-1}$, while the states of higher energy deviate more distinctly from the experimental values, not only in terms of energy, but also in the sequence of the states (see Table 6.5). The hypersensitive transition $^4G_{5/2} \leftarrow {}^4I_{9/2}$, for example, has an experimental transition energy of 17,193 $cm^{-1}$, while the calculated values are 20,934 $cm^{-1}$ ($Nd^{3+}$ 1) and 20,931 $cm^{-1}$ ($Nd^{3+}$ 2), respectively, i.e. the deviation lies in the order of $10^3$ $cm^{-1}$. The sequence of the $^4F_{5/2}$ and $^2H_{9/2}$, of the $^4G_{5/2}$ and $^2G_{7/2}$ and of the $^4G_{9/2}$ and $^2K_{15/2}$ states is reversed in the calculations compared to the experiments.
Only few *ab initio* studies have examined the $f \leftrightarrow f$ transitions of $Nd^{3+}$. Hatanaka & Yabushita[134] have found 21,748 $cm^{-1}$ for the hypersensitive transition of $NdBr_3$ with the multi-reference spin-orbit configuration interaction (MRSOCI) method, which is about 800 $cm^{1-}$ larger than the transition energy found in the relativistic KRCI calculations of $Nd^{3+}$ performed in this thesis.

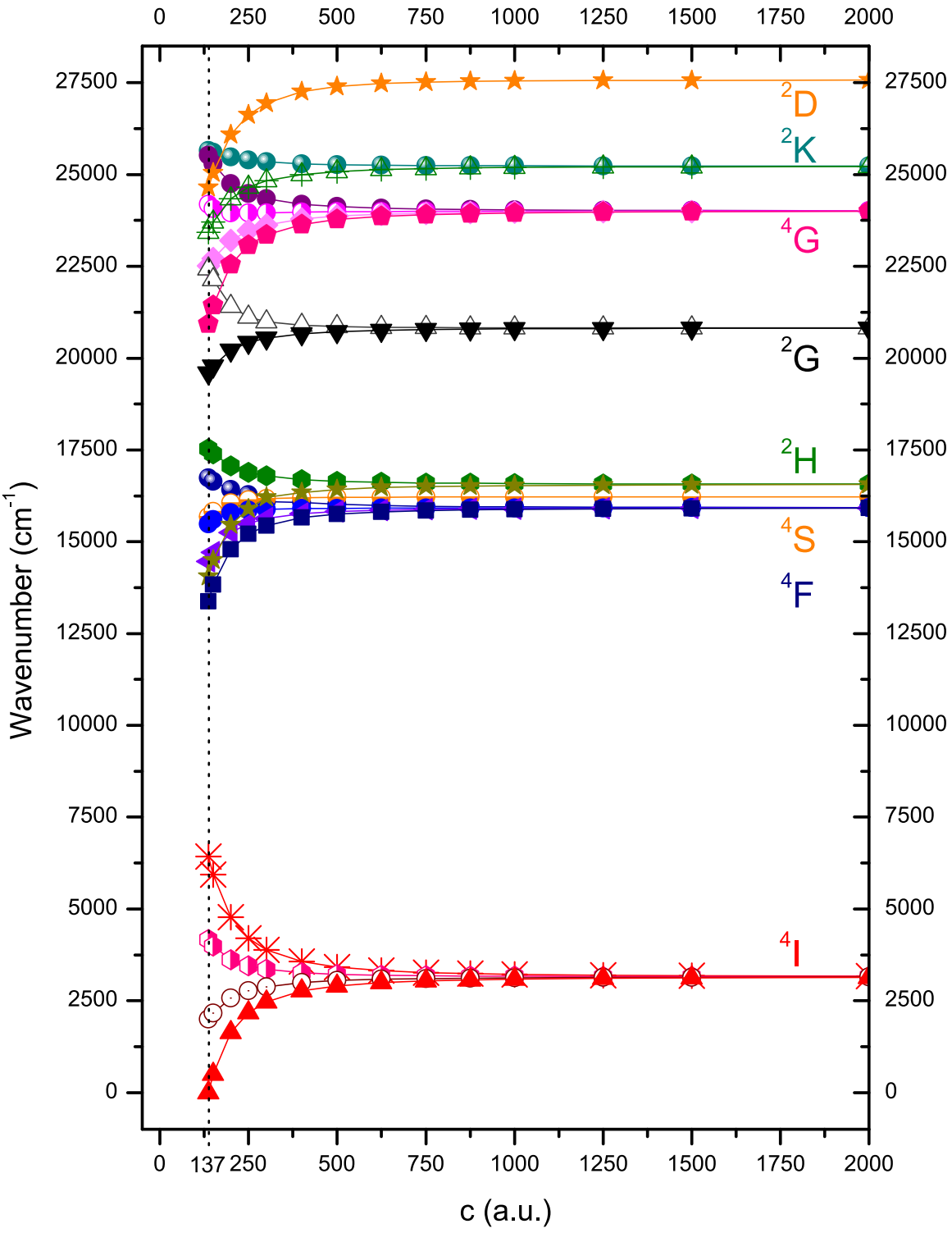


Figure 6.3.: Energy levels of $Nd^{3+}$ (X2C KRCI Dyall cv3z) with increasing speed of light c equivalent to decreasing spin-orbit coupling (all states).

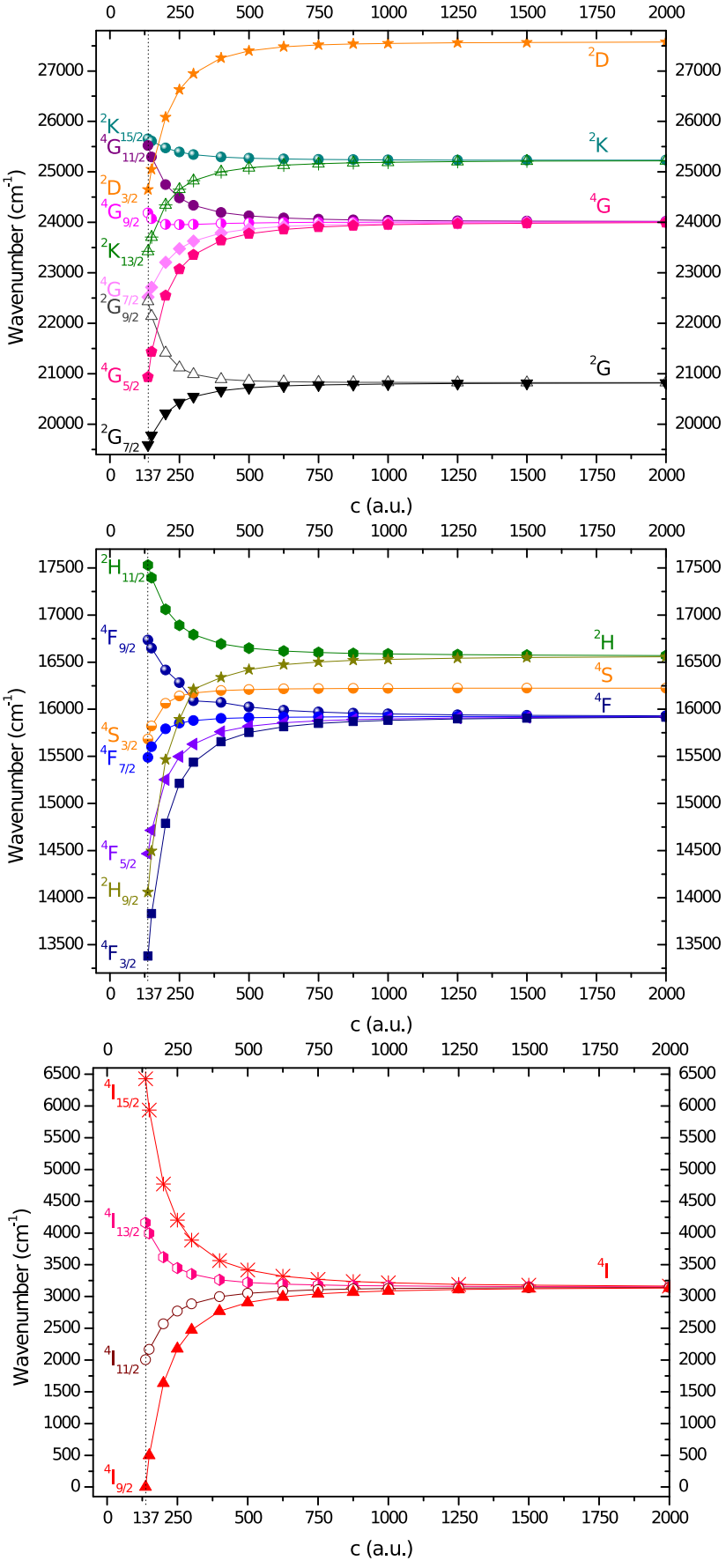




Figure 6.4.: Energy levels of $Nd^{3+}$ (X2C KRCI Dyall cv3z) with increasing speed of light c equivalent to decreasing spin-orbit coupling.

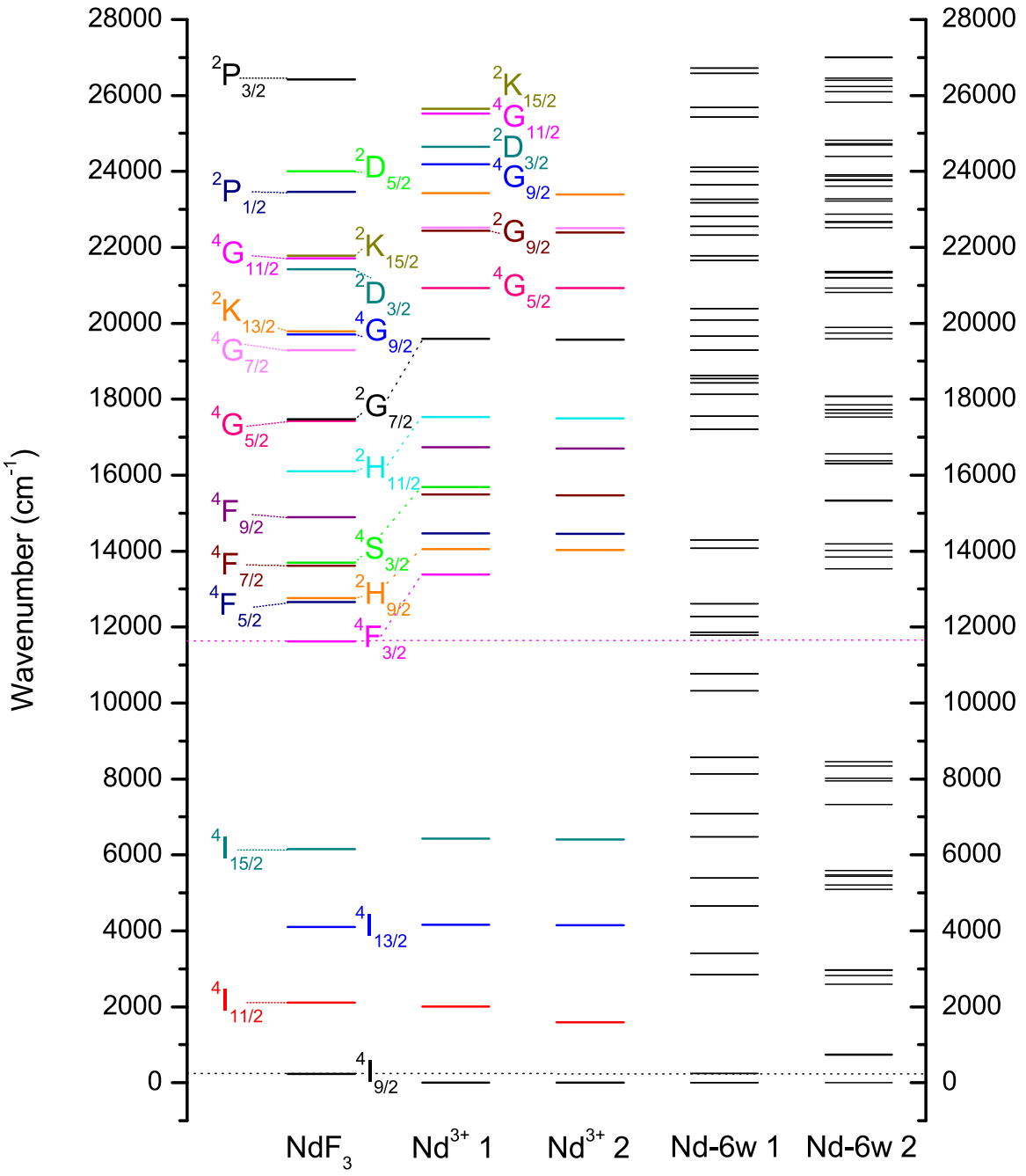


Figure 6.5.: Energy levels of $Nd^{3+}$ and $[Nd(H_2O)_6]^{3+}$ at different levels of theory compared with experimental values of $NdF_3$[28]; **$Nd^{3+}$ 1** = X2C KRCI (29,29) cv3z, **$Nd^{3+}$ 2** = Dirac-Coulomb Hamiltonian KRCI (29,29) cv3z, **Nd-6w 1** = $[Nd(H_2O)_6]^{3+}$ $T_h$ DKH SOC-CASSCF (3,7) TZVP-DKH, **Nd-6w 2** = $[Nd(H_2O)_6]^{3+}$ $T_h$ X2C4 DHF TZVP cv3z.

Table 6.5.: Computed energies of the $Nd^{3+}$ free ion states compared to experimental values of $NdF_3$[28] and computed values of $NdBr_3$[134]; $Nd^{3+}$ 1 (2c) at X2C KRCI (29,29) cv3z level of theory, $Nd^{3+}$ 2 (4c) Dirac-Coulomb Hamiltonian KRCI (29,29) cv3z level of theory.

| **States** | **Wavenumber ($cm^{-1}$)** | | |
|---|---|---|---|
| | $NdF_3$[28] | $Nd^{3+}$ 1 (2c) | $Nd^{3+}$ 2 (4c) |
| $^4I_{9/2}$ | 235 | 0 | 0 |
| $^4I_{11/2}$ | 2114 | 2004 | 1591 |
| $^4I_{13/2}$ | 4098 | 4163 | 4144 |
| $^4I_{15/2}$ | 6148 | 6430 | 6402 |
| $^4F_{3/2}$ | 11621 | 13379 | |
| $^4F_{5/2}$ | 12660 | 14467 | 14035 |
| $^2H_{9/2}$ | 12768 | 14058 | 14454 |
| $^4F_{7/2}$ | 13619 | 15487 | 15467 |
| $^4S_{3/2}$ | 13691 | 15684 | |
| $^4F_{9/2}$ | 14899 | 16734 | 16704 |
| $^2H_{11/2}$ | 16105 | 17530 | 17495 |
| $^4G_{5/2}$ | 17428 | 20934 | 20931 |
| $^2G_{7/2}$ | 17469 | 19591 | 19565 |
| $^2G_{9/2}$ | | 22433 | 22389 |
| $^4G_{7/2}$ | 19293 | 22519 | 22502 |
| $^4G_{9/2}$ | 19709 | 24185 | |
| $^2K_{13/2}$ | 19785 | 23427 | 23397 |
| $^2D_{3/2}$ | 21425 | 24646 | |
| $^4G_{11/2}$ | 21714 | 25521 | |
| $^2K_{15/2}$ | 21780 | 25653 | |
| $^2P_{1/2}$ | 23458 | | |
| $^2D_{5/2}$ | 24004 | | |
| $^2P_{3/2}$ | 26424 | | |

| **Transition** | **Wavenumber ($cm^{-1}$)** | | | |
|---|---|---|---|---|
| | $NdF_3$[28] | $Nd^{3+}$ 1 (2c) | $Nd^{3+}$ 2 (4c) | $NdBr_3$[134] |
| $^4G_{5/2} \leftarrow {}^4I_{9/2}$ | 17193 | 20934 | 20931 | 21748 |

To sum up, the assignment of the $Nd^{3+}$ states of higher energy is difficult due to the high density of states in the region above the $^4I$ manifold, but it was possible using calculations with increasing speed of light. The four-component KRCI calculations of $Nd^{3+}$ yielded the best agreement with the experimental energy levels, however the states of higher energy still differ significantly from the experimental results.

## 6.4. Computational results of $Eu^{3+}$

### 6.4.1. Structures and energetics

The relative energies and point groups of the optimized $Eu^{3+}$-water complexes are presented in Table 6.6. The same notation is used as for $Nd^{3+}$, i.e. imaginary frequencies are indicated with the superscript $*(i)$, where $i$ denotes the number of imaginary frequencies. The results are in line with the findings of neodymium. The highly symmetric structures exhibit in most cases high relative energies and imaginary frequencies, especially the cubic $D_{4h}$ structures of $[Eu\ (H_2O)_8]^{3+}$, while the lower symmetric geometries correspond to minima. The only exception is Eu-6w-Th, which has the lowest energy of the optimized $[Eu(H_2O)_6]^{3+}$ complexes despite the high symmetry (octahedron of oxygens, $T_h$). The actual used structures for the further correlated multi-reference calculations are marked in bold. The coordination number of $Eu^{3+}$ in water is nine,[1,133,135] however none of the multi-reference calculations of the $[Eu(H_2O)_9]^{3+}$ complexes converged.
Figures 6.6, 6.7 and 6.8 show selected structures of the $[Eu(H_2O)_x]^{3+}$ complexes.

### 6.4.2. States of $Eu^{3+}$

The band assignment in the case of the $Eu^{3+}$ water complexes is straightforward because of the greater spacing between the states. As a consequence, no problems due to intervening levels or wrong sequence of the states are observed, in contrast to $Nd^{3+}$. C. Holzer[128] has already investigated the free ion states of $Eu^{3+}$ with relativistic KRCI calculations and various GA spaces, as shown in Figure 6.11.

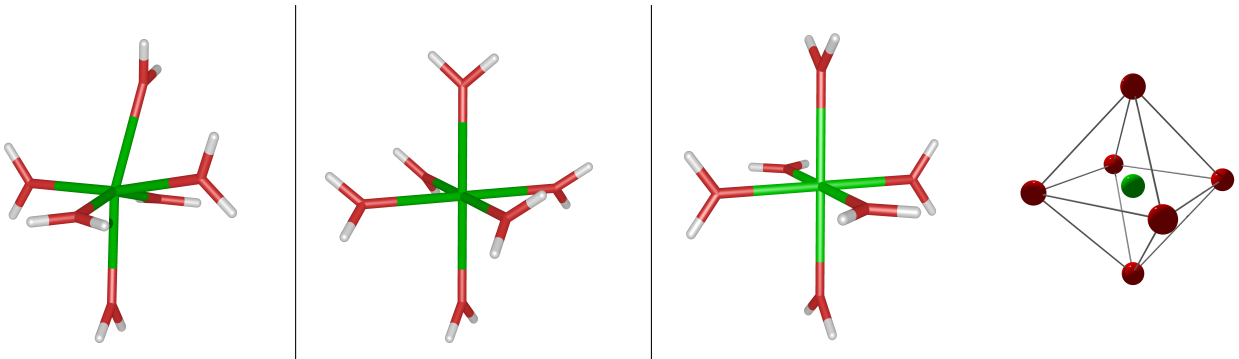

(a) $C_1$: **Eu-6w-C1-2** (b) $T_d$ ($D_2$) (c) $T_h$ ($D_{2h}$): **Eu-6w-Th**

Figure 6.6.: $[Eu\ (H_2O)_6]^{3+}$ (B3LYP ECP52MWB TZVP).

Table 6.6.: Relative energies $E_{rel}$, point group and structural characterization of optimized $[Eu(H_2O)_x]^{3+}$ complexes (B3LYP ECP52MWB TZVP), * imaginary frequencies (number).

| **Name** | **Number $H_2O$** | **$E_{rel}$ (kJ mol$^{-1}$)** | **Point group** (largest Abelian subgroup) | **Coordination polyhedron of O** |
|---|---|---|---|---|
| **Eu-6w-Th** | **6** | **0.00** | **$T_h$ ($D_{2h}$)** | **octahedron** |
| Eu-6w-Cs | 6 | 0.1103 | $C_s$ | distorted octahedron |
| **Eu-6w-C1-1** | **6** | **0.1129** | **$C_1$** | **octahedron** |
| **Eu-6w-C1-2** | **6** | **31.13** $*^{(2)}$ | **$C_1$** | **"twisted" oxygens** |
| Eu-6w-Td | 6 | 27.99 $*^{(6)}$ | $T_d$ ($D_2$) | octahedron |
| **Eu-8w-C1-1** | **8** | **0.00** | **$C_1$** | **quadratic antiprism** |
| Eu-8w-C1-2 | 8 | 0.005251 | $C_1$ | quadratic antiprism |
| Eu-8w-C1-3 | 8 | 19.18 | $C_1$ | "twisted" oxygens |
| Eu-8w-C2 | 8 | 11.91 $*^{(1)}$ | $C_2$ | dist. quadratic antiprism |
| Eu-8w-C4 | 8 | 18.52 $*^{(1)}$ | $C_4$ ($C_2$) | "twisted" oxygens |
| Eu-8w-D2d | 8 | 18.53 $*^{(1)}$ | $D_{2d}$ ($C_{2v}$) | distorted cube |
| Eu-8w-S4 | 8 | 19.16 | $S_4$ ($C_2$) | cube |
| Eu-8w-C4v | 8 | 43.28 $*^{(8)}$ | $C_{4v}$ ($C_{2v}$) | quadratic antiprism |
| Eu-8w-D4h-1 | 8 | 107.2 $*^{(10)}$ | $D_{4h}$ ($D_{2h}$) | cube |
| Eu-8w-D4h-2 | 8 | 108.2 $*^{(9)}$ | $D_{4h}$ ($D_{2h}$) | cube |
| Eu-9w-D3-1 | 9 | 0.00 | $D_3$ ($C_2$) | |
| Eu-9w-D3-2 | 9 | 0.04463 | $D_3$ ($C_2$) | triaugmented |
| Eu-9w-C1 | 9 | 0.07614 | $C_1$ | triangular |
| E-9w-D3h | 9 | 23.96 $*^{(4)}$ | $D_{3h}$ ($C_{2v}$) | prism |

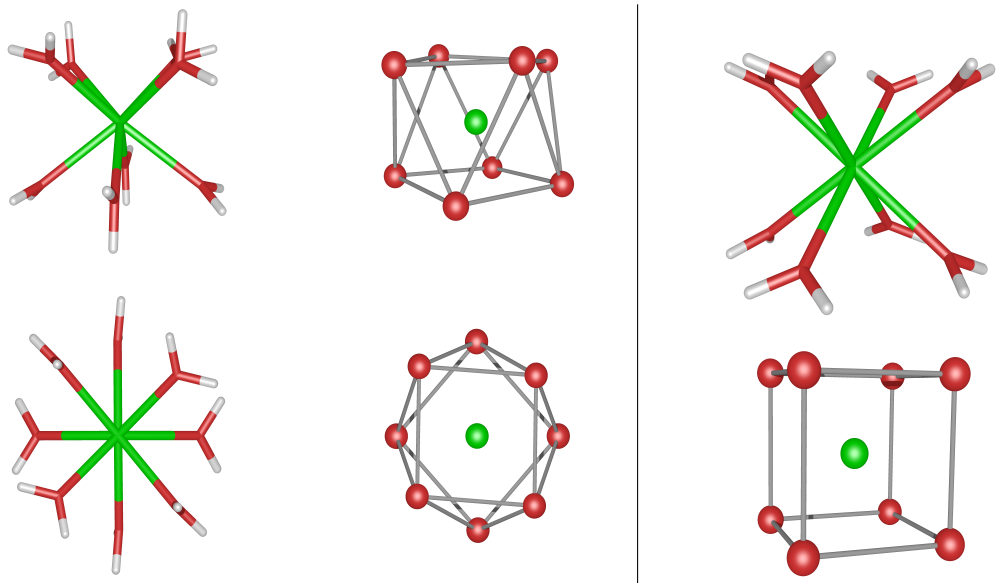

(a) $C_2$ (b) $D_{4h}$ ($D_{2h}$)

Figure 6.7.: $[Eu\ (H_2O)_8]^{3+}$ (B3LYP ECP52MWB TZVP).

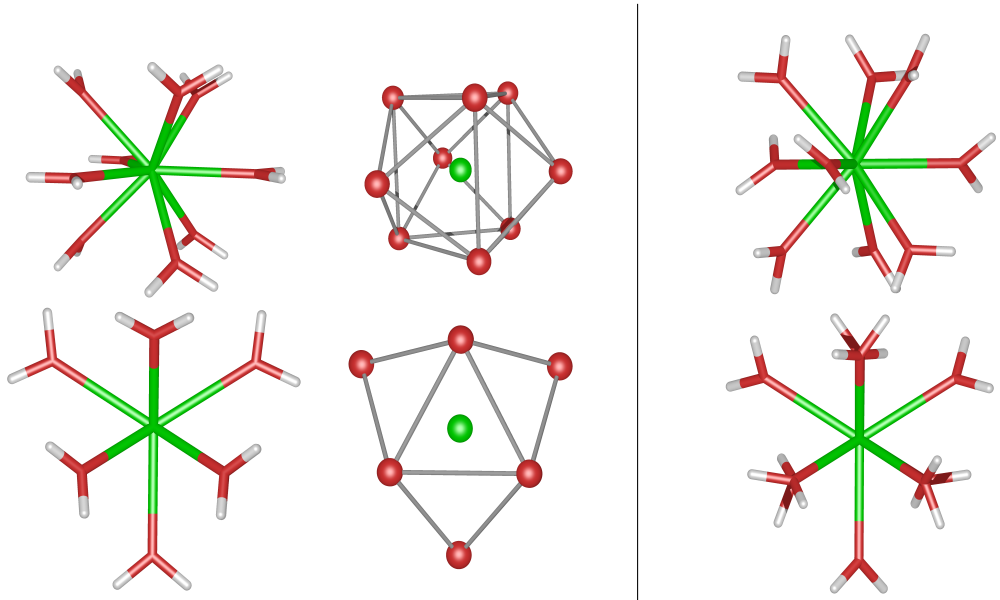

(a) $D_{3h}$ ($C_{2v}$) (b) $D_3$ ($C_2$)

Figure 6.8.: $[Eu\ (H_2O)_9]^{3+}$ (B3LYP ECP52MWB TZVP).

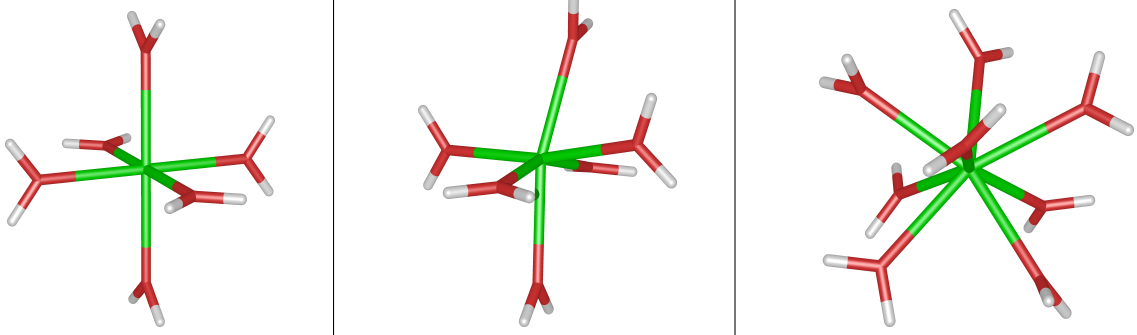

(a) Eu-6w-C1-1 (b) Eu-6w-C1-2 (c) Eu-8w-C1-1

Figure 6.9.: $C_1$ structures of $\left[Eu\,(H_2O)_{6,8}\right]^{3+}$ (B3LYP ECP52MWB TZVP) used for multi-reference calculations.

In this thesis, SOC-CASSCF (6,7) calculations of the water complexes with six (Eu-6w-Th, Eu-6w-C1-1, Eu-6w-C1-2) and eight water molecules (Eu-8w-C1-1) were performed. The computed average energy levels, i.e. the levels after averaging the crystal field states belonging to one $^{2S+1}L_J$ term, are shown in Figure 6.10 and Table 6.7. It can be seen that number of states in the same energy range is much smaller than for neodymium(III). The crystal field splitting of Eu-8w-C1-1 is also shown in Figure 6.10, demonstrating the small influence of the environment on the energy levels of rare earth ions. The computed crystal field splittings of these $Eu^{3+}$-water complexes, i.e. Eu-6w-Th, Eu-6w-C1-1, Eu-6w-C1-2, are listed in the Appendix. It was found to be mostly in the order of $1-10\ cm^{-1}$ and sometimes also $10^{-1}$ and $10^{2}\ cm^{-1}$.
The results of the Eu-6w-C1-1 structure are similar to those of Eu-6w-C1-2 and therefore not shown explicitly in the tables and figures. The deviation in the transition energies lies in the order of $10-10^{2}\ cm^{-1}$, however the oscillator strengths of the Eu-6w-C1-2 structure are significantly larger than those of the Eu-6w-C1-1 geometry, where the oxygens form a nearly perfect octahedron and only the orientation of the hydrogens leads to the $C_1$ "symmetry". It is concluded that the symmetry of the coordination polyhedron formed by the oxygens in the Eu-6w-C1-1 structure is still too high, or to put it another way too close to inversion symmetry, to yield substantial oscillator strengths. The $C_1$ structures used in the calculations are shown in Figure 6.9.

Comparison to the experimental energies of $Eu^{3+}$ doped $LaF_3$ published by Carnall *et al.*[28], or to the aqueous $Eu^{3+}$ solution measured in this thesis, shows the good agreement of the computed $^7F$ states with the literature values. The deviation is in the order of approximately 10 - 100 $cm^{-1}$. The problem is the F–D gap, i.e. the states of higher energy, like in the case of $Nd^{3+}$. The computed $^5D$ states exhibit far too high energies. The largest deviation from

the experimental values is found for the highly symmetric Eu-6w-Th structures.
Eu-6w-C1-2 yields better results for the $^7F_J$ states, while Eu-8w-C1-1 gives a better agreement for the $^5D_J$ states, but is still differing some thousand $cm^{-1}$ from the experimental energies. The best agreement is reached for the $^7F_5$ term, i.e. 3,863 $cm^{-1}$ (Eu-6w-C1-2) instead of 3,849 $cm^{-1}$ ($EuF_3$). Comparison with the $Eu^{3+}$ water solution gives analogous results. The transition energies of the hypersensitive transitions $^5D_2 \leftarrow {}^7F_0$ and $^5D_0 \rightarrow {}^7F_2$ are overestimated by about 3,000 $cm^{-1}$ and 5,000 $cm^{-1}$, respectively.
It remains to be seen if complexes with nine water molecules, i.e. the preferred coordination number in water, yield better results.

The KRCI calculations of $Eu^{3+}$ by Holzer[128] yielded significantly better results for the $^5D$ states, see Figure 6.11. A successive inclusion of electrons and orbitals in the GA spaces resulted in a lowering of the $^5D$ states.[128] However, at the same time the spacing between the $^7F$ states increases leading to a worse description of the lower states than with the SOC-CASSCF calculations of the water complexes performed in this thesis. A next step would be to perform Dirac-Hartree-Fock calculations of $Eu^{3+}$-water complexes with DIRAC and compare these results to the ORCA SOC-CASSCF calculations.

The SOC-CASSCF calculations yield better results for the $^7F_2 \leftarrow {}^7F_0$ transition energy than Hatanaka & Yabushita[134] with their SOCI calculations, however their $^5D_2 \leftarrow {}^7F_0$ excitation energy (23,991 $cm^{-1}$) is in better agreement with the experiment,[134] owing to the poor description of the $^7F$–$^5D$ separation in the SOC-CASSCF calculations. Naleway *et al.*[136] have investigated the energy levels of europium with a SOCI method and their relativistic effective core potential. They found comparatively good results for the splitting of the $^7F$ and $^5D$ manifolds into *SO*-coupled states with an CI expansion with single and double excitations including 5*s*, 5*p* excitations in the singles, while the description of the $^7F$–$^5D$ separation was found to be better without 5*s*, 5*p* excitations.[136]

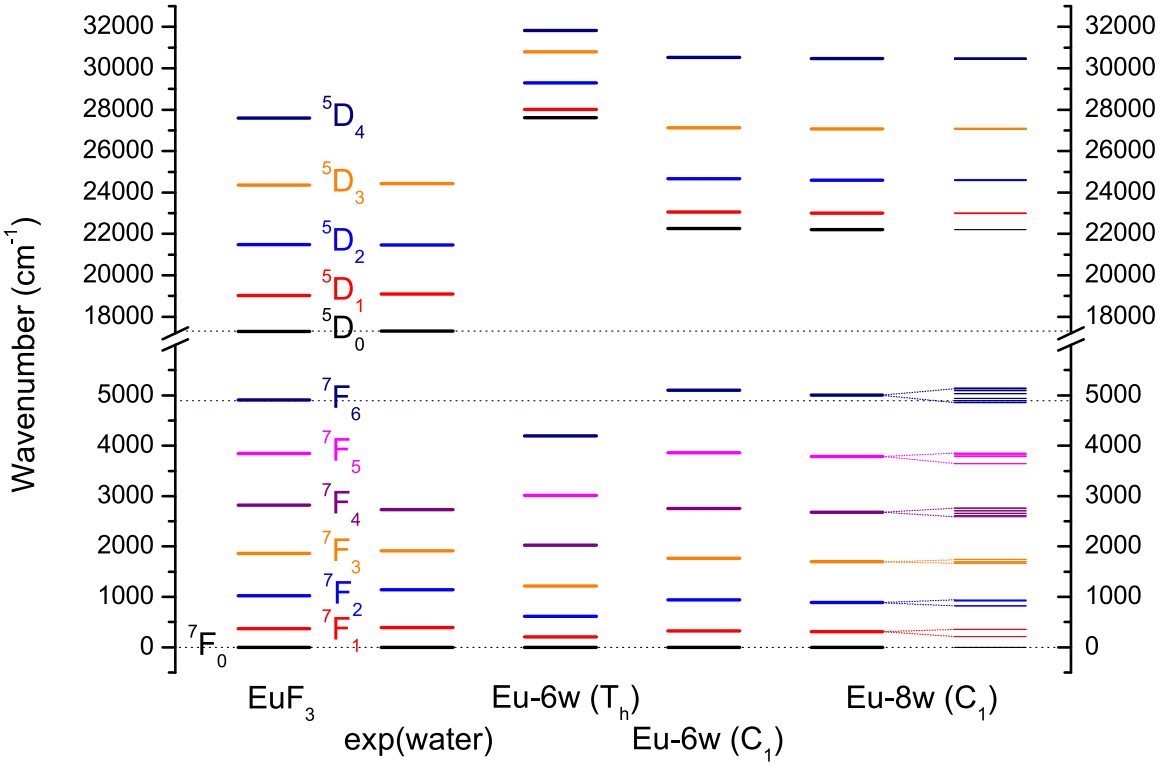


Figure 6.10.: Computed energy levels of $[Eu(H_2O)_{6,8}]^{3+}$ (DKH SOC-CASSCF (6,7) TZVP-DKH) compared with experimental values of $Eu^{3+}$ water solution and $EuF_3$[28]; **Eu-6w ($T_h$)** corresponds to the Eu-6w-Th structure, **Eu-6w ($C_1$)** to the Eu-6w-C1-2 structure and **Eu-8w ($C_1$)** to Eu-8w-C1-1.

Table 6.7.: Computed average energies of the $[Eu(H_2O)_x]^{3+}$ ($x = 6, 8$) states at DKH SOC-CASSCF (6,7) TZVP-DKH level of theory compared to experimental values of $EuF_3$[28] and computed values for $EuBr_3$[134].

| **States** | **Wavenumber ($cm^{-1}$)** | | | |
|---|---|---|---|---|
| | $EuF_3$[28] | Eu-6w-Th | Eu-6w-C1-2 | Eu-8w-C1-1 |
| $^7F_0$ | 0 | 0 | 0 | 0 |
| $^7F_1$ | 372 | 206 | 327 | 307 |
| $^7F_2$ | 1026 | 614 | 938 | 888 |
| $^7F_3$ | 1866 | 1220 | 1763 | 1698 |
| $^7F_4$ | 2823 | 2022 | 2750 | 2676 |
| $^7F_5$ | 3849 | 3015 | 3863 | 3787 |
| $^7F_6$ | 4907 | 4196 | 5099 | 5003 |
| $^5D_0$ | 17293 | 27605 | 22269 | 22207 |
| $^5D_1$ | 19027 | 28007 | 23057 | 22996 |
| $^5D_2$ | 21483 | 29294 | 24663 | 24602 |
| $^5D_3$ | 24355 | 30788 | 27133 | 27074 |
| $^5D_4$ | 27586 | 31820 | 30516 | 30460 |

| **Transitions** | **Wavenumber ($cm^{-1}$)** | | | | |
|---|---|---|---|---|---|
| | $EuF_3$[28] | Eu-6w-Th | Eu-6w-C1-2 | Eu-8w-C1-1 | $EuBr_3$[134] |
| $^7F_2 \leftarrow {}^7F_0$ | 1026 | 614 | 938 | 888 | 1132 |
| $^5D_2 \leftarrow {}^7F_0$ | 21483 | 29294 | 24663 | 24602 | 23991 |
| $^5D_0 \rightarrow {}^7F_2$ | 16267 | 26991 | 21331 | 21319 | |

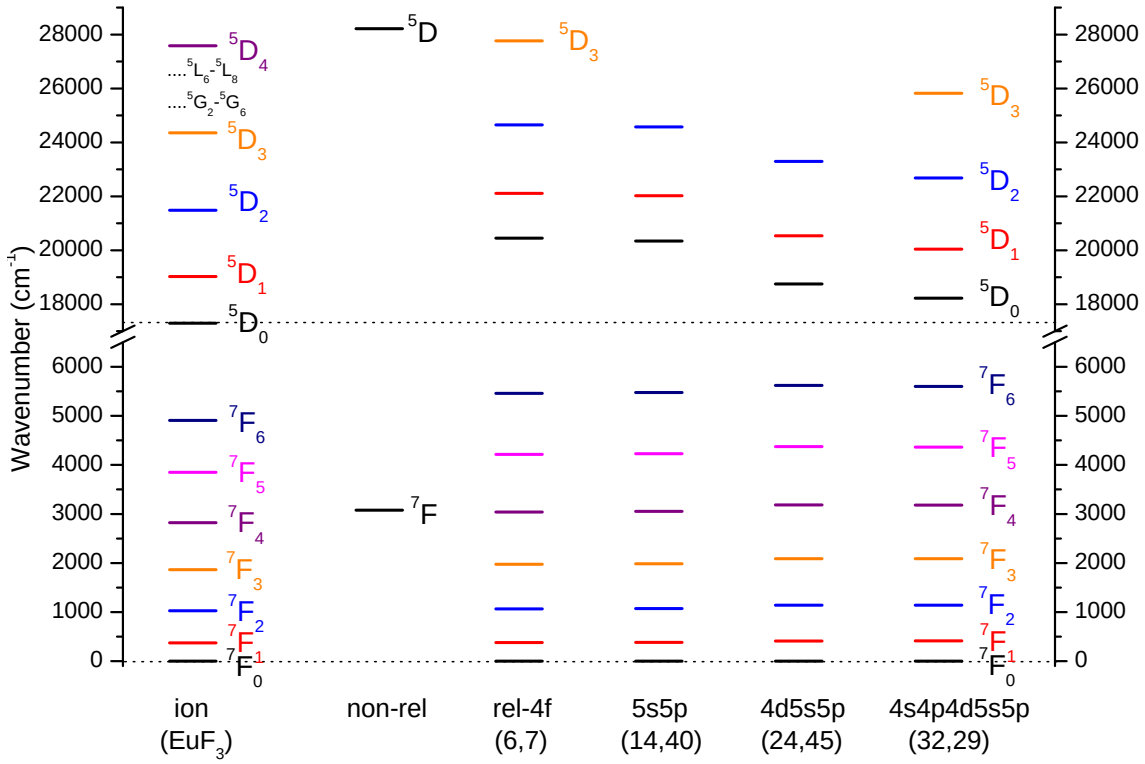


Figure 6.11.: Holzer[128]: Computed energy levels of $Eu^{3+}$ and $[Eu\ (H_2O)_6]^{3+}$ at different levels of theory (Dirac-Coulomb Hamiltonian KRCI cv3z) compared with experimental values of $EuF_3$[28], with permission of C. Holzer to reprint.

Table 6.8.: $f$-orbitals of $Eu^{3+}$ (by C. Holzer) and of the water complexes Eu-6w-Th, Eu-6w-C1-2 and Eu-8w-C1-1 (DKH SOC-CASSCF (6,7) TZVP-DKH).

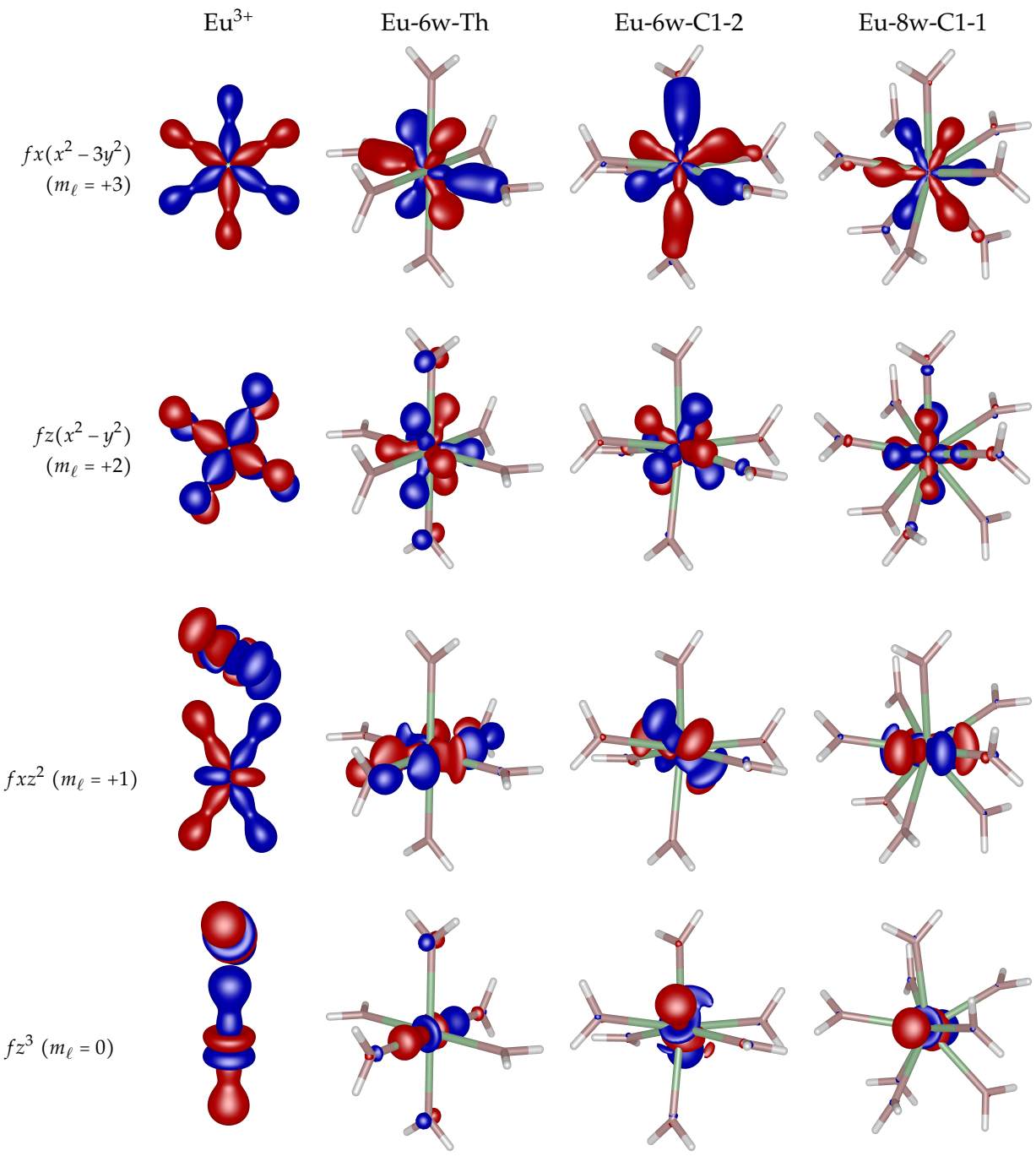

Table 6.8.: $f$-orbitals of $Eu^{3+}$ (by C. Holzer) and of the water complexes Eu-6w-Th, Eu-6w-C1-2 and Eu-8w-C1-1 (DKH SOC-CASSCF (6,7) TZVP-DKH).

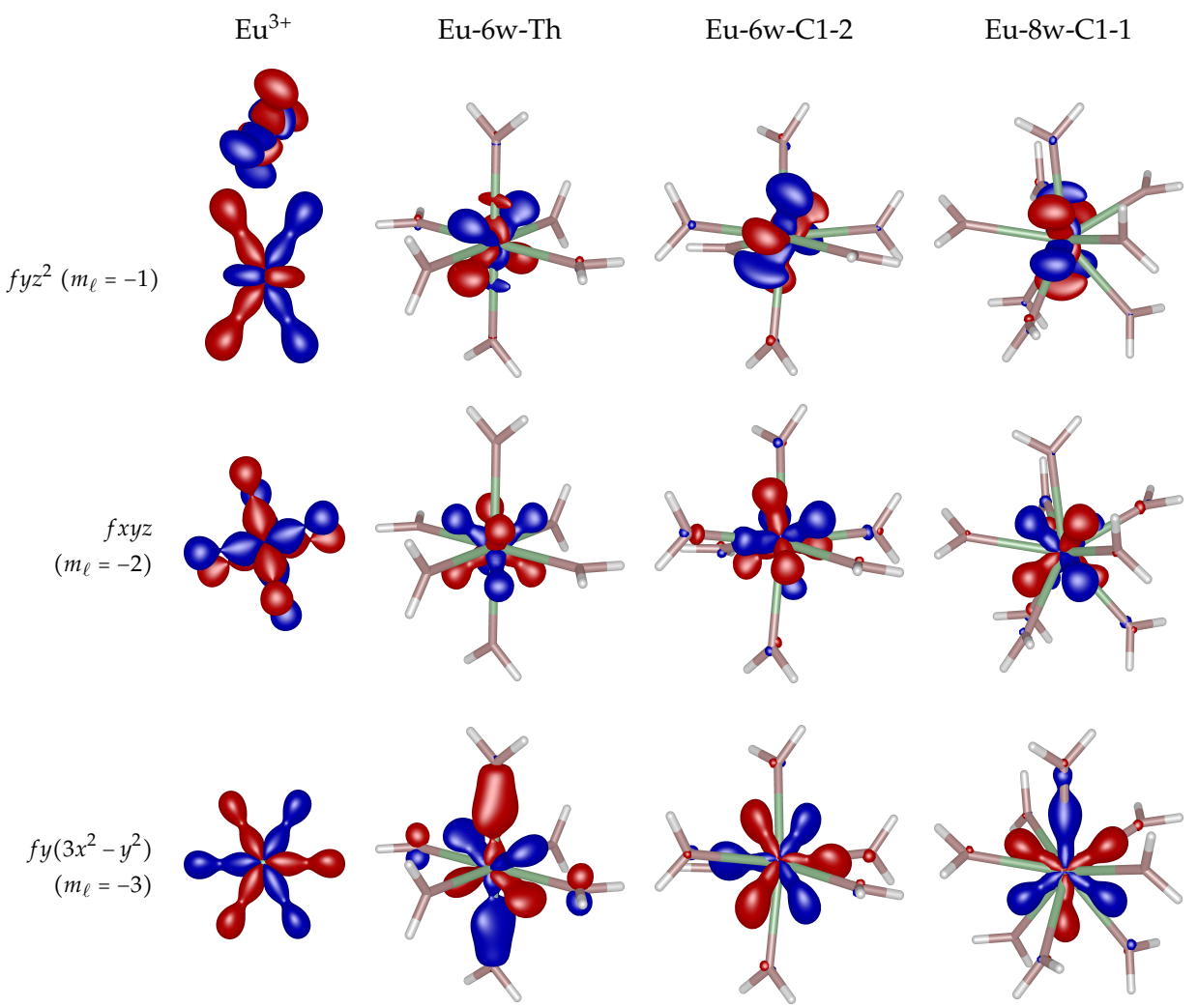


Figure 6.8 shows the $f$-orbitals of the $Eu^{3+}$-water complexes and compares them to the orbitals of the free ion, $Eu^{3+}$, calculated at the same levels of theory, i.e. DKH SOC-CASSCF (6,7) TZVP-DKH, by C. Holzer. No general tendency was observed when going from the free ion to the complex with eight water molecules. The orbitals of $Eu^{3+}$ in the water complexes are generally similar to those of the free ion. In the case of the Eu-6w-Th complex, $p$-orbitals of two opposite oxygens mix to some extent with the $fz(x^2-y^2)$, $fxz^2$ and $fz^3$ orbitals of $Eu^{3+}$, indicating that "purer" $f$-orbitals were obtained for the $C_1$ water complexes, which

could be a reason for the better agreement of the energy levels of the latter geometries. The $fx(x^2-3y^2)$ and $fy(3x^2-y^2)$ orbitals of the $Eu^{3+}$-water complexes expanded along two Eu–O bonds towards the oxygens, especially in the Eu-6w-Th and Eu-6w-C1-2 structures in the former case and in Eu-6w-Th and Eu-8w-C1-1 in the latter case.

### 6.4.3. Spectroscopy and Judd-Ofelt analysis

The computed absorbance spectra (SOC-CASSCF) of the $Eu^{3+}$-water complexes of $C_1$ symmetry, particularly Eu-6w-C1-2 and Eu-8w-C1, yielded non-zero oscillator strengths in the order of $10^{-8}-10^{-9}$, which is smaller than the experimental values ($10^{-6}-10^{-8}$).[41,43,99] None of the calculations, however, has found non-zero oscillator strengths for the hypersensitive transition or other transitions observed in the experimental spectra as only intensities for the $^7F_{J'} \leftarrow {}^7F_J$ and $^5D_4 \leftarrow {}^7F_J$ transitions were obtained. Hatanaka & Yabushita[134] obtained oscillator strengths for the transitions of $EuBr_3$ comparable to the experiment in the order of $10^{-6}-10^{-7}$. This suggests that these SOC-CASSCF calculations are not the method of choice for computing oscillator strengths of the $f \leftrightarrow f$ transitions of $Eu^{3+}$.
The maximum oscillator strengths of a manifold of transitions to the different Stark levels were used to compute Judd-Ofelt parameter $\Omega_\lambda$ ($\lambda = 2,4,6$) for $Eu^{3+}$. Tables 6.9 and 6.10 summarize the results of the Judd-Ofelt calculations based on equation (2.60), see chapter 2.60 on page 23. The Judd-Ofelt program used for the analysis of $Nd^{3+}$ was extended to calculate computed $\Omega_\lambda$ parameters from a fit to computed oscillator strengths of $Eu^{3+}$; these results are listed in Table 6.11.

Similar values for the $\Omega_\lambda$ parameters are obtained using either the average transition energy, $\Delta E_{av}$, or the energy corresponding to the used maximum oscillator strengths, $\Delta E_{f_{max}}$, and either equation (2.60) or a least squares fit with the Judd-Ofelt program. The relation $\Omega_2 < \Omega_4 \approx \Omega_6$ is found, which is on the whole consistent with the published experimental Judd-Ofelt parameters for aqueous solutions of $Eu^{3+}$.[41] However, the values of the computed Judd-Ofelt parameters strongly vary from the experimental values as a consequence of the underestimated computed oscillator strengths.

These results also reflect the generality of the semi-empirical Judd-Ofelt parameters, which contain electric dipole as well as magnetic dipole or electric quadrupole contributions and possibly also vibronic interactions and other mechanisms. A lot of these contributions are not accounted for in the computations, which consider for example only electric dipole transitions. In the case of the $^7F_1 \leftarrow {}^7F_0$ and $^5D_1 \leftarrow {}^7F_0$ transitions, Carnall *et al.*[41] have found

Table 6.9.: Average computed transition energies of $[Eu(H_2O)_6]^{3+}$ $C_1$ (Eu-6w-C1-2) with non-zero oscillator strengths $f_{osc}$ (DKH SOC-CASSCF (6,7) TZVP-DKH) and computed Judd-Ofelt parameter $\Omega_\lambda$ ($\lambda$ = 2, 4, 6) using transition energy belonging to $f_{osc}$ (max.), $E_{f_{max}}$, and the squared reduced matrix elements $\langle\|U^{(\lambda)}\|\rangle^2$ published by Carnall *et al.*[28].

| **Transition** | **ΔE ($cm^{-1}$)** | | **$f_{osc}$ (max.)** | **$\Omega_\lambda$ ($\times10^{-20}$ $cm^2$)** | | | **$\langle\|U^{(\lambda)}\|\rangle^2$** | | |
|---|---|---|---|---|---|---|---|---|---|
| | **av.** | **$E_{f_{max}}$** | **($\times10^{-5}$)** | **$\Omega_2$** | **$\Omega_4$** | **$\Omega_6$** | $U^{(2)}$ | $U^{(4)}$ | $U^{(6)}$ |
| $^7F_2 \leftarrow {}^7F_0$ | 937.96 | 854.90 | $1.00{\cdot}10^{-4}$ | 0.00658 | / | / | 0.1374 | 0 | 0 |
| $^7F_4 \leftarrow {}^7F_0$ | 2750.0 | 2804.8 | $1.70{\cdot}10^{-3}$ | / | 0.0334 | / | 0 | 0.1402 | 0 |
| $^7F_5 \leftarrow {}^7F_0$ | 3862.9 | 3909.2 | $2.00{\cdot}10^{-4}$ | | | | | | |
| $^7F_6 \leftarrow {}^7F_0$ | 5098.7 | 4752.5 | $3.20{\cdot}10^{-3}$ | / | / | 0.0359 | 0 | 0 | 0.145 |
| $^5D_4 \leftarrow {}^7F_0$ | 30516 | 30579 | $1.00{\cdot}10^{-4}$ | / | 0.0230 | / | 0 | 0.0011 | 0 |
| $^7F_3 \leftarrow {}^7F_1(1)$ | 1626.1 | 1596.1 | $1.00{\cdot}10^{-4}$ | | | | 0.2092 | 0.1281 | 0 |
| $^7F_4 \leftarrow {}^7F_1(1)$ | 2613.4 | 2686.5 | $2.00{\cdot}10^{-4}$ | / | 0.0099 | / | 0 | 0.1741 | 0 |
| $^7F_5 \leftarrow {}^7F_1(1)$ | 3726.2 | 3772.6 | $1.00{\cdot}10^{-4}$ | | | | 0 | 0.1192 | 0.0544 |
| $^7F_6 \leftarrow {}^7F_1(1)$ | 4962.0 | 4614.7 | $2.00{\cdot}10^{-3}$ | / | / | 0.0266 | 0 | 0 | 0.3774 |
| $^7F_4 \leftarrow {}^7F_1(2)$ | 2362.8 | 2463.9 | $1.00{\cdot}10^{-4}$ | / | 0.00540 | / | 0 | 0.1741 | 0 |
| $^7F_5 \leftarrow {}^7F_1(2)$ | 3475.7 | 3482.4 | $1.00{\cdot}10^{-4}$ | | | | 0 | 0.1192 | 0.0544 |
| $^7F_6 \leftarrow {}^7F_1(2)$ | 4711.5 | 4783.2 | $4.00{\cdot}10^{-4}$ | / | / | 0.00514 | 0 | 0 | 0.3774 |

Table 6.10.: Average computed transition energies of $[Eu(H_2O)_6]^{3+}$ $C_1$ (Eu-6w-C1-2) with non-zero oscillator strengths $f_{osc}$ (DKH SOC-CASSCF (6,7) TZVP-DKH) and computed Judd-Ofelt parameter $\Omega_\lambda$ ($\lambda$ = 2, 4, 6) using these average energies and the squared reduced matrix elements $\langle||U^{(\lambda)}||\rangle^2$ published by Carnall *et al.*[28].

| **Transition** | **Av. ΔE** ($cm^{-1}$) | $f_{osc}$ **(max.)** ($\times 10^{-5}$) | $\Omega_\lambda$ ($\times 10^{-20}$ $cm^2$) | | | $\langle\|\|U^{(\lambda)}\|\|\rangle^2$ | | |
|---|---|---|---|---|---|---|---|---|
| | | | $\Omega_2$ | $\Omega_4$ | $\Omega_6$ | $U^{(2)}$ | $U^{(4)}$ | $U^{(6)}$ |
| $^7F_2 \leftarrow {}^7F_0$ | 937.96 | $1.00 \cdot 10^{-4}$ | 0.00599 | / | / | 0.1374 | 0 | 0 |
| $^7F_4 \leftarrow {}^7F_0$ | 2750.0 | $1.70 \cdot 10^{-3}$ | / | 0.0341 | / | 0 | 0.1402 | 0 |
| $^7F_5 \leftarrow {}^7F_0$ | 3862.9 | $2.00 \cdot 10^{-4}$ | | | | | | |
| $^7F_6 \leftarrow {}^7F_0$ | 5098.7 | $3.20 \cdot 10^{-3}$ | / | / | 0.0334 | 0 | 0 | 0.145 |
| $^5D_4 \leftarrow {}^7F_0$ | 30516 | $1.00 \cdot 10^{-4}$ | / | 0.0230 | / | 0 | 0.0011 | 0 |
| $^7F_3 \leftarrow {}^7F_1(1)$ | 1626.1 | $1.00 \cdot 10^{-4}$ | | | | 0.2092 | 0.1281 | 0 |
| $^7F_4 \leftarrow {}^7F_1(1)$ | 2613.4 | $2.00 \cdot 10^{-4}$ | / | 0.0102 | / | 0 | 0.1741 | 0 |
| $^7F_5 \leftarrow {}^7F_1(1)$ | 3726.2 | $1.00 \cdot 10^{-4}$ | | | | 0 | 0.1192 | 0.0544 |
| $^7F_6 \leftarrow {}^7F_1(1)$ | 4962.0 | $2.00 \cdot 10^{-3}$ | / | / | 0.0248 | 0 | 0 | 0.3774 |
| $^7F_4 \leftarrow {}^7F_1(2)$ | 2362.8 | $1.00 \cdot 10^{-4}$ | / | 0.00563 | / | 0 | 0.1741 | 0 |
| $^7F_5 \leftarrow {}^7F_1(2)$ | 3475.7 | $1.00 \cdot 10^{-4}$ | | | | 0 | 0.1192 | 0.0544 |
| $^7F_6 \leftarrow {}^7F_1(2)$ | 4711.5 | $4.00 \cdot 10^{-4}$ | / | / | 0.00521 | 0 | 0 | 0.3774 |

Table 6.11.: Computed Judd-Ofelt parameter $\Omega_\lambda$ ($\lambda$ = 2, 4, 6) of Eu-6w-C1-2 (DKH SOC-CASSCF (6,7) TZVP-DKH) using Judd-Ofelt program; $\Delta E_{f_{max}}$: using transition energy belonging to $f_{osc}$ (max.), $\Delta E_{av}$: using average transitions energies.

| | $\Omega_\lambda$ ($\times 10^{-20}$ $cm^2$) | | |
|---|---|---|---|
| | $\Omega_2$ | $\Omega_4$ | $\Omega_6$ |
| $\Delta E_{f_{max}}$ [a] | 0.00657 ± 0.0051 | 0.0334 ± 0.0015 | 0.0334 ± 0.00081 |
| $\Delta E_{av}$ [b] | 0.00599 ± 0.0029 | 0.0340 ± 0.0010 | 0.0334 ± 0.00050 |

[a] rms = $7.74 \cdot 10^{-10}$.
[b] rms = $4.78 \cdot 10^{-10}$.

significant magnetic dipole oscillator strengths, while the other $^{2S+1}L_J \leftarrow {}^7F_0$ transitions exhibit predominantly electric dipole character.
In the *ab initio* study of the cause of hypersensitivity by Hatanaka & Yabushita[134] it was concluded that ligand-to-metal charge-transfer (LMCT), especially in the case of europium, and dynamic coupling are important contributions to the oscillator strengths of the majority of $f \leftrightarrow f$ transitions, based on a decomposition of transition dipole moments.[134]

In summary, the band assignment did not pose any difficulties for $Eu^{3+}$, even for the water complexes where also crystal field splitting arises. It could be shown that the crystal fields acts only as a small perturbation, as was expected. The $^7F$ are described properly with the SOC-CASSCF calculations, but the F–D spacing is overestimated by some thousand $cm^{-1}$. No significant difference between the $f$-orbitals of the Eu-6w-Th, Eu-6w-C1-2 and Eu-8w-C1-1 structures and the free ion $Eu^{3+}$ was observed. In some cases the orbitals expanded along the Eu–O bonds. In the Eu-6w-Th geometry, $p$-orbitals of opposite oxygens also mix to some extent with the $f$-orbitals of europium(III).
The $C_1$ structures yielded non-zero oscillator strengths for the $f \leftrightarrow f$ transitions, however only for transitions that are not in the recorded range of the experimental spectra. The computed oscillator strengths and Judd-Ofelt parameters are about two orders of magnitude smaller than the experimental values, thus suggesting that the used method is not suitable to calculate the desired transitions and other effects should be accounted for in the computations as well.

# 7. Conclusion

In this thesis, the hypersensitive transitions of $Nd^{3+}$ and $Eu^{3+}$ were investigated in different environments and symmetries. The experimental part focused on absorbance and emission spectra of the rare earth ions in solvent mixtures as well as in CAB glasses. Furthermore, a semi-empirical Judd-Ofelt analysis was performed.
The theoretical part consisted of relativistic *ab initio* calculations of $Nd^{3+}$ as well as of water complexes of $Nd^{3+}$ and $Eu^{3+}$ in different symmetries at the one-component Douglas-Kroll-Hess, two-component X2C and four-component Dirac-Coulomb level of theory using different multi-reference methods.

## Experiments

In summary, the hypersensitivity of the $^2G_{7/2} \leftarrow {}^4I_{9/2}$ and $^5D_2 \leftarrow {}^7F_0$ transitions of $Nd^{3+}$ and $Eu^{3+}$, respectively, could be observed in the absorbance spectra of the solvent mixtures. The mixtures showed a continuous variation of the intensity of the hypersensitive transitions yielding the highest intensities in acetone and the lowest intensities in water. Intermediate intensities were found in the water-methanol mixtures. The same findings were obtained for the $^5D_0 \rightarrow {}^7F_2$ transition of $Eu^{3+}$ in the emission spectra.
This tendency, which was also reproduced by the oscillator strengths, is in line with the polarisabilities of the solvents, $\alpha(\text{water}) < \alpha(\text{methanol}) < \alpha(\text{acetone})$. Early studies have already proposed the dependence of the hypersensitive transitions of rare earth ions on the polarisability of the environment,[34,51] which seems to be confirmed by this present investigation. The concept of polarisability is included in the *dynamic coupling* model in terms of a dynamic contribution to the $\Omega_2$ intensity parameter. Other suggested explanations for the hypersensitivity like the $pK_a$ value of the solvents or ligands could not be confirmed by the present study, as the $pK_a$ values of acetone, methanol and water do not follow the observed intensity tendency. However, the experimental spectra of the rare earth ions in solvent mixtures cannot be used for an interpretation in terms of symmetry, because

there is no definite point group in this dynamic environment. Yet, the symmetry of the environment was also discussed by many authors as a cause of hypersensitivity and is for example also accounted for in the dynamic coupling model. Presumably a combination of some effects like the polarisability and symmetry of the environment should be considered when describing hypersensitive transitions of rare earth ions.

The CAB glasses prepared in this thesis served as a model system of low symmetry. The highest oscillator strength for the $^2G_{7/2} \leftarrow {}^4I_{9/2}$ transition of $Nd^{3+}$ was found in the CAB glass. However, the asymmetry ratio, i.e. the ratio of the intensities of the hypersensitive transition to a magnetic dipole transition, of the Eu-CAB-glass yielded a value of only 2.78, which is smaller than the asymmetry ratio found in methanol. In the case of $Eu^{3+}$, the following order of the asymmetry ratios was found: water < CAB glass ≈ methanol < acetone.

A Judd-Ofelt analysis of the absorbance spectra of $Nd^{3+}$ and emission spectra of $Eu^{3+}$ confirmed these results. The expected variation of the $\Omega_2$ parameter, which is sensitive to the environment, was observed in the different solvent mixtures, while $\Omega_4$ and $\Omega_6$ remained nearly constant. In the case of neodymium(III), the relation $\Omega_2 < \Omega_4 < \Omega_6$ was found in water, in methanol $\Omega_4 < \Omega_2 \approx \Omega_6$ and in acetone $\Omega_4 < \Omega_6 < \Omega_2$. These results are in line with the change of intensity or oscillator strength of the hypersensitive transition. The Judd-Ofelt analysis of $Eu^{3+}$ yielded the relation $\Omega_4 < \Omega_2$ for all pure solvents and solvent mixtures. However, for both ions the highest value of $\Omega_2$ was found in acetone.
In the spectra of $Nd^{3+}$ or $Eu^{3+}$ in water-methanol, a broader range could be resolved than in the water-acetone mixtures, because of the starting absorption of acetone in the (UV)-VIS region. Therefore, more bands were available for a Judd-Ofelt analysis. In the case of neodymium(III), the analysis, i.e. the least squares fit, was performed in two ways. First, without the additional transitions (m1) and then taking the the $^4D_{1/2}$, $^4D_{3/2}$, $^4D_{5/2}$, $^2I_{11/2} \leftarrow {}^4I_{9/2}$ transitions into account as well. The results significantly differ, yielding for example $\Omega_2(m1) = 0.514 \pm 0.52 \cdot 10^{-20}$ cm$^2$, $\Omega_4(m1) = 6.28 \pm 0.79 \cdot 10^{-20}$ cm$^2$ and $\Omega_6(m1) = 7.49 \pm 0.39 \cdot 10^{-20}$ cm$^2$ compared to $\Omega_2(m2) = 2.07 \pm 0.41 \cdot 10^{-20}$ cm$^2$, $\Omega_4(m2) = 3.70 \pm 0.38 \cdot 10^{-20}$ cm$^2$ and $\Omega_6(m1) = 8.16 \pm 0.53 \cdot 10^{-20}$ cm$^2$ in water. However, both the (m1) analysis and the (m2) analysis showed the same tendency of the $\Omega_\lambda$ parameters. In summary, the (m1) analysis gave a better agreement with literature values, better rms values and better fit between $f_{exp}$ and $f_{calc}$(JO) for most transitions, while the (m2) analysis yielded Judd-Ofelt parameters with a smaller standard error.

The Nd-CAB-glass yielded a high value for $\Omega_2$ compared to other $Nd^{3+}$-doped glasses,

while a relatively small $\Omega_2$ parameter was found for the Eu-CAB-glass compared to other borate glasses.

The results of the oscillator strengths and Judd-Ofelt intensity parameters $\Omega_\lambda$ are in agreement with the literature and lie in the observed range.

An evaluation of the experimental energy levels of $Nd^{3+}$ and $Eu^{3+}$ and comparison to published values of the rare earth ions in $LaF_3$[28] showed that the shift of the energies in the different environments is indeed very small. It can be concluded that the environment of the rare earth ion has no substantial influence on the position of the states, which can be explained by the shielding of the $f$-electrons by the filled $5s$ and $5p$ shells.[11,13]

Broad emissions were observed in the spectra of $Nd^{3+}$ in the water-DMSO mixtures and in acetone, which are presumably caused by metal-to-ligand charge-transfer and not by $f \leftrightarrow f$ transitions of $Nd^{3+}$, because of their linewidth and lifetime.[10] Besides, $Nd^{3+}$ exhibits luminescence at lower energies in the NIR region.[103,104]

In the $Nd^{3+}$ solutions in water-acetone and water-methanol a preferred coordination of water was observed as the increase in intensity of the hypersensitive transition started only at 50 v-% acetone or methanol in water.
Since the $^2G_{7/2} \leftarrow {}^4I_{9/2}$ and $^4G_{5/2} \leftarrow {}^4I_{9/2}$ bands overlap in the experimental spectra, a change of the band shape and a shift of the barycentre towards lower energies was observed, which is explained by an increasing contribution of the hypersensitive $^4G_{5/2} \leftarrow {}^4I_{9/2}$ transition.

## Computations

To sum up the *ab initio* calculations, it was found in this thesis that most high symmetric water complexes of $Nd^{3+}$ and $Eu^{3+}$ exhibited high relative energies and imaginary frequencies, while the low symmetric geometries correspond to minima. The only exceptions were the optimized $[Nd,Eu(H_2O)_6]^{3+}$ complexes of $T_h$ symmetry, i.e. the octahedra of oxygens. The preferred coordination number of $Nd^{3+}$ and $Eu^{3+}$ in water is nine,[1,133,135] however none of the structures with nine water molecules was used for further multi-reference calculations due to convergence problems.

The assignment of the free ion $^{2S+1}L_J$ states was straightforward for $Eu^{3+}$. $Nd^{3+}$, on the contrary, has a high density of states in the region of higher energy above the $^4I$ states, thus leading to intervening states and complicating the assignment. Still this was accomplished in the present thesis using calculations with increasing speed of light corresponding to a

decreasing spin-orbit coupling. The results of the relativistic four-component KRCI calculations of the free ion, $Nd^{3+}$, yielded the best agreement with the experimental energy levels of $NdF_3$,[28] however the states of higher energy still differ from the published experimental results both in the energy of the states and in their sequence. The hypersensitive $^4G_{5/2} \leftarrow {}^4I_{9/2}$ transition is overestimated by about $3.7 \cdot 10^3$ $cm^{-1}$. Still, this result is by about 800 $cm^{-1}$ better than other published values based on an *ab initio* study of $NdBr_3$.[134]

The results of the SOC-CASSCF calculations of the $Eu^{3+}$-water complexes are consistent with the findings of $Nd^{3+}$. The $^7F$ states are in good agreement with the experimental energy levels of $EuF_3$[28] and yielded better results than the *ab initio* study of $EuBr_3$ by Hatanaka & Yabushita[134]. Yet, the spacing between the $^7F$ and $^5D$ states is overestimated by some thousand $cm^{-1}$, in analogy to the KRCI calculations of $Nd^{3+}$. Hatanaka & Yabushita[134] have found a slightly better energy for the hypersensitive $^5D_2 \leftarrow {}^7F_0$ transition, i.e. a deviation of $2.5 \cdot 10^3$ $cm^{-1}$ instead of the $3.1 \cdot 10^3$ $cm^{-1}$ encountered in this thesis. The four-component KRCI calculations of Holzer[128] yielded the best agreement with the experimental transition energy because the F–D spacing is lowered, but at the expense of a worse description of the $^7F$ states compared to the present study.
These SOC-CASSCF calculations of $Eu^{3+}$-water complexes also revealed the small crystal field splitting, which was found to be mostly in the order of $1 - 10$ $cm^{-1}$ and sometimes also $10^{-1}$ and $10^2$ $cm^{-1}$. The splitting caused by spin-orbit coupling is in the order of $10^2 - 10^3$ $cm^{-1}$ for $Eu^{3+}$. This demonstrates the small influence of the environment on the energy levels.

The computed oscillator strengths using SOC-CASSCF deviate significantly from the observed oscillator strengths in the experimental spectra or from published values in the literature. All centrosymmetric structures yielded zero oscillator strengths due to symmetry selection rules, while the $C_1$ geometries showed small oscillator strengths for some $^{2S'+1}L_{J'} \leftarrow {}^7F_J$ transitions.
As a consequence, the computed Judd-Ofelt parameters, which were obtained using these small oscillator strengths, are one to two orders of magnitude smaller than the experimental $\Omega_\lambda$ parameters of $Eu^{3+}$ in water. However, the observed relation $\Omega_2 < \Omega_4 \approx \Omega_6$ is consistent the literature.[41] It is concluded that the SOC-CASSCF method applied in this thesis is not the method of choice for computing oscillator strengths of $f \leftrightarrow f$ transitions and more effects have to be accounted for in the *ab initio* calculations, like electric quadrupole oscillator

strengths, ligand-to-metal charge-transfer and dynamic coupling.[134]

In conclusion, the results of this thesis indicate that the dynamic coupling model[137–140] is the preferred theory to describe the hypersensitive transitions of neodymium(III) and europium(III), since it explains the dependence on the polarisability as well as on the symmetry of the environment, which were both confirmed in the present experimental and theoretical study.

# Appendix

## Judd-Ofelt program

JuddOfelt is a software module written in Python 3 to calculate Judd-Ofelt parameters and oscillator strengths for the specified ion $Nd^{3+}$ and $Eu^{3+}$. The software mainly relies on an existing GAUSS-implementation provided by Dr. K. Gatterer and makes extensive use of NumPy, a package for scientific numerical computation.

For $Nd^{3+}$ and $Eu^{3+}$ literature values for the squared reduced matrix elements of the unit tensor operator $\langle \|\mathbf{U}^{(\lambda)}\| \rangle$ by Carnall et al.[28] are already provided. Otherwise a new element specification file must be defined.
Input files contain information about the experimental setup and its result, i.a. the concentration $c$, light path $l$, $J$-value of initial state and refractive index $n$. Output files supply the calculated Judd-Ofelt parameters $\Omega_2$, $\Omega_4$ and $\Omega_6$ as well as two tables with experimental and calculated oscillator strengths.

1. Input preparation: Build matrices
2. Calculate experimental oscillator strengths
3. Perform a linear regression and obtain the Judd-Ofelt parameters
4. Calculate oscillator strengths
5. Calculate standard deviation and standard error

Technically the calculation is preceded by a an input parser and succeeded by an exporter which uses the prettytable package.

First, the experimental oscillator strengths are calculated with equation (2.62)

$$\begin{aligned} f_{exp} &= 4.318 \cdot 10^{-9} \int \varepsilon(\tilde{\nu})\, d\tilde{\nu} \\ &= \frac{4.318 \cdot 10^{-9}}{c \cdot l} \int A(\tilde{\nu})\, d\tilde{\nu} \quad . \end{aligned}$$

where the integral $\int A(\tilde{\nu})\, d\tilde{\nu}$ denotes the area of bands measured in the experimental spectra. They form the vector $\mathbf{f}_{exp}$, which comprises the oscillator strengths of all observed transitions.
Second, a matrix $\mathbf{C}$ is build of all transitions $a$

$$C_a = \frac{8\pi^2 m_e c}{3h} \frac{(n^2+2)^2}{9n} \frac{1}{2J+1} \tilde{\nu}_a \langle \|\mathbf{U}^{(\lambda)}\| \rangle_a^2$$

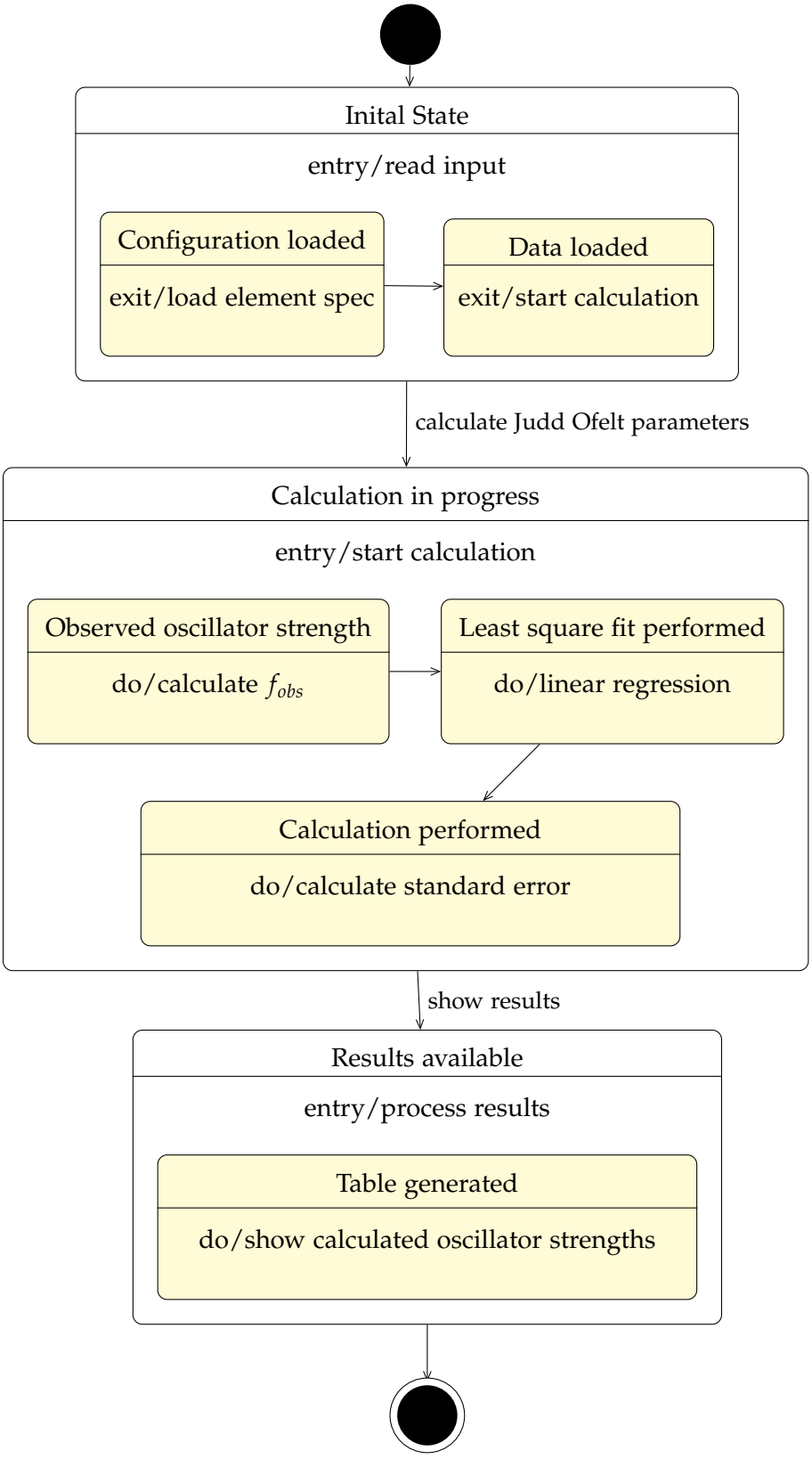


Figure .1.: State diagram describing the Judd-Ofelt program

based on the expression for the oscillator strengths of the Judd-Ofelt theory, equation (2.60)

$$f_{calc} = \frac{8\pi^2 m_e c\,\tilde{\nu}}{3h(2J+1)} \frac{(n^2+2)^2}{9n} \sum_{\lambda=2,4,6} \Omega_\lambda \left| \left\langle 4f^N \alpha' [S'L'] J' \left\| \mathbf{U}^{(\lambda)} \right\| 4f^N \alpha [SL] J \right\rangle \right|^2 \quad .$$

Then, a linear regression is performed based on the least squares principle to obtain the Judd-Ofelt intensity parameters $\Omega_\lambda$ ($\lambda = 2,4,6$)

$$\begin{pmatrix} \Omega_2 \\ \Omega_4 \\ \Omega_6 \end{pmatrix} = \left(\mathbf{C}^T \cdot \mathbf{C}\right)^{-1} \cdot \mathbf{C}^T \cdot \mathbf{f}_{exp} \quad .$$

The next step is to calculate oscillator strengths, $f_{calc}$, using the $\Omega_\lambda$ parameters and equation (2.60).
Finally, the standard deviation or root mean square deviation (rms) is determined according to equation (2.69)

$$\begin{aligned} \text{rms} &= \left( \frac{\text{sum of squares of deviations}}{\text{number of observations} - \text{number of parameters}} \right)^{\frac{1}{2}} \\ &= \left( \frac{\Sigma (f_{calc} - f_{exp})^2}{\text{number of bands} - 3} \right)^{\frac{1}{2}} \end{aligned}$$

and the standard error (se) of the $\Omega_\lambda$ parameters using the rms

$$\text{se} = \text{rms} \sqrt{\text{diag}\left( \{\mathbf{C}^T \cdot \mathbf{C}\}^{-1} \right)} \quad .$$

The Judd-Ofelt program was extended for $Eu^{3+}$ in order to fit Judd-Ofelt oscillator strengths, "$f_{calc}$", to the computed oscillator strengths.

## Input file example

```
# Nd-50-H-A

el=Nd3+
j=9/2
c=0.0523498303 mol/l
n=1.358
```

```
l=1.0 cm

table (name, RS term symbol, nu, area)
R 4F3/2 11520.09251 24.15931
S 4F5/2,2H(2)9/2 12532.00488 109.91915
A 4F7/2,4S3/2 13483.14895 110.50763
B 4F9/2 14698.85366 6.86615
C 2H(2)11/2 15899.40869 1.87028
D 4G5/2,2G(2)7/2 17309.30166 142.22387
E,F 4G7/2,4G9/2,2K13/2 19327.3831 83.32383
G,H 2D3/2,4G11/2,2K15/2,2G(1)9/2 21370.03871 21.88655
I 2P1/2,2D5/2 23395.76052 4.8309
```

## Output file example

```
JuddOfelt 0.1.0
# Nd-50-H-A

JO-parameters:
omega_2 = 1.0792560486513352e-20
omega_4 = 6.289661723484508e-20
omega_6 = 7.546242822320441e-20

Observed oscillator strength:
+------+---------------------------------+-------------------+
| Name |          RS term symbol         |       p_exp       |
+------+---------------------------------+-------------------+
|  R   |              4F3/2              | 1.99366872064e-06 |
|  S   |         4F5/2, 2H(2)9/2         | 9.07072143842e-06 |
|  A   |           4F7/2, 4S3/2          | 9.11928384226e-06 |
|  B   |              4F9/2              | 5.66606765103e-07 |
|  C   |            2H(2)11/2            | 1.54338792575e-07 |
|  D   |         4G5/2, 2G(2)7/2         | 1.17365637076e-05 |
| E,F  |       4G7/2, 4G9/2, 2K13/2      | 6.87602889135e-06 |
```

```
| G,H  | 2D3/2, 4G11/2, 2K15/2, 2G(1)9/2 | 1.80611657112e-06 |
|  I   |           2P1/2, 2D5/2          | 3.98654358198e-07 |
+------+---------------------------------+-------------------+

Calculated oscillator strength:
+------+---------------------------------+-------------------+
| Name |          RS term symbol         |       p_calc      |
+------+---------------------------------+-------------------+
|  R   |              4F3/2              | 2.80914093447e-06 |
|  S   |         4F5/2, 2H(2)9/2         | 8.94326077222e-06 |
|  A   |           4F7/2, 4S3/2          | 9.31658220934e-06 |
|  B   |              4F9/2              | 7.04241757365e-07 |
|  C   |            2H(2)11/2            | 1.99116559334e-07 |
|  D   |         4G5/2, 2G(2)7/2         |  1.1784640473e-05 |
| E,F  |       4G7/2, 4G9/2, 2K13/2      | 6.30168355522e-06 |
| G,H  | 2D3/2, 4G11/2, 2K15/2, 2G(1)9/2 | 1.56868937271e-06 |
|  I   |           2P1/2, 2D5/2          | 8.07687969225e-07 |
+------+---------------------------------+-------------------+

Standard deviation:
4.6493374941711964e-07

Normal termination
```

## Computations

Table .1.: Energy levels of $Nd^{3+}$ (X2C KRCI Dyall cv3z) with increasing speed of light c or decreasing spin-orbit coupling.

| c (a.u.) | Wavenumber ($cm^{-1}$) | | | | | | |
|---|---|---|---|---|---|---|---|
| | $^4I_{9/2}$ | $^4I_{11/2}$ | $^4I_{13/2}$ | $^4I_{15/2}$ | $^4F_{3/2}$ | $^2H_{9/2}$[a] | $^4F_{5/2}$ |
| 137 | 0 | 2004.27 | 4163.27 | 6429.81 | 13379.18 | 14057.90 | 14467.15 |
| 150 | 497.41 | 2168.73 | 3994.58 | 5936.64 | 13828.47 | 14494.13 | 14714.16 |
| 200 | 1636.62 | 2567.80 | 3619.14 | 4773.81 | 14788.75 | 15466.19 | 15253.58 |

| | | | | | | | |
|---|---|---|---|---|---|---|---|
| 250 | 2177.58 | 2768.70 | 3446.90 | 4204.19 | 15213.09 | 15892.75 | 15498.91 |
| 300 | 2473.65 | 2881.91 | 3354.51 | 3887.28 | 15436.87 | 16214.53 | 15630.60 |
| 400 | 2769.00 | 2997.23 | 3263.81 | 3567.31 | 15654.08 | 16336.12 | 15760.23 |
| 500 | 2905.89 | 3051.50 | 3222.29 | 3417.67 | 15752.69 | 16420.89 | 15819.74 |
| 625 | 2993.53 | 3086.53 | 3195.90 | 3321.40 | 15815.12 | 16474.18 | 15857.67 |
| 750 | 3041.14 | 3105.64 | 3181.62 | 3268.95 | 15848.80 | 16502.59 | 15878.21 |
| 875 | 3069.85 | 3117.20 | 3173.03 | 3237.27 | 15869.04 | 16519.52 | 15890.58 |
| 1,000 | 3088.48 | 3124.72 | 3167.47 | 3216.69 | 15882.14 | 16530.41 | 15898.60 |
| 1,250 | 3110.39 | 3133.57 | 3160.93 | 3192.46 | 15897.51 | 16543.13 | 15908.02 |
| 1,500 | 3122.29 | 3138.38 | 3157.39 | 3179.29 | 15905.84 | 16550.00 | 15913.13 |
| 2,000 | 3134.12 | 3143.17 | 3153.86 | 3166.19 | 15914.12 | 16556.80 | 15918.22 |
| 5,000 | 3146.90 | 3148.35 | 3150.06 | 3152.04 | 15923.05 | 16564.11 | 15923.70 |
| 10,000 | 3148.73 | 3149.09 | 3149.52 | 3150.01 | 15924.32 | 16565.15 | 15924.49 |
| 100,000 | 3149.33 | 3149.34 | 3149.34 | 3149.35 | 15924.74 | 16565.49 | 15924.75 |
| 500,000 | 3149.34 | 3149.34 | 3149.34 | 3149.34 | 15924.75 | 16565.50 | 15924.75 |
| 1,000,000 | 3149.34 | 3149.34 | 3149.34 | 3149.34 | 15924.75 | 16565.50 | 15924.75 |

| **c (a.u.)** | **Wavenumber ($cm^{-1}$) (cont.)** | | | | | | |
|---|---|---|---|---|---|---|---|
| | $^4F_{7/2}$ | $^4S_{3/2}$ | $^4F_{9/2}$[a] | $^2H_{11/2}$ | $^2G_{7/2}$ | $^4G_{5/2}$ | $^2G_{9/2}$[b] |
| 137 | 15486.87 | 15683.70 | 16733.83 | 17530.34 | 19590.59 | 20934.09 | 22433.16 |
| 150 | 15601.01 | 15821.96 | 16648.18 | 17396.32 | 19778.97 | 21432.42 | 22141.33 |
| 200 | 15792.10 | 16061.06 | 16416.89 | 17061.09 | 20214.45 | 22548.04 | 21416.95 |
| 250 | 15853.12 | 16138.97 | 16281.21 | 16889.88 | 20427.08 | 23071.03 | 21120.42 |
| 300 | 15879.65 | 16172.36 | 16089.61 | 16793.23 | 20545.63 | 23356.81 | 20990.55 |
| 400 | 15901.81 | 16199.30 | 16070.68 | 16694.87 | 20665.56 | 23642.15 | 20892.39 |
| 500 | 15910.75 | 16209.66 | 16022.75 | 16648.65 | 20721.73 | 23774.61 | 20859.37 |
| 625 | 15916.06 | 16215.58 | 15989.12 | 16618.86 | 20757.90 | 23859.52 | 20842.78 |
| 750 | 15918.81 | 16218.57 | 15970.05 | 16602.60 | 20777.61 | 23905.69 | 20835.33 |
| 875 | 15920.43 | 16220.29 | 15958.29 | 16592.78 | 20789.52 | 23933.54 | 20831.37 |
| 1,000 | 15921.47 | 16221.38 | 15950.56 | 16586.40 | 20797.26 | 23951.62 | 20829.03 |
| 1,250 | 15922.66 | 16222.63 | 15941.37 | 16578.88 | 20806.37 | 23972.89 | 20826.49 |
| 1,500 | 15923.31 | 16223.29 | 15936.33 | 16574.80 | 20811.32 | 23984.45 | 20825.21 |
| 2,000 | 15923.94 | 16223.94 | 15931.28 | 16570.73 | 20816.25 | 23995.94 | 20824.02 |

| | | | | | | | |
|---|---|---|---|---|---|---|---|
| 5,000 | 15924.62 | 16224.63 | 15925.80 | 16566.34 | 20821.57 | 24008.35 | 20822.81 |
| 10,000 | 15924.72 | 16224.73 | 15925.01 | 16565.71 | 20822.33 | 24010.12 | 20822.64 |
| 100,000 | 15924.75 | 16224.76 | 15924.75 | 16565.50 | 20822.58 | 24010.71 | 20822.58 |
| 500,000 | 15924.75 | 16224.76 | 15924.75 | 16565.50 | 20822.58 | 24010.71 | 20822.58 |
| 1,000,000 | 15924.75 | 16224.76 | 15924.75 | 16565.50 | 20822.58 | 24010.71 | 20822.59 |

| c (a.u.) | Wavenumber ($cm^{-1}$) (cont.) | | | | | |
|---|---|---|---|---|---|---|
| | $^4G_{7/2}$ | $^2K_{13/2}$ | $^4G_{9/2}$[b] | $^2D_{3/2}$ | $^4G_{11/2}$ | $^2K_{15/2}$ |
| 137 | 22518.81 | 23427.36 | 24185.00 | 24645.70 | 25520.88 | 25652.73 |
| 150 | 22713.38 | 23706.29 | 24070.55 | 25049.48 | 25293.70 | 25611.15 |
| 200 | 23209.72 | 24346.36 | 23957.26 | 26083.29 | 24747.76 | 25472.74 |
| 250 | 23475.00 | 24655.50 | 23951.85 | 26630.68 | 24482.87 | 25391.17 |
| 300 | 23629.59 | 24827.22 | 23960.00 | 26943.92 | 24337.95 | 25343.39 |
| 400 | 23791.10 | 25000.77 | 23976.31 | 27258.76 | 24194.09 | 25293.93 |
| 500 | 23868.58 | 25082.07 | 23986.85 | 27397.93 | 24127.79 | 25270.50 |
| 625 | 23919.09 | 25134.43 | 23994.66 | 27478.17 | 24085.51 | 25255.36 |
| 750 | 23946.84 | 25162.99 | 23999.26 | 27515.90 | 24062.61 | 25247.08 |
| 875 | 23963.68 | 25180.24 | 24002.17 | 27535.66 | 24048.81 | 25242.08 |
| 1,000 | 23974.65 | 25191.46 | 24004.10 | 27546.99 | 24039.87 | 25238.83 |
| 1,250 | 23987.59 | 25204.66 | 24006.43 | 27558.67 | 24029.37 | 25235.00 |
| 1,500 | 23994.64 | 25211.84 | 24007.72 | 27564.30 | 24023.66 | 25232.91 |
| 2,000 | 24001.67 | 25218.98 | 24009.02 | 27573.11 | 24018.00 | 25230.84 |
| 5,000 | 24009.27 | 25226.70 | 24010.44 | 27574.22 | 24011.88 | 25228.60 |
| 10,000 | 24010.35 | 25227.81 | 24010.65 | 27574.52 | 24011.01 | 25228.28 |
| 100,000 | 24010.71 | 25228.17 | 24010.71 | 27574.49 | 24010.72 | 25228.18 |
| 500,000 | 24010.71 | 25228.17 | 24010.71 | 27574.36 | 24010.72 | 25228.18 |
| 1,000,000 | 24010.71 | 25228.18 | 24010.71 | 27574.57 | 24010.72 | 25228.18 |

[a] $^2H_{9/2}$ or $^4F_{9/2}$.
[b] $^2G_{9/2}$ or $^4G_{9/2}$.

Table .2.: Computed crystal field splittings of $Eu^{3+}$-water complexes at the DKH SOC-CASSCF (6,7) TZVP-DKH level of theory in $T_h$ and $C_1$ symmetries with 6 and 9 water molecules.

| | Wavenumber (cm-1) | | |
|---|---|---|---|
| **Free ion term** | **Eu-6w-Th** | **Eu-6w-C1-2** | **Eu-8w-C1-1** |
| $^7F_0$ | 0 | 0 | 0 |
| $^7F_1$ | 152.76 | 136.64 | 216.60 |
| | 224.82 | 387.22 | 352.01 |
| | 239.95 | 455.99 | 352.25 |
| $^7F_2$ | 576.18 | 829.90 | 821.43 |
| | 594.05 | 854.86 | 821.61 |
| | 613.74 | 907.13 | 920.94 |
| | 639.96 | 1017.49 | 936.62 |
| | 648.21 | 1080.35 | 937.29 |
| $^7F_3$ | 1190.51 | 1697.73 | 1665.71 |
| | 1202.07 | 1714.20 | 1672.19 |
| | 1213.93 | 1732.77 | 1672.33 |
| | 1223.33 | 1754.04 | 1696.08 |
| | 1225.89 | 1803.72 | 1696.18 |
| | 1234.94 | 1809.28 | 1742.40 |
| | 1246.40 | 1827.66 | 1742.63 |
| $^7F_4$ | 1931.27 | 2588.94 | 2593.24 |
| | 1976.40 | 2607.26 | 2610.63 |
| | 1984.92 | 2621.88 | 2610.64 |
| | 1988.68 | 2785.89 | 2659.99 |
| | 2037.24 | 2804.75 | 2660.15 |
| | 2055.23 | 2820.44 | 2711.37 |
| | 2059.70 | 2823.14 | 2711.52 |
| | 2077.96 | 2846.87 | 2763.42 |
| | 2089.98 | 2851.09 | 2764.03 |
| | 2922.40 | 3621.80 | 3645.64 |
| | 2951.79 | 3622.00 | 3645.64 |
| | 2970.88 | 3804.81 | 3788.93 |

Table .2.: Computed crystal field splittings of $Eu^{3+}$-water complexes at the DKH SOC-CASSCF (6,7) TZVP-DKH level of theory in $T_h$ and $C_1$ symmetries with 6 and 9 water molecules.

| | Wavenumber (cm-1) | | |
|---|---|---|---|
| **Free ion term** | **Eu-6w-Th** | **Eu-6w-C1-2** | **Eu-8w-C1-1** |
| | 2998.76 | 3817.44 | 3789.07 |
| | 3000.88 | 3825.39 | 3794.85 |
| $^7F_5$ | 3013.21 | 3869.57 | 3795.38 |
| | 3025.26 | 3909.21 | 3835.34 |
| | 3045.36 | 3959.95 | 3835.42 |
| | 3072.56 | 4009.23 | 3835.57 |
| | 3074.59 | 4021.32 | 3835.65 |
| | 3090.11 | 4030.97 | 3854.64 |
| | 4057.72 | 4751.31 | 4856.60 |
| | 4058.61 | 4752.49 | 4856.60 |
| | 4159.78 | 4855.72 | 4890.29 |
| | 4175.09 | 4859.65 | 4890.29 |
| | 4179.03 | 5028.01 | 4939.22 |
| | 4185.23 | 5035.87 | 4939.22 |
| $^7F_6$ | 4187.26 | 5170.38 | 5030.76 |
| | 4219.87 | 5187.79 | 5030.79 |
| | 4224.76 | 5254.88 | 5095.39 |
| | 4269.20 | 5294.56 | 5095.68 |
| | 4272.43 | 5313.44 | 5132.10 |
| | 4274.94 | 5388.70 | 5132.44 |
| | 4280.21 | 5390.25 | 5144.06 |
| $^5D_0$ | 27604.59 | 22268.88 | 22206.56 |
| | 27604.60 | 23022.25 | 22979.02 |
| $^5D_1$ | 28204.51 | 23067.70 | 23004.23 |
| | 28210.41 | 23082.05 | 23004.27 |
| | 28806.94 | 24627.94 | 24573.41 |
| | 28814.13 | 24636.08 | 24599.13 |
| $^5D_2$ | 29413.94 | 24645.42 | 24599.35 |

Table .2.: Computed crystal field splittings of $Eu^{3+}$-water complexes at the DKH SOC-CASSCF (6,7) TZVP-DKH level of theory in $T_h$ and $C_1$ symmetries with 6 and 9 water molecules.

| | Wavenumber (cm-1) | | |
|---|---|---|---|
| **Free ion term** | **Eu-6w-Th** | **Eu-6w-C1-2** | **Eu-8w-C1-1** |
| | 29414.78 | 24700.64 | 24619.88 |
| | 30020.61 | 24703.27 | 24619.96 |
| | 30020.61 | 27077.07 | 27047.87 |
| | 30539.33 | 27107.48 | 27048.05 |
| | 30539.33 | 27107.97 | 27069.44 |
| $^5D_3$ | 30915.60 | 27120.44 | 27069.45 |
| | 30915.82 | 27157.56 | 27087.87 |
| | 31289.54 | 27166.73 | 27087.95 |
| | 31294.63 | 27193.65 | 27104.21 |
| | 31668.44 | 30437.75 | 30430.72 |
| | 31668.44 | 30438.18 | 30430.72 |
| | 31735.64 | 30491.81 | 30447.95 |
| | 31735.64 | 30495.00 | 30447.95 |
| $^5D_4$ | 31817.09 | 30530.48 | 30464.76 |
| | 31817.14 | 30536.30 | 30464.79 |
| | 31844.03 | 30555.85 | 30483.06 |
| | 32044.76 | 30579.25 | 30483.12 |
| | 32044.76 | 30583.54 | 30491.16 |

## Optimized structures

**Nd-6w-Th**:

```
 19
 Nd-6w-Th       B3LYP   ECP49MWB        TZVP
 Nd          0.000000   0.000000   0.000000
 O           0.000000   0.000000  -2.492117
 O           2.492117   0.000000   0.000000
 O          -2.492117   0.000000   0.000000
 O           0.000000   2.492117   0.000000
 O           0.000000  -2.492117   0.000000
 O           0.000000   0.000000   2.492117
 H           0.770801   0.000000  -3.089127
 H          -0.770801   0.000000  -3.089127
 H          -0.770801   0.000000   3.089127
 H           3.089127   0.770801   0.000000
 H          -3.089127   0.770801   0.000000
 H          -3.089127  -0.770801   0.000000
 H           3.089127  -0.770801   0.000000
 H           0.000000   3.089127   0.770801
 H           0.000000  -3.089127   0.770801
 H           0.000000  -3.089127  -0.770801
 H           0.000000   3.089127  -0.770801
 H           0.770801   0.000000   3.089127
```

**Eu-6w-Th**:

19

| Eu-6w-Th | B3LYP | ECP52MWB | TZVP |
|---|---|---|---|
| O | 0.000000 | 0.000000 | -2.431906 |
| Eu | 0.000000 | 0.000000 | 0.000000 |
| O | 0.000000 | 0.000000 | 2.431906 |
| O | 2.431906 | 0.000000 | 0.000000 |
| O | -2.431906 | 0.000000 | 0.000000 |
| O | 0.000000 | 2.431906 | 0.000000 |
| O | 0.000000 | -2.431906 | 0.000000 |
| H | 0.771580 | 0.000000 | -3.028086 |
| H | -0.771580 | 0.000000 | -3.028086 |
| H | -0.771580 | 0.000000 | 3.028086 |
| H | 3.028086 | 0.771580 | 0.000000 |
| H | -3.028086 | 0.771580 | 0.000000 |
| H | -3.028086 | -0.771580 | 0.000000 |
| H | 3.028086 | -0.771580 | 0.000000 |
| H | 0.000000 | 3.028086 | 0.771580 |
| H | 0.000000 | -3.028086 | 0.771580 |
| H | 0.000000 | -3.028086 | -0.771580 |
| H | 0.000000 | 3.028086 | -0.771580 |
| H | 0.771580 | 0.000000 | 3.028086 |

**Eu-6w-C1-1**:

19

| Eu-6w-C1-1 | B3LYP | ECP52MWB | TZVP |
|---|---|---|---|
| O | 0.009375 | -0.019158 | -2.432483 |
| Eu | 0.007040 | -0.000003 | -0.000026 |
| O | 0.016581 | -2.432416 | 0.019551 |
| O | 0.004858 | 0.018963 | 2.432417 |
| O | 2.439567 | 0.009926 | 0.002256 |
| O | -2.425433 | -0.009799 | -0.002390 |
| O | -0.002561 | 2.432410 | -0.019571 |
| H | 0.781821 | -0.023119 | -3.027731 |
| H | -0.761432 | -0.025173 | -3.029835 |
| H | -0.767402 | 0.018242 | 3.027920 |
| H | 3.032665 | 0.783999 | -0.004497 |
| H | -3.024866 | 0.759376 | -0.008830 |
| H | -3.018561 | -0.783859 | 0.003152 |
| H | 3.039053 | -0.759189 | 0.010643 |
| H | -0.007260 | 3.034980 | 0.747159 |
| H | 0.019826 | -3.022427 | 0.796015 |
| H | 0.018177 | -3.035000 | -0.747189 |
| H | -0.002764 | 3.022374 | -0.796068 |
| H | 0.775813 | 0.029875 | 3.029507 |

**Eu-6w-C1-2**:

```
19
Eu-6w-C1-2      B3LYP   ECP52MWB       TZVP
O             0.000000   0.000000   0.000000
Eu            0.000000   0.000000   2.443078
O             2.215807   0.000000   3.458060
O            -2.364941   0.417003   2.125529
O            -0.588237   0.418984   4.787231
O            -0.494351  -2.280646   3.129662
O             0.950579   2.112022   1.537288
H            -0.131182  -0.731205  -0.632482
H             0.140918   0.788957  -0.550716
H            -0.592765   1.265225   5.272330
H             0.137353  -3.005498   3.297423
H             1.882116   2.296240   1.322299
H             0.484664   2.939357   1.317064
H            -1.369165  -2.676423   3.299811
H             2.389841   0.001660   4.416802
H            -3.058243   0.537606   2.799988
H            -2.830309   0.500587   1.272940
H             3.101616  -0.001354   3.050888
H            -0.872206  -0.242036   5.444019
```

**Eu-8w-C1-1**:

19

| Eu-8w-C1-1 | B3LYP | ECP52MWB | TZVP |
|---|---|---|---|
| O | -1.507129 | 1.506824 | 1.310336 |
| Eu | 0.000256 | 0.001440 | 0.002246 |
| O | 1.472281 | 1.496305 | 1.360424 |
| O | -1.516247 | -1.474807 | 1.331995 |
| O | 1.464415 | -1.484847 | 1.378728 |
| O | 0.033510 | 2.094348 | -1.363532 |
| O | -2.081922 | 0.000572 | -1.380659 |
| O | 0.011978 | -2.112160 | -1.331276 |
| O | 2.125800 | -0.018976 | -1.310981 |
| H | -1.671387 | 2.454016 | 1.175092 |
| H | -2.462377 | -1.641335 | 1.192208 |
| H | 1.997485 | -1.218047 | 2.145060 |
| H | 0.584137 | 2.883368 | -1.234686 |
| H | -2.871130 | 0.555264 | -1.272003 |
| H | -0.543013 | -2.899134 | -1.208826 |
| H | 2.337860 | 0.546418 | -2.071164 |
| H | 2.911479 | -0.570772 | -1.167600 |
| H | -0.525458 | 2.287781 | -2.133372 |
| H | -2.269561 | -0.576496 | -2.138475 |
| H | 0.594807 | -2.316611 | -2.080302 |
| H | 1.631144 | -2.434030 | 1.261799 |
| H | 1.196353 | 2.047509 | 2.110523 |
| H | -2.064859 | 1.249536 | 2.062248 |
| H | -1.266332 | -2.014305 | 2.099533 |
| H | 2.422581 | 1.661298 | 1.250200 |

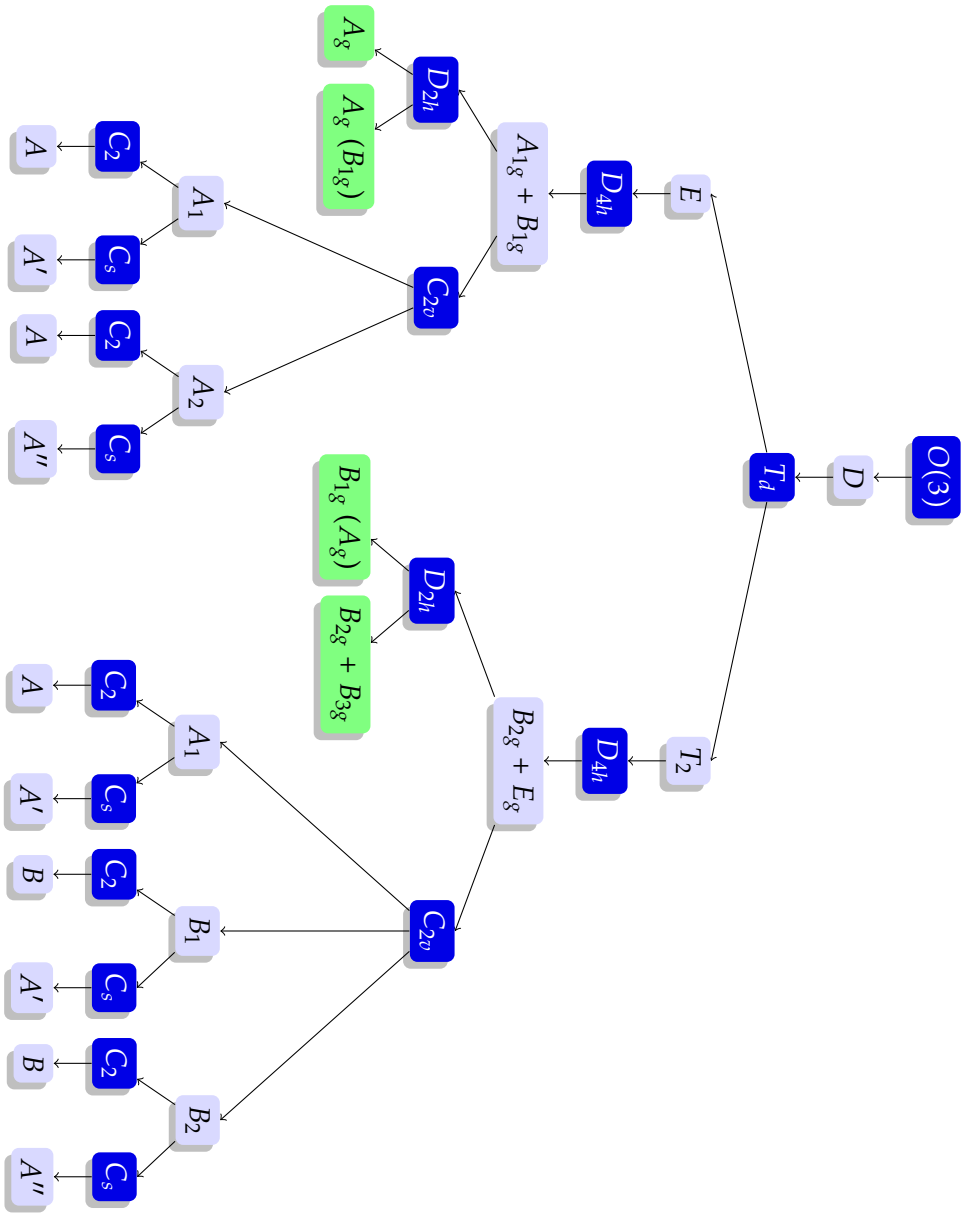


Figure .2.: Descent in symmetry of D (O(3)).

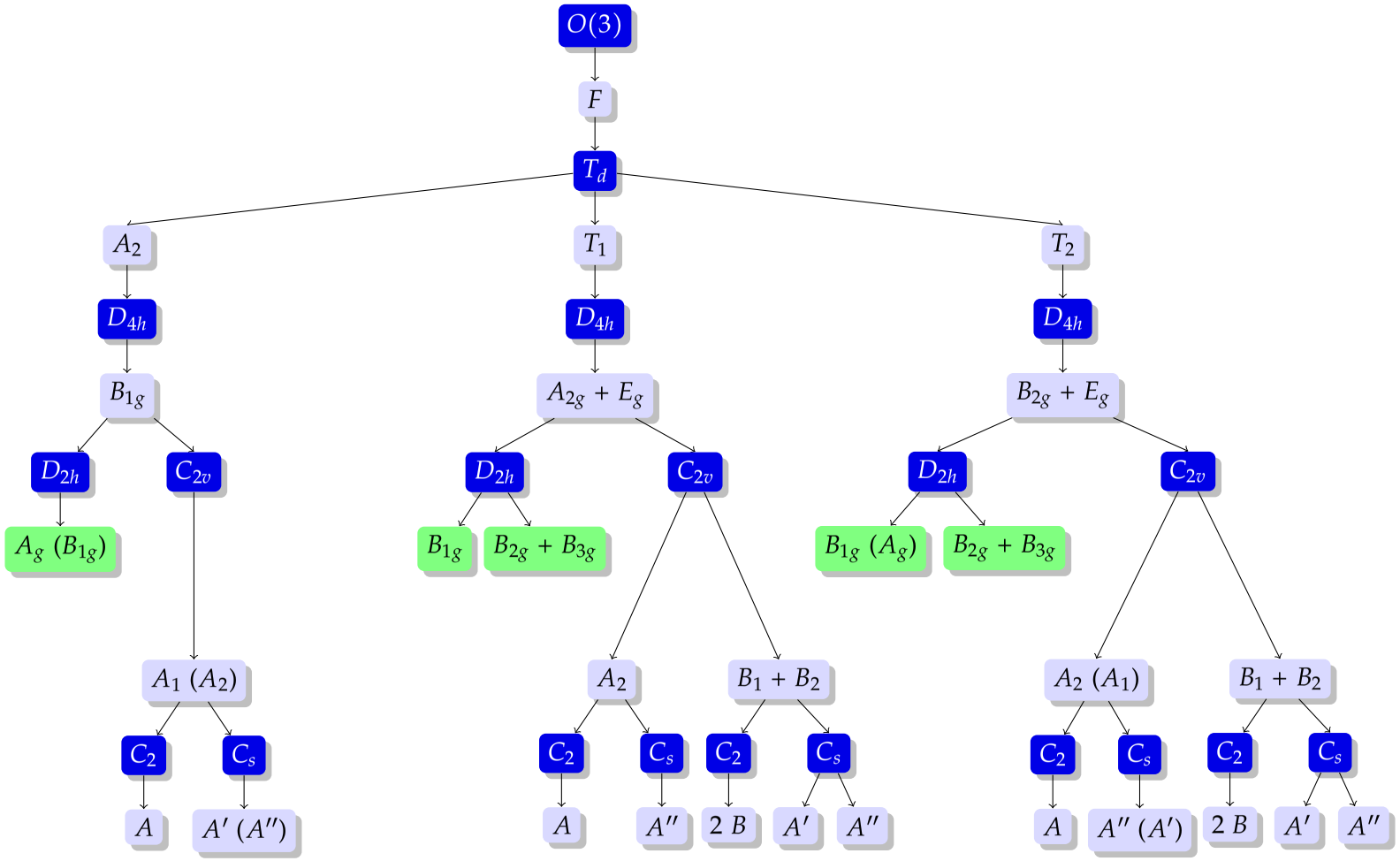


Figure .3.: Descent in symmetry of F ($O(3)$).

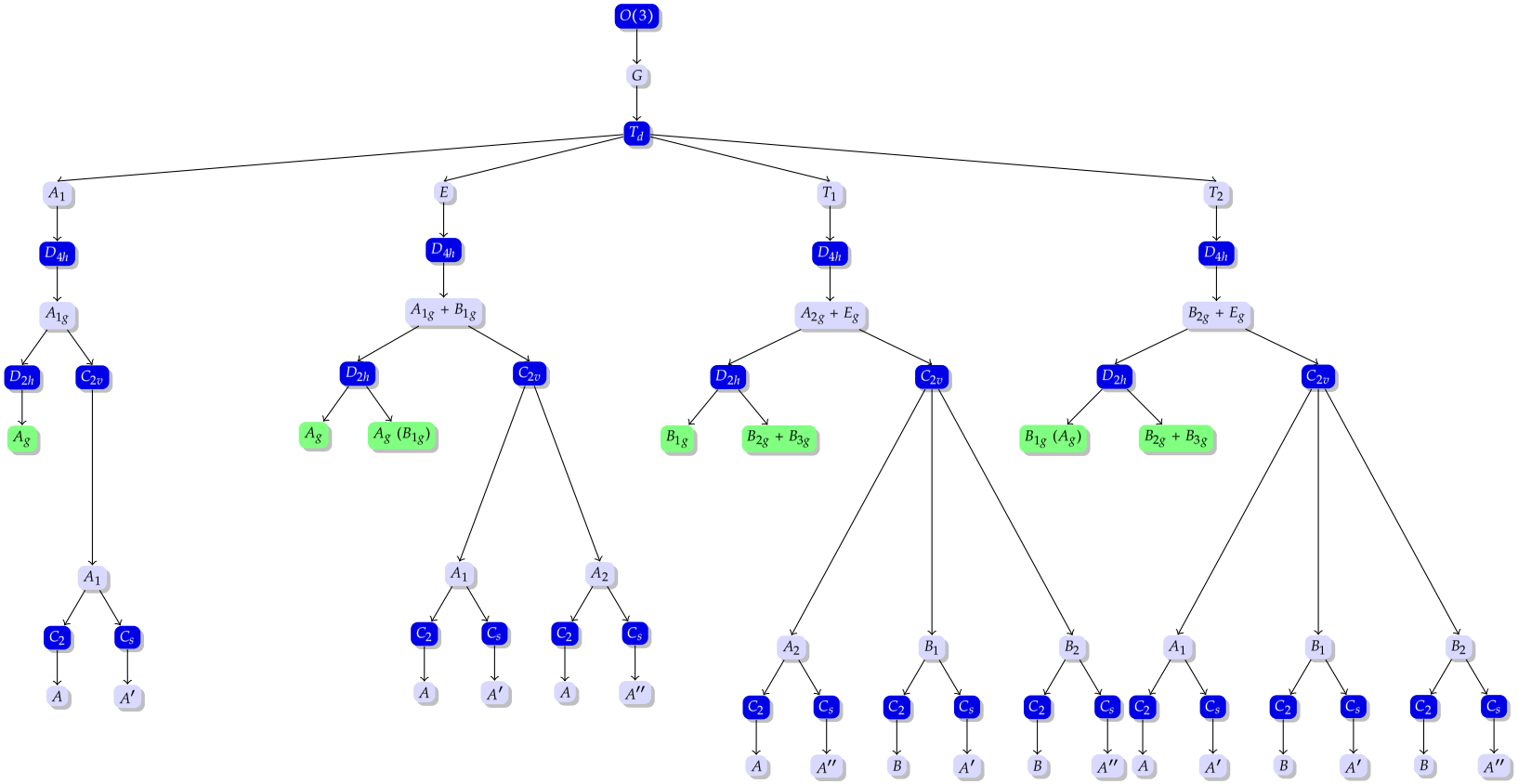


Figure .4.: Descent in symmetry of G ($O(3)$).

# Bibliography


1. Atwood, D. *The Rare Earth Elements: Fundamentals and Applications* <http://books.google.at/books?id=JJguj5Pq-8oC> (Wiley, 2013).
2. Bünzli, J.-C. & Piguet, C. Taking advantage of luminescent lanthanide ions. *Chemical Society Reviews* **34,** 1048–1077 (2005).
3. Buschow, K. H. J. *New Permanent Magnet Materials* <http://books.google.at/books?id=aZkicgAACAAJ> (North-Holland, 1986).
4. Croat, J. J. Neodymium-iron-boron permanent magnets prepared by rapid solidification. English. *Journal of Materials Engineering* **10,** 7–13 (1988).
5. Herbst, J. F. Permanent Magnets. *American Scientist* **81,** 252–260 (1993).
6. Wimmer, A. C. *Die Chemischen Elemente* (SMT Metalle Wimmer, Weinburg, Österreich, 2012).
7. Geusic, J. E., Marcos, H. M. & Van Uitert, L. G. Laser Oscillations in Nd-doped Yttrium Aluminium, Yttrium Gallium and Gadolinium Garnets. *Applied Physics Letters* **4,** 182–184 (1964).
8. Yariv, A. *Quantum Electronics* 3rd ed., 704 (Wiley, 1989).
9. Yao, M. & Chen, W. Hypersensitive Luminescence of $Eu^{3+}$ in Dimethyl Sulfoxide As a New Probing for Water Measurement. *Analytical Chemistry* **83,** 1879–1882 (2011).
10. Yao, M. *et al.* Luminescence of Lanthanide–Dimethyl Sulfoxide Compound Solutions. *The Journal of Physical Chemistry B* **115,** 9352–9359 (2011).
11. Smentek, L. Theoretical description of the spectroscopic properties of rare earth ions in crystals. *Physics Reports* **297,** 155–237 (1998).
12. Hüfner, S. *Optical spectra of transparent rare earth compounds* (Academic Press, Inc., 1978).
13. De Bettencourt-Dias, A. in *The Rare Earth Elements: Fundamentals and Applications* (ed Atwood, D. A.) (Wiley, 2013).

14. Maron, L. & Eisenstein, O. Do f Electrons Play a Role in the Lanthanide–Ligand Bonds? A DFT Study of $Ln(NR_2)_3$; R = H, $SiH_3$. *The Journal of Physical Chemistry A* **104,** 7140–7143 (2000).

15. Culberson, J. C., Knappe, P., Rösch, N. & Zerner, M. C. An intermediate neglect of differential overlap (INDO) technique for lanthanide complexes: studies on lanthanide halides. English. *Theoretica chimica acta* **71,** 21–39 (1987).

16. De Sá, G. F *et al.* Spectroscopic properties and design of highly luminescent lanthanide coordination complexes. *Coordination Chemistry Reviews* **196,** 165–195 (2000).

17. Richardson, F. S. Terbium(III) and europium(III) ions as luminescent probes and stains for biomolecular systems. *Chemical Reviews* **82,** 541–552 (1982).

18. Claude G. Bünzli, J. The europium(III) ion as spectroscopic probe in bioinorganic chemistry. *Inorganica Chimica Acta* **139,** 219–222 (1987).

19. Jørgensen, C. K. & Judd, B. Hypersensitive pseudoquadrupole transitions in lanthanides. *Molecular Physics* **8,** 281–290 (1964).

20. Knecht, S. *Parallel Relativistic Multiconfiguration Methods: New Powerful Tools for Heavy-Element Electronic-Structure Studies.* PhD thesis (Mathematisch-Naturwissenschaftliche Fakultät, Heinrich-Heine-Universität Düsseldorf, Deutschland, 2009).

21. Reiher, M. & Wolf, A. *Relativistic Quantum Chemistry* (WILEY-VCH Verlag GmbH & Co. KGaA, Weinheim, 2009).

22. Smentek, L. & Wybourne, B. G. Relativistic f ↔ f transitions in crystal fields. *J. Phys. B: At. Mol. Opt. Phys* **33,** 3647–3651 (2000).

23. Tinkham, M. *Group Theory and Quantum Mechanics* unabridged republication of the work originally published by McGraw-Hill Book Company, New York, in 1964 (Dover Publications, Inc., Mineola, New York, 2003).

24. Gatterer, K. & Bettinelli, M. in *Advanced Materials and Techniques: Structure, Spectroscopy, Sol-Gel Glasses and Lasers* (The American University in Cairo, The Science Department, 2000).

25. Reinhold, J. *Quantentheorie der Moleküle* 3rd ed. (eds Sandten, U. & Hoffmann, K.) (Vieweg+Teubner, Wiesbaden, 2009).

26. Szabo, A. & Ostlund, N. S. *Modern Quantum Mechanics* (Dover, Mineola, New York, 1996).

27. Reinhold, J. *Quantentheorie der Moleküle. Eine Einführung* 3rd ed. (eds Sandten, U. & Hoffmann, K.) (Vieweg+Teubner, Wiesbaden, 2009).

28. Carnall, W., Crosswhite, H. & Crosswhite, H. *Energy level structure and transition probabilities of the trivalent lanthanides in $LaF_3$* (Argonne National Laboratory, 1977).

29. Lueken, H. *Magnetochemie: Eine Einführung in Theorie und Anwendung* Hrsg.: Ch. Elschenbroich, F. Hensel, H. Hopf (B. G. Teubner, 1999).

30. Wigner, E. P. *Group Theory* (Academic Press, New York, 1959).

31. Eckart, C. The Application of Group Theory to the Quantum Dynamics of Monatomic Systems. *Rev. Mod. Phys.* **2,** 305–380 (1930).

32. Campbell, M. *Energy Transfer Processes in Erbium Elpasolites* PhD thesis (Department of Chemistry, Birkbeck College, University of London, 1997).

33. Deutschbein, O. Experimentelle Untersuchungen über die Vorgänge bei der Lichtemission. *Annalen der Physik* **428,** 183–188 (1939).

34. Peacock, R. D. The Intensities of Lanthanide f ↔ f Transitions. *Struct. Bond.* **22,** 83–122 (1975).

35. Van Vleck, J. H. The Puzzle of Rare-earth Spectra in Solids. *The Journal of Physical Chemistry* **41,** 67–80 (1937).

36. Judd, B. R. Optical Absorption Intensities of Rare-Earth Ions. *Phys. Rev.* **127,** 750–761 (3 1962).

37. Ofelt, G. S. Intensities of Crystal Spectra of Rare-Earth Ions. *The Journal of Chemical Physics* **37,** 511–520 (1962).

38. Smentek, L. Judd—Ofelt theory: past, present and future. *Molecular Physics* **101,** 893–897 (2003).

39. Nielson, C. & Koster, G. *Spectroscopic Coefficients for the $p^n$, $d^n$, and $f^n$* (MIT Press, 1963).

40. Görller-Walrand, C. & Binnemans, K. in *Handbook on the Physics and Chemistry of Rare Earths* (eds Jr., K. A. G. & Eyring, L.) 101–264 (Elsevier, 1998). <http://www.sciencedirect.com/science/article/pii/S0168127398250069>.

41. Carnall, W. T., Fields, P. R. & Rajnak, K. Spectral Intensities of the Trivalent Lanthanides and Actinides in Solution. II. $Pm^{3+}$, $Sm^{3+}$, $Eu^{3+}$, $Gd^{3+}$, $Tb^{3+}$, $Dy^{3+}$, and $Ho^{3+}$. *The Journal of Chemical Physics* **49,** 4412–4423 (1968).

42. French, A. & Taylor, E. F. *An Introduction to Quantum Physics* 696 (W. W. Norton & Company, Inc., 1978).

43. Babu, P. & Jayasankar, C. Optical spectroscopy of $Eu^{3+}$ ions in lithium borate and lithium fluoroborate glasses. *Physica B: Condensed Matter* **279,** 262–281 (2000).

44. Wen, S., Zhang, X., Hu, S., Zhang, L. & Liu, L. Fluorescence and Judd-Ofelt analysis of rare earth complexes with maleic anhydride and acrylic acid. *Journal of Rare Earths* **26,** 787–791 (2008).

45. De Mello Donegá, C, S. Alves, J. & de Sá, G. F. Synthesis, luminescence and quantum yields of Eu(III) mixed complexes with 4,4,4-trifluoro-1-phenyl-1,3-butanedione and 1,10-phenanthroline-N-oxide. *Journal of Alloys and Compounds* **250,** 422–426 (1997).

46. Wybourne, B. G. Effective Operators and Spectroscopic Properties. *The Journal of Chemical Physics* **48,** 2596–2611 (1968).

47. Carnall, W. T., Fields, P. R. & Wybourne, B. G. Spectral Intensities of the Trivalent Lanthanides and Actinides in Solution. I. $Pr^{3+}$, $Nd^{3+}$, $Er^{3+}$, $Tm^{3+}$, and $Yb^{3+}$. *The Journal of Chemical Physics* **42,** 3797–3806 (1965).

48. Mason, S. F., Peacock, R. D. & Stewart, B. Ligand-polarization contributions to the intensity of hypersensitive trivalent lanthanide transitions. *Molecular Physics* **30,** 1829–1841 (1975).

49. Henrie, D., Fellows, R. & Choppin, G. Hypersensitivity in the electronic transitions of lanthanide and actinide complexes. *Coordination Chemistry Reviews* **18,** 199–224 (1976).

50. Malta, O. Lanthanide f ↔ f transitions hypersensitive to the environment. *Molecular Physics* **42,** 65–72 (1981).

51. Malta, O. L. *Intensities of 4f - 4f Transitions in Glass Materials* English. tópico IV. Departamento de Química Fundamental - CCEN - UFPE. Cidade Universitária. <http://sampa.iq.unesp.br/EAMGM/Curso-Espec-Ln2013-PDF/Intensidades%20f-f%20em%20vidros.pdf>.

52. Blasse, G., Bril, A. & Nieuwpoort, W. On the $Eu^{3+}$ fluorescence in mixed metal oxides: Part I—The crystal structure sensitivity of the intensity ratio of electric and magnetic dipole emission. *Journal of Physics and Chemistry of Solids* **27,** 1587–1592 (1966).

53. Dyall, K. G. & Knut Fægri, J. *Introduction to Relativistic Quantum Chemistry* (Oxford University Press, Inc., New York, 2007).

54. Gell-Mann, M. The interpretation of the new particles as displaced charge multiplets. English. *Il Nuovo Cimento* **4,** 848–866 (1956).

55. Saue, T. Relativistic Hamiltonians for Chemistry: A Primer. *ChemPhysChem* **12,** 3077–3094 (2011).

56. Born, M. & Oppenheimer, R. Zur Quantentheorie der Molekeln. *Annalen der Physik* **389,** 457–484 (1927).

57. Breit, G. The Effect of Retardation on the Interaction of Two Electrons. *Phys. Rev.* **34,** 553–573 (4 1929).

58. Saue, T. *Principles and Application of Relativistic Molecular Calculations.* PhD thesis (Department of Chemistry, Faculty of Mathematics and Natural Sciences, University of Oslo, Norway, 1995).

59. Saue, T. Spin-Interactions and the Non-relativistic Limit of Electrodynamics. *Advances in Quantum Chemistry* **48** (ed Sabin, J.) 383–405 (2005).

60. Talman, J. D. Minimax Principle for the Dirac Equation. *Physical Review Letters* **57,** 1091–1094 (1986).

61. DIRAC, a relativistic ab initio electronic structure program, Release DIRAC12 (2012), written by H. J. Aa. Jensen, R. Bast, T. Saue, and L. Visscher, with contributions from V. Bakken, K. G. Dyall, S. Dubillard, U. Ekström, E. Eliav, T. Enevoldsen, T. Fleig, O. Fossgaard, A. S. P. Gomes, T. Helgaker, J. K. Lærdahl, Y. S. Lee, J. Henriksson, M. Iliaš, Ch. R. Jacob, S. Knecht, S. Komorovský, O. Kullie, C. V. Larsen, H. S. Nataraj, P. Norman, G. Olejniczak, J. Olsen, Y. C. Park, J. K. Pedersen, M. Pernpointner, K. Ruud, P. Sałek, B. Schimmelpfennig, J. Sikkema, A. J. Thorvaldsen, J. Thyssen, J. van Stralen, S. Villaume, O. Visser, T. Winther, and S. Yamamoto (see http://www.diracprogram.org). 2012. <http://www.diracprogram.org>.

62. Heully, J. L., Lindgren, I, Lindroth, E, Lundqvist, S & Mårtensson-Pendrill, A. M. Diagonalisation of the Dirac Hamiltonian as a basis for a relativistic many-body procedure. *Journal of Physics B: Atomic and Molecular Physics* **19,** 2799 (1986).

63. Foldy, L. L. & Wouthuysen, S. A. On the Dirac Theory of Spin 1/2 Particles and Its Non-Relativistic Limit. *Phys. Rev.* **78,** 29–36 (1 1950).

64. Douglas, M. & Kroll, N. M. Quantum electrodynamical corrections to the fine structure of helium. *Annals of Physics* **82,** 89–155 (1974).

65. Hess, B. A. Relativistic electronic-structure calculations employing a two-component no-pair formalism with external-field projection operators. *Phys. Rev. A* **33,** 3742–3748 (6 1986).

66. Neese, F. & Wennmohs, F. *ORCA - An ab initio, DFT and semiempirical SCF-MO package* Version 3.0. Max-Planck-Institute for Chemical Energy Conversion (45470 Mülheim a. d. Ruhr, Germany, 2013).

67. Fleig, T, Olsen, J & Marian, C. M. The generalized active space concept for the relativistic treatment of electron correlation. I. Kramers-restricted two-component configuration interaction. *J. Chem. Phys.* **114,** 4775 (2001).

68. Fleig, T., Olsen, J. & Visscher, L. The generalized active space concept for the relativistic treatment of electron correlation. II. Large-scale configuration interaction implementation based on relativistic 2- and 4-spinors and its application. *The Journal of Chemical Physics* **119,** 2963–2971 (2003).

69. Fleig, T., Jensen, H. J. A., Olsen, J. & Visscher, L. The generalized active space concept for the relativistic treatment of electron correlation. III. Large-scale configuration interaction and multiconfiguration self-consistent-field four-component methods with application to $UO_2$. *The Journal of Chemical Physics* **124,** 104106–1 (2006).

70. Fleig, T. *Wave Function Based Multi-Reference Electron Correlation Methods for the Relativistic Computation of Atomic and Molecular Properties. Development and Application.* Habilitationsschrift (Mathematisch-Naturwissenschaftliche Fakultät, Heinrich-Heine-Universität Düsseldorf, Deutschland, 2006). <http://dirac.chem.sdu.dk/thesis/06.Timo_Fleig_Habilitation.pdf>.

71. Jensen, F. *Introduction to Computational Chemistry* 2nd ed. (John Wiley & Sons Ltd, 2007).

72. Neese, F. The ORCA program system. *Wiley interdisciplinary Reviews - Computational Molecular Science* **2.** ORCA 3.0, 73–78 (2012).

73. Heß, B. A., Marian, C. M., Wahlgren, U. & Gropen, O. A mean-field spin-orbit method applicable to correlated wavefunctions. *Chemical Physics Letters* **251,** 365–371 (1996).

74. Neese, F. Efficient and accurate approximations to the molecular spin-orbit coupling operator and their use in molecular g-tensor calculations. *The Journal of Chemical Physics* **122,** 034107/1 (2005).

75. Dyall, K., Gomes, A. & Visscher, L. *Theor. Chem. Acc.* (2010).

76. Dunning, T. H. Gaussian basis sets for use in correlated molecular calculations. I. The atoms boron through neon and hydrogen. *The Journal of Chemical Physics* **90,** 1007–1023 (1989).

77. *Pick the right basis for your calculation* The authors of DIRAC. <http://diracprogram.org/doc/master/molecule_and_basis/basis.html> (28.02.2014).

78. Dyall, K. *Dyall Basis Sets* <http://dirac.chem.sdu.dk/basisarchives/dyall/index.html> (28.02.2014).

79. Dolg, M. *Effective Core Potentials* in *Modern Methods and Algorithms of Quantum Chemistry* (ed Grotendorst, J.) **3** (2000), 507–540. <http://www.uni-koeln.de/math-nat-fak/tcchem/mitarbeiter/dolg/dolg/dolg.pdf>.

80. Dolg, M., Stoll, H., Savin, A. & Preuss, H. *Theor. Chim. Acta* **75,** 369–87 (1989).

81. Wood, J. H. & Boring, A. M. Improved Pauli Hamiltonian for local-potential problems. *Phys. Rev. B* **18,** 2701–2711 (6 1978).

82. Dolg, M., Stoll, H. & Preuss, H. *Theor. Chim. Acta* **85,** 441–50 (1993).

83. *Pseudopotentials, ECPs* Universität Stuttgart. <http://www.theochem.uni-stuttgart.de/pseudopotentials/index.en.html> (28.02.2014).

84. Hohenberg, P. & Kohn, W. Inhomogeneous Electron Gas. *Phys. Rev.* **136,** B864–B871 (3B 1964).

85. Vosko, S. H., Wilk, L. & Nusair, M. Accurate spin-dependent electron liquid correlation energies for local spin density calculations: a critical analysis. *Canadian Journal of Physics* **58,** 1200–1211 (1980).

86. Becke, A. D. Density-functional exchange-energy approximation with correct asymptotic behavior. *Phys. Rev. A* **38,** 3098–3100 (6 1988).

87. Lee, C., Yang, W. & Parr, R. G. Development of the Colle-Salvetti correlation-energy formula into a functional of the electron density. *Phys. Rev. B* **37,** 785–789 (2 1988).

88. Perdew, J. P., Burke, K. & Ernzerhof, M. Generalized Gradient Approximation Made Simple. *Phys. Rev. Lett.* **77,** 3865–3868 (18 1996).

89. Becke, A. D. A new mixing of Hartree-Fock and local density-functional theories. *The Journal of Chemical Physics* **98,** 1372–1377 (1993).

90. Becke, A. D. Density-functional thermochemistry. III. The role of exact exchange. *The Journal of Chemical Physics* **98,** 5648–5652 (1993).

91. Desrochers, P. J. *et al.* Electronic Structure of Nickel(II) and Zinc(II) Borohydrides from Spectroscopic Measurements and Computational Modeling. *Inorganic Chemistry* **51,** 2793–2805 (2012).

92. Bühl, M., Reimann, C., Pantazis, D. A., Bredow, T. & Neese, F. Geometries of Third-Row Transition-Metal Complexes from Density-Functional Theory. *Journal of Chemical Theory and Computation* **4,** 1449–1459 (2008).

93. Altmann, S. L. & Herzig, P. *Point-Group Theory Tables* 2nd. <https://phaidra.univie.ac.at/detail_object/o:104731> (Wien, 2011).

94. Kramers, H. A. *Théorie générale de la rotation paramagnétique dans les cristaux* in *Koninklijke Akademie van Wetenschappen* **33** (1930), 959–972. <http://www.dwc.knaw.nl/DL/publications/PU00015981.pdf>.

95. Saue, T. & Jensen, H. J. A. Quaternion symmetry in relativistic molecular calculations: The Dirac–Hartree–Fock method. *The Journal of Chemical Physics* **111,** 6211–6222 (1999).

96. Wedler, G. *Lehrbuch der Physikalischen Chemie* 5th ed. (Wiley, Weinheim, 2004).

97. Fuchs, E. C. & Gatterer, K. Colour change of co-doped yttrium aluminium borate crystals under illumination with different white light sources. English. *Central European Journal of Chemistry* **6,** 497–504 (2008).

98. Kuo, Y.-P., Lu, H.-C., Wu, Y.-J., Cheng, B.-M. & Ogilvie, J. Absorption spectra in the vacuum ultraviolet region of methanol in condensed phases. *Chemical Physics Letters* **447,** 168–174 (2007).

99. Wachtler, M. *Preparation and Optical Investigation of Rare-Earth Doped Lead Germanate Glasses* Diplomarbeit (Technische Universität Graz, 1996).

100. Krupke, W. F. Optical Absorption and Fluorescence Intensities in Several Rare-Earth-Doped $Y_2O_3$ and $LaF_3$ Single Crystals. *Phys. Rev.* **145,** 325–337 (1 1966).

101. Balakrishna, A., Rajesh, D. & Ratnakaram, Y. Structural and optical properties of $Nd^{3+}$ in lithium fluoro-borate glass with relevant modifier oxides. *Optical Materials* **35,** 2670–2676 (2013).

102. Mahamuda, S. *et al.* Spectroscopic properties and luminescence behavior of $Nd^{3+}$ doped zinc alumino bismuth borate glasses. *Journal of Physics and Chemistry of Solids* **74,** 1308–1315 (2013).

103. Beeby, A. & Faulkner, S. Luminescence from neodymium(III) in solution. *Chemical Physics Letters* **266,** 116–122 (1997).

104. But, S. *et al.* Spectroscopic properties of neodymium(III)-containing polyoxometalates in aqueous solution. *Spectrochimica Acta Part A: Molecular and Biomolecular Spectroscopy* **62,** 478–482 (2005).

105. Van Duijnen, P. T. & Swart, M. Molecular and Atomic Polarizabilities: Thole's Model Revisited. *J. Phys. Chem. A* **102,** 2399–2407 (1998).

106. Bayliss, N. & McRae, E. Solvent effects in the spectra of acetone, crotonaldehyde, nitromethane and nitrobenzene. *J. Phys. Chem.* **58,** 1006–1011 (1954).

107. Devi, A. & Jayasankar, C. Optical properties of $Nd^{3+}$ ions in lithium borate glasses. *Materials Chemistry and Physics* **42,** 106–119 (1995).

108. Lu, J. *et al.* Optical properties of $Nd(TTA)_3(TPPO)_2$ doped polymer and its potential laser application. *Optical Materials* **30,** 1531–1537 (2008).

109. Rajesh, D., Balakrishna, A., Seshadri, M. & Ratnakaram, Y. Spectroscopic investigations on $Pr^{3+}$ and $Nd^{3+}$ doped strontium-lithium-bismuth borate glasses. *Spectrochimica Acta Part A: Molecular and Biomolecular Spectroscopy* **97,** 963–974 (2012).

110. Ratnakaram, Y., kumar, A. V., Naidu, D., Chakradhar, R. & Ramesh, K. Optical absorption and luminescence properties of $Nd^{3+}$ in mixed alkali borate glasses–Spectroscopic investigations. *Journal of Luminescence* **110,** 65–77 (2004).

111. Pal, I., Agarwal, A., Sanghi, S., Aggarwal, M. & Bhardwaj, S. Fluorescence and radiative properties of $Nd^{3+}$ ions doped zinc bismuth silicate glasses. *Journal of Alloys and Compounds* **587,** 332–338 (2014).

112. Murthy, D. *et al.* Investigation on luminescence properties of $Nd^{3+}$ ions in alkaline-earth titanium phosphate glasses. *Optics Communications* **284,** 603–607 (2011).

113. Carnall, W. T., Fields, P. R. & Rajnak, K. Electronic Energy Levels of the Trivalent Lanthanide Aquo Ions. IV. $Eu^{3+}$. *The Journal of Chemical Physics* **49,** 4450–4455 (1968).

114. Chen, B. *et al.* Optical properties of a tetradentate bis($\beta$-diketonate) europium(III) complex. *Spectrochimica Acta Part A: Molecular and Biomolecular Spectroscopy* **70,** 1203–1207 (2008).

115. Luo, Y. *et al.* Judd–Ofelt treatment on luminescence of europium complexes with $\beta$-diketone and bis($\beta$-diketone). *Journal of Luminescence* **129,** 1309–1313 (2009).

116. Liang, H., Yang, Z., Xiao, L. & Xie, F. Radiative transition probability of a europium (III) chelating polymer. *OAM-RC* **4,** 1396–1399 (2010).

117. Xu, C.-J., Zhang, P.-F., Liu, F.-M. & Shi, Y.-Q. Photophysical properties and Judd-Ofelt analysis of a europium complex with 5-amino-1,10-phenanthroline. *Synthetic Metals* **162,** 18–21 (2012).

118. Dejneka, M., Snitzer, E. & Riman, R. Blue, green and red fluorescence and energy transfer of $Eu^{3+}$ in fluoride glasses. *Journal of Luminescence* **65,** 227–245 (1995).

119. Nageno, Y., Takebe, H., Morinaga, K. & Izumitani, T. Effect of modifier ions on fluorescence and absorption of $Eu^{3+}$ in alkali and alkaline earth silicate glasses. *Journal of Non-Crystalline Solids* **169,** 288–294 (1994).

120. Frisch, M. J. *et al. Gaussian 09 Revision C.01* Gaussian Inc. Wallingford CT 2009.

121. Schäfer, A., Horn, H. & Ahlrichs, R. Fully optimized contracted Gaussian-basis sets for atoms Li to Kr. *J. Chem. Phys.* **97,** 2571–77 (1992).

122. Schäfer, A., Huber, C. & Ahlrichs, R. Fully optimized contracted Gaussian-basis sets of triple zeta valence quality for atoms Li to Kr. *J. Chem. Phys.* **100,** 5829–35 (1994).

123. Brecknell, D. J., Raber, D. J. & Ferguson, D. M. Structures of lanthanide shift reagent complexes by molecular mechanics computations. *Journal of Molecular Structure: THEOCHEM* **124,** 343–351 (1985).

124. Ferguson, D. M. & Raber, D. J. Molecular mechanics calculations of several lanthanide complexes: An application of the random incremental pulse search. *Journal of Computational Chemistry* **11,** 1061–1071 (1990).

125. *Drehmatrix* Wikipedia, Die freie Enzyklopädie. <http://de.wikipedia.org/wiki/Drehmatrix> (04.04.2014).

126. Iliaš, M. & Saue, T. An infinite-order two-component relativistic Hamiltonian by a simple one-step transformation. *The Journal of Chemical Physics* **126,** 064102–1 (2007).

127. Visscher, L., Visser, O., Aerts, P. J. C., Merenga, H. & Nieuwpoort, W. C. Relativistic quantum chemistry: the MOLFDIR program package. *Computer Physics Communications* **81,** 120–144 (1994).

128. Holzer, C. *Quantum Chemical Calculations on Eu-Quinolinate Complexes* in *Central European Symposium on Theoretical Chemistry* (eds Tarana, M. & Čurík, R.) Poster (J. Heyrovský Institute of Physical Chemistry, Znojmo, Czech Republic, 2013).

129. Pantazis, D. A., Chen, X. Y., Landis, C. R. & Neese, F. *J. Chem. Theory Comput.* **4,** 908 (2008).

130. Pantazis, D. A. & Neese, F. *J. Chem. Theory Comput.* **5,** 2229 (2009).

131. Ahlrichs, R. & coworkers. H - Kr.

132. Gschneidner, K. A., Bünzli, J.-C. & Pecharsky, V. K. *Handbook on the Physics and Chemistry of Rare Earths: Optical Spectroscopy* <http://books.google.at/books?id=7SeUxda5ffEC> (Elsevier Science, 2011).

133. Cotton, S. *Lanthanide and actinide chemistry* (Wiley, England Hoboken, NJ, 2006).

134. Hatanaka, M. & Yabushita, S. An ab initio study on the f-f hypersensitive transition intensities of lanthanide tribromide molecules. *Chemical Physics Letters* **504,** 193–198 (2011).

135. Hazenkamp, M. F. & Blasse, G. Rare-earth ions adsorbed onto porous glass: luminescence as a characterizing tool. *Chemistry of Materials* **2,** 105–110 (1990).

136. Naleway, C. *et al.* An ab initio study of the ionization potentials and f–f spectroscopy of europium atoms and ions. *The Journal of Chemical Physics* **116,** 5481–5493 (2002).

137. Mason, S., Peacock, R. & Stewart, B. Dynamic coupling contributions to the intensity of hypersensitive lanthanide transitions. *Chemical Physics Letters* **29,** 149–153 (1974).

138. Mason, S. F., Peacock, R. D. & Stewart, B. Ligand-polarization contributions to the intensity of hypersensitive trivalent lanthanide transitions. *Molecular Physics* **30,** 1829–1841 (1975).

139. Peacock, R. D. The charge-transfer contribution to the intensity of hypersensitive trivalent lanthanide transitions. *Molecular Physics* **33,** 1239–1246 (1977).

140. Peacock, R. D. The intensities of laporte forbidden transitions of the d- and f-block transition metal ions. *Journal of Molecular Structure* **46,** 203–227 (1978).